Design of Luminescent Magnetic Nanostructures for Sensor, Drug Delivery and Bioimaging Applications

A Dissertation

Submitted to

National Institute of Technology, Rourkela

for the Degree of

Doctor of Philosophy

in

Chemistry

By

Ms. Swagatika Sahu

Department of Chemistry
National Institute of Technology
Rourkela-769008

Dedicated to My Parents

CERTIFICATE

Dr. Sasmita Mohapatra
Assistant Professor
Department of Chemistry
National Institute of Technology
Rourkela, India

This is to certify that the thesis entitled "**Design of luminescent magnetic nanostructures for sensor, drug delivery and bioimaging applications**" being submitted by Ms. Swagatika Sahu, to the National Institute of Technology, Rourkela, India, for the award of the degree of **Doctor of Philosophy** is a record of bonafide research carried out by her under my supervision. I am satisfied that the thesis has reached the standard fulfilling the requirements of the regulations relating to the nature of the degree. The contents of the thesis have not been submitted to any other university or institute for the award of any degree.

Date: **Dr. Sasmita Mohapatra**

Department of Chemistry, National Institute of Technology, Rourkela-769 008, India
sasmitam@nitrkl.ac.in, sasmita05@gmail.com
Voice: + (91)-661 246 2661

Acknowledgement

First, I would like to express my most genuine gratitude to my advisor Prof. Sasmita Mohapatra for recruiting me and providing consistent support during the entire period of my research work. Thanks to her disciplinary supervision, inspiring instruction and generous help, I am able to successfully finish my work in time.

I would like to record my sincere thanks to Prof. N. Panda, Head, Department of Chemistry, NIT Rourkela for his valuable suggestions and providing me the necessary facilities required to make this program a success.

I sincerely thank my DSC members Prof. A. Sahoo, Prof. S. Patel and Prof. U. Subuddhi for their valuable inputs during the entire course of my work.

I wish to express my thanks to numerous technical and non-technical staffs of chemistry department and other departments of NIT Rourkela for their continuous cooperation throughout the Ph. D. programme.

I want to thank our collaborators, Prof. T. K. Maiti and Prof. S. K. Ghosh from Department of Biotechnology, IIT Kharagpur, Prof. S. K. Bhutia from Department of Life Science, NIT Rourkela and Dr. M. Majhi from Department of Radiology, Ispat General Hospital, Rourkela for their brilliant input in carrying out all biological work. I owe my appreciation to my collaborator Birendra Behera, Niharika Sinha and Santoshi Nayak without whom it would not have been possible for me to complete such an interdisciplinary work.

I would especially like to thank my friends Banalata Sahoo, Suryakanta Nayak (IIT Kharagpur), Biswonath Biswal, Gobinda Chandra Behera, Niranjan Biswal, Satyabadi Martha, Sanjeet Majhi, K. K. Nanda (IMMT Bhubaneswar), Yashbanta Narayan Singhababu (NML Jamshedpur), Harakrishna Sahoo (IIT Guwhati), Ashish Das (IIT, Madaras), Sanjit Mana and my sister Smaranika Sahu (Utkal University, Bhubaneswar) for their magnanimous help in doing various characterization such as Raman, TEM, XPS, Low angle XRD, magnetic measurement required for my dissertation work. This list is incomplete without acknowledging Dr. J. Dandpat, Head, Department of Biotechnology, Utkal University, who provided fluorimeter facility to carry out my research work.

I am indebted to Ashis Kumar Jena and Raghavender Muthukori for providing me experimental hands-on-training on different aspects of organic reactions. I would like to thank my labmates Rahul and Smruti for providing funfilled and enjoyable atmosphere in laboratory. Specially, I am very much fortunate to have a helpful supportive labmate like Rahul at the last year of my research work.

I am thankful to the "NIT Rourkela", for financial assistance and various facilities extended by the NIT, Rourkela.

My time at NIT Rourkela was made enjoyable in large part due to my many friends and my uncle, aunt along with their kids.

A special thanks to my family. Words cannot express how grateful I am to my mother, father, mother-in law, father-in-law, my brother, and sister for all of the sacrifices that they have made on my behalf. Your prayer for me was what sustained me thus far. I would also like to thank my beloved husband, Dr. Ashis Kumar Jena for supporting me for everything and inspiring me throughout this experience.

Finally I thank God for letting me through all the difficulties. You are the one who made me finish my degree.

Date:

NIT Rourkela, India **Swagatika Sahu**

Biography

Ms. Swagatika Sahu was born on 20th June 1985 and brought up in Baripada, Odisha, India. After graduating she joined Department of Chemistry, Utkal University, Odisha for carrying out her post-graduation study. She has received her post-graduate degree in 2008 and then migrates to School of Chemistry, Sambalpur University for her Master of Philosophy degree in Inorganic Chemistry. She has qualified Graduate Aptitude Test in Engineering in 2010 and 2011. She has also worked as project assistant in Department of Colloid and Material Chemistry, Institute of Mineral and Material Technology (CSIR laboratory in INDIA) from July 2009 to December 2010. After cultivating great interest in material chemistry, she has joined for doctoral research programme on December 2010 in Department of Chemistry, National Institute of Technology, Rourkela, India under the supervision of Prof. Sasmita Mohapatra. During her doctoral studies she has published several scientific papers in various international journals like *Chemical Communication, Journal of Material Chemistry B, Dalton Transactions, Analyst* etc. Her research work has been presented in many national and international conferences. Swagatika's research interest lies in fabrication of luminescent magnetic nanomaterials for sensor and biomedical applications.

Abstract

The present dissertation entitled, "**Design of Luminescent Magnetic Nanostructures for Sensor, Drug delivery and Bioimaging Applications**" is an embodiment of the investigations intended at developing simple inexpensive synthetic methods for producing luminescent carbon quantum dot and multifunctional magnetic luminescent nanostructures applicable for sensor and biomedical application. The in vitro applications of synthesized materials have also been investigated. The thesis is divided into two parts.

The first part of the thesis includes the low cost synthetic route for fabrication of carbon quantum dots (CD) and their composites for sensing and bioimaging applications. Highly photoluminescent CDs with a quantum yield of 26% have been synthesized in one step by hydrothermal treatment of orange juice (*Citrus nobilis deliciosa*). Due to high photostability and low toxicity these CDs have been demonstrated as excellent probes in cellular imaging. These synthesized CD has been also used for the development of reusable novel magnetic silica/CD based hybrid nanostructure for monitoring and separation of fluoride ion through fluorescence sensing and external magnetic field respectively. The assay is based on the binding of fluoride ion into magnetic receptor substituting already bound CD. This method is highly sensitive, fast and selective for fluoride ion in aqueous solution having a linear response range of 1 to 20 μM (R^2=0.992). The practical utility of the method is well tested with tap water and also extended for fluoride detection in cellular environment. Furthermore an easily separable sensitive CD based fluorescence glucose sensor comprising of CD deposited mesoporous silica nocomposite (m-SiO_2-CD) and 3-aminophenylboronic acid (APBA) has been prepared. The observed fluorescence recovery of quenched APBA adsorbed m-SiO_2-CD on addition of glucose is due to the formation of glucoboronate ester which could lift out the APBA from close vicinity of fluorophore. The boronic acid modified (m-SiO_2-CD-APBA) fluorescent probe is also explored for targeted imaging of colon cancer cell overexpressed with sialyl Lewis A (sLe^a) receptors. To improve the luminescence properties of the CD, nitrogen, sulphur co-doped carbon quantum dot (NSCD) with an improved fluorescent quantum yield of 69% have been synthesized from single molecular

precursor. The synthesized NSCD exhibits high selectivity and sensitivity towards mercury ion in aqueous environment. Due to high photostability, low toxicity and low detection limit as 0.05 nM, these NSCDs are demonstrated as excellent probes for the detection of Hg^{2+} in living cells

The second part of this thesis demonstrates the design and fabrication of multifunctional fluorescent magnetic nanostructures which are of special interest in cancer diagnostic and therapy. Multifunctional luminescent magnetic Fe_3O_4@mesoporous silica-YPO_4:Tb core-shell nanoparticle has been prepared for the storage as well as controlled targeted release of 5-fluorouracil (5-FU). The hydrophobic anticancer drug 5-FU has been successfully loaded on the fluorescent magnetic nanoparticles via formation of 5-FU/β-cyclodextrin inclusion complex which favors more sustained release at lower pH owing to stability of inclusion complex. These findings show that the developed multifunctional nanocomposite can be potentially used in magnetically guided delivery of 5-FU. Furthermore, hierarchical theranostic hollow magnetic mesoporous spherical particles with fluorescent carbon encapsulated within mesoporous framework have been prepared by hydrothermal carbonization approach. These fluorescent magnetic nanoparticles have been conjugated with hydrophobic drug camptothecin and a molecular marker folic acid using appropriate surface chemistry to ensure the targeted specific delivery of the camptothecin. The drug conjugated hybrid nanoparticles inhibit cell growth through induction of apoptosis as demonstrated in HeLa cells. In addition to this, the particles show MR contrast behaviour by affecting the proton relaxation with transverse relaxivity (r_2) 150.03 $mM^{-1}S^{-1}$.

Table of Contents

Part I: Fabrication of carbon quantum dot: Application in fluorescence sensing and bioimaging

Part I

Fabrication of Carbon Quantum Dot: Application in Fluorescence Sensing and Bioimaging

Chapter-1

Literature survey on carbon quantum dots and their application as fluorescent nanoprobe

1.1. Preface

Since last decades remarkable effort has been devoted for the development of luminescent materials due to their promising and diverse applications ranging from optoelectronics to biomedical fields, such as cellular imaging, biosensing, and drug delivery.[1-3] Among fluorescent nanomaterials organic dyes, quantum dots, metal nanoparticles and lanthanide nanomaterials are widely used.[4-7] Usually, dye molecules suffer from photobleaching and quenching due to interactions with solvent molecules when they are exposed to a variety of harsh environments.[8,9] More over poor aqueous solubility, broad absorption and emission bands, chemical instability, blinking properties and moderate quantum yields associated with these materials restrict their use. In the development of fluorescent nanomaterials, the discovery of semiconductor quantum dots (QDs) is considered as a major milestone. Semiconductor QDs usually have tunable and narrow emission spectral features, bright fluorescence, high photo-stability, and resistance to metabolic degradation in bioapplications.[10,11] However issues of toxicity due to use of heavy metal ions, photo-oxidation, and difficult surface conjugation chemistry associated with QDs limit their application.[12]

Recently, fluorescent carbon dots (CDs) have been proposed as a new generation of luminescent materials and as a viable alternative to these conventional fluorescent materials due to their excellent luminescence properties, including large two-photon excitation cross-sections, lack of blinking, high water solubility, low cytotoxicity, and excellent biocompatibility.[13-16] CDs are new class of recently discovered quasi-spherical nanocarbons with sizes below 10 nm comprising amorphous to nanocrystalline cores with predominantly graphitic or turbostratic carbon (sp^2 carbon) or graphene and graphene oxide sheets fused by diamond-like sp^3 hybridized carbon insertions.[13,17] CDs were first obtained accidentally by Xu *et al.* during the separation and purification of single-walled carbon nanotubes (SWCNTs), which triggered subsequent studies to exploit the fluorescence properties of CDs.[18] Since their discovery, these fluorescent carbon nanoparticles have come to be known as carbon dots and fabricated by numerous research groups to achieve better synthetic routes with improved properties, assemble a better understanding into the origins of their photophysical behavior and develop novel

applications of these nanomaterials. Similar to CD, another carbon based nanomaterials named as graphene quantum dots (GQDs) have generated exciting features and wide application, which has been extensively reviewed.[15,19] Basically GQDs are kind of CD with a large conjugated domain and regular structure, exhibiting excellent performance of graphene. Though the GQDs are even considered as a kind of CDs, still there are some differences exist between them. As GQDs are generally produced from graphene based starting materials, they clearly have graphitic lattices inside the dots,[20] whereas CDs can be either amorphous or crystalline.[21] Moreover, luminescent CDs comprise discrete, quasi-spherical carbon nanoparticles with sizes below 10 nm,[13,22] whereas GQDs consist of graphene sheets with lateral dimensions less than 100 nm in single-, double- and few- (3 to <10) layers.[23]

These CDs also possess several additional distinctive features, such as size- and wavelength-dependent luminescence emission, ease of production and bioconjugation, use of cheap and abundant raw materials. The various surface functional groups such as hydroxyl, carboxylic acid moieties present on CD surface imparts excellent water solubility and the suitability for subsequent functionalization with various organic, inorganic polymeric or biological species. Upon surface passivation, the fluorescence properties of CDs are enhanced.[24] Moreover these CDs exhibit excellent up- and down-conversion photoluminescence properties of CDs similar to semiconductor quantum dots.[25] With their bright one- and multi-photon fluorescence emissions and other linear and nonlinear optical properties, CDs have been pursued for a wide variety of applications including bioimaging, photodynamic therapy, fluorescent probing and analysis, and photocatalysis.[26-29] Particularly near-infrared excited photoluminescence emission of CD is significant and useful for in vivo bioimaging because of the transparency of body tissues in the NIR ‘‘water window’’.[30] Moreover the fluorescence properties of CDs can be quenched efficiently by either electron acceptor or electron donor molecules in solution, which offer exciting opportunities for light energy conversion, photovoltaic devices and related applications.[31,32] These interesting photoinduced electron transfer properties of CD can also be utilized for sensitive ion detection.[33,34] Owing to superior luminescence properties and potential applicability of CD, much effort has been made in the development of facile synthetic methodologies for

the synthesis of highly fluorescent CD suitable for above mentioned applications. Although there have been numerous efforts for synthesis of high quality CDs, there remain substantial challenges like to control particle aggregation, size and surface properties for particular application.

In this prospective our current exploration involves the development of facile synthetic method for quantitative production of high quality fluorescent CDs for sensing and imaging application. The detailed efforts in this field have been discussed in subsequent chapters. Relevant to our work, here we present the updated literature review on different synthetic approaches for CD and their sensing applications. We also discuss the fluorescence mechanism of CD in detail.

1.2.Synthesis of carbon dots

CDs are generally synthesized by two routes, namely the top-down route and the bottom-up route, and they can be modified during preparation or post-treatment. Top-down approaches consist of arc discharge,[18] electrochemical oxidation[35,36] and laser ablation technique,[31,37] where CDs are formed from break down of larger carbon structures, such as nanodiamonds,[38] graphite,[39] carbon nanotubes,[1] carbon soot,[2] activated carbon[40] and graphite oxide.[41] On the other hand bottom-up methods involve synthesis of CDs from molecular precursor such as citrate,[3] carbohydrates,[30,42] and polymeric molecule[43] through supported synthetic route,[44] combustion/thermal/hydrothermal treatment,[45-47] microwave/ultrasonic [48,49] and solution chemistry route.[50]

Top-down approach

Arc-discharge Method: CDs were first obtained ironically by Xu *et al.* while purifying single-walled carbon nanotubes (SWCNTs) from arc-discharged soot.[18] The arc-discharged soot was first oxidized with nitric acid to introduce carboxyl functional group, then extracted using sodium hydroxide solution, from which CDs were separated through gel electrophoresis. They also isolate different fractions of carbonaceous materials, which show size dependent fluorescent properties similar to semiconductor quantum dots.

Laser-Ablation Method: Sun and coworkers pioneered the synthesis of CDs by laser ablation of a carbon target in the presence of water vapour with argon as a carrier gas at 900 °C and 75 kPa.[39] The obtained non-fluorescent nanosized carbon particles on acid oxidative treatment followed by surface passivation using different polymeric agents such as diamine-terminated poly(ethylene glycol), poly(propionyl-ethylenimine-co-ethylenimine) showed bright fluorescence. A slightly modified technique using ^{13}C powder and more rigorous control was introduced to produce CDs with high quantum yield of 20%.[51] Hu *et al.* introduced a single-step procedure that integrated synthesis and passivation.[52] They used a pulsed Nd:YAG laser to irradiate graphite or carbon black dispersed in diamine hydrate, diethanolamine, or PEG200N for 2h, which serve as surface passivating agent. After laser irradiation centrifugation was carried out to obtain bright luminescent CD suspension. Subsequently a simple laser ablation technique was introduced by Li *et al.* to prepare CDs using nanocarbon and a simple solvent such as ethanol, acetone or water as liquid media.[53]

Electrochemical Oxidation: Electrochemical oxidation is a prevailing method to prepare CDs using various bulk carbon materials as precursors.[1,35] For the first time, Zhou's group demonstrated an electrochemical method to prepare CDs.[1] They grew multi-walled carbon nanotubes (MWCNTs) obtained from scrolled graphene layers on a carbon paper, which was then inserted into an electrochemical cell containing degassed acetonitrile with 0.1 M tetrabutylammonium perchlorate as the supporting electrolyte. They found that CDs were not formed from carbon paper devoid of MWCNTs. CDs were also synthesized by Chi and co-worker through electrochemical oxidation of graphite rod with a Pt mesh counter electrode, and Ag/AgCl reference electrode assembly in phosphate buffer solution (pH 7.0).[36] Ionic liquid (IL) assisted electro-oxidation of graphite produce a variety of carbon-based nanoparticles including CDs. Later an alkali-assisted electrochemical method was introduced by Kang *et al.* to prepare CDs with controlled sizes.[54] They used the graphite rods as both anode and cathode, and NaOH/EtOH as electrolyte, where alkaline environment is the key factor, and OH groups are essential for the formation of CDs. Subsequently large-scale synthesis of highly photocatalytic active CDs was synthesized by the same group using only pure water as an electrolyte without

any other chemical additives.[55] Interestingly the prepared CDs show both down- and up-conversion fluorescence emissions.

Bottom-up Approach

Microwave/Ultrasonic Synthesis: One of the rapid and low cost methods to synthesize CD is microwave irradiation of organic compounds. A microwave pyrolysis was introduced to synthesize CDs by combining PEG200 and a saccharide (for example, glucose, fructose) in water to form a transparent solution, followed by heating in a 500 W microwave oven for 2 to 10 min.[48] The duration of microwave heating controlled the size and fluorescence properties of these CDs. Qu *et al.* proposed a facile one-step microwave synthetic method to synthesize CDs without any surface passivating agent.[56] Microwave treatment of the mixture of carbohydrate (glycerol, glycol, glucose, sucrose, etc.) and a tiny amount of an inorganic ion in water produced CDs in few minutes. Zheng *et al.* explore the microwave-hydrothermal synthesis of fluorescent CDs using graphite oxide.[41] Green luminescent diethylene glycol stabilized CDs were obtained on microwave irradiation of sucrose.[57] There was no noticeable emission peak shift for synthesized CD over an excitation range from 320-380 nm. Moreover, these CDs could be used as a potential bioimaging agent, which were efficiently ingested by C6 glioma cells. Liu *et al.* promoted microwave-mediated pyrolysis of citric acid with various amine molecules to synthesize highly luminescent CDs.[58] In this technique the amine molecules serve dual roles as N-doping precursors and surface passivation agents, both of which considerably enhanced the fluorescence of the CDs. These highly fluorescent CDs are highly biocompatible and have great potential for biomedical application. Very recently Wang *et al.* prepared CDs through microwave technique using benzenediol isomer (catechol, resorcinol and hydroquinone) as carbon precursor and sulphuric acid as catalyst.[59] These CDs could easily penetrate into cells in a short time (30 min) and possess low cytotoxicity and good biocompatibility.

Supported Synthetic Methods: It is important to synthesize monodisperse size controlled CDs for particular applications and mechanistic study. In this regard supported synthetic method has been widely used for the synthesis of monodisperse CDs using molecular sieve, porous carbon, mesoporous silica nanoparticles and so on. In this method, the used

support serves to localize the growth of CDs by blocking nanoparticle agglomeration during high temperature treatment. For instance, Li *et al.* reported a synthetic method for synthesis of monodisperse CDs using silica spheres as carriers and resols as carbon precursors.[44] Porous silicas are the most widely used support for synthesis of CDs due to their various, tunable and easily obtained textures, thermal stability and easy removal. Hydrophilic CDs were synthesized by Zhu *et al.* using mesoporous silica nanospheres as nanoreactors by impregnation of a citric acid precursor.[60] The synthesized CDs showed good photostability, low toxicity, excellent luminescence, and up-conversion properties. Following different approach, CDs were synthesized using NaY zeolites as supports.[61] The ion exchanged zeolite on thermal oxidation produced CD decorated zeolite. The CDs were mainly decorated on the surface of zeolite as ion exchange took place mostly on the surface opposed to the interior. The zeolitic material was then etched away by hydrophilic acid to produce fluorescent CDs.

Combustion/Hydrothermal/Solvothermal Method: A simple source of CDs is the soot derived from the combustion of unscented candles or natural gas burners.[2,44] Mao and co-workers for the first time, produced water soluble multicolor fluorescent CDs (< 2 nm) from the candle soot through oxidative acid treatment, which introduced OH and COOH groups to the CD surfaces.[2] The particles were purified by using polyacrylamide gel electrophoresis (PAGE) fraction. Ray *et al.* synthesized CDs by refluxing the candle soot with 5M HNO_3 for 12 h adopting similar approach.[44] The CDs were collected by high speed centrifugation and the size separation was achieved using water/ethanol/chloroform solvent mixture through stepwise high-speed centrifugation. In a further study, Chen and co-workers purified CDs from the combustion soot of natural gas. Hydrophilic fluorescent CD was synthesized from pollutant soot of diesel engine by treatment of nitric acid.[62] The purified CDs displayed multicolored emissions covering the green to red and extended to the near-infrared region, which was used for bioimaging and sensing cholesterol.

The above-described various synthetic approaches generally need costly precursors, complex instrumental set-ups or post-treatments to synthesize fluorescent CDs. In this context recently introduced hydrothermal carbonization or solvothermal

carbonization is a low cost, environmentally friendly, and nontoxic route to produce fluorescent CDs from various precursors.[63,64] In this technique a solution of carbon precursor is sealed and reacted in a high pressure reactor at high temperature. Giannelis *et al.* employed one-step thermal decomposition of low-temperature melting molecular precursor to obtain CDs.[46] Careful selection of the carbon source and surface modifier resulted better control over the geometry and physical properties of the CDs. Hydrothermal treatment of carbohydrates (glucose, sucrose, fructose, glucosamine etc.) was an important approach to obtain CDs.[65-67] Wu *et al.* exploited a high-yield synthesis of hydrophilic CDs by controlled carbonization of sucrose.[66] The green luminescent CDs and non-luminous CDs, which on functionalization with PEG emitted blue fluorescence, were effectively separated. Chitosan carbonization leads to the production of amino functionalized CDs.[68] Thereafter, the uses of other inexpensive starting materials, like ethanol, citrate, ascorbic acid, saccharides, and gelatin were developed to produce CDs with high quantum yields.[3,69-72] Recently Liu *et al.* demonstrated a hydrothermal method to simultaneously enhance the up-conversion fluorescence and tune the down-conversion luminescence of CDs from blue to green light by simply adding H_2O_2 in during hydrothermal treatment.[73]

Fabrication of CDs from renewable bioprecursors is an exciting achievement in the area of bottom-up synthesis. Fluorescent CDs was synthesized from fresh tender ginger juice which provide high suppression of the growth of human hepatocellular carcinoma cells (HepG2), with low toxicity to normal mammary epithelial cells (MCF-10A) and normal liver cells (FL83B).[74] The hydrothermal treatment of pommel peel,[75] egg,[76] water-melon peel[77] and potato[78] produced CDs. However the quantum yield (QY) of obtained CDs was lower than 8% and not suitable for bioimaging. Subsequently high quality fluorescent CDs were produced using various natural precursor such as plant leaf,[79] banana juice,[80] soya milk,[81] bombyx mori silk,[82] citrus pectin,[83] honey[84] and so on. The produced CDs have high fluorescence QY suitable for various applications including bioimaging, fluorescence sensing, multicolor printing etc. Fluorescent CDs isolated from sweet pepper shows up-conversion fluorescent properties suitable for hypochlorite detection.[85] These approaches are less costly and easier to manage, and the CDs produced were found to possess desirable fluorescence properties along with high aqueous

solubility and photostability. The various chemical constituents such as carbohydrate, proteins, vitamins, ascorbic, citric acids, crude fibers, lipid, fatty acids, and amino acids present in natural sources serve as the molecular precursor during carbonization for the synthesis of CDs.

1.3. Light emission properties of carbon dots

One of the most fascinating features of CD is its light emitting properties. Till date numerous CDs with different fluorescence properties ranging from visible to near-infrared region have been reported. Although several theories have been proposed for the fluorescence phenomenon including excitons of carbon, emissive traps, quantum confinement effect, aromatic structures, oxygen-containing groups, free zigzag sites and edge defects,[1,14,30,86] the exact mechanism of fluorescence is still enigma.

The quantum confinement and edge effects associated with CD play important role in the luminescence. The band gap transitions in CD (π-π^*) arise from conjugated π domains and the energy gap depends on the size of the graphene fragments. Such size effect can produce different fluorescence emission with variable sized CDs. Moreover the different types of edges (armchair and zigzag edges) produced during CD synthesis plays an important role in tuning the electronic, magnetic, and optical properties. The quantum confinement effect is responsible for size dependence of the band gap in CDs which gives rise to unique, size-dependent optical and spectroscopic properties.[87] The quantum confinement effect and size-dependent optical properties of CD was reported by Li and co-worker.[54] They prepared fluorescent CDs by alkali-assisted electrochemical method and separated through column chromatography to obtain different sized CDs. They found that the fluorescence properties strongly depend on CDs size: small CDs (1.2 nm) give UV light emission, medium-sized CDs (1.5-3 nm) give visible light emission and large CDs (3.8 nm) give near-infrared emission.

The surface defect (any sites that have non-perfect sp^2 domains) associated with CD will result in surface energy trap. Most of the CDs have various oxygen-containing functional groups, such as hydroxyl, epoxy/ether, carbonyl and carboxylic acid groups.

Along with these functionalized surface defect (carbonyl-related localized electronic state), both sp^2 and sp^3 hybridized carbons present in CDs contribute to their multicolor emissions that are concentrated in the blue and green regions of the visible light spectrum. These surface defects are responsible for multicolor emissions in CD due to the existence of multiple surface defects with different excitation and emission properties.[88] Moreover the surface passivation plays an important role in certain CDs leading to luminescent properties. The presence of surface energy traps became emissive (through radiative recombination of excitons) upon stabilization as a result of surface passivation.[44]

Most of the fluorescent CDs exhibit excitation-dependent fluorescence properties with bathochromic shift of emission peaks.[3,69-71] They exhibit multicolor fluorescence properties under different excitation wavelength, which is important for certain practical applications. These interesting excitation dependent luminescence properties are not only due to the effects from particles of different sizes in the sample, but also a distribution of different emissive sites on each CD surface.[13,14] Thus the excitation dependent properties may result from optical selection of differently sized CDs and/or different emissive sites on CDs. There were also some exceptions, where CDs showed excitation independent fluorescence properties. For example in case of CDs derived from alkoxy silane, the emission wavelength remained at 547 nm for the excitation wavelength changed from 340-450 nm.[89] This phenomenon was attributed to both the uniform size and the surface state of those sp^2 clusters contained in CDs.

Up-conversion Fluorescence: In addition to the strong down-conversion fluorescence, some CD shows up-conversion fluorescence.[60,90] Up-conversion luminescence is an attractive feature of CD, which devise many promising applications. The sequential absorption of two or more photons leading to shorter wavelength fluorescence emission is attributed as up-conversion photoluminescence. The emission is an anti-stokes type where the photon energy of emission is higher than the excitation energy. For the first time Sun *et al.* synthesized CDs which were strongly emissive in the visible region under irradiation by an argon-ion laser (458 nm) or a femtosecond pulsed laser for two-photon excitation in the near-infrared range (800 nm) indicating the up-conversion

photoluminescence properties.[91] Subsequently several other groups synthesized CDs exhibiting up-conversion luminescence properties using different synthetic route and they attributed the properties to multiphoton active process.[54,92] However the Shen group argued considering the constant energy difference (1.1 eV) between the up-converted emission (Em) and excitation light (Ex) that multi-photon excitation is inadequate to account for the up-conversion fluorescence emission properties of CDs.[93] According to their view, the up-conversion fluorescence emission originates from the relaxation of electrons from a higher energy state of the p orbital (LUMO) to the s orbital since some electrons would inevitably transit to the LUMO when a large number of low-energy photons excite the electrons in the p orbital. Along with p orbital electrons, electrons in the s orbital can also be excited, but their relaxation process leads to only conventional down-conversion fluorescence. On the other hand Gan *et al.* summarized several reports on up-converted fluorescent CD, where the up-conversion fluorescence emissions are artefacts originating from the conventional down-conversion emissions.[94] These emissions have been usually excited by the leaking component from the second order diffraction in the monochromator of the spectrofluorometer.[95] By removing the leaking component through simply inserting a long pass filter into the excitation pathway, real up-conversion properties can be monitored.

1.4. Fluorescence sensor application of carbon dot

Fluorescent sensing is found to be a convenient and inexpensive approach for the sensitive and selective detection with rapid and easy manipulation. Advances in synthesis and surface modification technologies made CDs appealing platforms for fluorescent detection of DNA,[96] phosphate,[97] thrombin,[98] nitrite,[99] glucose,[100] biothiol,[39] pH,[101] proteins,[102] metal ions,[103,104] anions[105,106] and so on. CDs have been used as excellent fluorescent probe owing to their intrinsic sensitivity, selectivity and capacity for rapid, real-time monitoring. By monitoring the changes in their fluorescence intensity under external physical or chemical stimuli, CDs were used to detect the various substances and quantities. The recent progresses in the development of CD-based sensors have been discussed in the followings.

Metal ion sensing

Heavy metal ion detection is important due to their toxic effects on the environment and human health. Mercury (II) ion (Hg^{2+}) is one of the most hazardous and ubiquitous pollutants causing serious environmental and health threat. CDs were first explored for the detection of mercury in aqueous solution[107-111] and live cell [112]. Hg^{2+} detection using CD solution and sol-gel immobilized CD was achieved by Gonclaves *et al.*.[113,114] They demonstrated that the fluorescence quenching was probably due to static quenching arising from the formation of stable non-fluorescent complex between CD and Hg^{2+} as evidenced by large Stern-Volmer constant. The improvement in the sensitivity of mercury detection was later achieved using nitrogen doped CD (N-CD).[115] The presence of nitrogen element in the N-CD is probably responsible for improved performance of Hg^{2+} sensing. Very recently N, S co-doped CD was utilized by Wang group for sensitive and selective detection of Hg^{2+} with a lower detection limit of 0.05 nM.[116] The high selectivity of the system was due to specific thiol-Hg^{2+} interaction. It was observed that the fluorescence intensity increased linearly with mercury from 1 nM to 50 μM. The significant reduced life time of CD on Hg^{2+} binding suggested dynamic quenching through electron transfer process occurred in Hg-S bands.

Apart from Hg^{2+} sensing, fluorescent CDs have been used for the sensing of other metal ions such as Cu^{2+},[117,118] Co^{2+},[119] Fe^{3+},[120] Pb^{2+},[121] Sn^{2+},[122] Cr(VI)[123] and Ag^{+}.[124] Most of these sensing method involves the fluorescence quenching by metal ions similar to the Hg^{2+} sensing. Branched poly(ethylenimine) (BPEI)-functionalized CD was utilized by Chi *et al.* for selective detection of Cu^{2+} with a detection limit of 6 nM over a dynamic range from 10 to 1100 nM.[117] They argued that Cu^{2+} ions could be captured by the amino groups of the BPEI-CDs to form an absorbent complex at the surface of CDs, resulting in a strong quenching of the CDs through an inner filter effect. Similar mechanistic pathway for Cu^{2+} quenching through the interaction of -COOH and -NH_2 groups of CD was also demonstrated by Liu group.[125] They modified the surface of CD with lysine and bovine serum albumin. Later the sensitivity of the fluorescent probe toward Cu detection was improved using metal-organic frameworks (ZIF-8–zinc imidazolate frameworks)[126] and silica coating[127] on CD apart from polymeric coating. A sensitive and reliable approach

was established for ratiometric fluorescent detection of intracellular Cu ion in living cells.[128] For this purpose a dual-emission hybrid fluorophore composed of CD and CdSe/ZnS quantum dot with integrated amino-TPEA (N-(2-aminoethyl)-N,N',N'-tris(pyridine-2-yl-methyl)ethane-1,2-diamine) was synthesized. The inorganic-organic fluorescent probe showed good cell permeability and low cytotoxicity demonstrating the imaging and biosensing of Cu^{2+} ions in living cells. More interestingly the fluorescence properties of CDs were explored for label-free detection of Fe^{3+} and dopamine with high sensitivity and selectivity.[120] Fe^{3+} induced oxidized hydroquinone species on CD surface quench the fluorescence of CD, which can be restored by the addition of dopamine due to their competition with CDs to react with Fe^{3+}. The developed method was simple and cost-effective as no further chemical modification of CD was required.

Most of the reported metal ion sensing by CD based fluorophore involve fluorescence quenching of CD due to interaction of metal ions. The fluorescence quenching may be due to either dynamic quenching through electron transfer process or static quenching through the formation of stable metal ion-CD complex.

Anion sensing

A number of fluorescent assay for anion detection have been developed owing to their critical roles in biological and chemical processes, as well as in environmental pollution. In this line CD based fluorophore have been explored for the detection of various anions such as $C_2O_4^{2-}$,[118] PO_4^{3-},[97] NO_2^-,[99] CN^-,[129] F^-,[105] I^-,[106] S^{2-}[130] and ClO^-.[85] However many of the anion detection methods involve fluorescence recovery of the already quenched CD-metal complexes. For example, the quenched fluorescence of CD due to mercury metal ion was recovered by the addition of I^-.[106] The iodide ion formed more stable complexes with the metal ions displacing CD from CD-metal complexes. An off-on fluorescence probe of europium-adjusted CD was applied to the phosphate detection in very complicated matrixes such as artificial wetlands system.[86] Eu^{3+} induced the aggregation of the CD by coordinating with the carboxylate group of CD, which resulted in fluorescence quenching through the charge- or energy- transfer process. However the presence of phosphate induced disassociation of the CDs aggregation species due to higher affinity of Eu^{3+} towards oxygen donor atoms from phosphate than

that of carboxylate groups on CD surface, which resulted turn-on fluorescence. Interestingly both down- and up-conversion fluorescence of the CD was utilized for the detection of ClO^- with a low detection limit of 0.05 μmol L^{-1} and 0.06 μmol L^{-1} respectively.[85] Liu group reported a fluorescent probe ($Zr(CDs–COO)_2EDTA$) for F^- detection whose working principle based on F^- induced fluorescence quenching.[105] The quenching of fluorescence signal was due to the formation of non-fluorescent complex $Zr(F)_2EDTA$ based on the stronger affinity of F than the -COOH in the CDs to Zr(IV). The method was also explored for F^- detection in toothpaste.

Biosensing

Apart from metal ion and anion detection CDs have also been used for the detection of biologically important molecules. The wide scope of CD surface functionalization facilitates the formation of tailored biologically compatible probes with high QY, good stability and low-toxicity against living species. Cost effective, stable sensitive CDs are mainly applied as fluorescent labels in immunoassays.[131,132] Based on fluorescence resonance energy transfer (FRET) principle, an immunosensor comprising of CD and gold nanoparticle was developed by Zhuang group for the determination of small size persistent organic pollutant 4,4'-dibrominated biphenyl (PBB15).[132] The gold nanoparticle (AuNP)-modified-anti-PBB15 antibodies acts as fluorescence energy acceptor and CD-labelled PBB15 antigens that donors for FRET process. They showed that in the absence of PBB15, FRET between CD and gold nanoparticles resulted in fluorescence quenching. On the other hand, presence of PBB15 induced fluorescence recovery due to release of CD-labelled antigen from gold nanoparticle surface through competitive immunoreaction. The sensor found a good liner range of 0.05-4 μg/mL, with a low detection limit of 0.039 μg/mL. Based on the same FRET principle a multifunctional CD probe was demonstrated for detecting and imaging mitochondrial H_2O_2.[133] Recently, naphthalimide-azide coupled CDs were reported as a highly selective and sensitive H_2S detector base on the FRET between CDs and the H_2S induced reduction product of naphthalimide-azide.[134]

CDs have been used as an effective fluorescent sensor for nucleic acid detection, where the level of selectivity was so high that even a single-base mismatch could be

identified.[135] The working principle was based on the fluorescence quenching of fluorescent dye due to the adsorption of the fluorescently labeled single-stranded DNA (ssDNA) probe on CD surface followed by specific hybridization with its target to form double-stranded DNA (dsDNA). The formation of dsDNA resulted in desorption of the hybridized dsDNA from CD surface leading to fluorescence recovery. This strategy was also employed for determination of metal ions such as Hg^{2+} and Ag^{+} through T-Hg^{2+}-T and C-Ag^{+}-C base pairs, respectively.[124,136] Highly specific assay of thrombin using aptamer biosensor with a detection limit of 1 nM was demonstrated by Xu's group.[137] The generalized working principle involves the detectable change in radiometric response due to conformational change of coupled aptamers induced by the target. Based on FRET from up-converting phosphors to CDs, another aptamer biosensor was recently constructed for thrombin detection.[138] Fluorescent CDs were also employed for the protein detection by staining it and the sensitivity were found to be comparable with conventional staining agents such as Coomassie Brilliant Blue and Ag^{+}.[139]

Along with the microbiomolecule sensing CDs have also been utilized for the detection of small bioanalytes such as dopamine,[140] ascorbic acid,[123] anti-bacterial drugs[141] and glucose.[142,143] The anti-bacterial drug amoxicillin was successfully detected using N-CD. The increase in fluorescence intensity of the N-CD via interaction with amoxicillin was the basis for fluorescent detection of anti-bacterial drug.[141] Recently Shen and Xia reported CD based fluorescence sensor for non-enzymatic blood glucose sensing.[143] The fluorescence of boronic acid modified CD was found to be quenched on addition of glucose due to assembling of CDs. These CDs showed excellent sensitivity and selectivity with minimal interference from various biomolecule.

1.5. Objective of the present work

Though several simple and efficient routes have been proposed for the synthesis of CDs, still there remain sufficient scope to improve the fabrication methods to achieve precise control over the particle size, structure and surface chemistry. Furthermore issues like the low product yield and quantum yield, the confusing PL mechanism, the narrow

spectral coverage, the lack of tenability in optical properties need to be addressed. In the direction of luminescence sensing, although a wide variety of CD based fluorescent sensors have been reported in last couple of years, many of them suffer from complicated sensing mechanism, less selectivity and high detection limit. In this context, our present investigation involves:

- Development of facile, cost-effective and green synthetic method for quantitative production of CD from naturally available molecular precursors.
- Enhancement of optical and surface properties of the CD through heteroatom doping or size controlled growth in a mesoporous host material.
- Design of CD-based fluorescence sensors for high sensitive, selective and accurate detection of metal ions, anions and bioanalytes.
- Evaulation of diagnostic and sensing applicability of the synthesized materials in vitro.

Our work involves synthesis of highly luminescent CD using cheap and readily available natural precursor through bottom-up strategy. The luminescent character of the synthesized CD has been explored for bioimaging application. Subsequently the optical and surface properties of the CD have been improved through heteroatom doping or controlled growth in mesoporous host material. The synthesized luminescent CD based nanoprobes have been characterized through standard techniques and their sensing properties for metal ion, anion and glucose have been evaluated in both water and living cells. The complete efforts of the research work have been described in subsequent chapters.

1.6. References

1. J. Zhou, C. Booker, R. Li, X. Zhou, T. Sham, X. Sun and Z. Ding, *J. Am. Chem. Soc.*, 2007, **129**, 744-745.
2. H. P. Liu, T. Ye, C. D. Mao, *Angew. Chem. Int. Ed.*, 2007, **46**, 6473-6475.
3. A. B. Bourlinos, A. Stassinopoulos, D. Anglos, R. Zboril, M. Karakassides, E. P. Giannelis, *Small*, 2008, **4**, 455-458.

4. A. Quarta, R. D. Corato, L. Manna, S. Argentiere, R. Cingolani, G. Barbarella, T. Pellegrino, *J. Am. Chem. Soc.*, 2008, **130**, 10545-10555.
5. P. Kshirsagar1, S. S. Sangaru, V. Brunetti, M. A. Malvindi, P. P. Pompa1, *Nanotechnology*, 2014, **25**, 045601.
6. J. Fang, M. Saunders, Y. Guo, G. Lu, C. L. Raston, K. S. Iyer, *Chem. Commun.*, 2010, **46**, 3074-3076.
7. L. Y. Wang, P. Li, J. Zhuang, F. Bai, J. Feng, X. Y. Yan, Y. D. Li, *Angew. Chem. Int. Ed.*, 2008, **47**, 1054-1057.
8. Y. X. Zhang, G. K. Das, R. Xu, T. T. Y. Tan, *J. Mater. Chem.*, 2009, **19**, 3696-3703.
9. F. Wang, W. B. Tan, Y. Zhang, X. Fan, M. Wang, *Nanotechnology*, 2006, **17**, R1.
10. Y. W. Cao, U. Banin, *J. Am. Chem. Soc.*, 2000, **122**, 9692-9702.
11. J. K. Jaiswal, H. Mattoussi, J. M. Mauro, S. M. Simon, *Nat. Biotechnol.*, 2003, **21**, 47-51.
12. A. M. Derfus, W. C. W. Chan, S. N. Bhatia, *Nano Lett.*, 2004, **4**, 11-18.
13. S. N. Baker, G. A. Baker, *Angew. Chem. Int. Ed.*, 2010, **49**, 6726-6744.
14. H. Li, Z. Kang, Y. Liu, S. T. Lee, *J. Mater. Chem.*, 2012, **22**, 24230-24253.
15. J. Shen, Y. Zhu, X. Yang, C. Li, *Chem. Commun.*, 2012, **48**, 3686-3699.
16. Y. Wang, A. Hu, *J. Mater. Chem. C*, 2014, **2**, 6921-6939.
17. P. Demchenko, M. O. Dekaliuk, *Methods Appl. Fluoresc.*, 2013, **1**, 042001.
18. X. Xu, R. Ray, Y. Gu, H. J. Ploehn, L. Gearheart, K. Raker and W. A. Scrivens, *J. Am. Chem. Soc.*, 2004, **126**, 12736-12737.
19. L. Li, G. Wu, G. Yang, J. Peng, J. Zhao, J. J. Zhu, *Nanoscale*, 2013, **5**, 4015-4039.
20. X. Zhou, Y. Zhang, C. Wang, X. Wu, Y. Yang, B. Zheng, H. Wu, S. Guo, J. Zhang, *ACS Nano*, 2012, **6**, 6592-6599.
21. S. Y. Lim, W. Shen, Z. Gao, *Chem. Soc. rev.*, 2015, **44**, 362-381.
22. Z. Zhang, J. Zhang, N. Chen, L. Qu, *Energy Environ. Sci.*, 2012, **5**, 8869-8890.
23. L. A. Ponomarenko, F. Schedin, M. I. Katsnelson, R. Yang, E. W. Hill, K. S. Novoselov, A. K. Geim, *Science*, 2008, **320**, 356-358.
24. A. Sachdev, I. Mataia, P. Gopinath, *RSC Adv.*, 2014, **4**, 20915-20921.

25. A. S. Castillo, M. A. Avidad, C. Pritz, M. C. Robles, B. Fernandez, M. J. R. Rama, A. M. Fernandez, A. L. Fernandez, F. S. Gonzalez, A. S. Fischerb, L. F. Capitan-Vallveya, *Chem. Commun.,* 2013, **49**, 1103-1105.
26. J. H. Liu, S. T. Yang, X. Chen, H. Wang, *Curr. Drug Metab.*, 2012, **13**, 1046-1056.
27. C. Fowley, N. Nomikou, A. P. McHale, B. McCaughan, J. F. Callan, *Chem. Commun.,* 2013, **49**, 8934-8936.
28. J. C. G. E. da Silva, H. M. R. Gonçalves, *Trends Anal. Chem.*, 2011, **30**, 1327-1336.
29. L. Cao, S. Sahu, P. Anilkumar, C. E. Bunker, J. A. Xu, K. A. S. Fernando, P. Wang, E. A. Guliants, K. N. Tackett, Y. P. Sun, *J. Am. Chem. Soc.*, 2011, **133**, 4754-4757.
30. H. T. Li, X. D. He, Y. Liu, H. Huang, S. Y. Lian, S. T. Lee, Z. H. Kang, *Carbon*, 2011, **49**, 605-609.
31. X. Wang, L. Cao, F. S. Lu, M. J. Meziani, H. Li, G. Qi, B. Zhou, B. A. Harruff, F. Kermarrec, Y. P. Sun, *Chem. Commun.*, 2009, 3774-3776.
32. Y. Li, Y. Hu, Y. Zhao, G. Shi, L. Deng, Y. Hou, L. Qu, *Adv. Mater.*, 2011, **23**, 776-780.
33. L. Zhou, Y. H. Lin, Z. Z. Huang, J. S. Ren, X. G. Qu, *Chem. Commun.,* 2012, **48**, 1147-1149.
34. Z. Yang, Z. Li, M. Xu, Y. Ma, J. Zhang, Y. Su, F. Gao, H. Wei, L. Zhang, *Nano Micro Lett.*, 2013, **5**, 247-259.
35. L. Bao, Z. L. Zhang, Z. Q. Tian, L. Zhang, C. Liu, Y. Lin, B. Qi and D. W. Pang, *Adv. Mater.*, 2011, **23**, 5801-5806.
36. L. Zheng, Y. Chi, Y. Dong, J. Lin, B. Wang, *J. Am. Chem. Soc.*, 2009, **131**, 4564-4565.
37. S. T. Yang, L. Cao, P. G. Luo, F. S. Lu, X. Wang, H. F. Wang, M. J. Meziani, Y. F. Liu, G. Qi, Y. P. Sun, *J. Am. Chem. Soc.*, 2009, **131**, 11308-11309.
38. S. J. Yu, M. W. Kang, H. C. Chang, K. M. Chen, Y. C. Yu, *J. Am. Chem. Soc.*, 2005, **127**, 17604-17605.
39. Y. P. Sun, B. Zhou, Y. Lin, W. Wang, K. A. S. Fernando, P. Pathak, M. J. Meziani, B. A. Harruff, X. Wang, H. F. Wang, P. G. Luo, H. Yang, M. E. Kose, B. L. Chen, L. M. Veca, S. Y. Xie, *J. Am. Chem. Soc.*, 2006, **128**, 7756-7757.

40. Y. Q. Dong, N. N. Zhou, X. M. Lin, J. P. Lin, Y. W. Chi and G. N. Chen, *Chem. Mater.*, 2010, **22**, 5895-5899.
41. Q. L. Wang, H. Z. Zheng, Y. J. Long, L. Y. Zhang, M. Gao, W. J. Bai, *Carbon*, 2011, **49**, 3134-3140.
42. H. Peng, J. Travas-Sejdic, *Chem. Mater.*, 2009, **21**, 5563-5565.
43. B. Zhu, S. Sun, Y. Wang, S. Deng, G. Qian, M. Wanga, A. Hu, *J. Mater. Chem. C*, 2013, **1**, 580-586.
44. R. L. Liu, D. Q. Wu, S. H. Liu, K. Koynov, W. Knoll, Q. Li, *Angew. Chem. Int. Ed.*, 2009, **48**, 4598-4601.
45. S. C. Ray, A. Saha, N. R. Jana, R. Sarkar, *J. Phys. Chem. C*, 2009, **113**, 18546-18551.
46. M. J. Krysmann, A. Kelarakis, P. Dallas, E. P. Giannelis, *J. Am. Chem. Soc*., 2012, **134**, 747-750.
47. F. Wang, M. Kreiter, B. He, S. Pang, C. Liu, *Chem. Commun*., 2010, **46**, 3309-3311.
48. H. Zhu, X. L. Wang, Y. L. Li, Z. J. Wang, F. Yang, X. R. Yang, *Chem. Commun.*, 2009, 5118-5120.
49. H. T. Li, X. D. He, Y. Liu, H. Yu, Z. H. Kang, S. T. Lee, *Mater. Res. Bull.*, 2011, **46**, 147-151.
50. J. Wang, X. Xin, Z. Lin, *Nanoscale*, 2011, **3**, 3040-3048.
51. S. T. Yang, X. Wang, H. Wang, F. Lu, P. G. Luo, L. Cao, M. J. Meziani, J. H. Liu, Y. Liu, M. Chen, Y. Huang, Y. P. Sun, *J. Phys. Chem. C*, 2009, **113**, 18110-18114.
52. S. L. Hu, K. Y. Niu, J. Sun, J. Yang, N. Q. Zhao, X. W. Du, *J. Mater. Chem*., 2009, **19**, 484-488.
53. X. Li, H. Wang, Y. Shimizu, A. Pyatenko, K. Kawaguchi, N. Koshizaki, *Chem. Commun.*, 2011, **47**, 932-934.
54. H. T. Li, X. D. He, Z. H. Kang, H. Huang, Y. Liu, J. L. Liu, S. Y. Lian, C. H. A. Tsang, X. B. Yang, S. T. Lee, *Angew. Chem. Int. Ed.*, 2010, **49**, 4430-4434.
55. H. Ming, Z. Ma, Y. Liu, K. M. Pan, H. Yu, F. Wang, Z. H. Kang, *Dalton Trans.*, 2012, **41**, 9526-9531.
56. X. H. Wang, K. G. Qu, B. L. Xu, J. S. Ren, X. G. Qu, *J. Mater. Chem.*, 2011, **21**, 2445-2450.

57. Y. Liu, N. Xiao, N. Gong, H. Wang, X. Shi, W. Gu, L. Ye, *Carbon*, 2014, **68**, 258-264.
58. X. Zhai, P. Zhang, C. Liu, T. Bai, W. Li, L. Dai, W. Liu, *Chem. Commun.*, 2012, **48**, 7955-7957.
59. J. Wang, C. Cheng, Y. Huang, B. Zheng, H. Yuan, L. Bo, M. W. Zheng, S. Y. Yang, Y. Guo, D. Xiao, *J. Mater. Chem. C*, 2014, **2**, 5028-5035.
60. J. Zong, Y. H. Zhu, X. L. Yang, J. H. Shen, C. Z. Li, *Chem. Commun.*, 2011, **47**, 764-766.
61. A. B. Bourlinos, A. Stassinopoulos, D. Anglos, R. Zboril, V. Georgakilas, E. P. Giannelis, *Chem. Mater.*, 2008, **20**, 4539-4541.
62. K. M. Tripathi, A. K. Sonker, S. K. Sonkar, S. Sarkar, *RSC Adv*., 2014, **4**, 30100-30107.
63. A. Jaiswal, S. S. Ghosh, A. Chattopadhyay, *Chem. Commun.*, 2012, **48**, 407-409.
64. B. Hu, K. Wang, L. Wu, S. H. Yu, M. Antonietti, M. M. Titirici, *Adv. Mater.*, 2010, **22**, 813-828.
65. Z. C. Yang, X. Li, J. Wang, *Carbon*, 2011, **49**, 5207-5212.
66. J. C. Zhang, W. Q. Shen, D. Y. Pan, Z. W. Zhang, Y. G. Fang, M. H. Wu, *New J. Chem.*, 2010, **34**, 591-593.
67. Z. C. Yang, M. Wang, A. M. Yong, S. Y. Wong, X. H. Zhang, H. Tan, A. Y. Chang, X. Li, J. Wang, *Chem. Commun.*, 2011, **47**, 11615-11617.
68. Y. Yang, J. Cui, M. Zheng, C. Hu, S. Tan, Y. Xiao, Q. Yang and Y. Liu, *Chem. Commun.*, 2012, **48**, 380-382.
69. B. Zhang, C. Liu, Y. Liu, *Eur. J. Inorg. Chem.*, 2010, 4411-4414.
70. Q. Liang, W. Ma, Y. Shi, Z. Li, X. Yang, *Carbon*, 2013, **60**, 421-428.
71. S. Chandra, P. Das, S. Bag, D. Laha, P. Pramanik, *Nanoscale*, 2011, **3**, 1533-1540.
72. H. T. Li, H. Ming, Y. Liu, H. Yu, X. D. He, H. Huang, K. M. Pan, Z. H. Kang, S. T. Lee, *New J. Chem.*, 2011, **35**, 2666-2670.
73. Y. Cui, Z. Hu, C. Zhang, X. Liu, *J. Mater. Chem. B*, 2014, **2**, 6947-6952.
74. C. L. Li, C. M. Ou, C. C. Huang, W. C. Wu, Y. P. Chen, T. E. Lin, L. C. Ho, C. W. Wang, C. C. Shih, H. C. Zhou, Y. C. Lee, W. F. Tzeng, T. J. Chiou, S. T. Chu, J. Cang, H. T. Chang, *J. Mater. Chem. B*, 2014, **2**, 4564-4571

75. W. B. Lu, X. Y. Qin, S. Liu, G. H. Chang, Y. W. Zhang, Y. L. Luo, A. M. Asiri, A. O. Al-Youbi, X. P. Sun, *Anal. Chem.*, 2012, **84**, 5351-5357.
76. J. Wang, C. F. Wang, S. Chen, *Angew. Chem. Int. Ed.*, 2012, **51**, 9297-9301.
77. J. J. Zhou, Z. H. Sheng, H. Y. Han, M. Q. Zou and C. X. Li, *Mater. Lett.*, 2012, **66**, 222-224.
78. V. N. Mehta, S. Jha, R. K. Singhal, S. K. Kailasa, *New J. Chem.*, 2014, **38**, 6152-6160.
79. L. Zhu, Y. Yin, C.F. Wang, Su Chen, *J. Mater. Chem. C*, 2013, **1**, 4925-4932.
80. B. De, N. Karak, *RSC Adv*., 2013, **3**, 8286-8290.
81. C. Zhu, J. Zhai, S. Dong, *Chem Commun*., 2012, **48**, 9367-9369.
82. Z. L. Wu, P. Zhang, M. X. Gao, C. F. Liu, W. Wang, F. Leng, C. Z. Huang, *J. Mater. Chem. B*, 2013, **1**, 2868-2873.
83. X. J. Zhao, W.L. Zhang, Z.Q. Zhou, *Colloids Surf. B*, 2014, **123**, 493-497.
84. X. Yang, Y. Zhuo, S. Zhu, Y. Luo, Y. Feng, Y. Dou, *Biosens. Bioelectron.*, 2014, **60**, 292-298
85. B. Yin, J. Deng, X. Peng, Q. Long, J. Zhao, Q. Lu, Q. Chen, H. Li, H. Tang, Y. Zhang, S. Yao, *Analyst*, 2013, **138**, 6551-6557.
86. H. X. Zhao, L. Q. Liu, Z. D. Liu, Y. Wang, X. J. Zhao, C. Z. Huang, *Chem. Commun.*, 2011, **47**, 2604-2606.
87. A. M. Smith, S. Nie, *Acc. Chem. Res.*, 2010, **43**, 190-200.
88. L. Cao, M. J. Meziani, S. Sahu, Y. P. Sun, *Acc. Chem. Res*., 2013, **46**, 171-180.
89. J. J. Huang, Z. F. Zhong, M. Z. Rong, X. Zhou, X. D. Chen, M. Q. Zhang, *Carbon*, 2014, **70**, 190-198.
90. C. F. Wang, X. Wu, X. P. Li, W. T. Wang, L. Z. Wang, M. Gu, Q. Li, *J. Mater. Chem.*, 2012, **22**, 15522-15525.
91. L. Cao, X. Wang, M. J. Meziani, F. S. Lu, H. F. Wang, P. G. Luo, Y. Lin, B. A. Harruff, L. M. Veca, D. Murray, S. Y. Xie, Y. P. Sun, *J. Am. Chem. Soc.*, 2007, **129**, 11318–11319.
92. X. F. Jia, J. Lia, E. K. Wang, *Nanoscale*, 2012, **4**, 5572-5575.
93. J. H. Shen, Y. H. Zhu, C. Chen, X. L. Yang, C. Z. Li, *Chem. Commun.*, 2011, **47**, 2580-2582.

94. Z. Gan, X. Wu, G. Zhou, J. Shen, P. K. Chu, *Adv. Optical Mater.*, 2013, **1**, 554-558.

95. X. M. Wen, P. Yu, Y. R. Toh, X. Q. Ma, J. Tang, *Chem. Commun.*, 2014, **50**, 4703-4706.

96. J. Zhao, G. Chen, L. Zhu, G. Li, *Electrochem. Commun.*, 2011, **13**, 31-33.

97. H. X. Zhao, L. Q. Liu, Z. D. Liu, Y. Wang, X. J. Zhao, C. Z. Huang, *Chem. Commun.*, 2011, **47**, 2604-2606.

98. J. Liu, J. Li, Y. Jiang, S. Yang, W. Tan, R. Yang, *Chem. Commun*., 2011, **47**, 11321-11323.

99. Z. Lin, W. Xue, H. Chen, J. M. Lin, *Anal. Chem*., 2011, **83**, 8245-8251.

100. W. B. Shi, Q. L. Wang, Y. J. Long, Z. L. Cheng, S. H. Chen, H. Z. Zheng, Y. M. Huang, *Chem. Commun*., 2011, **47**, 6695-6697.

101. M. J. Krysmann, A. Kelarakis, P. Dallas, E. P. Giannelis, *J. Am. Chem. Soc*., 2011, **134**, 747-750.

102. H. Dai, C. P. Yang, Y. J. Tong, G. F. Xu, X. L. Ma, Y. Y. Lin, G. N. Chen, *Chem. Commun*., 2012, **48**, 3055-3057.

103. Y. Q. Dong, R. X. Wang, H. Li, J. W. Shao, Y. W. Chi, X. M. Lin, G. N. Chen, *Carbon*, 2012, **50**, 2810-2815.

104. S. Liu, J. Tian, L. Wang, Y. Zhang, X. Qin, Y. Luo, A. M. Asiri, A. O. Al-Youbi, X. Sun, *Adv. Mater*., 2012, **24**, 2037-2041.

105. J. M. Liu, L. P. Lin, X. X. Wang, L. Jiao, M. L. Cui, S. L. Jiang, W. L. Cai, L. H. Zhang, Z. Y. Zheng, *Analyst*, 2013, **138**, 278-283.

106. F. K. Du, F. Zeng, Y. H. Ming, S. Z. Wu, *Microchim. Acta*, 2013, **180**, 453-460.

107. S. J. Zhu, Q. N. Meng, L. Wang, J. H. Zhang, Y. B. Song, H. Jin, K. Zhang, H. C. Sun, H. Y. Wang, B. Yang, *Angew. Chem. Int. Ed*., 2013, **52**, 3953-3957.

108. S. Liu, J. Q. Tian, L. Wang, Y. W. Zhang, X. Y. Qin, Y. L. Luo, A. M. Asiri, A. O. Al Youbi, X. P. Sun, *Adv. Mater*., 2012, **24**, 2037-2041.

109. X. Wang, L. Cao, S. T. Yang, F. Lu, M. J. Meziani, L. Tian, K. W. Sun, M. A. Bloodgood, Y. P. Sun, *Angew. Chem. Int. Ed*., 2010, **49**, 5310-5314.

110. P. Anilkumar, L. Cao, J. J. Yu, K. N. Tackett, P. Wang, M. J. Meziani, Y. P. Sun, *Small*, 2013, **9**, 545-551.

111. S. Barman, M. Sadhukhan, *J. Mater. Chem*., 2012, **22**, 21832-21837.

112. F. Y. Yan, Y. Zou, M. Wang, X. L. Mu, N. Yang, L. Chen, *Sens. Actuators B*, 2014, **192**, 488-495.

113. H. Goncalves, P. A. S. Jorge, J. R. A. Fernandes, J. C. G. Esteves da Silva, *Sens. Actuators B*, 2010, **145**, 702-707.

114. H. M. Goncalves, A. J. Duarte, J. C. E. da Silva, *Biosens. Bioelectron*., 2010, **26**, 1302-1306.

115. R. Zhang, W. Chen, *Biosens. Bioelectron*., 2014, **55**, 83-90.

116. W. Wang, Y. C. Lu, H. Huang, A. J. Wang, J. R. Chen, J. J. Feng, *Sens. Actuators B*, 2014, **202**, 741-747.

117. Y. Q. Dong, R. X. Wang, G. L. Li, C. Q. Chen, Y. W. Chi, G. N. Chen, *Anal. Chem*., 2012, **84**, 6220-6224.

118. S. R. Zhang, Q. Wang, G. H. Tian, H. G. Ge, *Mater. Lett*., 2014, **115**, 233-236.

119. J. X. Shi, C. Lu, D. Yan, L. N. Ma, *Biosens. Bioelectron*., 2013, **45**, 58-64.

120. K. G. Qu, J. S. Wang, J. S. Ren, X. G. Qu, *Chem. Eur. J*., 2013, **19**, 7243-7249.

121. S. S. Wee, Y. H. Ng, S. M. Ng, *Talanta*, 2013, **116**, 71-76.

122. S. N. A. M. Yazid, S. F. Chin, S. C. Pang, S. M. Ng, *Microchim. Acta*, 2013, 180, 137-143.

123. M. Zheng, Z. G. Xie, D. Qu, D. Li, P. Du, X. B. Jing, Z. C. Sun, *ACS Appl. Mater. Interfaces*, 2013, **5**, 13242-13247.

124. H. L. Li, J. F. Zhai, X. P. Sun, *Langmuir*, 2011, **27**, 4305-4308.

125. J. M. Liu, L. P. Lin, X. X. Wang, S. Q. Lin, W. L. Cai, L. H. Zhang, Z. Y. Zheng, *Analyst*, 2012, **137**, 2637-2642.

126. Z. S. Qian, J. J. Ma, X. Y. Shan, H. Feng, L. X. Shao, J. R. Chen, *Chem. Eur. J*., 2014, **20**, 2254-2263.

127. X. M. Lin, G. M. Gao, L. Y. Zheng, Y. W. Chi, G. N. Chen, *Anal. Chem*., 2014, **86**, 1223-1228.

128. A. Zhu, Q. Qu, X. Shao, B. Kong, Y. Tian, *Angew. Chem. Int. Ed*., 2012, **51**, 7185 - 7189.

129. Y. Q. Dong, R. X. Wang, W. R. Tian, Y. W. Chi, G. N. Chen, *RSC Adv*., 2014, **4**, 3701-3705.

130. X. F. Hou, F. Zeng, F. K. Du, S. Z. Wu, *Nanotechnology*, 2013, **24**, 335502–335510.

131. G. A. Posthuma-Trumpie, J. H. Wichers, M. Koets, L. B. J. M. Berendsen, A. V. Amerongen, *Anal. Bioanal. Chem*., 2012, **402**, 593-600.
132. D. Bu, H. S. Zhuang, G. X. Yang, X. X. Ping, *Sens. Actuators B*, 2014, **195**, 540-548.
133. F. Du, Y. Min, F. Zeng, C. Yu, S. Wu, *Small*, 2014, **10**, 964-972.
134. C. Yu, X. Li, F. Zeng, F. Zheng, S. Wu, *Chem. Commun*., 2013, **49**, 403-405.
135. H. L. Li, Y. W. Zhang, L. Wang, J. Q. Tian, X. P. Sun, *Chem. Commun*., 2011, **47**, 961-963.
136. H. Li, J. Zhai, J. Tian, Y. Luo, X. Sun, *Biosens. Bioelectron.*, 2011, **26**, 4656-4660.
137. L. Xu, C. Q. Zhao, W. L. Wei, J. S. Ren, D. Miyoshi, N. Sugimoto, X. G. Qu, *Analyst*, 2012, **137**, 5483-5486.
138. Y. Wang, L. Bao, Z. Liu, D. Pang, *Anal. Chem*., 2011, **83**, 8130-8137.
139. N. Na, T. T. Liu, S. H. Xu, Y. Zhang, D. C. He, L. Y. Huang, J. Ouyang, *J. Mater. Chem. B*, 2013, **1**, 787-792.
140. Y. Mao, Y. Bao, D. X. Han, F. H. Li, L. Niu, *Biosens. Bioelectron*., 2012, **38**, 55-60.
141. J. J. Niu, H. Gao, *J. Lumin*., 2014, **149**, 159-162.
142. S. Liu, J. Q. Tian, L. Wang, Y. L. Luo, X. P. Sun, *RSC Adv*., 2012, **2**, 411–413.
143. P. Shen, Y. Xia, *Anal. Chem*., 2014, **86**, 5323-5329.

Chapter-2

Simple one-step synthesis of highly luminescent carbon dots from orange juice: Application as an excellent bio-imaging agent

2.1. Introduction

Recently, fluorescent carbon-based materials which include carbon dots (CDs),[1-3] nanodiamonds,[4] carbon nanotubes,[5] fullerene,[6] and fluorescent graphene[7] have attracted tremendous attention because of their exceptional advantages such as high optical absorptivity, chemical stability, biocompatibility, and low toxicity.[8-10] Among them CDs are found a promising alternative to more toxic metal-based semiconductor quantum dots (QDs) for applications such as bioimaging. Subsequent to the pioneering work towards the synthesis of CDs by laser ablation,[11] several top down approaches and more reliable bottom up approaches have been proposed to produce fluorescent carbon dots.[12-17] However most of these synthesis methods need several steps and strong acids and post treatment with surface passivating agents are essential in order to improve their water solubility and luminescence property. Alternatively, several one-step strategies to fabricate surface-passivated CDs such as syntheses of amino-functionalized fluorescent carbon dots by hydrothermal carbonization of chitosan at high temperature,[18] microwave assisted hydrothermal carbonization of sucrose,[19] and carbonization of glucose in reverse micelle[20] offer facile methods for the fabrication of fluorescent CDs without any surface passivation. However, all these above-mentioned methods suffer some degree of drawbacks like requirement of complex and time-consuming processes, high temperature, severe synthetic conditions, and high cost, which limit their wide applications. On the other hand, fabrication of nanomaterials from renewable bioprecursors is a challenging concept in the area of bottom-up nanotechnology. Recently some successes to produce fluorescent CD have also been demonstrated by employing renewable bio-sources as starting materials such as sweet potato,[21] egg,[22] water-melon peel,[23] plant leaf,[24] strawberry juice,[25] banana juice,[26] soya milk,[27] bombyx mori silk,[28] sugar cane juice,[29] honey[30] and so on. These natural materials are found as excellent precursor to produce biocompatible luminescent CD beneficiated with low cost and bulk production. In spite of recent remarkable advances in the fabrication of CDs, there still remains broad research space for developing new synthetic strategy to produce high quality CD.

In the pursuit of exploring natural precursors for the synthesis of CDs, this chapter demonstrates a very simple one step hydrothermal synthesis of highly luminescent biocompatible CD from orange juice (*Citrus nobilis deliciosa)*. Owing to the existence of

sugar, citric acid and ascorbic acid as main constituents of orange juice, it could provide an alternative precursor to synthesize advantageous CD nanomaterials. The developed method has following notable advantages: 1) one step generation at comparatively low temperature 120 ºC) and less time (150 min), 2) easy isolation of highly luminescent CDs by simple optimization of the centrifugation speed, 3) high yield production 400 mg of CD from 40 mL pulp free juice, 4) synthesis of highly luminescent CD with fluorescence quantum yield of 26% 4) varstile application as fluorescent dye for in vitro optical imaging. The synthesized material has been characterized by X-ray diffraction, Raman spectrophotometry, TEM, SEM, FTIR, DLS and fluorescence spectrophotometry. The cytotoxicity of the fluorescent CD as well as in vitro optical imaging has also been investigated.

2.2. Experimental

Synthesis of fluorescent carbon dot (CD)

CDs were synthesized by hydrothermal treatment of orange juice in ethanol. In a typical procedure, 40 mL of pulp free orange juice was mixed with 30 mL ethanol, and then the mixture was transferred into an 80 mL Teflon-lined stainless-steel autoclave and was heated to 120 ºC (1 ºC/min) and held there for 150 minutes. After the reaction, the autoclave was cooled down naturally. The resulted dark brown solution was washed with dichloromethane (30 mL×3) to remove the unreacted organic moieties. The aqueous solution was centrifuged at 3000 rpm for 15 min to separate the less-fluorescent deposit (CP). Excess acetone (100 mL) was added to upper brown solution and centrifuged at speed of 10,000 rpm to obtain highly fluorescent carbon dots (CD, 400 mg) of average size 2.5-4.5 nm. The deposit coarse nanoparticles (CP, 250 mg) have larger diameters in the range of 30-50 nm and exhibits weak fluorescence in compared to CD.

In vitro cytotoxicity and intracellular uptake

In vitro cytotoxicity: L929 cells were harvested and the cell concentration was adjusted to 1×10^4 cells/mL, cells were placed in a 96 well flat bottom culture plates (180 µL/well) and incubated with various concentrations (0.78, 3.185, 12.5, 25.0, 50.0, 100.0, and 200.0

μg/mL) of CD (in 20 μL). All cultures were incubated for 72 h at 37 ºC and 5% CO_2 in a humidified incubator. Viable cell concentration was checked by MTT (3-(4,5-Dimethyl-2-2thiazolyl)-2,5-diphenyl-2H-tetrazolium bromide) assay. The assay experiment was performed in triplicate.

Intracellular uptake: Human osteosarcoma cell line MG63 (maintained in Dulbecco's Modified Eagle's Medium or DMEM supplemented with 10% Fetal Bovine Serum or FBS) was trypsinized and seeded in tissue culture plates at 3×10^4 cells/well. After overnight incubation inside humidified 5% CO_2 incubator for cell attachment, cells are treated with the CD at a final concentration of 200 μg/mL in 300 μL of media and incubated for 12 h. prior to fixation of the cells on the slide for imaging experiment the cells were washed three times with fresh media. Live-cell-imaging was done under confocal microscope with laser excitation of 405 and 488 nm and fluorescence was collected in blue and green region.

Quantum Yield Calculations

The quantum yield (Φ) of the carbon dot was calculated using quinine sulfate as reference.[31,32] For calculation of quantum yield, five concentrations of each CD and CP were made, all of which had absorbance less than 0.1 at 340 nm. Quinine sulfate (literature $\Phi = 0.54$) was dissolved in 0.1 M H_2SO_4 (refractive index (η) of 1.33) while the carbon sample was dissolved in water ($\eta = 1.33$). Their fluorescence spectra were recorded at same excitation of 340 nm. Then by comparing the integrated fluorescence intensities (excited at 340 nm) and the absorbance values (at 340 nm) of the carbon sample with the references quinine sulfate, quantum yield of the carbon sample was determined. The data was plotted (Figure 2.1) and the slopes of absorbance versus integrated fluorescence intensity curve for standards and samples were determined. The data showed good linearity with intercepts of approximately zero.

The quantum yield was calculated using the equation

$$\Phi_x = \Phi_{ST} \ (m_x / m_{ST}) \ (\eta^2_x / \eta^2_{ST})$$

Where Φ is the quantum yield, m is slope, η is the refractive index of the solvent, ST is the standard and X is the sample. The quantum yield for CD and CP is found to be 25.6% and 19.7% respectively.

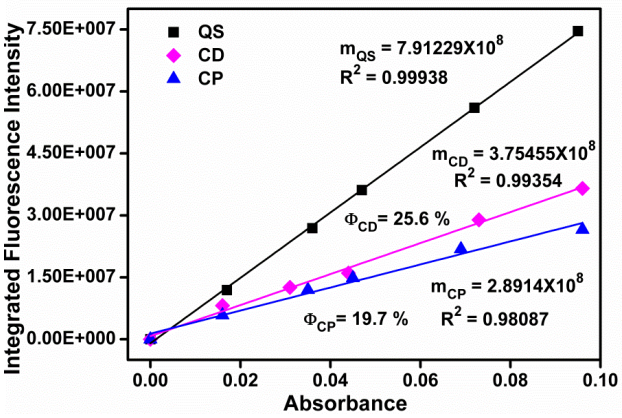

Figure 2.1 Fluorescence and absorbance of the CD, CP and quinine sulfate.

2.3. Characterization

The morphology and microstructure of CD and CP were analyzed by scanning electron microscope (HITACHI COM-S-4200) and high resolution transmission electron microscopy (JEOL 3010, Japan) operated at 300 kV respectively. Particle size and zeta potential were measured after suitable dilution of the CD solution at 25.0 ± 0.5 ºC, by laser light scattering using a particle size analyzer (Nano ZS 90, Malvern). The crystalline phase was investigated by an X'Pert Pro Phillips X-ray diffractometer. The Raman spectrum of as-prepared samples was recorded at ambient temperature on Renishaw in Via Raman (UK make). Fluorescence microscopy images were captured using Axiovert 40 carlzeiss india fluorescence microscope at excitation wavelength of 405 and 488 nm. The Fourier transform infrared spectroscopy (FTIR) spectra were measured by a Thermo Nicolet Nexus FTIR model 870 spectrometer with the KBr pellet technique ranging from 400 to 4000 cm^{-1}. The presence of different functional groups on the surface of CD was investigated by X-ray photoelectron spectroscopy using AlKα excitation source in an ESCA-2000 Multilab apparatus (VG microtech). Fluorescence spectroscopy was performed with a Horiba Fluoromax 4 spectrophotometer at different excitation energies ranging from 320 to 450 nm. UV-vis absorption spectra were obtained using a Shimadzu 220V (E) UV-vis spectrophotometer. Live-cell imaging was done under Olympus FV-1000 confocal microscope with laser excitations of 405 and 488 nm.

2.4. Results and Discussion

Synthesis

A simple one-step hydrothermal synthetic route was employed for the fabrication of highly green luminescent CDs. As illustrated in scheme 2.1, the CD sample has been synthesized from orange juice (*Citrus nobilis deliciosa)* at comparatively low temperature (120 ºC) and less time (150 min) without using either any strong acid or post-synthetic surface passivation. The starting material can be obtained from a single natural source and the synthesis method is cost-effective and green. More importantly, 400 mg of CDs can be produced from 40 mL of pulp free juice.

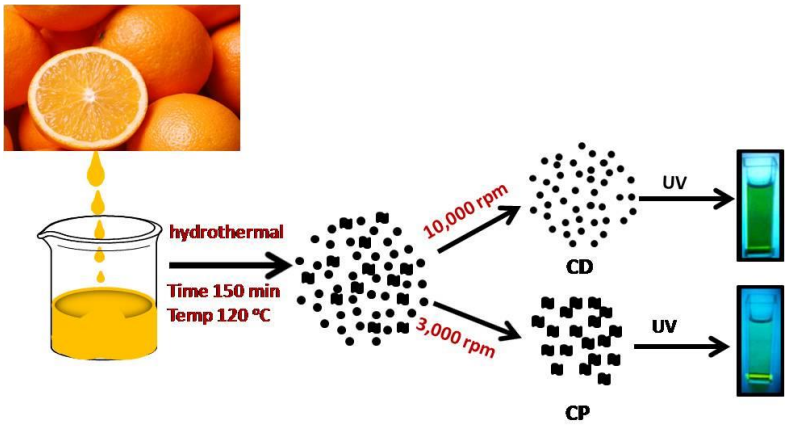

Scheme 2.1 Illustration of formation of CDs from hydrothermal treatment of orange juice.

Plausible mechanism for the formation of carbon dots

Hydrothermal carbonization of bioprecursor is an emerging technique for the production of novel carbon based materials for various potential applications.[33] The major constituents of orange juice are sucrose, glucose, fructose, ascorbic acid and citric acid[34] which are already been reported to act as excellent precursors for the synthesis of carbonaceous materials.[16,35,36] Thus we deemed to synthesize CDs from orange juice where constituents can act as efficient precursors.

The mechanism for synthesis of carbon dots from orange juice involves carbonization of its constituents. In fact, in the hydrothermal carbonization of sucrose for the formation of final material structure is complicated and a clear scheme has not yet been reported. The plausible mechanism for the formation of carbons dots may be illustrated as follows.

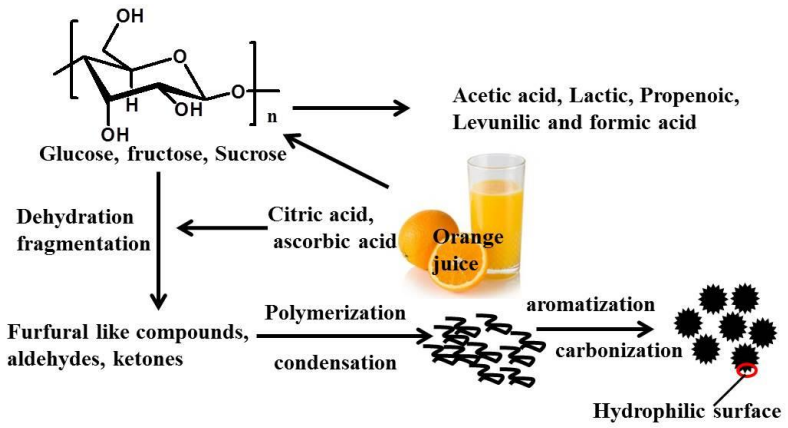

Figure 2.2 Schematic presentation of formation mechanism of carbon dots.

Sucrose when hydrothermally treated undergoes hydrolysis to form glucose which subsequently isomerises to form fructose.[37] The dehydration and decomposition of fructose/glucose gives rise to different soluble products such as furfural compounds (for ex: 5-hydroxymethyl furfural, furfural, 5-methyl furfural etc), several organic acids such as acetic, lactic, propionic, levulinic and formic acids, aldehydes and phenols. It is worth mentioning that the hydronium ion formed from these acids act as a catalyst in subsequent decomposition reaction stages. Here it is important to note that due to presence of weak acids like citric acid and ascorbic acid in orange juice the dehydration and decomposition reaction proceeds in a controlled manner. The polymerization and condensation of these products gives rise to soluble polymers. Aromatization and formation of aromatic clusters take place via aldol condensation, cycloaddition and a hydroxymethyl mediated furan resin condensation. When concentration of aromatic clusters reaches a critical supersaturation point a burst nucleation takes place and carbon dots are formed.

XRD and Raman study

The X-ray diffraction pattern of CDs and coarse particles (CP) are shown in Figure 2.3a. The XRD pattern of the CD shows a broad peak centered at $2\theta = 19.1$degree which is assigned to [002] diffraction pattern of graphitic carbon. The broadening of the peak is due to small size and amorphous nature of the synthesized CD. The [002] peak centered at 19.1degree in CDs has been shifted to 21 degree in case of coarse particles (CP). The corresponding interlayer spacing in graphite (0.34 nm) becomes larger in CP

(0.46 nm) which shifts to further larger end in CD (0.46 nm). The increase in *d* value indicates increase in amorphous nature attributed to the introduction of more oxygen containing groups.[14]

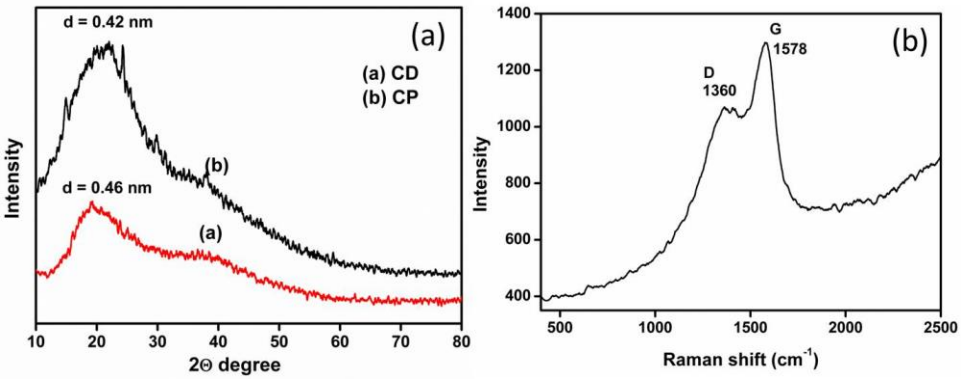

Figure 2.3 (a) XRD patterns of CD and CP, (b) Raman spectrum of CP.

In the Raman spectrum (Figure 2.3b) of coarse particles (CP), the peak at 1360 cm^{-1} is assigned to D-band arising from vibrations of carbon atoms with dangling bonds of the disorder carbon structure. The peak at 1578 cm^{-1} due to vibration of sp^2-bonded carbon atoms in a 2D hexagonal lattice of graphite cluster matches well with the 1st order G band of graphitic carbon. The overlapping of the D-line and G-line indicates amorphous nature of the sample. The intensity ratio of the D and G band (I_D /I_G) is a measurement of the disorder extent, as well as the ratio of sp^3/sp^2 carbons. The relative intensity of disorder D band to crystalline G band is I_D/I_G is 0.75, which is supportive to the partial amorphous nature of the coarse particles and consistent with reported studies.[13]

Microstructure, Hydrodynamic size and Stability

HRTEM images (Figure 2.4a) clearly reveal that the CDs are spherical, monodisperse and have a narrow size distribution between 1.5-4.5 nm with maximum population at 2.5 nm. The inset in Figure 2.4a shows the lattice spacing of 0.18 nm which corresponds to [102] facet of graphitic carbon. The SEM images of coarse particles appear like 2D exfoliated GO sheets consisting of layered structures (Figure 2.4c), while the TEM image taken after ultrasonication shows particles with uniform size in the range of 50-60 nm (Figure 2.4d).

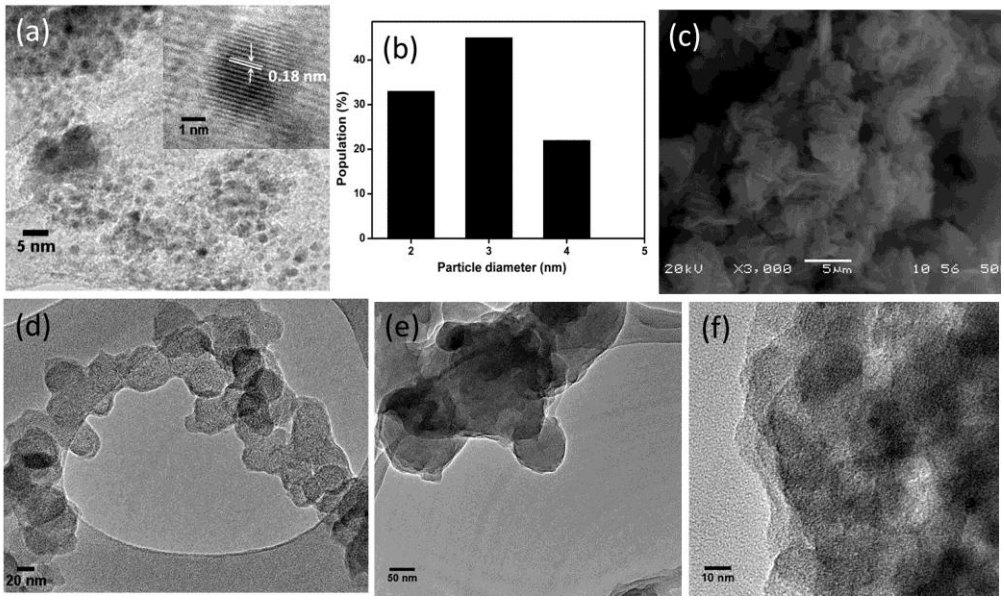

Figure 2.4 (a) TEM image with lattice imaging (inset), (b) particle size distribution of CDs, (c) SEM image and (d-f) TEM images of CP.

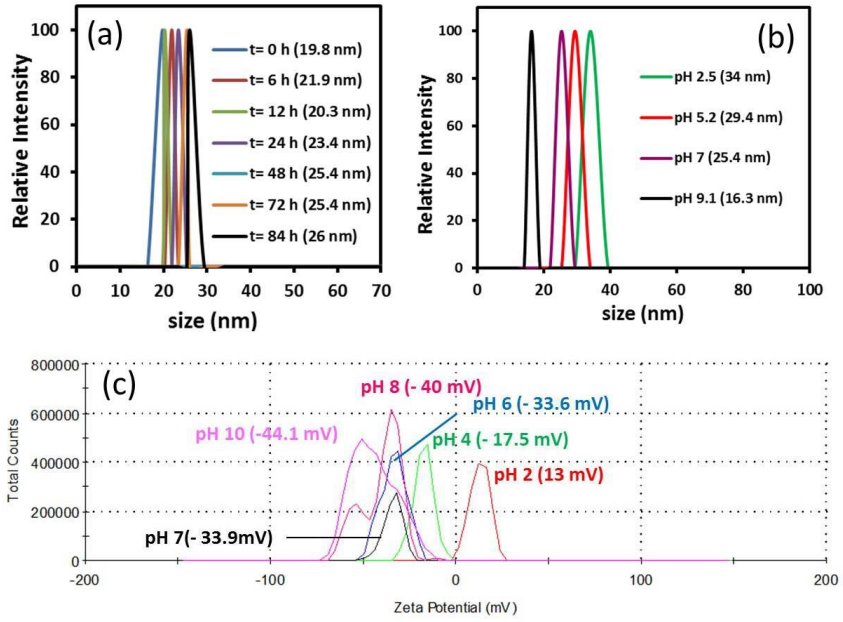

Figure 2.5 Variations of hydrodynamic size with (a) time and (b) pH, (c) zeta potential variation with pH.

The as-synthesized CDs without any further surface modification could be easily dispersed in deionized water with an average size of 16 nm at pH 9.1 being measured by DLS. The dispersion of the particles is highly stable without any precipitation for months. It is observed that HD size increases with decrease in pH (Figure 2.5b) indicating the

presence of –COOH groups on the surface. The presence of surface –COOH group is also evidenced of zeta potential measurement. Variation of zeta potential from positive to negative with increase in pH (Figure 2.5c) demonstrates the presence of –COOH groups on the surface. The existence of certain hydrophilic functional groups on the surface of the CDs makes the hydrodynamic diameter larger than observed from TEM. The hydrophilic functional groups in aqueous dispersion extended in water and were counted by the DLS.

Surface Properties

FTIR spectrum (Figure 2.6a) was recorded to investigate the bonding composition of the carbon dot and its functional groups. Sharp peak centered at 1650 cm^{-1} for CD and 1627 cm^{-1} for CP were attributed to aromatic C=C stretching, which is the elementary unit of the CDs. The appearance of broad peak centering at 3300-3500 cm^{-1} (O–H vibrational stretch), a sharp peak at 1708 cm^{-1} (C=O vibrational stretch) and peaks at 1081 and 1043 cm^{-1} (C–O–C/C-O vibrational stretch) suggest the existence of carboxylate and hydroxyl groups on the surfaces. The presence of these functional groups imparts excellent solubility in water without further chemical modification. Furthermore these functional groups can be modified for potential applications in drug delivery, biosensing and biomedical imaging.

To further confirm the surface functional groups and composition of the CD, XPS measurements have been done. The atomic ratio of C/O is 6.2. In a typical survey spectrum (Figure 2.6b) of the CD, the peaks at binding energies 275-290 and 525-539 eV are ascribed to C1s and O1s regions respectively. The high resolution scan of C1s region shows carbons present in five different chemical environments (Figure 2.6c), corresponding to sp^2 (C=C) at 284.1 eV, sp^3 (C-C and C-H) at 285.5 eV, C-OH/C-O-C at 285.7 eV, C=O at 288 and –COOH at 289.3 eV. The high resolution scans of the O1s regions can be fitted into three peaks (Figure 2.6d). The peak appeared at 532.7 is attributed to carbonyl (C=O) group, whereas the C-O group and adsorbed CO appears at slightly lower binding energies at 531.7 and 530 eV respectively. These functional groups confirm the highly oxidized surface of carbon dot.

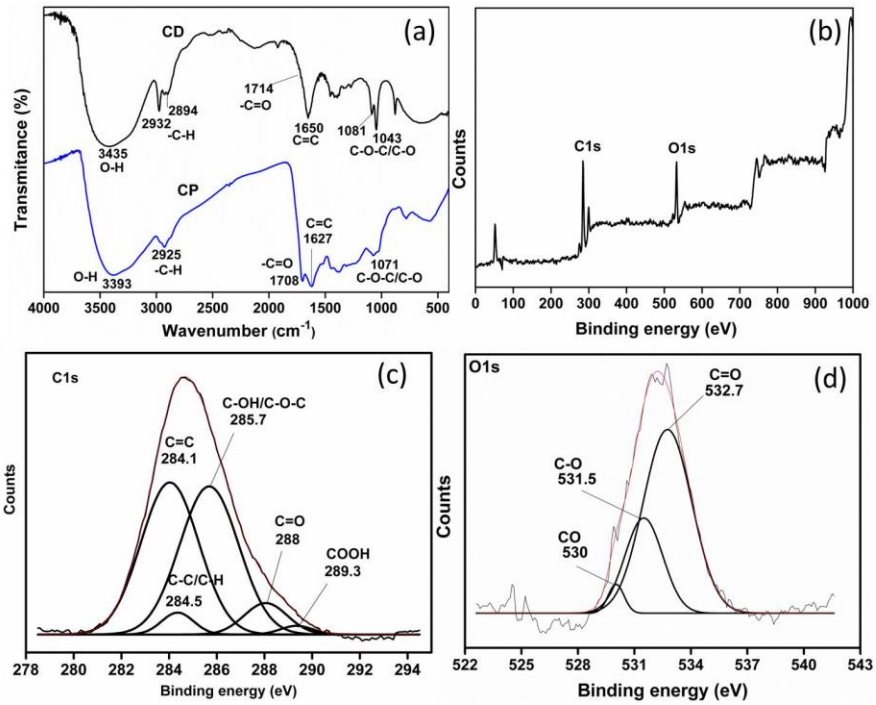

Figure 2.6 (a) FTIR spectra of CD and CP, (b) XPS survey and high resolution scan of the (c) C1s, (d) O1s region of CD.

Optical Properties

The UV-visible absorption and emission spectra have been presented in Figure 2.7a. CDs show broad UV absorption at 288 nm which is consistent with carbon nanoparticles synthesized by carbonization of chitosan.[18] The aqueous solution is yellow and transparent in daylight but changes to intense green under UV excitation (insets Figure 2.7a). In case of coarse particles the absorption in the visible region intensifies and the shoulder in UV region becomes more prominent. This change in optical property with increase in particle size is consistent with that of graphene quantum dots (GQDs) prepared by Kwon *et al.* by reverse micellar method.[20] The absorption is typically ascribed to the presence of aromatic π orbitals of which CPs have plenty more. The size dependent absorption is associated with a red shift in the emission spectrum. At a fixed λ_{ex}=390 nm, CDs show emission peak at 455 nm while the corresponding peak for CP appears at 474 nm. This difference in position of emission peak is attributed to the variation in size, as recently reported by Peng *et al.*[14] The optical properties of CDs vary with size which could also result in the variation in density and the nature of sp^2 sites

available in CDs. The energy gap decreases with increase in size parallel to the trend observed in other semiconductor quantum dots due to quantum confinement effect.[38] In case of CD a broad emission spectrum was observed (390-580 nm centered at 441 nm) at λex = 360, which indicates size distribution of CDs is broad as supported by TEM image and is consistent with reported observations.[18,39,40] Furthermore, the unique phenomemon of excitation dependent photoluminescence was observed in case of both synthesized CDs and CPs in consistency with the PL property of CDs reported by other groups (Figure 2.7c,d).

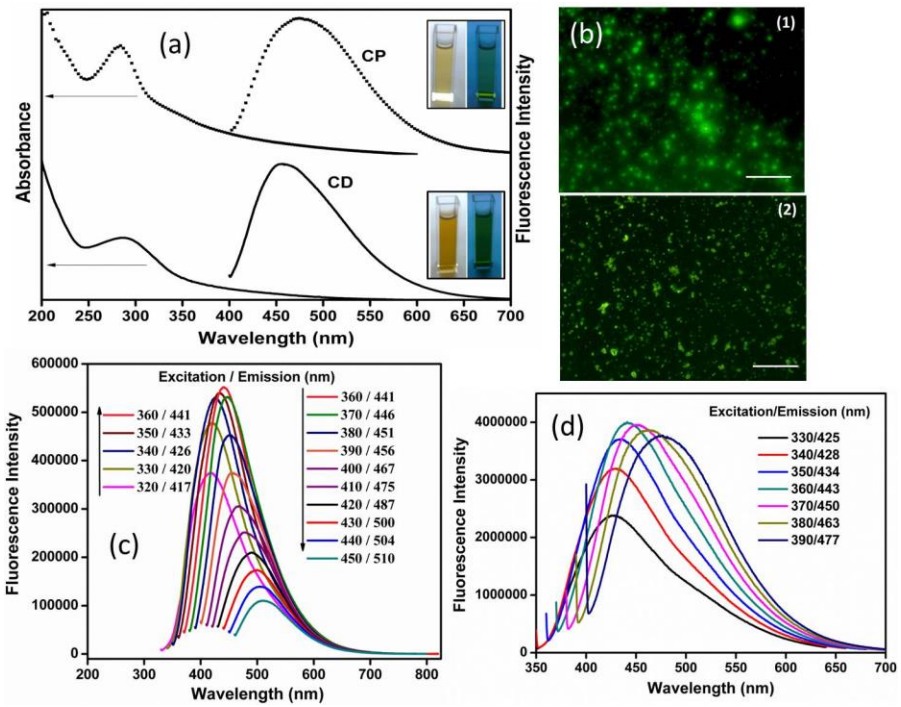

Figure 2.7 (a) UV absorption and PL emission spectra (λ_{ex} = 390 nm) of CD and CP, inset: optical images under daylight (left) and UV light (right), (b) Fluorescence microscopy images of CD (1) and CP (2) with excitation wavelength at 488 nm, emission spectra of CD (c) and CP (d) recorded for progressively longer excitation wavelength of 10 nm increments.

Another interesting phenomenon here is the pH dependent PL behavior. PL intensity decreased at very high pH and slightly decreased at low pH, but remained almost unchanged at pH 4.8-8.7 (Figure 2.8a). This pH dependent behavior is in accordance with that of GQDs synthesized by one-step solvochemical route from graphene oxide.[40] There were no changes in fluorescence intensity or peak characteristics

at different ionic strengths (Figure 2.8b), which is important during CDs use in the presence of physical salt concentrations in practical applications. The measurement of fluorescence intensity with time indicates that the CDs do not show photobleaching behavior for 3 h upon excitation at 360 nm (Figure 2.8c). Due to consistent PL within biological pH range this CD may be suitable for biological imaging. The fluorescence quantum yield of CD is 26% (taking quinine sulphate as standard, Figure 2.1) while that of CP is 20%. These values are appreciably higher than QY of carbon nanoparticles synthesized by other methods. As photoluminescence originates from surface emissive traps, smaller the carbon particles with a larger surface-to-volume ratio, the ratio of the number of trap sites-to-the number of photo excitable electrons increases and hence QY of CDs is more than that of CPs.

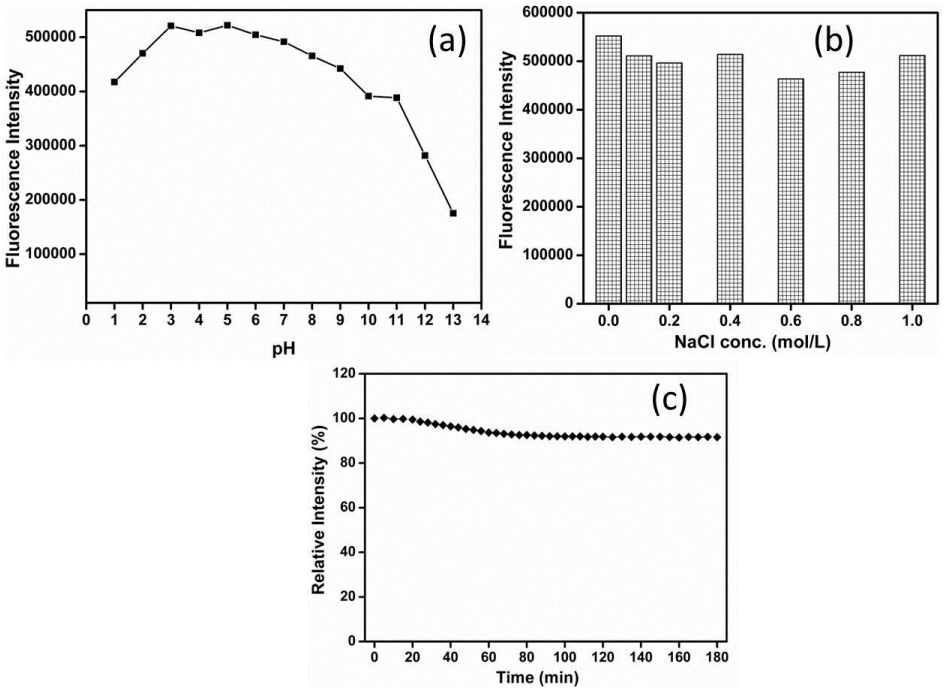

Figure 2.8 (a) Effect of pH on the fluorescence intensity of CD (b) Effect of ionic strengths on the fluorescence intensity of CD (ionic strengths were controlled by various concentrations of NaCl), (c) Effect of time on fluorescence intensity of CD in DI water.

To demonstrate orange juice as an efficient precursor for synthesis of highly luminescent CD, we have also synthesized a series of CDs using glucose, fructose, sucrose, ascorbic acid and citric acid which are main constituents of orange juice. These CDs were synthesized using similar hydrothermal condition as that of orange juice

decomposition. We found that all the synthesized CDs are highly water soluble due to presence of various functional group and show excitation dependent fluorescence properties similar to CD. The various optical properties of these CDs are summarized in Table-2.1. However the PL quantum yields of the synthesized CDs are much less than that of CD synthesized from orange juice. Furthermore isolation of these CDs are a tedious process, their separation requires dialysis followed by lyophilization instead of easy centrifugation followed in case of orange juice derived CD. In addition to this, these synthesized CDs do not show stable fluorescence in biological pH range demonstrating their incongruity towards biological applications. These findings clearly demonstrate that orange juice is a better reliable precursor for synthesis of CD.

Table 2.1 Comparative data of HD size, emission wavelength at λ_{ex} = 330 nm and PL quantum yield (ϕ) of carbon dots synthesized from different precursors.

SI No.	precursor	HD size (nm)	λemission (nm) at λ_{ex}=330 nm	PL QY (%)
1	Glucose	18.9	414	13.98
2	Fructose	38.3	433	8.8
3	Sucrose	25.3	421	13.5
4	Ascorbic acid	36.0	432	9.2
5	Citric acid	39.4	438	6.9
6	Glucose+Ascorbic acid	16.3	413	14.6
7	Glucose+Citric acid	29.4	419	3.2
8	Fructose+Ascorbic acid	19	412	12.7
9	Fructose+Citric acid	35.2	424	5.9
10	Sucrose+Ascorbic acid	16.3	416	9.7
11	Sucrose+Citric acid	34.03	427	7.3
12	**Orange juice**	**16**	**420**	**26**

Cellular uptake and fluorescence imaging

The excellent optical properties of the CD can be used for noninvasive monitoring of disease, therapy and other biological metabolic process. In this regard, the possible application of synthesized CD as cell-imaging agent was explored. The inherent cytotoxicity of CD was evaluated using L929 cell lines through MTT assay (Figure 2.9a). Here it is noteworthy that CdSe QDs cause 76% reduction in cell viability with a concentration of 6.25 μg mL^{-1} and 24 h exposure time.[43] In contrast, these synthesized

CD do not impose any significant toxicity to cells and tolerable even at high dose (200µg/mL) and long incubation time (72 h). Hence it is safe for *in vitro* and *in vivo* applications. We have performed *in vitro* cellular uptake experiments in human osteosarcoma (MG-63). Figure 2.9 shows confocal images of MG-63 cells treated with CDs at bright field, excitation wavelengths 488 nm and 405 nm. The phase contrast images of MG-63 cells at λ_{ex}= 488 nm clearly shows the agglomeration of green fluorescent carbon nanoparticles inside the cells leaving clear zones of nuclei (Figure 2.9c). Furthermore, the excitation dependent luminescence of synthesize CDs gives rise to several visible consequences in imaging. When the laser excitation was changed to 405 nm fluorescent blue color was observed. In addition to this there is no reduction in luminescence intensity even after excitation for a prolonged time. All these preludes demonstrate that the CDs obtained from orange juice can serve as a potential substitute for organic dyes or semiconductor QDs in bioimaging.

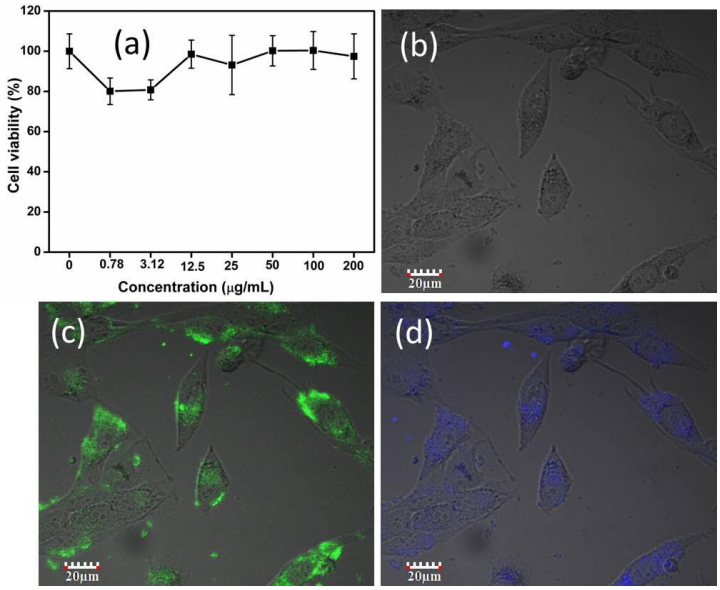

Figure 2.9 (a) Cell viability by MTT assay, (b) MG-63 cells under bright field, at excitation (c) 488 nm and (d) 405 nm.

2.5. Conclusion

- In this chapter highly luminescent carbon dots with fluorescence quantum yield of 26% have been synthesized in one-step hydrothermal treatment of orange juice.

- These partially crystalline carbon nanoparticles show strong and stable photoluminescence which is dependent on excitation wave length and pH.
- The CDs do not show any cytotoxicity and efficiently taken up by the cells.
- Due to the combined advantages of green synthesis, high aqueous stability, good and tunable luminescence and high biocompatibility these CDs can promise potential applications in biolabelling as well as solution state optoelectronics.

2.6. References

1. X. Wang, L. Cao, S. T. Yang, F. Lu, M. J. Meziani, L. Tian, K. W. Sun, M. A. Bloodgood, Y. P. Sun, *Angew. Chem. Int. Ed.,* 2010, **49**, 5310-5314.
2. M. J. Krysmann, A. Kelarakis, P. Dallas, E. P. Giannelis, *J. Am. Chem. Soc.*, 2012, **134**, 747-750.
3. X. Zhai, P. Zhang, C. Liu, T. Bai, W. Li, L. Dai, W. Liu, *Chem. Commun.,* 2012, **48**, 7955-7957.
4. A. Krueger, *Adv. Mater.,* 2008, **20**, 2445-2449.
5. K. Welsher, Z. Liu, S. P. Sherlock, J. T. Robinson, Z. Chen, D. Daranciang, H. Dai, *Nat. Nanotechnol.,* 2009, **4**, 773-780.
6. J. Jeong, M. Cho, Y. T. Lim, N. W. Song, B. H. Chung, *Angew. Chem. Int. Ed.*, 2009, **48**, 5296-5299.
7. K. P. Loh, Q. Bao, G. Eda, M. Chhowalla, *Nat. Chem.,* 2010, **2**, 1015-1024.
8. L. Cao, M. J. Meziani, S. Sahu, Y. P. Sun, *Acc. Chem. Res.,* 2013, **46**, 171-180.
9. S. N. Baker, G. A. Baker, *Angew. Chem. Int. Ed.,* 2010, **49**, 6726-6744.
10. H. Li, Z. Kang, Y. Liu, S. T. Lee, *J. Mater. Chem.,* 2012, **22**, 24230-24253.
11. Y. P. Sun, B. Zhou, Y. Lin, W. Wang, K. A. S. Fernando, P. Pathak, M. J. Meziani, B. A. Harruff, X. Wang, H. F. Wang, P. G. Luo, H. Yang, M. E. Kose, B. L. Chen, L. M. Veca and S. Y. Xie, *J. Am. Chem. Soc.,* 2006, **128**, 7756-7757.
12. L. Y. Zheng, Y. W. Chi, Y. Q. Dong, J. P. Lin, B. B. Wang, *J. Am. Chem. Soc.*, 2009, **131**, 4564-4565.
13. R. L. Liu, D. Q. Wu, S. H. Liu, K. Koynov, W. Knoll, and Q. Li, *Angew. Chem. Int. Ed.,* 2009, **48**, 4598-4601.

14. J. Peng,W. Gao, B. K. Gupta, Z. Liu, R. Romero-Aburto, L. Ge, Li Song, L. B. Alemany, X. Zhan, G. Gao, S. A. Vithayathil, B. A. Kaipparettu, A. A. Marti, T. Hayashi, J. Zhu and Pulickel M. Ajayan, *Nano Lett.*, 2012, **12**, 844-849.
15. F. Wang, M. Kreiter, B. He, S. Pang, C. Liu, *Chem. Commun.*, 2010, **46**, 3309-3311.
16. H. Zhu, X. L. Wang, Y. L. Li, Z. J. Wang, F. Yang, X. R. Yang, *Chem. Commun.*, 2009, 5118-5120.
17. S. C. Ray, A. Saha, N. R. Jana, R. Sarkar, *J. Phys. Chem. C*, 2009,**113**, 18546-18551.
18. Y. Yang, J. Cui, M. Zheng, C. Hu, S. Tan, Y. Xiao, Q. Yang and Y. Liu, *Chem. Commun.*, 2012, **48**, 380-382.
19. L. Tang, R. Ji, X. Cao, J. Lin, H. Jiang, X. Li, K.S. Teng, C. M. Luk, S. Zeng, J. Hao, S. P. Lau, *ACS Nano*, 2012 , **6**, 5102-5110.
20. W. Kwon, S. W. Rhee, *Chem. Commun.*, 2012, **48**, 5256-5258.
21. W. Lu, X. Qin, A. M. Asiri, A. O. Al-Youbi, X. Sun, *J. Nanopart. Res.*, 2013, **15**, 1344-1351.
22. J. Wang, C. F. Wang, S. Chen, *Angew. Chem. Int. Ed.*, 2012, **51**, 9297-9301.
23. J. J. Zhou, Z. H. Sheng, H. Y. Han, M. Q. Zou and C. X. Li, *Mater. Lett.*, 2012, **66**, 222-224.
24. L. Zhu, Y. Yin, C.F. Wang, Su Chen, *J. Mater. Chem. C*, 2013, **1**, 4925-4932.
25. H. Huang, J. J. Lv, D. L. Zhou, N. Bao, Y. Xu, A. J. Wang, J. J. Feng, *RSC Adv.*, 2013, **3**, 21691-21696.
26. B. De, N. Karak, *RSC Adv.*, 2013, **3**, 8286-8290.
27. C. Zhu, J. Zhai, S. Dong, *Chem Commun.*, 2012, **48**, 9367-9369.
28. Z. L. Wu, P. Zhang, M. X. Gao, C. F. Liu, W. Wang, F. Leng, C. Z. Huang , *J. Mater. Chem. B*, 2013, **1**, 2868-2873.
29. V. N. Mehta, S. Jha, S. K. Kailasa, *Mater. Sci. Eng. C*, 2014, **38**, 20-27.
30. X. Yang, Y. Zhuo, S. Zhu, Y. Luo, Y. Feng, Y. Dou, *Biosens. Bioelectron.*, 2014, **60**, 292-298.
31. D. Pan, J. Zhang, Z. Li, C. Wu, X. Yan, M. Wu, *Chem. Commun.*, 2010, **46**, 3681-3683.

32. J. Zhou, C. Booker, R. Li, X. Zhou, T. K. Sham, X. Sun, Z. Ding, *J. Am. Chem. Soc.*, 2007, **129**, 744-745.
33. B. Hu, K. Wang, L. Wu, S. H. Yu, M. Antonietti, M. M. Titirici, *Adv. Mater.*, 2010, **22**, 813–828.
34. W. Li, P. Goovaerts, M. Meurens, *J. Agric. Food Chem.*, 1996, **44**, 2252-2259.
35. B. Zhang, C. Liu, Y. Liu, *Eur. J. Inorg. Chem.*, 2010, 4411-4414.
36. F. Wang, Z. Xie, H. Zhang, C. Liu, Y. Zhang, *Adv. Funct. Mater.*, 2011, **21**, 1027–1031.
37. M. Sevilla, A.B. Fuertes, *Carbon*, 2009, **47**, 2281-2289.
38. D. V. Melnikov, J. R. Chelikowsky, *Phys. Rev. Lett.*, 2004, **92**, 046802.
39. P. C. Hsu, Z. Y. Shih, C. H. Lee, H. T. Chang, *Green Chem.*, 2012, **14**, 917-920.
40. S. Zhu, J. Zhang, C. Qiao, S. Tang, Y. Li, W. Yuan, B. Li, L. Tian, F. Liu, R. Hu, H. Gao, H. Wei, H. Zhang , H. Sun, B. Yang, *Chem. Comm.*, 2011, **47**, 6858-6860.
41. V. N. Mochalin, Y. Gogotsi. *J. Am. Chem. Soc*., 2009, **131**, 4594-4595.
42. D. Y. Pan, J. C. Zhang, Z. Li and M. H. Wu, *Adv. Mater.*, 2010, **22**, 734-738.
43. A. M. Derfus, W. C. W. Chan and S. N. Bhatia, *Nano Lett.*, 2004, **4**, 11-18.

Chapter-3

Design of Fe_3O_4@SiO_2/CD based nanostructure for simultaneous fluorescence sensing, magnetic separation and live cell imaging of fluoride ion

3.1. Introduction

In past few years, generous effort has been devoted to the design of sensors for the detection of fluoride anion due to its high analytical significance in environmental and biological processes.[1-6] Fluoride anion is an essential element of human body and plays a beneficial role in treating osteoporosis and protecting dental health.[7,8] However, excessive fluoride ingestion may cause kidney disorders, fluorosis and urolithiasis in humans, and exposure to very high levels of fluoride can cause death.[9-11] The maximum permissible limit of F^- in drinking water is set at 1.5 mg/L by the World Health Organization.[12] Currently, many people still regularly drink the water containing fluoride above this level all over the world. In order to decrease the possibility of excessive fluoride intake, a simple, economical, and selective assay is highly desirable for practical purpose.

The fluorescence sensing method has been used as an useful technique for detecting anions and metal ions due to high sensitivity and selectivity, simplicity, and real-time detection.[13-15] Considerable efforts have been devoted to design F^- selective fluorescent probes by exploiting different strategies including supramolecular recognition,[16-18] hydrogen bonding,[19,20] Lewis acid base interactions,[21-24] and F^- ion-induced chemical reactions.[25-29] In most cases, the measurements need to be conducted in purely organic solvents or less efficiently in organic solvent/water mixtures due to competitive interactions with water molecules. Moreover, interference from the presence of $H_2PO_4^-$, AcO^-, and CN^- ions is unavoidable and the detection selectivity is a severe issue.[30] To solve the selectivity problem, fluoride-induced chemical reactions have been utilized to design fluoride fluorescence sensors. The chemical reaction-based fluorometric F^- probes are exclusively based on small molecule dyes which operate in organic medium. Water-insolubility and concentration quenching effect of conventional fluorophores result in organic solvent dependence and slow sensing response limiting their practical utility. In addition to this, fluorophores which operate in UV excitation are not preferable for sensing fluoride in biological system. Therefore the prime challenges in designing fluoride sensors are 1) must be based on turn-on principle rather than turn-off as it enable small amounts of light to be measured relative to a dark back ground, 2) high

selectivity and sensitivity of the system in the back ground of competing anions, 3) low detection limit and fast usability in totally aqueous medium, 4) good luminescence under visible light excitation 5) cost effectiveness.

In recent times, carbon dots (CDs) have drawn great attention of interdisciplinary scientists owing to their small sizes, excellent water solubility, strong fluorescence, high photostability and non-toxicity and excellent biocompatibility.[31-33] These superior properties make these materials promising alternatives to common toxic metal-based quantum dots in sensing applications. Although carbons dots have been exploited for fluorescence sensing of a wide range of cations and anions, organic/biological molecules, and target gases,[34] the literature on the design of CD based sensor for potential sensing on fluoride ion in aqueous medium is inadequate. The scanty example includes zirconium complexed CD fluorescent probe for fluoride ion detection which is based on the competitive ligand reactions between the carboxylate groups (–COOH) on the surface of the luminescent carbon dots (CDs) and F^- coordinated to $Zr(H_2O)_2EDTA$.[35] In spite of conscious effort to develop a fluoride sensor to be operated in aqueous medium, the number of fluoride probes suitable for cell-imaging applications is still very sparse. For effective sensitivity in biological medium the probe has to meet stringent requirements such as a high selectivity for F^- in presence of other competitive anions, a high cell permeability, and low/no toxicity.

On the other hand, heterogeneous fluoride sensors, based upon the immobilization of molecular anion receptors to solid supports, are technologically attractive due to their potential ease of use and reusability. However, only limited examples of such heterogeneous sensors have been reported. The use of complex architectures employing surfactant micelles, silica nanoparticles, or other functionalized substrates has allowed one to overcome several innate limitations.[36-38] More specifically among solid supports, silica based nanomaterials provide an excellent choice for designing sensors because of their chemical stability, large surface area, biocompatibility and ease of surface modification.[39,40] Nonetheless, the use of silica nanoparticles and other solid supports in water treatment is limited due to their tedious separation process. In order to simplify the separation, incorporation of magnetic nanoparticles would be a good choice. Magnetic

nanoparticles would facilitate the magnetic separation and recuperation of the anion from the detection system using external magnetic field.

Following this line of thought, we demonstrate a robust reusable fluorescent sensor for fluoride ion detection and removal from aqueous solution. The design of a fluorescent probe includes two fundamental moieties, a receptor in charge of the recognition and a fluorophore responsible to signal the recognition event. We have used highly fluorescent CD as fluorophore and magnetically separable EDTA-Ni complex functionalized silica coated magnetite as fluoride ion receptor. The sensing principle involves the binding of CD onto the magnetic receptor inducing reduction of fluorescence intensity of the CD solution. On addition of fluoride ion to the system, the fluorescence intensity was gradually recovered due to substitution of bound CD by F^- ion. It is important to note that the fluoride deposited magnetic silica particles can be recovered and reused without significant loss of its activity. This technique is found to be extremely sensitive to achieve selective recognition of F^- in competitive aqueous environments. The technique has been further extended to monitor F^- in living cells as experimented in HT29 cells.

3.2. Experimental

Chemicals

Anhydrous ferric chloride ($FeCl_3$), ferrous sulphate ($FeSO_4 \cdot 7H_2O$), nickel chloride ($NiCl_2$), ammonia, ethanol and anionic compounds such as NaF, NaCl, NaBr, CH_3COONa, Na_2CO_3, $NaHCO_3$, Na_3PO_4, Na_2HPO_4, NaH_2PO_4, $NaNO_2$, $NaNO_3$, Na_2S, $NaHSO_3$, $NaHSO_4$, Na_2SO_3 were procured from Merck, Germany. Tetraethylorthosilicate (TEOS) and 3-aminopropyltriethoxysilane (APTES) were purchased from Sigma Aldrich, USA. Thionyl chloride ($SOCl_2$) and ethylenediaminetetraacetic acid (EDTA) were purchased from Spectrochem Private Limited. Comercially available dichloromethane and toluene were purified by distillation over phosphorous pentoxide and sodium metal with benzophenol, respectively. All other reagents and solvents were used without further purification.

Synthesis of Fe_3O_4 nanoparticles

Fe_3O_4 nanoparticles were prepared by chemical co-precipitation method. $FeCl_3$ (0.324 g, 2 mmol) and $FeSO_4.7H_2O$ (0.278 g, 1 mmol) were dissolved in 40 mL of deionized water under vigorous stirring at 70-80 °C for 10 min under a nitrogen atmosphere. Subsequently, 5 mL ammonia solution (25%) was added drop wise into the solution and stirring continued for another 30 min. The solution was then cooled to room temperature and the resulting particles were subjected to magnetic decantation followed by repeated washing with millipore water and finally dried in a vacuum oven at 70 °C.

Synthesis of amine modified silica coated magnetite nanoparticle (Fe_3O_4@SiO_2-NH_2)

Prior to amine modification, silica coated Fe_3O_4 nanoparticles were prepared. For the synthesis, 50 mg of the iron oxide nanoparticles were well dispersed in a mixture of 50 mL ethanol, 10 mL millipore water and 1 mL 28% ammonia solution. Then, 0.5 mL TEOS was added drop wise under vigorous stirring conditions to the above nanoparticle suspension. After continuous stirring for 12 h at room temperture, the silica coated magnetic nanoparticles were recovered and washed with ethanol and dried. For amine modification, about 0.3 g of Fe_3O_4@SiO_2 particles were added to 30 mL of dry toluene with 0.7 mL (3 mmol) of 3- aminopropyltriethoxysilane (APTES) under refluxing in N_2 atmosphere for 24 h. The functionalized particles were magnetically separated, washed extensively with acetone, and dried.

Synthesis of EDTA bound silica coated Fe_3O_4 nanoparticle (Fe_3O_4@SiO_2-EDTA)

The EDTA modification of Fe_3O_4-SiO_2-NH_2 was carried out in an anhydrous condition using dichloromethane as solvent.[41] To the mixture of EDTA (3.72 g, 0.01 mol) and 40 mL dichloromethane, $SOCl_2$ (0.72 ml, 0.01 mol) was slowly added with continuous stirring under argon atmosphere. Immediately after $SOCl_2$ was completely dropped, 0.5 g of Fe_3O_4@SiO_2-NH_2 was rapidly added to the mixture and allowed to stir for 2 h under room temperature. Then EDTA modified silica coated magnetite sample was separated magnetically and washed in a row with DCM, acetone, milipore water, $NaHCO_3$ (0.1 M), milipore water and acetone. Finally it was dried overnight at 50 °C.

Synthesis of EDTA-Ni complex modified Fe_3O_4@SiO_2 nanoparticle (Fe_3O_4@SiO_2-EDTA-Ni)

The complexation of Fe_3O_4@SiO_2-EDTA was carried out with Ni^{2+} ion by equilibration method. The functionalized magnetic support Fe_3O_4@SiO_2-EDTA (200 mg) was stirred with excess $NiCl_2$ salt for 30 min. Then the pH of the solution was set at 8 and allowed to stir overnight. The Fe_3O_4@SiO_2-EDTA-Ni complex was collected by magnetic separation, washed with aqueous solution to remove non-complexed metal ion and oven dried at 50 °C.

Fluorescence sensing and removal of Fluoride anion

The detection of F^- ion was performed in milipore water, tap water and phosphate buffer solution. In a typical assay, 5 mg Fe_3O_4@SiO_2-EDTA-Ni was added into CD (10 mL, 2 ppm) dispersion and the fluorescence (FL) spectra was recorded after and before the addition of Ni complex bound magnetic support. To the above mixture different concentrations of F^- ion was added and the change in FL intensity was monitored. The selectivity for F^- was confirmed by adding other anion stock solutions instead of F^- in a similar way at a concentration of 500 μM. All experiments were performed at room temperature. The fluoride bound magnetic support was recovered through external magnet.

In vitro cytotoxicity and fluorescence imaging

In vitro cytotoxicity: Human colon adenocarcinoma cell line HT29 cells (3×10^3 cells) were seeded into 96-well plates and incubated in 200 μL DMEM containing 10% FBS for 24 h (37 °C, 5% CO_2). Then the cells were incubated with different concentration of Fe_3O_4@SiO_2-EDTA-Ni@CD (12.5, 25, 50, 100, 200, 300, 400, 500 μg/mL) in fresh DMEM without serum for another 24 h and after incubation viable cell concentration was checked by MTT (3-(4,5-Dimethyl-2-2thiazolyl)-2,5-diphenyl-2H-tetrazolium bromide) assay. All the experiments were performed in triplicate.

Fluorescence Imaging: For live cell imaging, the HT29 cells were incubated with Fe_3O_4@SiO_2-EDTA-Ni@CD (100 μg/mL) for 12 h at 37 °C inside humidified 5% CO_2

incubator. After being washed with fresh PBS three times the cells were imaged through confocal microscope at 488 nm excitation. Then F^- (500 mM) was added and incubated for 2 h and the cells were imaged again after washing three times with PBS at same excitation wavelength of 488 nm.

3.3. Characterization

The prepared materials were characterized by standard analytical techniques as described in characterization section of chapter-2. In addition, the morphology and microstructure of the samples were analyzed by Field Emission Scanning electron microscope (Nova NanoSEM/ FEI-450). The magnetic property of Fe_3O_4@m-SiO_2-EDTA-Ni nanoparticle was determined using a SQUID-VSM instrument (Evercool SQUID VSM DC Magnetometer) at 25.0 ± 0.5 °C.

3.4. Results and discussion

Synthesis

The magnetically separable fluorescent sensor comprising of two components one fluorophore (CD) for FL signal recognition and other EDTA-Ni complex bound silica coated magnetite nanoparticle, which serve as recipient of fluoride ion. The fluorescent CD was synthesized by hydrothermal treatment of orange juice, whereas the fluoride ion receptor magnetic particle was synthesized by a multistep process (Scheme-3.1). The silica-coated magnetite nanoparticles were synthesized using modified Stöber's method, which were further amine functionalized by APTES. The superparamagnetic nature of the F_3O_4 would facilitate their easy and quantitative separation using external magnetic field, whereas silica coating stabilize the magnetic nanocore and eliminate the interaction of magnetic core with fluorophore CD. Moreover silica coating provides enough sites for further surface modification. In the second step, the surface of the nanoparticles was modified with EDTA in order to prepare Ni-EDTA complex bound silica coated

magnetite nanoparticle which would serve as fluoride ion receptor. The metal complexation was done using excess $NiCl_2$ salt at pH 8.

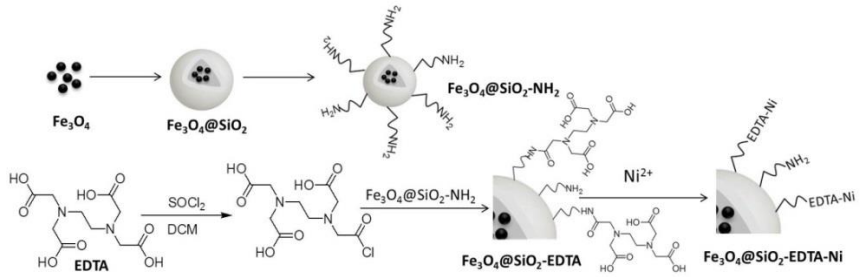

Scheme 3.1 Illustration of synthesis of EDTA-Ni complex conjugated Fe_3O_4@m-SiO_2.

Characterization of fluoride ion receptor

Structure and morphology

The crystal structures and the phase purity of the Fe_3O_4@SiO_2 were determined by XRD. The diffraction peak of Fe_3O_4 and Fe_3O_4@SiO_2 (Figure 3.1a) can be easily indexed to a crystalline cubic spinel structure of Fe_3O_4 (JCPDS No. 82-1533). No other impurity peaks were detected. The broad band at 2θ=22° can be assigned to the amorphous silica shell (JCPDS No. 29-0085).

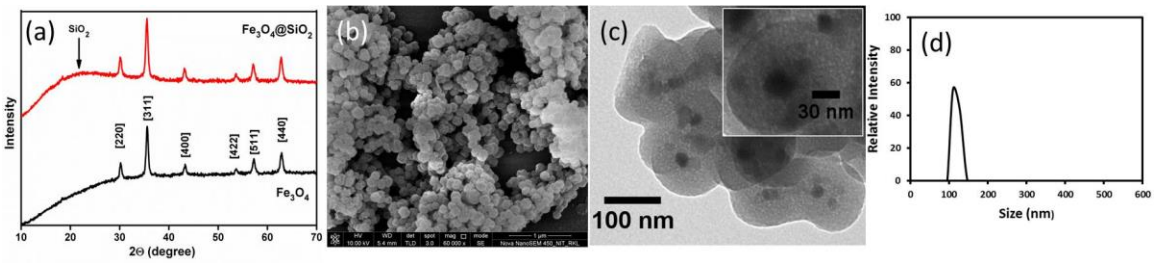

Figure 3.1 (a) XRD patterns of Fe_3O_4 and Fe_3O_4@SiO_2, (b) FESEM image, (c) TEM image of Fe_3O_4@SiO_2, the inset is at high magnification showing the core-shell structure and (d) hydrodynamic size of Fe_3O_4@SiO_2.

The morphology and size distribution of the silica coated magnetite nanoparticles were obtained from FESEM and HRTEM analysis. The FESEM image (Figure 3.1b) clearly showed the formation of monodisperse spherical particles with a smooth surface. The average particle size of Fe_3O_4@SiO_2 was found to be 120 nm. The TEM image (Figure 3.1c) of Fe_3O_4@SiO_2 particles shows the formation of core-shell structure of size

100-120 nm. The dark core of the Fe_3O_4 and the grey silica shell of thickness 35-40 nm were clearly observed. Each silica sphere contains one or more magnetite nanocrystals embedded within its structure. However, aggregation/coalescence of individual $Fe_3O_4@SiO_2$ was found, and the aggregation might occur during TEM sample preparation and drying effect as observed in other cases.[42] The average size of the particle in dispersion was found to 117 nm as measured by dynamic light scattering.

Surface properties

The various stages of synthesis of $Fe_3O_4@SiO_2$-EDTA-Ni were verified through FTIR spectroscopy (Figure 3.2a). $Fe_3O_4@SiO_2$ particles show strong absorptions at 555 cm^{-1}, characteristic vibration of Fe-O in the magnetite lattice. The bands at 1000-1200 and 942 cm^{-1} were attributed to the Si-O-Si asymmetric stretching vibration and bending vibration of Si-OH. Furthermore appearance of bands for OH (3300 cm^{-1}), H_2O (1627 cm^{-1}), Si-O-Si (υ_{sym}, 802 cm^{-1}) and Si-O (δ, 458 cm^{-1}) bonds confirms the successful silica coating on Fe_3O_4 nanoparticle. The presence of broad band centered at 3300 cm^{-1} and intense band at 1635 cm^{-1} suggest the presence of large number of H_2O and –OH groups on the surface which play the major role not only in high aqueous stability but also provides enough scope for further surface modification with APTES. The appearance of methylene peak at 2882 cm^{-1} confirms the successful amine modification by APTES. However, the asymmetric and symmetric stretching vibrations of the N-H bond, located at wavenumbers 3366 and 3296 cm^{-1} on the spectrum of APTES, are not seen, possibly owing to the overlapping with the stretching vibration of the hydroxyl group. The band at about 1698 cm^{-1} in $Fe_3O_4@SiO_2$-EDTA spectrum was assigned to the –C=O stretching vibration of the acylamide group, which was the principal band of the acytamide ligand (EDTA). The bands corresponding to the C-N stretching and/or C-O stretching vibration overlap in the silica vibrational region 1300–1000 cm^{-1}. The shift of –C=O stretching vibration of carboxylic group to 1661 cm^{-1} in case of $Fe_3O_4@SiO_2$-EDTA-Ni can be attributed to EDTA co-ordination to Ni through carboxylic group. In a typical survey spectrum (Figure 3.2b) of the fluoride bound nanoparticles, the peaks at binding energies 100, 285-290, 402.3, 530-538, 683-692, 705-730, 855-880 eV are ascribed to binding energy in Si2p, C1s, N1s, O1s, F1s, Fe2p and Ni2p regions respectively. High resolution scan for C1s (Figure 3.2c) shows that the curve is well fitted

into five peaks centered at 283.7, 285.2, 286.2, 288.5 eV corresponding to the C-Si, C-C/C-H, C-N, -NHCO/-COOH carbon respectively. The broad peaks for O1s binding 530.4 and 532.5 eV correspond to M-O and -COOH/NHCO respectively (Figure 3.2d). The high resolution scans of the N1s (Figure 3.2e) can be fitted into three peaks. The peak at 400.1 eV corresponds to unreacted-NH_2 group of the magnetic receptor. The peaks appearing at 401 and 402.4 eV are attributed to nitrogen in amide (CONH) and C-N respectively. $Fe2p_{3/2}$ and $Fe2p_{1/2}$ electrons show binding energy at 711.7 and 725.4 eV which is consistent with the Fe2p binding energy of magnetite nanoparticles (Figure 3.2f). Presence of $Ni2p_{3/2}$ and $Ni2p_{1/2}$ at 859 and 876.9 eV confirms the formation of Ni complex on Fe_3O_4@SiO_2-EDTA (Figure 3.2g). The high resolution spectrum of F1s at 689.8 eV corresponds to semi ionic bonded fluoride (Figure 3.2h).

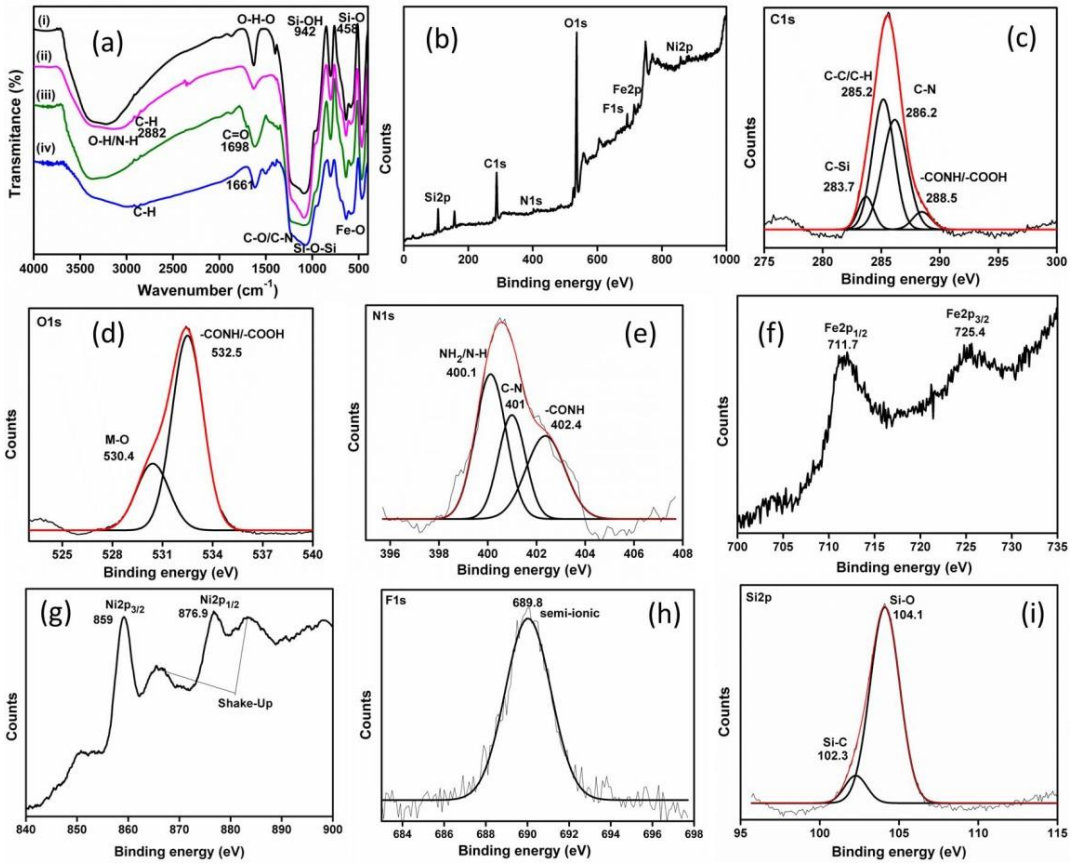

Figure 3.2 (a) FTIR spectra of (i) Fe_3O_4@SiO_2, (ii) Fe_3O_4@SiO_2-NH_2, (iii) Fe_3O_4@SiO_2-EDTA (iv) Fe_3O_4@SiO_2-EDTA-Ni, and (b) Survey spectrum, high resolution scan corresponding to (c) C1s, (d) O1s, (e) N1s, (f) Fe2p, (g) Ni2p, (h) F1s, (i) Si2p of fluorine bound Fe_3O_4@SiO_2-EDTA-Ni sample.

Magnetic Properties

The magnetic properties of the Fe_3O_4@SiO_2-EDTA-Ni receptor were investigated by using a vibrating sample magnetometer (VSM) with the magnetic field cycle between -15000 and +15000 Oe at room temperature. Field dependent magnetization curve (Figure3.3a) of Fe_3O_4@SiO_2-EDTA-Ni receptor at room temperature shows that the magnetization value increased rapidly as the applied field increased up to 8000 Oe and reached at a saturation point at 12000 Oe. The saturation magnetization (Ms) was found to be 94 emu g^{-1} which is much higher than the as prepared Fe_3O_4@SiO_2 (40 emu g^{-1}). The higher saturation magnetization can be interpreted as the synergistic magnetization effect of Ni^{2+} in bound nickel complex on silica coated magnetite and Fe_3O_4 core. The room temperature magnetic curve for both the sample exhibit no hysteresis and completely reversible at room temperature indicating the superparamagnetic nature. The above observation indicates that although complexation of Ni to Fe_3O_4@SiO_2 has led to a significant increase in saturation magnetization (Ms), but the superparamagnetic behavior remain unaffected on complexation. The complete magnetic separation by external magnetic field near the fluoride bound Fe_3O_4@SiO_2-Ni nanocomposite (Figure 3.3b) demonstrates the strong magnetic sensitivity of the fluoride receptor. The high saturation magnetization and superparamagnetic behavior enable the magnetic receptor to be used as an efficient recoverable fluoride receptor which can be easily removed by applying external magnetic field after binding with fluoride ion.

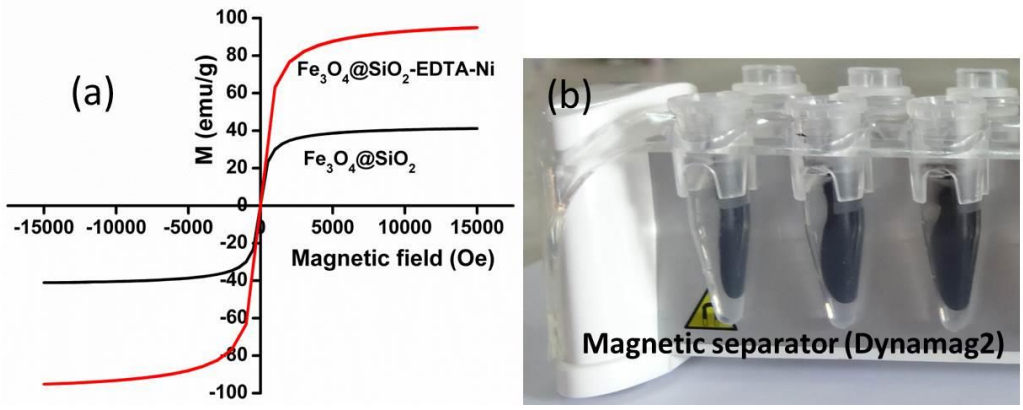

Figure 3.3 Field dependent magnetization curves of Fe_3O_4@SiO_2 and Fe_3O_4@SiO_2-EDTA-Ni, (b) Magnetic separation of Fe_3O_4@SiO_2-EDTA-Ni through Dynamag2.

Fluorescence detection of Fluoride ion

We explored the combined features of CD (FL behavior) and magnetic Fe_3O_4@SiO_2-EDTA-Ni nanoparticles (fluoride ion receptor) for selective fluoride ion detection and removal in aqueous solution. The fluorescence property of CD is utilized for fluorescence monitoring of fluoride ion, whereas the magnetic nature of the receptor is used for recovery and reusability of the nanosystem. The CD exhibits strong and stable fluorescence signal at 420 nm on excitation to 340 nm. As expected the addition of Fe_3O_4@SiO_2-EDTA-Ni to the aqueous CD solution shows sharp decline in the fluorescence intensity (Figure 3.4a). The observed sensations can be attributed to the binding of the CD to the magnetic receptor resulting in reduction of CD level available in the analytic sample which ultimately leads to fluorescence quenching. However addition of the fluoride ion results in gradual restore of the fluorescence. As shown in Figure 3.4a, the PL intensity of the CD at around 420 nm increases gradually with increasing concentration of F^-, indicating that addition of F^- ions can effectively recover the fluorescence of the CD. This fluorescence regain can be ascribed to the replacement of the bound CD into the solution by F^-. To evaluate the sensitivity of the system, different concentrations of F^- ranging from 1µM-1mM were studied and found that the fluorescence intensity of the CD is recovered to 95% with addition of 1mM F^-. By plotting relative intensity (F/F_0) against fluoride concentration, we established good linearity for fluoride in the range 1-20 µM with R^2=0.992 (Figure 3.4c). These results suggest that the PL of CD solution can be recovered due to the strong binding of F^- to Ni bound receptor. On applying external magnetic field, the magnetic support along with F^- can be simply removed from the medium as illustrated in the Figure 3.3b. Although the mechanism of fluorescence sensing is not clear, we suggest a possible approach for the interaction between the sensor and fluoride. We anticipate that the surface –COOH group of CD interacts with postively charged Ni centre and free amine group present on magnetic receptor through electrostatic interaction which results in binding of the CD on to the magnetic receptor leds to diminished fluorescence signal. The diminished fluorescence intensity is recovered on addition of F^- due to its high binding affinity to the receptor. After adding F^-, it occupies the binding sites and thus replaces CD into the

analytical solution. The binding of the fluoride is clearly evidenced by the semi-ionic fluoride in high resolution F1s XPS spectrum (Figure 3.2h).

To investigate the response time of the receptor towards the fluoride anion, we measured the fluorescence intensity variation as a function of time upon addition of fluoride anion. Figure 3.4d clearly indicates that the fluorescence intensity of the system reached its maximum value within fifteen minutes upon addition of fluoride anion. This demonstrates that the coordination of fluoride ion with receptor (Fe_3O_4@SiO_2-EDTA-Ni) is 15 minute.

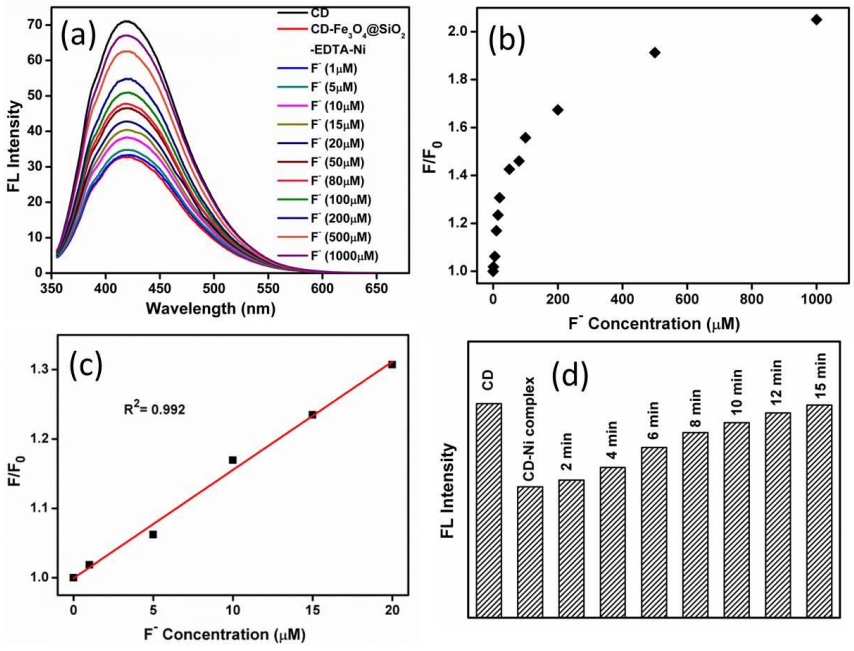

Figure 3.4 (a) Fluorescence spectra of CD-Fe_3O_4@SiO_2-EDTA-Ni with gradual addition of F^- in millipore water, (b) Relative fluorescence (F/F_0) vs F^- concentration, (c) the linear response, (d) Fluorescence recovery in response to times after addition of F^-.

Selectivity of the receptor for F^- detection

To evaluate the selectivity of the developed system towards F^-, fluorescence screening experiment was carried out. Figure 3.5a shows the histogram of fluorescence response with different anions and very little FL enhancement was observed after the addition of $H_2PO_4^-$, S^{2-} and NO_3^- ions. The fluorescence of CD solution was recovered almost completely in the presence of F^-, whereas negligible recovery was observed in presence of other anions like Cl^-, Br^-, CO_3^{2-}, HPO_4^{2-}, PO_4^{3-}, HCO^{3-}, NO^{2-} and CH_3COO^-

indicating that synthesized sensor is highly specific and selective for F^-. Fluorine is the strongest electronegative element and that can recognize a positively charged center which assists the release CD from the magnetic receptor into the analytic solution ensuing fluorescence enhancement.

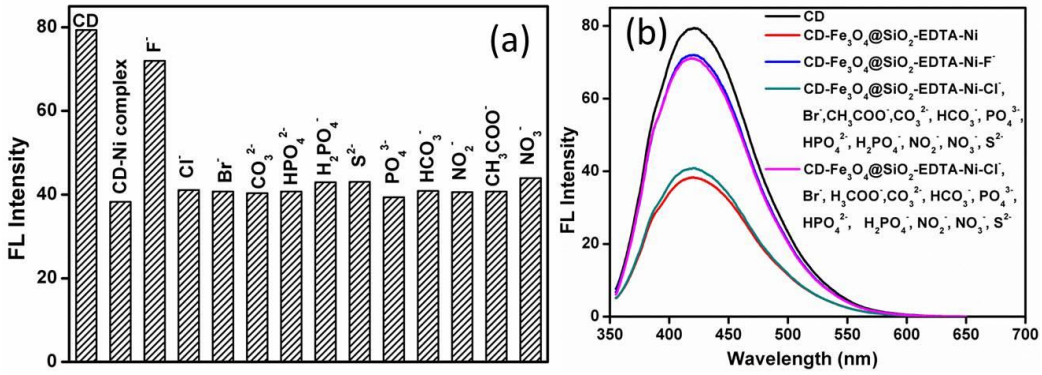

Figure 3.5 Fluorescence recoveries (a) in the presence of different anion (500 µM), and (b) mixture of anions (500 µM).

Figure 3.5b presents the fluorescence response of CD towards F^- in the presence of above mentioned anions. Evidently, the co-existence of these anions does not interfere with the coordination of fluoride anion with the receptor as well as the subsequent fluorescence enhancement. These results suggest that the probe can function as a highly selective sensor for F^-.

Application of Fluoride ion sensing

Efficient F^- detection in water samples and PBS

To evaluate the efficacy of this sensing system in some real samples, the sensor was applied for sensing fluoride ions in tap water and PBS. Prior to use all the samples were filtered through a 0.22 µm membrane to remove any suspended particles. As shown in Figure 3.6a, this sensing system worked quite well in tap water with the recovery of 96%. It was observed that the fluorescence intensity increased with increasing concentration of F^-. The present approach provides a linear response to F^- ions at concentrations over the range from 0 to 10 µM having R^2 = 0.9978 (Figure 3.6c). Although numerous organic/inorganic impurities and minerals exist in the tap water, this sensing system can still selectively respond to F^-, satisfying the practical detection of F^-

in real samples. Although the flourescence recovery rate on F^- addition in PBS was found to be slow in the lower concentration range (1-20 µM) compared to milipore water and tap water, it worked quite well in higher concentration range (50-1000 µM) with recovery of 92% (Figure 3.6d). This discrepancy may be due to the trivial interference of $H_2PO_4^-$ ion present in PBS.

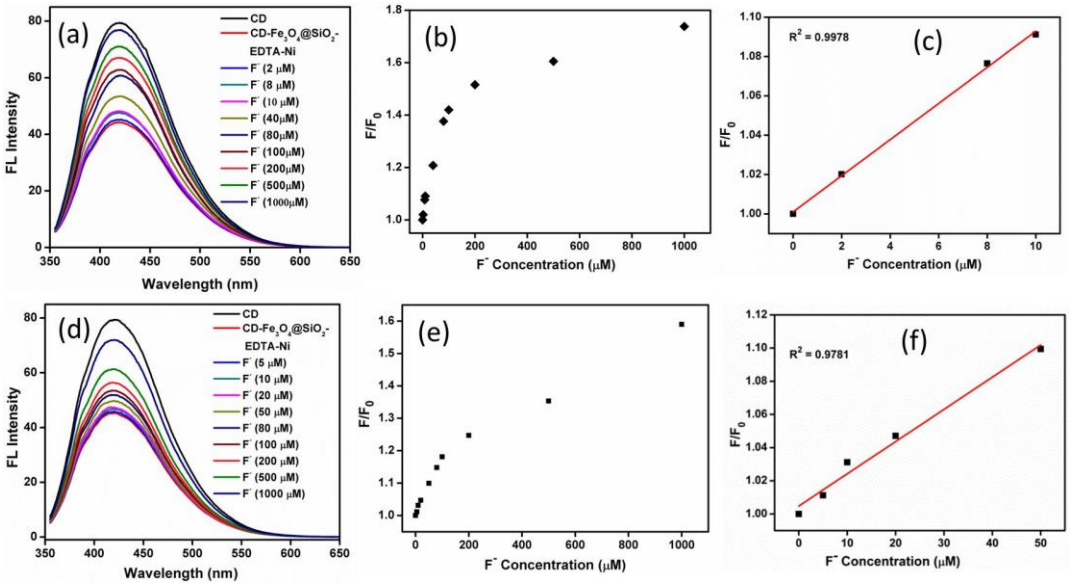

Figure 3.6 Fluorescence spectra of CD-Fe_3O_4@SiO_2-EDTA-Ni with gradual addition of F^- in (a) tap water and (d) PBS, Relative fluorescence (F/F_0) vs F^-concentration in (b) tap water and (e) PBS, the linear response in (c) tap water and (f) PBS.

Imaging of fluoride ion in live cells

To investigate the biocompatibility of the sensor, the cytotoxicity of the Fe_3O_4@SiO_2-EDTA-Ni@CD sensor was evaluated in HT29 cells. The viability of the cells was declined by 10% upon addition of the sensor at up to 100 µg/mL for an incubation period of 72 h (Figure 3.7a). Thus the sensor is nontoxic and biocompatible, thus can be explored for bioimaging of F^- inside the living cell. We performed in vitro cellular uptake experiment with HT29 cells. The cells were first incubated with the probe (Fe_3O_4@SiO_2-EDTA-Ni@CD) for 12 h at 37 ºC. After the uptake, the particles were monitored by confocal microscopy and found to reside mainly in the cell membrane. It was observed that in absence of F^- hardly any green fluorescence was observed under excitation of 488 nm. However when the cells were supplemented with F^- a clear green

signal was observed surrounding the nuclear region indicating the ability of our nanoprobe to show turn-on behavior in presence of F^- inside the cell (Figure 3.7).

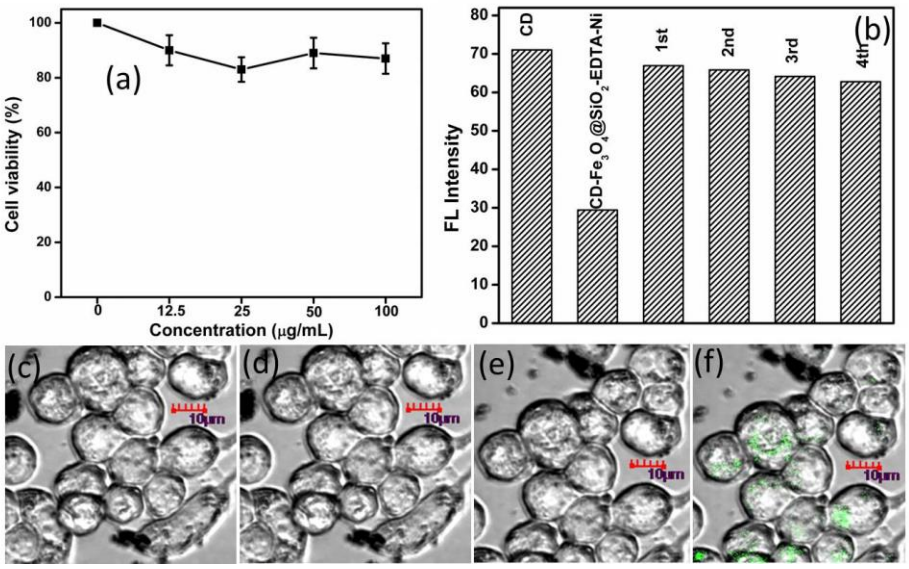

Figure 3.7 (a) Cell viability by MTT assay and (b) Reusability of the receptor for detection of F^-, The confocal image of HT29 cells stained with Fe_3O_4@SiO_2-EDTA-Ni@CD (c), (e) Bright-field transmission image of HT29 cells (d) confocal image of cells visualized at excitation wavelength of 488 nm, (f) confocal image of cells post-incubated in 100 mM F^- solution.

Table 3.1 Fluoride binding capacity of the receptor for conjugative cycle.

No. of Cycle	Fluoride binding capacity
1st	16.4 mg/g
2nd	16.0 mg/g
3rd	15.6 mg/g
4th	14.8 mg/g

Fluoride removal, separation and reusability of the system

The reusability of the system was further investigated by separating the fluoride bound Fe_3O_4@SiO_2-EDTA-Ni using an external magnet. The recovered nanoreceptor was recycled three times for F^- detection with negligible loss of its activity (Figure 3.7b). At the end of each cycle the recovered nanoreceptor was first treated with excess of calcium solution to form the insoluble CaF_2 precipitate followed by repeated washing with milipore water and, finally magnetically separated and dried for further use. The

bound fluoride ion in each cycle is quantified by analyzing the residual aqueous fluoride solution through fluoride electrode analysis (Table 3.1).

3.5. Conclusion

- In summary, we have presented here a novel strategy for the selective detection and removal of fluoride ion from aqueous solution using a nontoxic fluorescent probe and a magnetic receptor.
- The assay is based on the exchange reaction between the CD and F^-, which induces the binding of fluoride to magnetic receptor resulting in recovery of fluorescence.
- This proposed sensing method has been successfully applied in the detection of fluorine in tap water which can have promising applicability in drinking water quality monitoring.
- The excellent magnetic properties of the nanoreceptor offers an advantage for easy, rapid and assessable separation of the fluoride bound receptor from analytic solution which allows quantification of fluoride ion.
- The probe can also be used for monitoring fluoride anion inside cells.
- In comparison with existing fluorescence fluoride assay, our method possess several remarkable advantages including (1) easy removal of F^- through magnetic separation (2) reusability of the system for successive study (3) quantification of fluoride ion (4) wide linear response range 1-20 µM.
- The present strategy may offer a new approach for developing reusable low-cost, high sensitive and selective F^- sensors in environmental applications.

3.6. References

1. R. M. Duke, E. B. Veale, F. M. Pfeffer, P. E. Kruger, T. Gunnlaugsson, *Chem. Soc. Rev.,* 2010, **39**, 3936-3953.
2. V. Amendola, D. Esteban-Gomez, L. Fabbrizzi, M. Licchelli, *Acc. Chem. Res.*, 2006, **39**, 343-353.
3. R. Martinez-Manez, F. Sancenon, *Chem. Rev.,* 2003, **103**, 4419-4776.
4. Z. M. Hudson, S. Wang, *Acc. Chem. Res.,* 2009, **42**, 1584-1596.

5. Z. H. Zeng, A. A. J. Torriero, A. M. Bond, L. Spiccia, *Chem. Eur. J.*, 2010, **16**, 9154-9163.
6. E. Galbraith, T. D. James, *Chem. Soc. Rev.*, 2010, **39**, 3831-3842.
7. X. Zheng, W. Zhu, D. Liu, H. Ai, Y. Huang, Z. Lu, *ACS Appl. Mater. Interfaces*, 2014, **6**, 7996-8000.
8. M. Kleerekoper, Endocrinol. *Metab. Clin. North Am.*, 1998, **27**, 441-452.
9. S. Ayoob, A. K. Gupta, *Crit. Rev. Environ. Sci. Technol*., 2006, **36**, 433-487.
10. P. P. Singh, M. K. Barjatiya, S. Dhing, R. Bhatnagar, S. Kothari, V. Dhar, *Urol. Res.*, 2001, **29**, 238-244.
11. B. D. Gessner, M. Beller, J. P. Middaugh, G. M. Whitford, *N. Engl. J. Med.*, 1994, **330**, 95-99.
12. H. Yiping and W. Caiyun, *Anal. Chim. Acta,* 2010, **661**, 161-166.
13. R. Hu, J. Feng, D. Hu, S. Wang, S. Li, Y. Li, G. Yang, *Angew. Chem. Int. Ed.*, 2010, **49**, 4915-4918.
14. B. C. Zhu, F. Yuan, R. X. Li, Y. M. Li, Q. Wei, Z. M. Ma, B. Du, X. L. Zhang, *Chem. Commun.,* 2011, **47**, 7098-7100.
15. Y. Kubo, M. Yamamoto, M. Ikeda, M. Takeuchi, S. Shinkai, S. Yamaguchi, K. Tamao, *Angew. Chem. Int. Ed.,* 2003, **42**, 2036.
16. M. Boiocchi, L. D. Boca, D. E. Gomez, L. Fabbrizzi, M. Licchelli, E. Monzani, *J. Am. Chem. Soc.*, 2004, **126**, 16507-16514.
17. Q. G. Wang, Y. B. Ding, X. Li, W. H. Zhu, Y. S. Xie, *Chem. Commun.*, 2010, **46**, 3669-3671.
18. X. M. He, V. W. W. Yam, *Org. Lett.*, 2011, **13**, 2172-2175.
19. A. S. F. Farinha, M. R. C. Fernandes and A. C. Tome, *Sens. Actuators B*, 2014, **200**, 332-338.
20. K. J. Chang, D. Moon, M. S. Lah, K. S. Jeong, *Angew. Chem., Int. Ed.*, 2005, **44**, 7926-7929.
21. S. Xu, K. C. Chen, H. Tian, *J. Mater. Chem.*, 2005, **15**, 2676-2680.
22. A. Saxena, M. Fujiki, R. Rai, S. Y. Kim, G. Kwak, *Macromol. Rapid Commun.*, 2004, **25**, 1771-1775.
23. X. Y. Liu, D. R. Bai, S. N. Wang, *Angew. Chem. Int. Ed.*, 2006, **45**, 5475-5478.

24. M. Melaimi, F. P. Gabbai, *J. Am. Chem. Soc.*, 2005, **127**, 9680-9681.
25. Y. M. Li, X. L. Zhang, B. C. Zhu, J. L. Yan, W. P. Xu, *Anal. Sci.*, 2010, **26**, 1077-1080.
26. X. F. Yang, H. P. Qi, L. P. Wang, Z. Su, G. Wang, *Talanta*, 2009, **80**, 92-97.
27. J. F. Zhang, C. S. Lim, S. Bhuniya, B. R. Cho, J. S. Kim, *Org. Lett.*, 2011, **13**, 1190-1193.
28. M. S. Baker, Phillips, S. T. *J. Am. Chem. Soc.*, 2011, **133**, 5170-5173.
29. C. M. Ray, N. Singh, N. Kaur, J. F. Callan, *Chem. Commun.*, 2009, 686-688.
30. J. Hu, G. Zhang, Y. Geng, S. Liu, *Macromolecules*, 2011, **44**, 8207–8214.
31. H. Li, Z. Kang, Y. Liu, S. T. Lee, *J. Mater. Chem.*, 2012, **22**, 24230-24253.
32. S. N. Baker and G. A. Baker, *Angew. Chem. Int. Ed.*, 2010, **49**, 6726-6744.
33. H. P. Liu, T. Ye, C. D. Mao, *Angew. Chem. Int. Ed.*, 2007, **46**, 6473-6475.
34. Z. Yang, Z. Li, M. Xu, Y. Ma, J. Zhang, Y. Su, F. Gao, H. Wei, *Nano-Micro Lett.*, 2013, **5**, 247-259.
35. J. M. Liu, L. Lin, X. X. Wang, L. Jiao, M. L. Cui, S. L. Jiang, W. L. Cai, L. H. Zhang, Z. Y. Zheng, *Analyst*, 2013, **138**, 278-283.
36. K. Ngamdee, S. Martwiset, T. Tuntulani, W. Ngeontae, *Sens. Actuators, B: Chem.*, 2012, **173**, 682-691.
37. Z. Zhou, Y. H. Zheng, Q. M. Wang, *Inorg. Chim. Acta*, 2013, **394**, 127-131.
38. Z. E. Jacobi, L. Li, J. W. Liu, *Analyst*, 2012, **137**, 704-709.
39. W. Lin, Y. W. Huang, X. D. Zhou, Y. Ma, *Toxicol. Appl. Pharmac.*, 2006, **217**, 252-259.
40. W. Tan, K. Wang, X. He, X. J. Zhao, T. Drake, L. Wang, R. P. Bagwe, *Med. Res. Rev.*, 2004, **24**, 621-638.
41. J. Huang, M. Ye, Y. Qu, L. Chu, R. Chen, Q. He, D. Xu, *J. Colloid. Interf. Sci.*, 2012, **385**, 137-146.
42. Z. Y. Ma, D. Dosev, M. Nichkova, S. J. Gee, B. D. Hammock, I. M. Kennedy, *J. Mater. Chem.*, 2009, **19**, 4695-4700.

Chapter-4

Carbon quantum dot decorated mesoporous silica nanoparticle for fluorescence sugar sensing and targeted imaging of colon cancer cells

4.1. Introduction

As one of the primary biological materials, saccharides play important roles in many biological processes[1,2] and can also act as important markers for different diseases, the most common of them being glucose for diabetes.[3] Furthermore owing to broad utility of saccharides in food, cosmetic and medicinal applications, saccharide sensing has attracted continuous concern. Much research has been carried out for monitoring glucose concentrations through various methods such as colorimetric,[4] electrochemical,[5] and fluorescence detection.[6] Among these methods, fluorescence sensing have attracted rising attention due to their intrinsic advantages, considerable research space and applicability to living cells.[7] The conventional glucose sensors mostly rely on the use of an enzyme such as glucose oxidase or glucose dehydrogenase.[8] However these methods are expensive, complex, time-consuming and inherently sensitive to factors influencing enzyme activity such as heat, solvent, pH which limit their practical application. In this respect synthetic chemosensors are more desired in terms of the stability, low cost and oxygen independence. Boronic acid-based synthetic sensors therefore represent promising alternatives for saccharide sensing owing to their tight yet reversible covalent complex formation ability with 1,2- and 1,3-cis diols to form five- or six-membered cyclic esters respectively.[9] Furthermore boronic acid can differentiate structurally similar saccharide molecule depending on its binding strength ability influenced by the orientation and relative position of hydroxyl groups. These features can boost the saccharide sensing with high selectivity and signify the real world saccharide sensing application.

On the other hand, recently discovered luminescent carbon quantum dots (CDs) have gained considerable attention as luminophore due to their sizes below 10 nm, high biocompatibility and excellent luminescent properties.[10-12] These features provide promising prospects for their application in biodetection and sensing, particularly in glucose sensors. For instance, Zheng *et al.* utilized the peroxidase-like catalytic activity of CDs to achieve colorimetric detection of H_2O_2 and glucose.[13] Subsequently a similar glucose sensor was developed by Liu and coworker using N-doped CDs.[14] They quantified the glucose by monitoring the coloration of 3,3,5,5-tetramethylbenzidine

(TMB) induced by the oxidation of hydrogen peroxide. Although CDs can act as a signal transduction substrate, they have no intrinsic recognition ability to bind or sense saccharide selectively. Thus a specific recognition unit is needed to prepare a highly selective probe for glucose detection. In this respect CD functionalized with boronic acid having the specific recognition ability to 1,2 and 1,3-cis diol are important for the development of glucose sensor. Qui *et al.* developed a label-free fluorescence assay for glucose detection using CDs and a boronic acid substituted bipyridinium salt, which was realized via fluorescence quenching with the salt and subsequent recovery by glucose.[15] Subsequently Shi *et al.* reported a boronic acid functionalized CDs for selective and sensitive glucose determination in microdialysate.[16] The added glucose induced the assembly of CDs based on the covalent binding between the cis-diols of glucose and boronic acid of the CD surface resulting in fluorescence quenching. This boronate-affinity sensing principle was further explored for blood sugar sensing[17] where the fluorescent probe was synthesized through one step hydrothermal carbonization of phenyl boronic acid. Although these reported sensing methods present efficient detection techniques for monitoring glucose, however the separation of water soluble CDs from the inspective medium are questionable. The isolation of carbon dot can be easily achieved by encapsulating CDs in a suitable matrix, which can preserve the luminescence properties of CDs and avoid the leaching of CDs abolishing any possible interference. In this respect, ordered mesoporous silica can serve as an efficient matrix for uniform growth of CDs in the mesoporous channels, due to their advantageous structural properties, such as high internal surface area and pore volume, tunable pore sizes, colloidal stability, and the low cytotoxicity.[18,19]

In the present chapter, we present a simple effective fluorescent platform for glucose sensing using easily recoverable CD deposited silica nanoparticles (m-SiO_2-CD) as fluorophore in association with 3-aminophenylboronic acid (APBA). The synthesized fluorophore was well characterized by standard spectrometric techniques such as XRD, FESEM, TEM, BET, FTIR, XPS etc. The quenched fluorescence signal due to π-π interaction of APBA and m-SiO_2-CD has effectively recovered in response to the binding of glucose which lift-off the APBA from the CD surface. Exploiting the excellent luminescent properties of synthesized m-SiO_2-CD and high affinity of APBA towards

cis-diol, we extend our work for targeted imaging of cancer cell overexpressed with sialyl Lewis A (sLe^a) receptor. The sLe^a is a tetrasaccharide having free cis diols, which can be detected by APBA through the formation of boronate ester. For this purpose, 3-aminophenylboronic acid modified m-SiO_2-CD (m-SiO_2-CD-APBA) has been prepared separately through amide linkage using the surface carboxyl group of CD. The cytocompatibilty and targeted imaging of the particle was evaluated on human colon adenocarcinoma cell HT29.

4.2. Experimental

Chemicals

Cetyltrimethylamminium bromide (CTAB), Tetraethyl orthosilicate (TEOS), 3-aminophenylboronic acid (APBA) were obtained from Sigma Aldrich, India. Glucose, methanol, ethanol, NaOH and HCl were procured from Merck, India. N-hydroxy-succinamide (NHS) and ethyl-(*N'*,*N'*-dimethylaminopropyl) carbodimide hydrochloride were purchased from Spectrochem, India. All the chemicals were used as such without any further purification. Milipore water was utilized throughout the experiment.

Synthesis of mesoporous silica nanoparticle (m-SiO_2)

Mesoporous silica nanoparticles were synthesized by following the general procedure. In a typical procedure, 500 mg of CTAB was dissolved in 250 mL milipore water, followed by the addition of NaOH aqueous solution (1.75 mL, 2M). The mixture was heated up to 80 °C under vigorous stirring. When the temperature was stabilized, 2.5 mL of TEOS was slowly added into the mixture solution and allowed to stir at 80 °C for another 2 h. Then nanoparticles were collected by centrifugation at 10000 rpm for 10 minutes and the product was washed with methanol and water thoroughly. To remove the surfactant (CTAB) the nanoparticles were suspended in 50 mL methanol containing 3 mL of concentrated HCl and subjected to reflux for 12 h. The product m-SiO_2 was collected by centrifugation at 1000 rpm for 15 minutes and repeatedly washed by methanol and water. The collected nanoparticles were vacuum dried.

Synthesis of luminescent carbon dot deposited mesoporous silica nanoparticle (m-SiO_2-CD)

Luminescent carbon dot integrated mesoporous silica nanoparticle was prepared by hydrothermal carbonization of orange juice in the template free channels of the mesoporous silica. Typically, dispersed m-SiO_2 nanoparticles (300 mg in 30 mL ethanol) were mixed with 20 mL of absolutely pulp free orange juice and then the mixture was transferred into an 80 mL Teflon-lined stainless-steel autoclave which was heated at constant temperature of 130 °C for 150 min (1 °C/min). After the reaction, the autoclave was cooled down naturally and the resulted luminescent nanocomposite (m-SiO_2-CD) was separated through centrifugation. The product was first washed thoroughly with dichloromethane followed by water to remove the unreacted organic moiety and water soluble adsorbed luminescent CDs respectively.

Detection procedure

For the sensing of sugar, to a 5 mL volumetric flask was sequentially added 1 mL of m-SiO_2-CD dispersion (1 mg/mL), 1 mL of 100 mM solution of 3-aminophenylboronic acid, different amount of glucose solution, and then diluted with milipore water to a final volume of 5 mL. After the solution was shaken for 2 minutes, the PL spectra of the resulting solution were recorded at the excitation wavelengths of 360 nm.

Synthesis of 3-aminophenylboronic acid conjugated m-SiO_2-CD

For targeted imaging experiment APBA modified m-SiO_2-CD nanoparticles were synthesized separately. In a typical procedure 5 mL of aqueous solution containing NHS (41 mg, 0.358 mmol) and EDC (18 mg, 0.0938 mmol) was taken in a 50 mL of round bottom flask and was kept in the dark for 2 h. After that the aqueous solution of APBA (74 mg in 12 mL water) was added to the above solution followed by addition of m-SiO_2-CD (100 mg) nanoparticles. The resulting suspension was stirred at room temperature for overnight and the particles (m-SiO_2-CD-APBA) were isolated through centrifugation. The particles were washed repeatedly with millipore water.

In vitro cytotoxicity and fluorescence imaging

In vitro cytotoxicity: Human colon adenocarcinoma cell line HT29 cells (3×10^3 cells) were seeded into 96-well plates and incubated in 200 μL DMEM containing 10% FBS for 24 h (37 °C, 5% CO_2). Then the cells were treated with different concentration of m-SiO_2-CD-APBA (12.5, 25, 50, 100, 200, 300, 400, 500 μg/mL) in fresh DMEM without serum and incubated for another 24 h. Viable cell concentration was checked by MTT (3-(4,5-Dimethyl-2-2thiazolyl)-2,5-diphenyl-2H-tetrazolium bromide) assay. The assay experiment was performed in triplicate.

Fluorescence Imaging: HT29 cells were seeded into 24 well plates and incubated in DMEM supplemented with 10% FBS and 1% antibiotic (penicillin, streptomycin) at 37 °C inside humidified 5% CO_2 incubator. After 24 h of incubation, media were replaced with fresh DMEM containing m-SiO_2-CD and m-SiO_2-CD-APBA separately at concentration 200 μg/mL and incubated for 4 h. Prior to fixation of the cells on the slide for imaging experiment the cells were washed three times with PBS. The cells were fixed with 2% Paraformaldehyde for 10 min at -20 °C and again washed with PBS. Live-cell imaging was carried out under confocal microscope (Olympus, Japan) with excitation at 488 nm.

4.3. Characterization

The synthesized materials were well characterized by using standard techniques as described in chapter-2. Additionally the specific surface areas and total pore volume were calculated by the Brunauer–Emmett–Teller (BET) and BJH methods respectively.

4.4. Results and Discussion

For selective detection of saccharide and glycan, the luminescent properties of m-SiO_2-CD in response to 3-aminophenylphenylboronic acid have been utilized. Addition

of boronic acid resulted in quenching of the fluorescence signals arising from m-SiO_2-CD, the fluorescence recovery was achieved by the addition of glucose.

Characterization of the carbon dot deposited mesoporous silica nanoparticle

Structural analysis

Structural characterization of the m-SiO_2-CD hybrids was carried out by means of XRD and Raman spectroscopy. In wide angle XRD pattern of m-SiO_2 (Figure 4.1a), a broad stronger diffraction peak centered at 2θ of 21.5º was observed, which can be assigned to amorphous silica (JCPDS No. 29-0085). XRD pattern of m-SiO_2-CD (Figure 4.1a) also exhibited a stronger diffraction peak in the wide 2θ region, suggesting the high structural stability after hydrothermal treatment. The peak corresponding to (002) plane of deposited CD overlaps with the silica region. However the peak is slightly shifted to higher angle at 2θ = 22.4º (lesser d value), which suggested the introduction of partial crystalline nature resulting from deposition of partially crystalline CDs in the mesopores of the m-SiO_2. Furthermore, hydrothermal decomposition of orange juice on m-SiO_2 also introduced a weak peak at 2θ=44.5° corresponding to (101) diffraction patterns of graphitic carbon suggesting successful deposition of CD. Low-angle XRD pattern of m-SiO_2-CD (Figure 4.1b) showed three characteristic diffraction peaks between 1 to 4.0° which could be indexed to (100), (110), and (200) diffractions associated with typical two-dimensional hexagonal symmetry (P6mm). The appearance of these peaks indicated that the long range hexagonal symmetry of m-SiO_2 was preserved even after the hydrothermal carbonization of orange juice.

The Raman spectra of the m-SiO_2-CD (Figure 4.1c) showed intense bands at about 1358 cm^{-1} and 1597 cm^{-1} corresponding to the characteristic D and G peaks of graphitic materials respectively. The G band arises due to the vibration of sp^2-bonded carbon atoms in a two-dimensional (2D) hexagonal lattice, whereas the D band is associated with the vibrations of carbon atoms with dangling bonds in the termination plane of disordered graphite or glassy carbon. The intensity ratio (I_D/I_G), which signifies the extent of disorderliness as well as the ratio of sp^3/sp^2 carbons was found to be 0.94 indicating partial crystalline nature with large disordered amorphous carbon in the hybrid

sample. This I_D/I_G ratio was slightly higher than the bare CD synthesized from orange juice reported in chapter-2. The relatively high value may be due to small size growth of CD in mesopores of mesoporous silica and the presence of abundant oxygen containing groups on the surface.

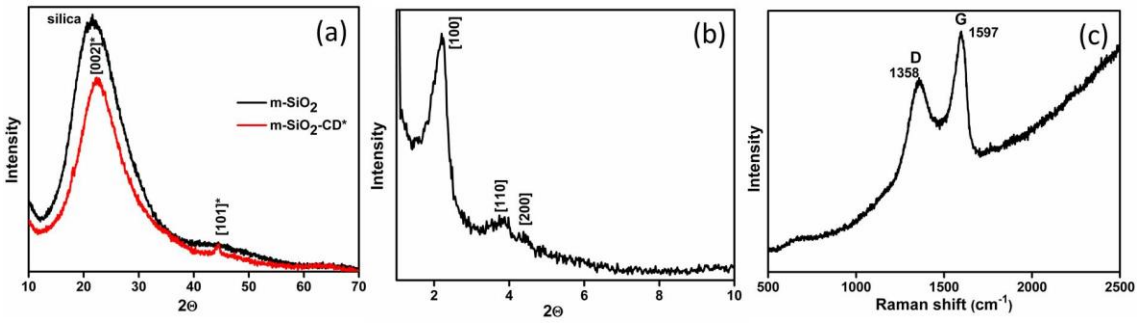

Figure 4.1 (a) Wide-angle X-ray diffraction pattern of m-SiO_2 and m-SiO_2-CD, (b) low-angle XRD, and (c) Raman spectrum of m-SiO_2-CD.

Microstructure and stability

The SEM image of m-SiO_2 (Figure 4.2a) indicates that prepared nanoparticles consist of monodisperse sphere with a mean particle size of 110 nm. These particles are non-aggregated with narrow size distribution. The morphological features such as the spherical shape, non-aggregation and narrow size distribution are observed to be retained in case of m-SiO_2-CD (Figure 4.2b). These results indicate that deposition of the CD in the mesopore of silica through hydrothermal treatment does not alter the structure and morphology. TEM was employed to further investigate the detailed structure and morphology of m-SiO_2-CD. The low-magnification TEM image (Figure 4.2c) shows that m-SiO_2-CD silica consists of spherical particles with a diameter of 110-130 nm. The corresponding high-magnification TEM image (Figure 4.2d,e) clearly shows the typical ordered mesostructure arrays consist of hexagonal porous channels with tunable pore diameters ranging from 3 to 4 nm. This uniform ordered mesoporous pore would facilitate the size controlled growth of CD which tunes its optical properties. Appearance of well-ordered mesostructure indicates that hydrothermal treatment has little influence on the structure of the CD deposited mesoporous silica. Numerous dark spots are noticed in the porous network of mesoporous silica, (Figure 4.2f) which confirms the successful deposition of CD in the mesopores of silica.

The hydrodynamic (HD) size of m-SiO_2 and m-SiO_2-CD (Figure 4.2g) demonstrates the formation of stable non-aggregated particles. The CD deposited particles showed a mean HD size of 112 nm, which is slightly smaller than m-SiO_2 (123 nm). The observed decrease in HD size in case of CD deposited sample may be due to the introduction of -COOH group in the particle surface associated with CD. These functionalized particles show a more stable dispersible colloidal suspension resulting from repulsion of carboxylic group. Measurement of zeta potential against pH (Figure 4.2h) shows that at low pH zeta potential is 30.4 mV which shifts to -33.2 mV at higher pH which specifies the presence of –COOH groups on the surface.

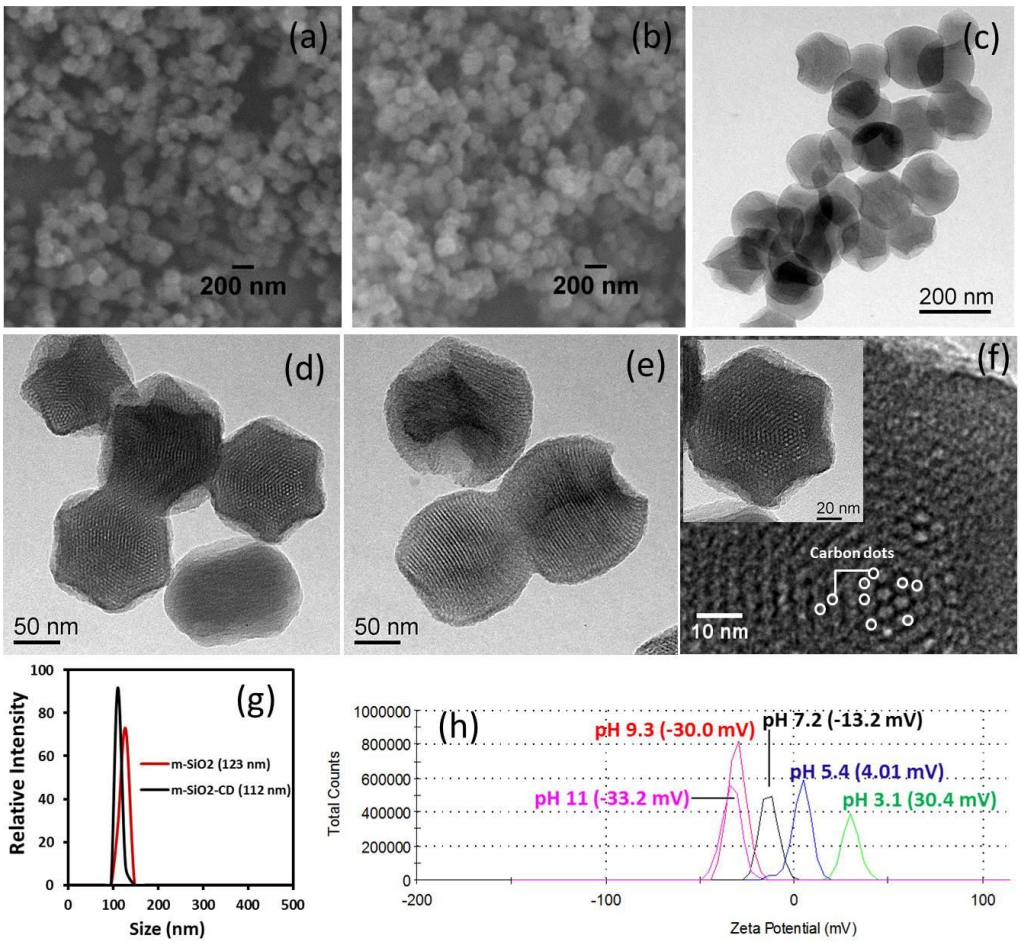

Figure 4.2 SEM images of (a) m-SiO_2 and (b) m-SiO_2-CD, (c) TEM image of m-SiO_2-CD, TEM images at higher magnification (d, e) at different tilting angles, (f) higher magnified TEM image representing deposition of CDs in the mesopores, inset is the TEM image of single m-SiO_2-CD showing hexagonal ordered mesopores, (g) Hydrodynamic size of m-SiO_2 and m-SiO_2-CD measured from DLS, (h) Zeta potentials of m-SiO_2-CD.

BET surface area

The synthesized samples exhibit high surface area, large pore volume, and narrow pore size distribution. The nitrogen adsorption-desorption isotherm (Figure 4.3a) of both m-SiO_2 and m-SiO_2-CD samples show the typical type IV isotherms with a hysteresis, which is a characteristic of mesoporous material. However, in case of m-SiO_2, the desorption curve of the isotherm is close to the closure point; around 0.06 P/P^0 which is extremely low than m-SiO_2-CD at 0.5 P/P^0. These results indicate the disordered pore structure in synthesized m-SiO_2 which is also evident from the pore size distribution curve. This discrepancy can be explained on the basis of synthetic process. It seems that during the synthesis of m-SiO_2 at 80 °C the loose crosslinking between the micelles takes place forming spherical structure, whereas hydrothermal treatment is responsible for the further ordering and ripening of the porous system. The hydrothermal treatment during the CD deposition in mesoporous silica induces the tightening of silica cross-linkage resulting ordered structure. Therefore the first step of m-SiO_2 formation is the setting phase where the forces controlling particle morphology can take precedence while the second hydrothermal treatment in m-SiO_2-CD is responsible for hardening and ordering of the structure. The BET surface area of the m-SiO_2 was found to be 1342 m^2g^{-1} which was slightly decreased to 834 m^2g^{-1} after deposition of CD. The pore diameter of m-SiO_2-CD (Figure 4.3b) as determined from BJH method was found to be 5 nm which is in close proximity to that determined from TEM.

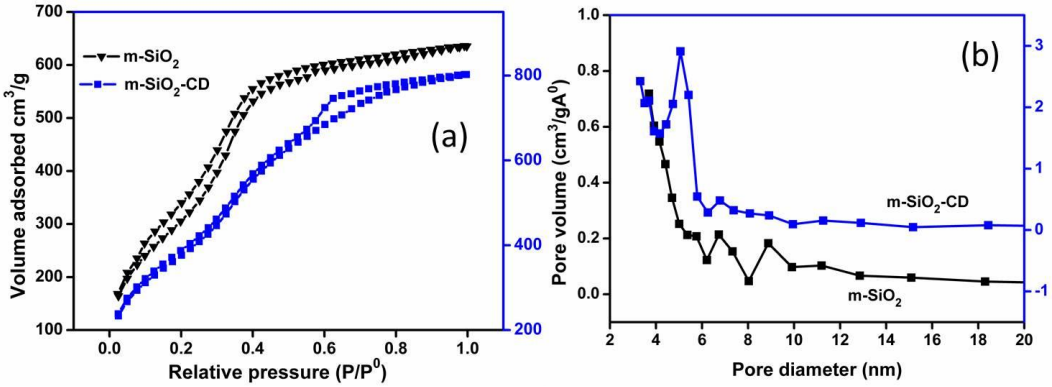

Figure 4.3 (a) Nitrogen adsorption-desorption isotherm and (b) pore-size distribution of m-SiO_2 and m-SiO_2-CD

Photoluminescence

The solution of m-SiO_2-CD shows two UV/Vis absorption bands at 228 and 288 nm (Figure 4.4a). The origin of these peaks is related to π electron transition in oxygen-containing CD. The absorption is typically ascribed to π→π* transition of aromatic cluster (288 nm) and n→π* transition of the C=O bond of oxygen containing functional groups. These particles exhibit strong emission in blue region under excitation at 380 nm (Figure 4.4a). Similar to CD synthesized in chapter-2, these hybrid particles show excitation-dependent emission (Figure 4.4b). By following the similar procedure described in chapter-2 (quinine sulfate as the standard and 340 nm as the excitation wavelength), the photoluminescent quantum yield of m-SiO_2-CD was calculated to be 14.9% (Figure 4.c).

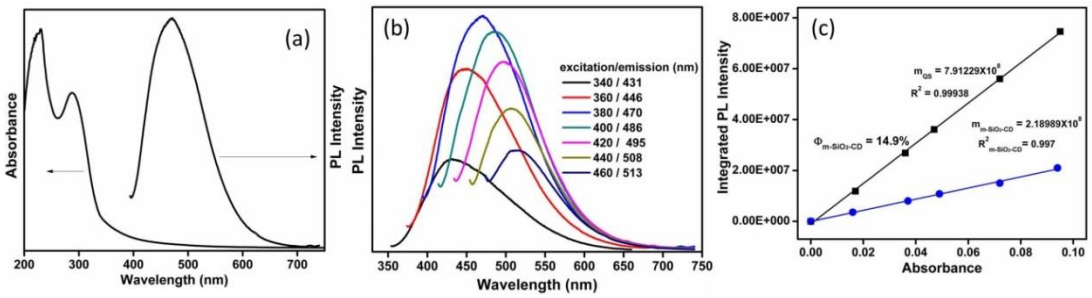

Figure 4.4 (a) UV absorption and PL emission spectra (λ_{ex}=380 nm), (b) excitation wavelength-dependent emission of m-SiO_2-CD, (c) PL and Absorbance of the m-SiO_2-CD and quinine sulfate

Surface properties

Figure 4.5a shows FTIR spectra of m-SiO_2, m-SiO_2-CD and m-SiO_2-CD-APBA. The appearance of typical bands due to OH (3455 cm^{-1}), H_2O (1635 cm^{-1}), Si-O-Si (1200-1000cm^{-1}), Si-OH (955 cm^{-1}) and Si-O (469 cm^{-1}) of silica confirms the successful synthesis of m-SiO_2. These results show that there is a large amount of OH groups and H_2O on the surface of m-SiO_2 which imparts excellent water dispersibility to the silica nanoparticle. After deposition of the CD, the peak at 1635 cm^{-1} gets broader and a small hump appears at 1704 cm^{-1} indicating the introduction of aromatic C=C cluster and -COOH functional group. Furthermore intensification of the 1200-1000 cm^{-1} region due to C–O–C/C-O vibrational stretching and appearance of new peaks at 2924, 2850 cm^{-1} for

C-H stretching indicates the successful deposition of CD. The appearance of these functional groups indicates that deposited CD has highly oxidized surface with hydroxyl, epoxy, carbonyl and carboxylic acid functional groups. These functional groups impart excellent solubility in water without further chemical modification. The successful conjugation of APBA on the surface of m-SiO_2-CD through amide linkage is evidenced by the appearance of characteristic peaks at 3638, 3272, 1650 cm^{-1} corresponding to N-H, C=O stretching of amide linkage.

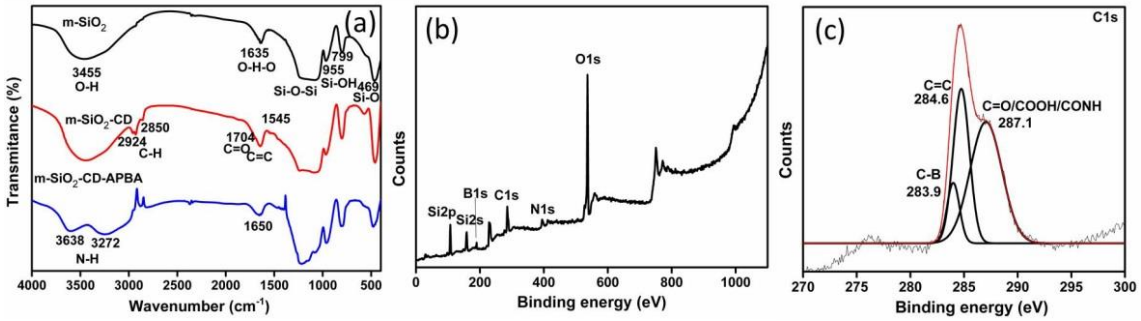

Figure 4.5 (a) FTIR spectra of m-SiO_2, m-SiO_2-CD and m-SiO_2-CD-APBA, (b) survey spectrum and (c) high resolution scan corresponding to C1s of m-SiO_2-CD-APBA.

In a typical survey spectrum of m-SiO_2-CD-APBA (Figure 4.5b), the peaks at binding energies 104, 156, 189, 280-290, 402 and 528-540 eV are ascribed to Si2p, Si2s, B1s, C1s, N1s and O1s electrons. High resolution scan for C1s (Figure 4.5c) can be well fitted into three peaks centered at 283.9, 284.6 and 287.1 eV. The lower binding energy at 283.9 corresponds to the C-B bond and peak at 284.6 eV accounts for reference and the aromatic carbons present in CD and APBA. The fitted peak at higher binding energy site 287.1 eV corresponds to the carbon present in C=O/-COOH/-CONH environment. The peaks at binding energies 189 and 402 eV matching to B1s and N1s regions respectively confirms the successful conjugation of APBA on m-SiO_2-CD, which was used for targeted cell imaging.

Fluorescence sensing of sugar

We explored the photoluminescence behavior of m-SiO_2-CD in association with APBA for designing highly sensitive OFF-ON fluorescent glucose sensor in aqueous solution. The bright luminescence of m-SiO_2-CD gets quenched on treatment with 3-aminophenyl boronic acid (APBA). The boronic acid absorbs on the m-SiO_2-CD through

π-π stacking interactions between the aromatic cluster of CD and pendent aromatic moiety of APBA, causing a fluorescence quenching. It is suggested that the π-π stacking interaction facilitates the non-radiative excited state electron transfer from CD to the boronic acids, leading to a decrease in PL intensity of the m-SiO_2-CD. As our expectation subsequent addition of glucose to the APBA adsorbed m-SiO_2-CD solution caused gradual fluorescence recovery (Figure 4.6a) and about 85% fluorescence recovery was achieved with 8 mM of glucose. As the glucose concentration increases, the absorbed APBA gets converted to tetrahedral glucoboronate esters resulting enhancement of PL intensity. Figure 4.6b shows the relative intensity of recovered PL signals (F/F_0) plotted against the concentration of glucose. In the range of 0 mM to 0.6 mM, the recovered PL intensity shows a good linear response with glucose concentration having linearly dependent coefficient of 0.998. These results suggest that the quenched PL of APBA adsorbed m-SiO_2-CD solution can be recovered in response to glucose demonstrating a low cost sensing platform for glucose. The influence of pH on fluorescence recovery was also investigated. As shown in Figure 4.6c, the fluorescence recovery efficiencies of glucose are low in the pH range of 4-6. As pH reaches to 8, the fluorescence recovery enhanced appreciable, this is the maximum in the pH range of 4-10. The observed pH effect is obvious as a basic condition is favorable for the interaction of boronic acid and glucose to form glucoboronate ester through the release of proton.

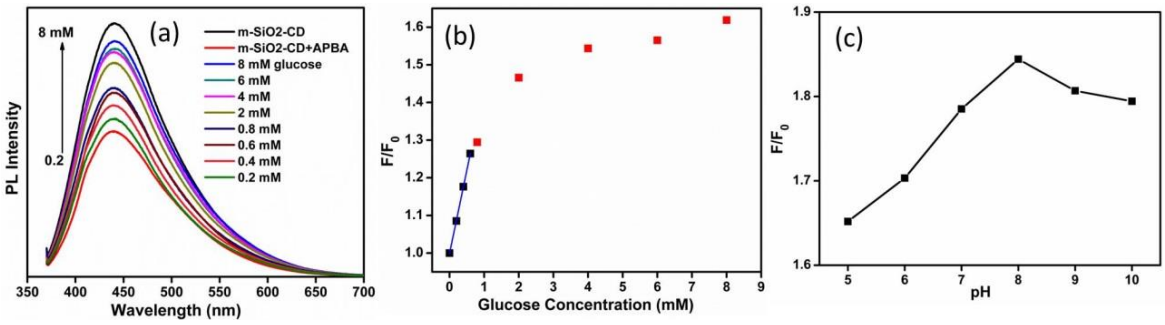

Figure 4.6 (a) Effect of different concentrations of glucose on the PL recovery of APBA adsorbed m-SiO_2-CD, (b) Plot of the relative PL intensity (F/F_0) vs glucose concentration, (c) Effects of pH on the detection of glucose. F_0 and F are PL intensities of the APBA adsorbed m-SiO_2-CD in the absence and presence of glucose respectively.

Proposed working principle for fluorescence sensing

Figure 4.7 depicts the proposed fluorescence sensing principle for the developed system. The boronic acid absorbs on the surface of m-SiO_2-CD through π-π stacking interactions with the aromatic cluster of CD in m-SiO_2-CD. We anticipate that π-π interaction facilitates the non-radiative photoinduced excited state electron transfer from m-SiO_2-CD to APBA, as reported by Strano in case of single walled carbon nanotube.[20] This non radiative electron transfer process resulted in diminution of PL intensity of m-SiO_2-CD with the addition APBA. The fluorescence energy transfer from m-SiO_2-CD to APBA can be ruled out as the absorption of APBA does not overlap with the emission spectrum of m-SiO_2-CD. The quenched fluorescence is gradually recovered on subsequent addition of glucose which can disrupt the non-radiative electron transfer process by lifting out the APBA from CD surface. APBA effectively bind with glucose forming tetrahedral glucoboronate ester, which effectively remove the quencher from the immediate vicinity of the m-SiO_2-CD fluorophore.

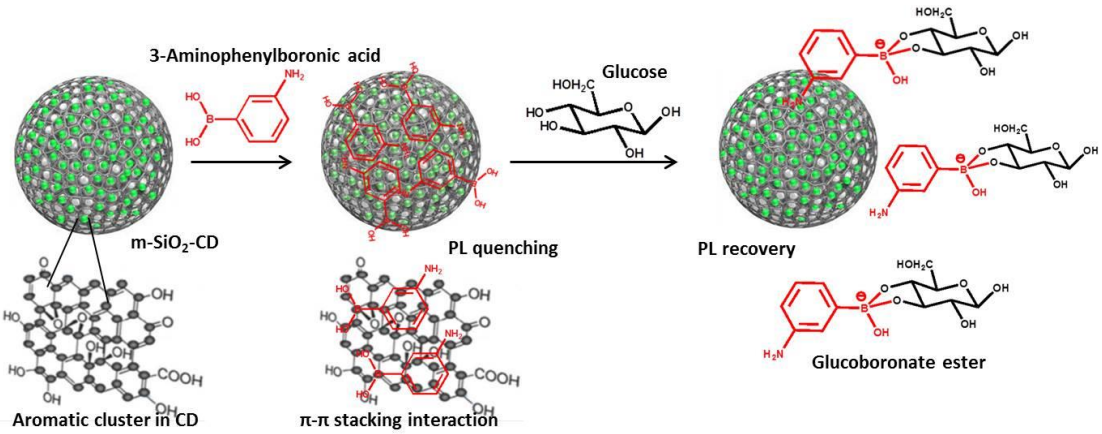

Figure 4.7 Schematic illustration of proposed working principle in glucose sensing.

Cellular uptake and targeted fluorescence imaging

The inherent cytotoxicity of synthesized m-SiO_2-CD-APBA was evaluated using human colon adenocarcinoma cell HT29 through MTT assay (Figure 4.8a). The m-SiO_2-CD-APBA do not impose any significant toxicity to cells and are tolerable even at high

dose (500 µg/mL) and long incubation time (24 h), hence it is safe for in vitro and in vivo applications.

As demonstrated above, the advantages of high binding affinity of APBA for cis-diol, together with remarkable stability, good biocompatibility of m-SiO_2-CD-APBA nanoparticles substantially provide a reliable platform for sLe^a receptor-mediated targeted imaging of cancer cell. Herein, to demonstrate its competence in targeting colon cancer cell, m-SiO_2-CD and m-SiO_2-CD-APBA samples were incubated with HT29 cell line for 4 h. Strong green fluorescence images (Figure 4.8c) were observed from m-SiO_2-CD-APBA treated cells upon 488 nm excitation. The perinuclear region localized visible green luminescence signal comes from carbon dots as already demonstrated in chapter-2. This suggests that m-SiO_2-CD-APBA nanoparticles are selectively targeted to the cells through the sLe^a receptor-mediated endocytosis and localize into the cytoplasm leaving clear zones of nuclei. As expected the m-SiO_2-CD treated cell lines shows negligible uptake of the particles indicated by very weak fluorescence signal (Figure 4.8e). The m-SiO_2-CD sample has devoid of marker (APBA) to induce sLe^a receptor mediated uptake. The observed low fluorescence is due to uptake of the particles through simple diffusion. These results suggested that the m-SiO_2-CD-APBA could allow efficient binding of sLe^a on the cell surface.

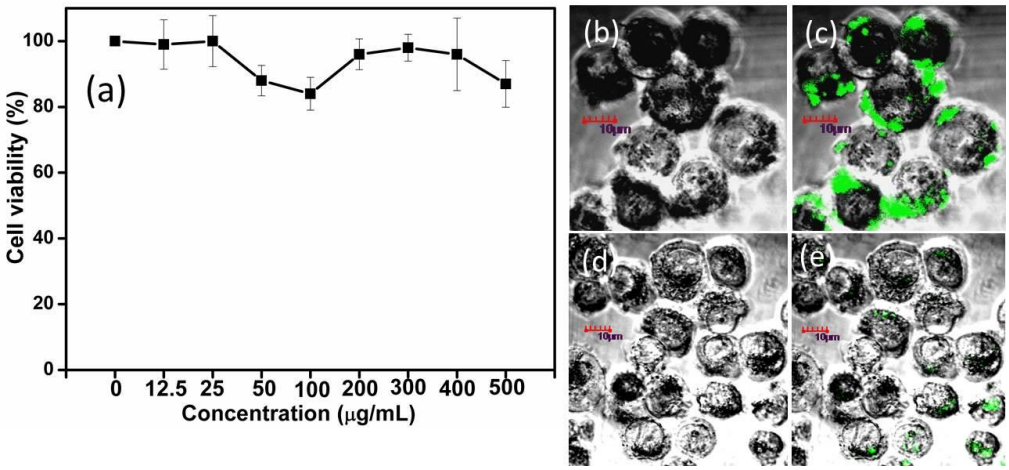

Figure 4.8 (a) In vitro cell viability of HT29 cells with m-SiO_2-CD-APBA, The fluorescence image of HT29 cells incubated with m-SiO_2-CD-APBA under (b) bright-field, (c) by excitation at 488 nm, and with m-SiO_2-CD under (d) bright field, (e) by excitation at 488nm.

4.5. Conclusion

- In summary, an easily separable sensitive CD based fluorescence glucose sensor comprising of m-SiO_2-CD and 3-aminophenylboronic acid has been reported.
- The working principle involves fluorescence recovery of quenched APBA adsorbed m-SiO_2-CD on addition of glucose due to the formation of glucoboronate ester which could lift out the APBA from close vicinity of fluorophore.
- The fluorescence modulation with glucose concentration in a physiological range and separation of fluorophore are two important aspects of the developed system.
- APBA conjugated m-SiO_2-CD nanoparticle have been sucessfully synthesized and applied for targeted imaging of human colon adenocarcinoma cell HT29 overexpressed with sialyl Lewis A (sLe^a) receptors.
- The sensitivity of the method provides a new approach for optical sensing and targeting.

4.6. References

1. A. P. Davis, R. S. Wareham, *Angew. Chem. Int. Ed.*, 1999, **38**, 2978-2996.
2. S. Hurtley, R. Service, P. Szuromi, *Science*, 2001, **291**, 2337.
3. A. F. B. Kernohan, C. G. Perry, M. Small, *Clin. Chem. Lab. Med*., 2003, **41**, 1239-1245.
4. C. Radhakumary, K. Sreenivasan, *Anal. Chem*., 2011, **83**, 2829-2833.
5. A. Heller, B. Feldman, *Chem. Rev.*, 2008, **108**, 2482-2505.
6. H. Y. Lee, J. J. Lee, J. Park, S. B. Park, *Chem. Eur. J*., 2011, **17**, 143-150.
7. M. S. Steiner, A. Duerkop, O. S. Wolfbesis, *Chem. Soc. Rev*., 2011, **40**, 4805-4839.
8. D. Odaci, B. N. Gacal, B. Gacal, S. Timur, Y. Yagci, *Biomacromolecules*, 2009, **10**, 2928-2934.
9. X. Wu, Z. Li, X. X. Chen, J. S. Fossey, T. D. James, Y. B. Jiang, *Chem. Soc. Rev*., 2013, **42**, 8032-8048.

10. S. N. Baker, G. A. Baker, *Angew. Chem. Int. Ed*., 2010, **49**, 6726-6744.
11. H. Li, Z. Kang, Y. Liu, S.-T. Lee, *J. Mater. Chem*., 2012, **22**, 24230-24253.
12. J. Shen, Y. Zhu, X. Yang, C. Li, *Chem. Commun*., 2012, **48**, 3686-3699.
13. A. Zheng, Z. Cong, J. Wang, J. Li, H. Yang, G. Chen, *Biosens. Bioelectron*., 2013, **49**, 519-524.
14. S. Liu, J. Q. Tian, L. Wang, Y. L. Luo, S. P. Sun, *RSC Adv*., 2012, **2**, 411-413.
15. Y. H. Li, L. Zhang, J. Huang, R. P. Liang, J. D. Qiu, *Chem. Commun*., 2013, **49**, 5180-5182.
16. Z. B. Qu, X. G. Zhou, L. Gu, R. M. Lan, D. D. Sun, D. J. Yu, G. Y. Shi, *Chem. Commun.*, 2013, **49**, 9830-9832.
17. P. Shen, Y. Xia, *Anal. Chem*., 2014, **86**, 5323-5329.
18. J. E. Lee, N. Lee, T. Kim, J. Kim, T. Hyeon, *Acc. Chem. Res*., 2011, **44**, 893-902.
19. C. Argyo, V. Weiss, C. Brauchle, T. Bein, *Chem. Mater*., 2014, **26**, 435-451.
20. K. Yum, J.-H. Ahn, T. P. McNicholas, P. W. Barone, B. Mu, J. H. Kim, R. M. Jain, M. S. Strano, *ACS Nano*, 2012, **6**, 819-830.

Chapter-5

High quantum yield N,S co-doped carbon dots as fluorescent probe for selective and sensitive detection of Hg^{2+} in water and living cells

5.1. Introduction

Luminescent carbon dots (CDs) as alternatives to common toxic metal-based quantum dots have drawn great attention for bioimaging,[1] biosensing,[2] catalysis[3] and drug delivery[4] applications because of their fascinating physical properties.[5] Much progress has been achieved for the preparation of fluorescent CDs by electrochemical oxidation,[6] chemical oxidation methods,[7] hydrothermal cutting process,[8] and carbonization of a wide variety of carbon precursor starting from small molecule to natural precursor.[9-12] There are still some drawbacks for CDs obtained at present, for example relatively low fluorescence quantum yield (usually less than 50%) compared to conventional inorganic quantum dots. Although surface passivation is an effective approach to improve the fluorescence of CDs, recent research work indicated that hetero element doping has greater advantage in increasing CD fluorescence quantum yields. Doping carbon nanomaterials with heteroatoms can effectively change their electron density and tune their optical and electrical properties.[13,14] The N atom, having a comparable atomic size and five valence electrons for bonding with carbon atoms, has been widely used for chemical modification of carbon nanomaterials.[15] In last few years tremendous work has been done for the development of one-step bottom-up approach to synthesize N-doped CD (NCD) and it has been revealed that NCD exhibit emission intensity dependent on the nitrogen content.[16-18] The enhanced fluorescence quantum yield and life time of NCD are owing to the introduction of new kind of surface states which trap electron and thus able to facilitate a high yield of radiative recombination. More importantly, if CDs are co-doped with N and S the effect of N is more enhanced through a cooperative effect as compared to NCD.[19] As a result, in last couple of years conscious effort has been made to develop simple synthetic methods to produce of N,S co-doped carbon dots (NSCDs). Dong *et al.* prepared NSCD through one-step hydrothermal treatment of L-cysteine and citric acid, which provide deep insights to their photoluminescence (PL) enhancement mechanism.[20] These prepared NSCD showed excitation independent emission different from the mostly reported un-doped and doped CD. Subsequent efforts involve carbonization of hair fiber in presence of sulphuric acid,[21] hydrothermal treatment of α-lipoic acid and ethylenediamine,[22] microwave assisted pyrolysis of rice and N-acetyl-L-cysteine,[23] and hydrothermal treatment of citric acid and thiourea.[24] These advances

provided a viable route to extend their applications in photocatalysis, bioimaging, biosensor. Very recently Feng and co-worker developed a solvent free method to prepare N,S co-doped CD from glutathione for mercury sensing.[25] Although these developed methods are quite promising, in most of these processes a mixture of chemicals as precursors and harsh reaction conditions complicate the synthesis methods. So there remains ample opportunity in developing a simple synthetic method N, S co-doped CD (NSCD) for sensing and bioimaging applications.

Mercury is a highly toxic and bioaccumulative heavy metal ion that causes serious health problems even at very low concentration.[26,27] Continuous exposure to mercury may cause severe damage to the central nervous system, kidney failure and various cognitive and motion disorders.[28] The maximum allowable Hg^{2+} level in drinking water as established by the Environmental Protection Agency (USA) is 2 ppb (10 nM). Various luminescent,[29,30] chemical,[31] electrochemical,[32] and bio-sensor-based[33] analytical methods have been developed for detecting mercury. Among these methods, fluorescence sensing is one of the reliable methods due to its high sensitivity, fast analysis, non-destructing and simple operation method which translates molecular recognition information into tangible fluorescence signals.[34] Although fluorescent sensors for Hg(II) detection such as organic molecule, metal nanoclusters, semiconductor quantum dots (QDs) have been reported, many of these are associated with certain limitations like poor aqueous solubility, cross-sensitivity towards other metal ions, short emission wavelengths, and/or weak fluorescence intensities.[35-37] Therefore the prime challenges in creating Hg^{2+} sensor are (1) high sensitivity and selectivity in detection, (2) selectivity against background of competing analytes, (3) consist of stable rceptors that associate with analytes selectively, (4) retain high aqueous solubility, and (5) cost-effectiveness of the sensor.

Newly the improved luminescence properties of NCD has been exploited for detection of Ag(I),[38] Fe(III),[39] Iodide,[40] mercury,[41-43] cupper[44] etc. have been developed. Although N-doped CD based Hg^{2+} sensor is found to be superior to undoped CD in terms of high fluorescence quantum yield, most of them suffer from high detection limit. Thus development of CD based fluorescent probe for highly sensitive and selective detection

of mercury is desirable. On the other hand, optical imaging with fluorescent metal ion probes is currently attracting much attention as a method to reveal the molecular functions of the metal ions and detection of level of metals in living cells. However, less attention is paid to explore the optical properties of carbon dot towards intracellular metal ion detection. Effective fluorescent probes for imaging metal ions in living cellular systems must meet several strict requirements. Most importantly, a sensor should be selective for a specific metal ion over other biologically abundant cations, including those that exist at much higher cellular concentrations. Principles like hard-soft acid-base interactions are crucial for designing and obtaining metal-selective responses. Thus efficient fluorescent sensors for Hg^{2+} may be designed based on the presence of soft donor such as sulphur on flurophore for effective binding of the metal. In this regard, nitrogen and sulphur co-doped carbon dot (NSCD) can serve as an efficient fluorophore towards selective mercury detection due to soft-soft interaction between NSCD and Hg^{2+}.

In this chapter, we have described a one-step synthesis of N,S co-doped carbon dots (NSCDs) with high PL quantum yield 69%. The synthesized NSCDs have been well characterized through standard technique such as XRD, Raman, TEM, Fluorescence spectrophotometry etc. These prepared NSCDs were employed for the selective and sensitive detection of Hg^{2+} in water and living cells. This sensor contains thiol and thioacid moiety in the metal binding site, which is expected to preferably bind to soft metal ion Hg^{2+} over other metal ions showing high selectivity.

5.2. Experimental

Reagents and Chemicals

3-Mercaptopropionic acid, ethylenediamine, diethylenetriamine and triethylenetetramine were purchased from Sigma Aldrich, USA. $FeCl_2$, $CuCl_2.2H_2O$, $HgCl_2$, $CaCl_2.2H_2O$, $CoCl_2.6H_2O$, $NiCl_2.6H_2O$, $MnCl_2.4H_2O$, $ZnCl_2$, $Pb(OAc)_2$ and $SnCl_2$ were purchased from Merck, India. Oxalyl chloride and DMF were obtained from Spectrochem, India. Dichloromethane and DMF were purified by distillation over

phosphorous pentoxide and anhydrous CaH_2 respectively. All other chemicals were used as received without further purification.

Synthesis of N,S Containing Carbon Precursor

The synthesis of N, S containing carbon precursors has been presented in scheme 5.1. A solution of 3-mercaptopropionic acid (0.87 mL, 10 mmol) in dichloromethane (5 mL) was cooled to 0 °C under nitrogen. Oxalyl chloride (2 mL, 20 mmol) was added followed by the addition of catalytic amount of DMF. The mixture was allowed to react for 4 h at room temperature. The solvent and unreacted oxalyl chloride was completely removed under vacuum. Then to it ethylenediamine (0.33 mL, 5 mmol) in dichloromethane was added and allowed to react for another 6 h under nitrogen atmosphere. The solid product was recovered through filtration and repeatedly washed with petroleum ether to remove the DMF. Other carbon precursors C-2 and C-3 with increased N atom were synthesized in similar process by reacting diethylenetriamine (0.53 mL, 5mmol) and triethylenetetramine (0.75 mL, 5mmol) respectively instead of ethylenediamine. The compounds are named as C-1, C-2 and C-3.

C-1: Elemental Analysis: (C 40.2, H 6.92, N 11.9, O 13.51, S 27.13), IR (KBr): 3369, 2973, 2926, 2893, 2742, 2540, 2410, 2139, 1923, 1656, 1451, 1415, 1380, 1328, 1274, 1088, 1048 cm^{-1}.^{1}H NMR (400 MHz, D_2O): δ 1.5 (bs, 2H), 2.42 (t, 4H), 2.94 (m, 4H,), 3.09 (m, 4H), 8.13 (bs, 2H). MS (ESI): m/z (relative intensity) 275 ([M+K], 90).

C-2: Elemental Analysis: (C 42.81, H 7.62, N 14.91, O 11.53, S 23.23) IR (KBr) 3379, 3018, 2966, 2914, 2847, 2706, 2572, 2450,1727, 1662, 1427, 1368, 1333, 1226, 1215, 1110 cm^{-1}.^{1}H NMR (400 MHz, D_2O): δ 1.5 (bs, 2H,), 2.02 (bs, 1H), 2.3 (t, 4H), 2.92 (m, 8H,), 3.08 (m, 4H), 8.05 (bs, 2H). MS (ESI): m/z (relative intensity) 314 ([M+N_2H_7], 100).

C-3: Elemental Analysis: (C 44.52, H 8.34, N 17.4, O 9.81, S 19.8) IR (KBr) 3414, 3018, 2967, 2918, 2840, 2557, 1740, 1640, 1440, 1366, 1323, 1228, 1048 cm^{-1}. ^{1}H NMR (400 MHz, D_2O): δ 1.5 (bs, 2H,), 2.0 (bs, 2H), 2.34-2.7 (m, 12H), 2.8-3.32 (m, 8H), 8.0 (bs, 2H). MS (ESI): m/z (relative intensity) 321 ([M-H], 84).

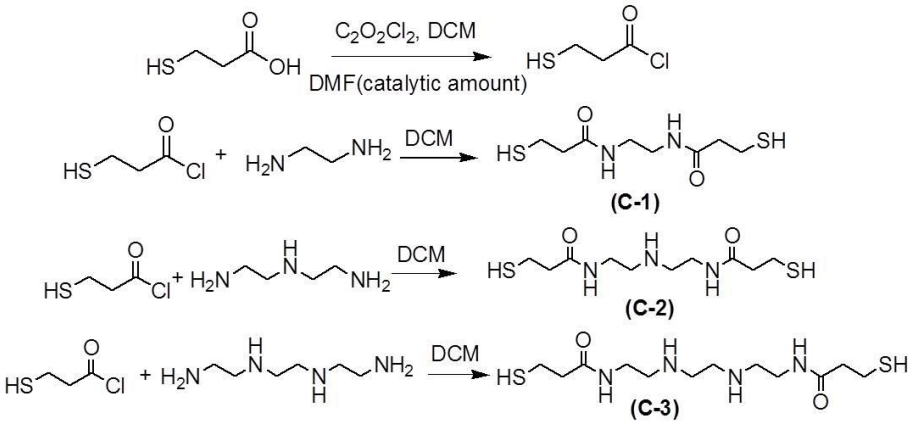

Scheme 5.1 Synthesis of N, S containing precursors.

Synthesis of Fluorescent NSCD

The N,S co-doped carbon dot (NSCD-1, NSCD-2 and NSCD-3) with different amount of nitrogen content were prepared by hydrothermal treatment of single molecular precursor C-1, C-2 and C-3 respectively. In a typical experiment, N,S containing carbon precursor (2 mmol) was dissolved into 50 mL milipore water with few drops of ammonia solution (28%) and stirred to form a clear solution. The solution was then transferred into 80 mL Teflon-lined stainless-steal autoclave and was heated at constant temperature of 160 °C for 10 h with a heating rate of 1ºC/min. When cooled down to room temperature, an orange solution was obtained, which implied the formation of the CDs. Then, the obtained dispersion were filtered with a 0.22 µm filter membrane to remove the larger product, and then dialyzed against deionized water by a dialyzator with molecular weight cut off 1000 Da for 24 h. Finally, an orange coloured aqueous solution containing NSCD was obtained. The NSCD was recovered by lyophilizing the solution.

Fluorescence Sensing of Hg^{2+}

The detection of Hg^{2+} ion was performed in milipore water, tap water and phosphate buffer solution. In a typical assay, NSCD (10 mL, 7 µg/mL) dispersion was added into water sample (400 mL), followed by the addition of different concentrations of Hg^{2+} ion. The PL spectra were recorded after the reaction for 30 min. The selectivity for Hg^{2+} was confirmed by adding other metal ion stock solutions instead of Hg^{2+} in a

similar way at a concentration of 60 µM. All experiments were performed at room temperature.

In vitro Cytotoxicity and Live Cell Imaging

HaCaT were harvested and the cell concentration was adjusted to 1×10^4 cells/mL, cells were plated in a 96 well flat bottom culture plates (180 µL/well) and incubated with various concentrations (0.78, 3.185, 12.5, 25.0, 50.0, 100.0, and 200.0 µg/mL) of NSCD (in 20 µL). All cultures were incubated for 72 h at 37 °C and 5% CO_2 in a humidified incubator. Viable cell concentration was checked by MTT (3-(4,5-Dimethyl-2-2thiazolyl)-2,5-diphenyl-2H-tetrazolium bromide) assay. For detecting living cells through fluorescence imaging, the cells are incubated with NSCD (200 µg/mL) for 24 h at 37 °C. After being washed with fresh PBS three times the cells were imaged through fluorescence microscope. Then Hg^{2+} (20 µM) was added and incubated for 2 h. the cells were imaged again after washing the culture medium three times with PBS.

Calculation of detection limit

All fluorescence emission spectra of the fluorophore were integrated vs. wavenumber, and calibration curves were generated, with the analyte concentration on the X-axis (in nM) and F_0/F on the Y-axis, where F = the integrated fluorophore emission at a particular Hg^{2+} concentration and F_0 = the integrated fluorophore emission in the absence of Hg^{2+}. The lower mercury concentrations yielded a linear relationship, and the equation for the line was determined. The limit of the blank was taken to be the average of the blank (NSCD emission without Hg^{2+})+30 times the standard deviation of the blank. This value was entered into the equation determined in (for the Y value), and the corresponding X value was determined. This value provided the Limit of detection in nM.

Measurement of fluorescence quantum yield (PLQY) and fluorescence life time

The PLQY of the sample was calculated using quinine sulfate as reference following the procedure described in chapter-2. Time resolved fluorescence decay traces were deconvoluted from the signal and fitted using the FluoFit 4.4 package (Picoquant).

The experimental decay traces were fitted to triexponential functions via a Levenberg–Marquardt algorithm based on nonlinear least-squares error minimization deconvolution method. Three different exponential terms were used to fit the experimental decay traces. The quality of the fits was judged by the reduced chi-squared method, χ^2, the weighted residuals and the correlation functions. The latter two were checked for random distributions. To compare the photoluminescence lifetime of the free NSCD and in presence of Hg^{2+} at different concentrations, it was necessary to determine their average lifetime using eqn:

$$\tau_{avg} = \sum \alpha_i \tau_i^2 / \sum \alpha_i \tau_i$$

Where α_i are the pre-exponential factors and τ_i are the lifetimes obtained in the triexponential fitting of the decay curves of carbon dot emission.

5.3. Characterization

The synthesized materials were all characterized by standard technique as described in Chapter-2. Fluorescence lifetime experiments were performed with a time-correlated single-photon counting (TCSPC) system under right-angle sample geometry. Live-cell imaging was done using Axiovert 40 carl zeiss india fluorescence microscope at excitation wavelength of 405 and 488 nm.

5.4. Results and discussion

Microstructure, HD size and stability

All three samples prepared with variable nitrogen content named as NSCD-1, NSCD-2 and NSCD-3 are well dispersed in water with hydrodynamic sizes of 19, 13 and 25 nm respectively without any precipitation for months (Figure 5.1a). The alteration of zeta potential from positive to negative with increase in pH (Figure 5.1b) demonstrates the presence of acidic functional groups like -COOH, -COSH on the surface of NSCD. The FESEM image of NSCD-2 (Figure 5.1c) clearly reveals that the synthesized particles

are spherical, monodisperse and have a narrow size distribution between 5-10 nm. High resolution TEM image in Figure 5.1d indicates that particles are nearly spherical in morphology with uniform size of 3-5 nm. The size of the synthesized material is within the quantum range exhibiting excellent luminescent properties. The well-defined crystal lattice (0.36 nm) of the NSCD-2 as shown in Figure 5.1e is in agreement with the basal spacing of graphite.

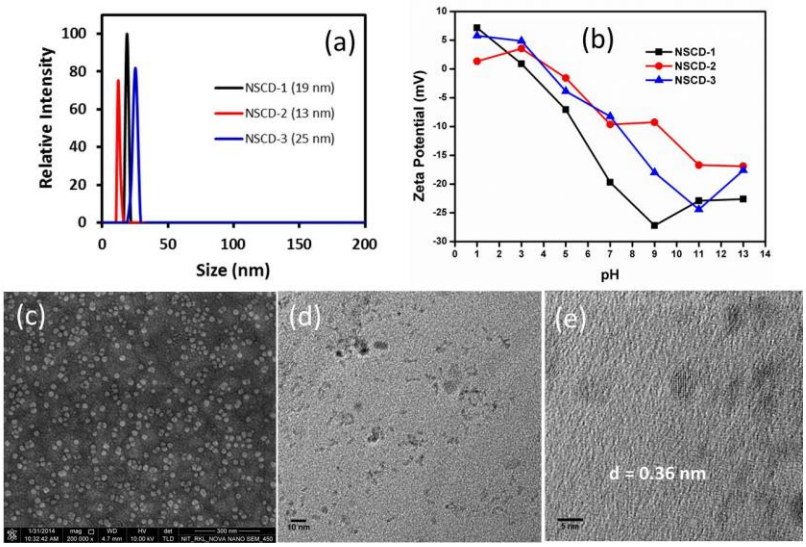

Figure 5.1 (a) Hydrodynamic sizes and (b) zeta potential measurement of NSCDs, (c) FESEM image, (d) TEM image and (e) Lattice imaging of NSCD-2.

XRD and Raman study

The phase and purity of the synthesized NSCD were analyzed by XRD (Figure 5.2a). The XRD pattern of the synthesized NSCDs show intense peak at $2\theta = 22.4°$ and a weak peak at $2\theta=42.1°$ which are assigned to (002) and (101) diffraction patterns of graphitic carbon respectively. The XRD result of the NSCD is similar to those of reported carbon dots.[45] The (002) peak corresponding to interlayer spacing in graphite (0.34 nm) becomes slightly longer in NSCD-1 (0.36 nm), showing good crystallization characteristics which shifts to further larger end in NSCD-2 (0.39 nm). The increase in d value indicates increase in amorphous nature attributed to the introduction of more defect site through increasing N-doping in the crystal lattice. Based on the XRD results, it can be seen that samples having higher nitrogen composition exhibited lower diffraction

intensity and broader peak (002), compared with the NSCD-1 having comparatively less N content.

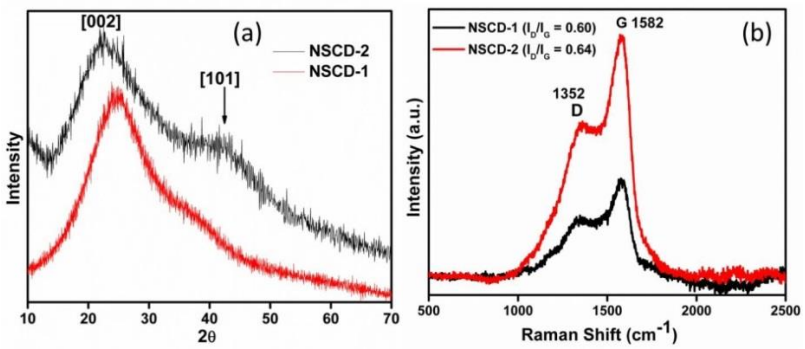

Figure 5.2 (a) XRD patterns and (b) Raman spectra of NSCD.

In the Raman spectrum of NSCD (Figure 5.2b), the peak at 1582 cm^{-1} assigned as G-band corresponds to the E_{2g} mode of the graphite and is related to the vibration of sp^2-bonded carbon atoms in a two-dimensional (2D) hexagonal lattice. The D-band at around 1352 cm^{-1} is associated with the vibrations of carbon atoms with dangling bonds in the plane terminations of disordered carbon structure. The intensity ratio (I_D/I_G), which is often used to correlate the structural purity to the graphite (measurement of the disorder extent, as well as the ratio of sp^3/sp^2 carbons), also indicates that the NSCDs are composed of mainly nanocrystalline graphite.[46] The I_D/I_G ratio slightly increases from 0.6 (NSCD-1) to 0.65 (NSCD-2) which can be attributed to origin of more structure defects in the sp^2 carbon site due to increased amount of nitrogen dopant. The size of the nanocrystalline graphite obtained from the relation $La = 44(I_D/I_G)^{-1}$ yields the value of about 7 nm which is close to the size observed in TEM images

Surface composition

The SEM-EDAX and XPS results indicate that NSCDs are mainly composed of carbon, nitrogen, oxygen and sulphur. The peaks in the survey spectrum (Figure5.3 a) at 165, 284-292, 398-406 and 528-540 eV correspond to binding energy of S2p, C1s, N1s and O1s with their atomic percentage 3.4, 64.9, 8.7 and 23 respectively. The high resolution scan of the C1s region (Figure 5.3b) shows carbons present in four different chemical environments, corresponding to sp^2 (C=C) at 286.4 eV, Sp^3 (C-C and C-H) at

285.3 eV, C-N/C-S/C-O at 287.6 eV and C=O/COOH/COSH at 289.6 eV. The C1s spectra corresponding to reference shows a shift of 1.8 eV to higher binding energy and hence taking the reference shift into consideration all other binding energies are to be evaluated. The high resolution spectra of N1s (Figure 5.3c) indicates the presence of both pyridinic type (401.3 eV) and pyrrolic (402.9 eV) N atoms. The high resolution scans of S2p region (Figure 5.3d) can be fitted into three peaks at 164.9, 166.2 and 169.5 eV, which represents $S2p_{3/2}$ of COSH[47] and $S2p_{1/2}$ of -C-S- covalent bond of thiophene/thiazine and oxidized sulphur S=O bonding respectively. The N1s and S2p clearly show that almost all of N was doped into the carbon as pyridine/pyrrole-like N, whereas most of the S remain as surface functional group (-COSH and S=O). Only 27% of total S was doped as thiophene/thiazine-like S into the core of carbon dots. Incorporation of sulphur into aromatic system compared to N requires harsh condition, which results lower percentage of S doping. Furthermore, high resolution O1s photoemissions (Figure 5.3e) were also obtained corresponding to S-O (530.3 eV) bond, C=O (532.9 eV) bond and C-OH/C-O-C (534.8 eV) bond. The presence of oxygen enhanced the solubility of NSCD in water.

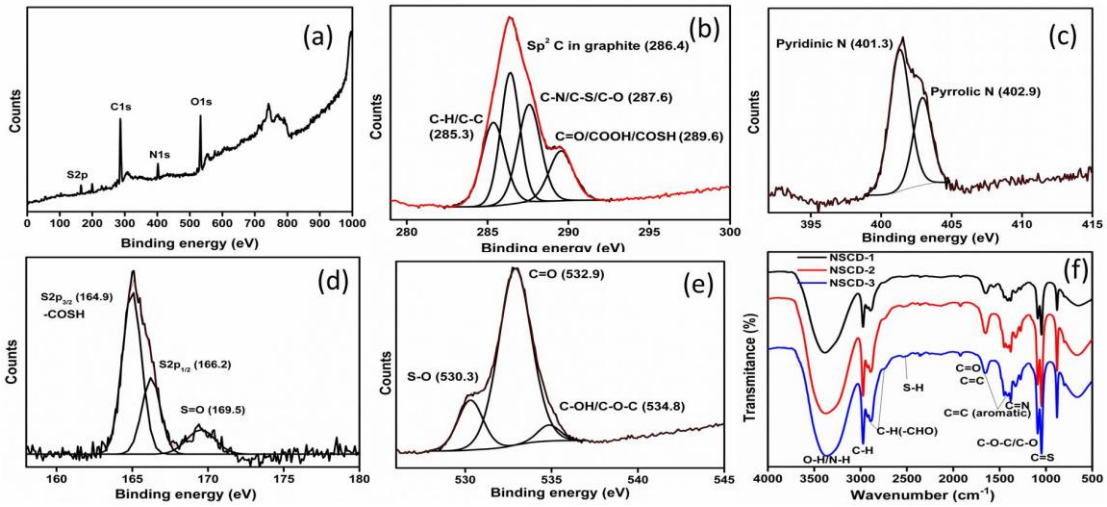

Figure 5.3 (a) XPS survey and high resolution scan of (b) C1s, (b) N1s, (c) S2p, (d) O1s of NSCD-2, and (e) FTIR spectra of NSCDs.

The evidence for C–N, N–H, C=S, S-H, C=C, C=O and C=N was also confirmed by FTIR spectra (Figure 5.3f). The broad absorption bands at 3000-3700 cm^{-1} in the FTIR spectrum are assigned to stretching vibrations of O-H and N-H, which indicates the

presence of lots of hydroxyl groups on the surface of NSCDs. The peaks corresponding to C=C stretch of aromatic hydrocarbons and the absorption from C=O (of COOH, COSH, CHO and CONH) is reflected in the wide range of 1750-1580 cm^{-1}. The C=N and C=S stretch were observed at 1350 cm^{-1} and 1043 cm^{-1}, thereby showing the formation of NSCDs. Weak S-H stretching at 2534 cm^{-1} and C=S stretching (1043 cm^{-1}) give the evidence for existence of -COSH, -CSOH and -SH functional group on the surface of NSCD. As evidenced from FTIR the presence of various functional groups like hydroxyl, carboxy, amide, amine, carboxylic group, thioacids, epoxy, thiol imparts excellent water solubility to synthesized NSCD.

Luminescent Properties

NSCD samples exhibit multiple excitonic bands different from commonly observed single exitonic band. This can be attributed to the formation of different types of excitation energy trap on the surface of NSCD by insertion of N and S atom to the hexagonal carbon lattice. The excitation spectra of NSCDs (Figure 5.4a) shows two major peaks at 275-280 nm and 355-370 nm ascribed to the π-π^* transition of aromatic domains and trapping of excited state energy by surface states. In addition to this with increasing N content, shifting of the emission center towards higher wavelength (Figure 5.4b) was observed which suggests that new emission centers were produced with increasing N content. Qain *et al.* reported that the pyridinic and pyrolic nitrogen atom can break the large conjugated carbon structure and induces the defect on which enhance the fluorescence properties of N-CD.[48] We anticipate that in this case the introduced sulphur atom would enhance the effect of N atoms by creating more defects through thiophenic, thiol or thioacid sulphur atom along with pyridinic and pyrrolic nitrogen atom. In all cases excitation dependent emission (Figure 5.4c-e) was observed because of existence of a number of surface emissive traps as well like different size and morphology of the material. Nitrogen and sulphur bonding to carbon in CD improve the emission and thus NSCD shows higher PLQY than undoped carbon dot. However, the PLQY of the NSCDs (Figure 5.4f) obtained from different precursor do not correlate with their nitrogen content. With increase in N content the PLQY of NSCD-2 (69%) is found to be more than NSCD-1 (62%), but NSCD-3 with highest N content has lower PLQY (38%).

This may be due to the incomplete carbonization of the long chain polymer precursor for NSCD-3. The low PLQY of NSCD-3 is in good agreement with smaller fluorescence lifetime compared to NSCD-2 (Table 5.1). The calculated PLQY of NSCD-2 (λex 360 nm) is found to be higher than NSCD reported earlier.[21,25] The measurement of fluorescence intensity on the exposure time of 2 h under fluorescence lamp indicates that the NSCD are highly photostable (Figure 5.4g). Fluorescence intensity (Figure 5.4h) remains constant with different concentrations of NaCl indicating the emission behavior is independent of ionic strength of the medium. Similar to CDs the PL intensity for NSCD-2 (Figure 5.4i) remains unchanged with in the pH range 3-8, suitable for biological sensing and live cell imaging application.

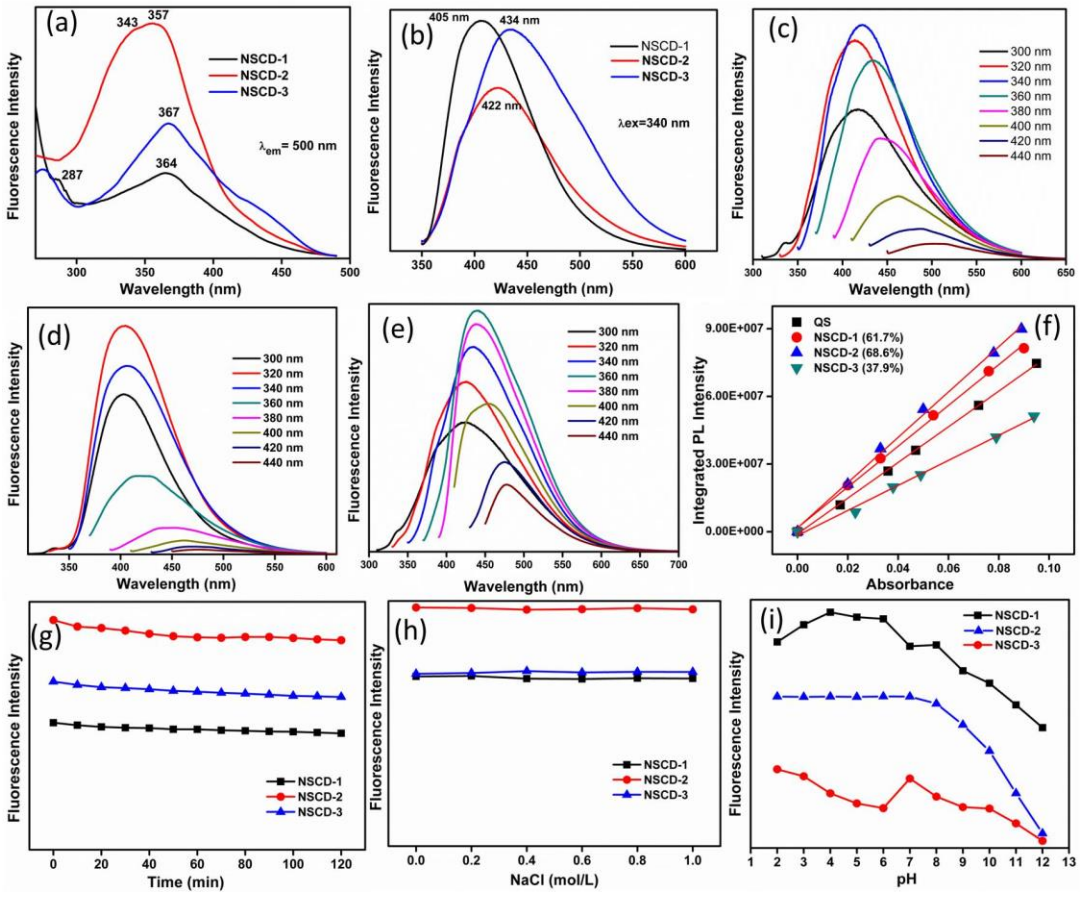

Figure 5.4 (a) Excitation and (b) emission spectra of NSCDs, Excitation dependent emission spectra of (c) NSCD-1, (d) NSCD-2 and (e) NSCD-3, (f) fluorescence and absorbance of the NSCDs and Quinine Sulfate (g) Change in fluorescence intensity w.r.t. time, (b) Effect of ionic strengths on the fluorescence intensity of NSCDs (ionic strengths

were controlled by various concentrations of NaCl), (c) Effect of pH on the fluorescence intensity of NSCDs.

Table 5.1 The Fluorescence parameters of all synthesized NSCDs.

N,S co-doped CD	λ_{em} (nm)	ϕ_f (%)	τ (ns)
NSCD-1	405	62	4.3
NSCD-2	422	69	5.8
NSCD-3	434	38	2.7

Fluorescence detection of Hg^{2+}

We explored the PL behavior of NSCD in designing highly selective and sensitive ON-OFF fluorescent Hg^{2+} sensor in aqueous solution. To our expectation, there was 65% decrease in fluorescence intensity (Figure 5.5a) at 435 nm as soon as 80 µM Hg^{2+} was gradually added; indicating that addition of Hg^{2+} can effectively quench the fluorescence of NSCD. The fluorescence quenching is owing to the nonradiative electron transfer from the excited state to the d-orbital of Hg^{2+}. To evaluate the sensitivity of the system, different concentrations of Hg^{2+} within 80 µM were studied and found that the fluorescence intensity of the NSCD is sensitive to Hg^{2+} and decreases with the increase of Hg^{2+}. In the range of 0 to 0.1µM the relative fluorescence intensity (F_0/F) shows good linear response with Hg^{2+} concentration which indicates that the fluorescence quenching process is dynamic in the above range. The dynamic quenching mechanism results from diffusive collision between the fluorophore and quencher during the life time of the excited state. The dynamic fluorescence quenching is described by the Stern-Volmer equation.

$$\frac{F_0}{F} = 1 + K_{SV}[Q]$$

Where F_0 and F are the fluorescence intensities of fluorophore in the absence and presence of the quencher (Q). K_{SV} is the Stern-Volmer quenching constant and [Q] is the concentration of the quencher. The graph (Figure 5.5b) representing fluorescence intensity (F_0/F) versus concentration of Hg^{2+} ions could be perfectly described by the Stern-Volmer plot with a linear behaviour,

$$\frac{F_0}{F} = 1.002 + 1.992[Hg^{2+}]$$

in the range of 0 to 0.1×10^{-6} M, having R^2=0.996, indicating that the quenching mechanism follows dynamic quenching. At higher concentration of Hg^{2+}, there is deviation from linearity (Figure 5.5c), probably due to presence of both static and dynamic mechanism as observed by other researchers.[49] The Stern-Volmer quenching constant was found as 1.99×10^6 $mol^{-1}dm^3$. The limit of detection (LOD) was estimated as 0.05 nM, which is lower than previously reported carbon dot based nanosensors.[41,50,51] The complexity of the intracellular system reasons a great challenge to the metal ions importantly in selectivity. To evaluate the selectivity of the NSCD towards Hg^{2+}, fluorescence screening experiment was carried out. Nearly no fluorescence intensity (Figure 5.5d) changes was observed in emission spectra of NSCD with various metal ions like Co^{2+}, Cu^{2+}, Mn^{2+}, Ni^{2+}, Fe^{2+}, Sn^{2+}, Zn^{2+}, Ca^{2+}. However under identical conditions fluorescence intensity was significantly quenched for Hg^{2+}. The selectivity coefficient (Table 5.2) for F_0/F for Hg^{2+} is much higher than for other metals indicating that NSCD possessed high selectivity for Hg^{2+}.

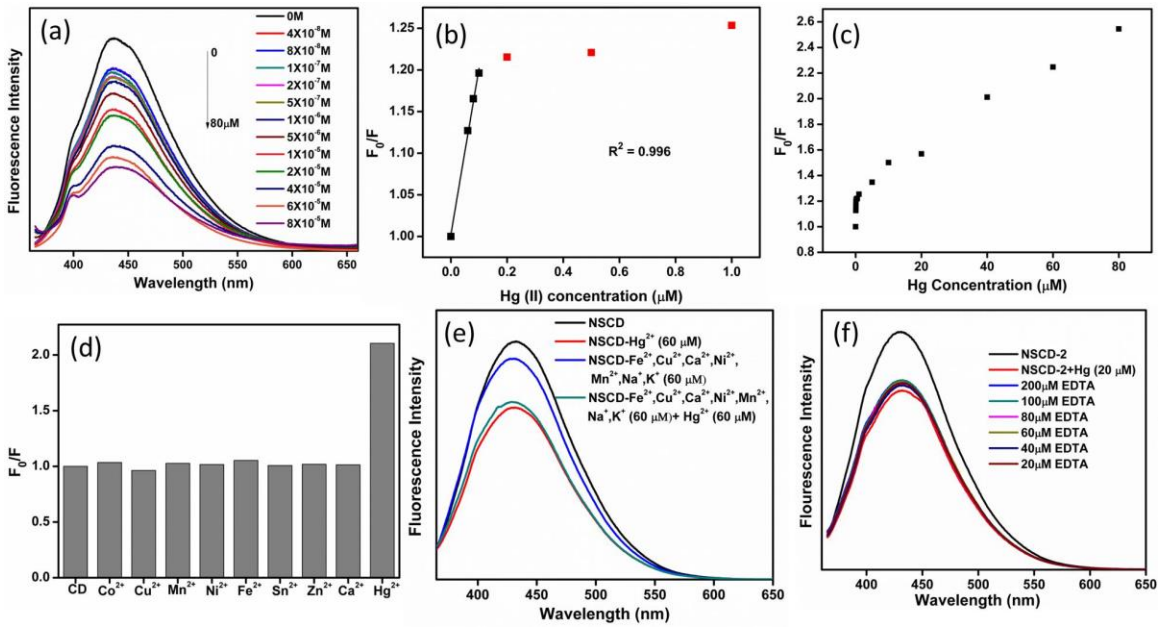

Figure 5.5 (a) Fluorescence spectra of NSCD probe upon exposure to different amounts of Hg^{2+}, (b) Linear dependence of fluorescence quenching of NSCD-2 with mercury concentration, Fluorescence quenching of NSCD with (c) Hg^{2+} concentration, (d) in the

presence of different cation, (e) mixture of cations, (f) Fluorescence response of NSCD-2 after adding EDTA to NSCD-Hg^{2+}.

Table 5.2 Selectivity coefficients of Hg^{2+} over other metal ions.

Metal ions	Selectivity coefficients	Metal ions	Selectivity coefficients
Co^{2+}	15	Fe^{2+}	10
Cu^{2+}	-14	Sn^{2+}	71
Mn^{2+}	21	Zn^{2+}	29
Ni^{2+}	33	Ca^{2+}	38

The strong quenching effect may originate from soft-soft acid base interaction of sulphur part of NSCD and Hg^{2+}. In another control experiment, Hg^{2+} alone and the mixtures of Hg^{2+} and above-mentioned metal ions were added into the NSCD aqueous solution respectively then the quenching effects of Hg^{2+} and the mixtures of Hg^{2+} on the fluorescence of NSCD were examined (Figure 5.5e). In comparison with efficient quenching effect of the Hg^{2+} the influence from the other coexisting metal ions is negligible. These observations indicate that the NSCD sensor is insensitive to other metal ions but selective to Hg^{2+} in the mixtures. Unlike reported carbon dot, in our case the quenched photoluminescence of NSCD was not recovered by adding a strong metal ion chelator such as EDTA (Figure 5.5f) implying that the Hg^{2+} interacts with NSCD through sulphur.

Investigation of the Sensing Mechanism

The proposed fluorescence quenching mechanism for our NSCD-Hg^{2+} system is depicted in Figure 5.6. We anticipate that fluorescence quenching is due to nonradiative electron transfer from excited state to the metal through soft-soft interaction between sulphur of NSCD and the metal center. Fluorescence lifetime measurements were conducted to gain further insight into the mechanism of fluorescence quenching of the NSCD by Hg^{2+}. The fluorescence lifetime of the NSCD is 5.8 ns, while the life time decays to 4.3 ns after Hg^{2+} addition. It indicates that the fluorescence quenching is dynamic and involves nonradiative electron transfer process. Though the thioacids (-COSH/CSOH) and thiol (-SH) functionalities at the edges of NSCDs could be the possible binding sites for Hg^{2+}, the absence of any significant changes in FTIR spectra of

NSCD-Hg^{2+} in comparison to NSCD rules out the possibility of complex formation in ground state. The nature of Stern-Volmer plot also eliminates the possibility of static quenching (complex formation).

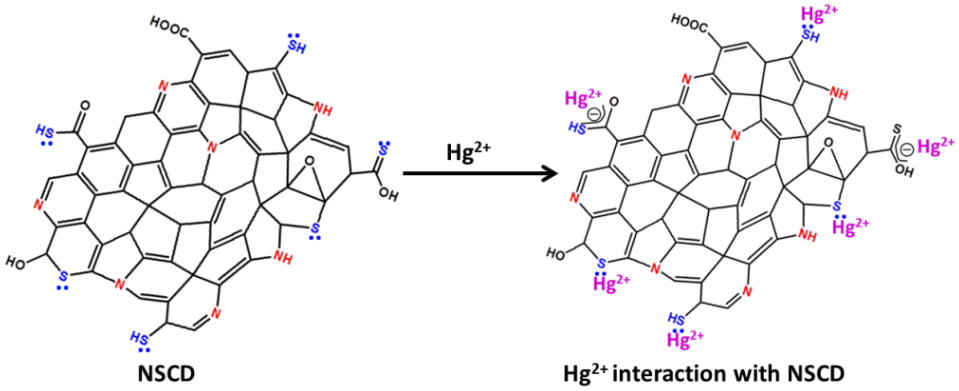

Figure 5.6 Plausible mechanism for fluorescence quenching of NSCD by Hg^{2+}.

Efficient Hg^{2+} detection in water samples and PBS

The excellent specificity combined with high sensitivity and selectivity of NSCD to Hg^{2+} ions suggests that the present chemosensor may be directly applied for detecting Hg^{2+} in practical fields. Thus we tested Hg^{2+} from natural water (tap water) and PBS. Prior to use all the samples were filtered through a 0.22 µm membrane to remove any suspended particles.

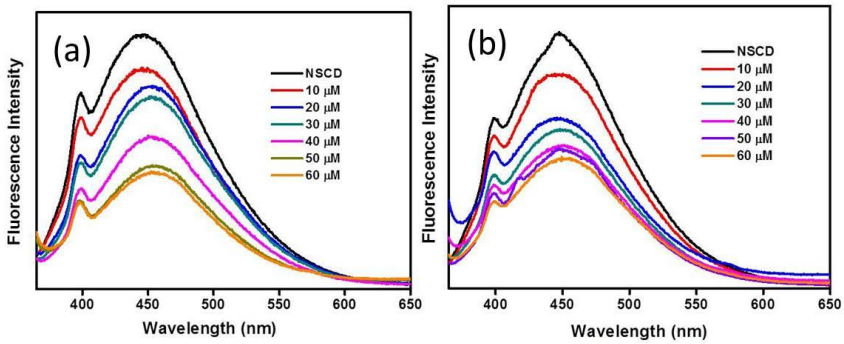

Figure 5.7 Fluorescence spectra of NSCD probe upon exposure to different amounts of Hg^{2+} in (a) Tap water and (b) PBS.

Figure 5.7 shows the fluorescence response of NSCD in presence of tap water and PBS containing different concentrations of Hg^{2+}. It was observed that in all the cases the

fluorescence intensity decreased with increasing concentration of Hg^{2+}. It clearly shows that although some organic/inorganic impurities and minerals exist in the tap water, the fluorosensor can still sensitively respond to 10 µM Hg^{2+}, satisfying the practical Hg^{2+} ion detection in real samples. Also due to sensitive fluorescence quenching with Hg^{2+} in PBS this NSCD may be suitable for Hg^{2+} detection in biological system through fluorescence imaging.

Effect of pH on fluorescence quenching

The influence of pH on NSCD and subsequently on the quenching phenomenon was investigated. In case of both NSCD and NSCD-Hg system the emission band is slightly shifted, which indicates that protons can regulate the emission. It was observed that at lower pH values the intensity of fluorescence was higher and at higher pH values the intensity is less (Figure 5.8a). However with in pH range 4-8 much change was not observed. Such a pH-dependent fluorescence is ascribed to the extent of proton acceptance by pyridine nitrogen/thiophenic sulphur atoms followed by possible proton transfer from protonated nitrogen to the conjugated carbon structure. The excellent specificity combined with high sensitive and selectivity of NSCD to Hg^{2+} ions suggests that the NSCD can be utilized to monitor Hg^{2+} in the living cell.

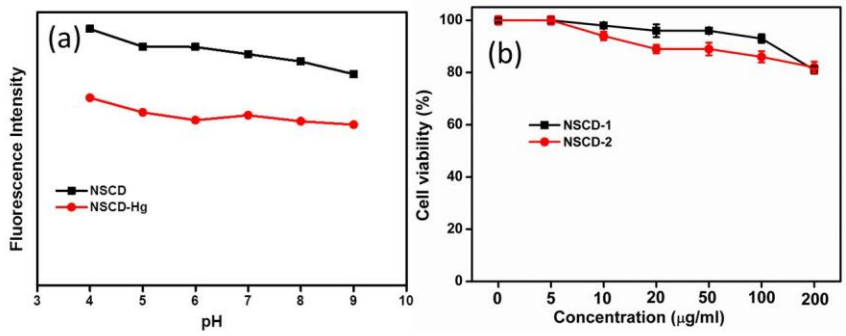

Figure 5.8 (a) Fluorescence quenching of NSCD w.r.t pH and (b) Cell viability by MTT assay.

Cytotoxicity and Intracellular bioimaging and biosensing of Hg^{2+}

In order to detect Hg^{2+} in living cells, HaCaT cells were used to evaluate the cytocompatibility of NSCD. As expected, the viability of the HaCaT cells declined only by <15% upon addition of the NSCD at up to 200 µg/mL for an incubation period of 72 h

(Figure 5.8a). Thus the as prepared NSCD probe can be considered to be low toxic and biocompatible which is consistent with previously reported carbon dots. Taking the advantage of small size, high selectivity and biocompatibility, we explored the bioimaging application of NSCD in monitoring Hg^{2+} in living cell. We performed in vitro cellular uptake experiment with HaCaT cells. The cells were first incubated with the probe (NSCD) for 12 h at 37 ºC, After the uptake, the particles were monitored by fluorescence microscopy and found to reside mainly in the cell membrane and the cytoplasmic area leaving the clear zones of the nuclei implying a good permeability to the cells. Then the intracellular Hg^{2+} imaging ability of the NSCD was tested. When the cells were supplemented with Hg^{2+} in the growth medium for 2 h the fluorescence intensity significantly decreased (Figure 5.9). The green signal from NSCD became dimmer with increasing concentration of Hg^{2+} signifying the ability of NSCD to display fluorescence turn-off behaviour in the living cells.

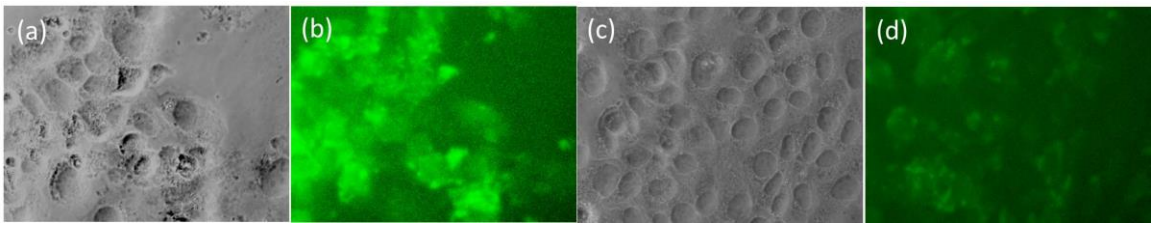

Figure 5.9 The fluorescence image of HaCaT cells stained with NSCD (a), (c) Bright-field transmission image of HaCaT cells (b) fluorescence image of cells visualized by green emission of NSCD, (d) fluorescence image of cells post-incubated in 20 µM Hg^{2+} solution.

5.5. Conclusions

- In summary, a simple, sensitive and selective N, S co-doped carbon dot based fluorescent sensor for Hg^{2+} detection has been demonstrated.
- The present sensor was prepared from hydrothermal treatment of single molecular precursor, exhibiting high fluorescence quantum yield (69%) in contrast to previous report.
- The soft-soft acid base interaction of sulphur part of NSCD and Hg^{2+} makes fluorescence probe more specific and selective towards Hg^{2+} contrast to other metal ions.

- The detection method is highly sensitive and the limit of detection of mercury ion is found to be 0.05 nM.
- The detection method exhibits excellent selectivity in tap water and also in the presence of complex metal ions in intracellular environment.
- Due to high photostability, low toxicity and low detection limit, these carbon dots are demonstrated as excellent probes for the detection of Hg^{2+} in the living cell.

.

5.6. References

1. P. G. Luo, F. Yang, S. T. Yang, S. K. Sonkar, L. Yang, J. J. Broglie, Y. Liu, Y. P. Sun, *RSC Adv.*, 2014, **4**, 10791-10807.
2. C. Ding, A. Zhu, Y. Tian, *Acc. Chem. Res.*, 2014, **47**, 20-30.
3. S. B. Yang, X. L. Feng, X. C. Wang, K. Mullen, *Angew. Chem. Int. Ed.*, 2011, **50**, 5339-5343.
4. L. Zhou, Z. Li, Z. Liu, J. Ren, X. Qu, *Langmuir*, 2013, **29**, 6396-6403.
5. Y. Wang, A. Hu, *J. Mater. Chem. C*, 2014, **2**, 6921-6939.
6. H. P. Liu, T. Ye, C. D. Mao, *Angew. Chem. Int. Ed.*, 2007, **46**, 6473-6475.
7. Q. L. Zhao, Z. L. Zhang, B. H. Huang, J. Peng, M. Zhang, D. W. Pang, *Chem. Commun.*, 2008, 5116-5118.
8. D. Pan, J. Zhang, Z. Li, M. Wu, *Adv. Mater.*, 2010, **22**, 734-738.
9. B. Zhang, C. Liu, Y.un Liu, *Eur. J. Inorg. Chem.*, 2010, 4411-4414.
10. Z. C. Yang, X. Li, J. Wang, *Carbon*, 2011, **49**, 5207-5212.
11. S. Sahu, B. Behera, T. K. Maiti, S. Mohapatra, *Chem. Commun.*, 2012, **48**, 8835-8837.
12. H. Zhu, X. L. Wang, Y. L. Li, Z. J. Wang, F. Yang, X. R. Yang, *Chem. Commun.*, 2009, 5118-5120.
13. Y. Q. Liu, K. Xiao, P. A. Hu, G. Yu, Y. M. Sun and D. B. Zhu, *J. Am. Chem. Soc.*, 2005, **127**, 8614-8617.
14. A. L. M. Reddy, A. Srivastava, S. R. Gowda, H. Gullapalli, M. Dubey, P. M. Ajayan, *ACS Nano*, 2010, **4**, 6337-6342.

15. Y. Li, Y. Zhao, H. Cheng, Y. Hu, G. Shi, L. Dai, L. Qu, *J. Am. Chem. Soc.*, 2012, **134**, 15-18.
16. L. Wang, H. S. Zhou, *Anal. Chem.*, 2014, **86**, 8902-8905.
17. C. Zhu, J. Zhai, S. Dong, *Chem. Commun.*, 2012, **48**, 9367-9369.
18. Y. Q. Zhang, D. K. Ma, Y. Zhaung, X. Zhang, W. Chen, L. L. Hong, Q. X. Yan, K. Yu, S. M. Huang, *J. Mater. Chem.*, 2012, **22**, 16714-16718.
19. Y. Dong, H. Pang, H. B. Yang, C. Guo, J. Shao, Y. Chi, C. M. Li and T. Yu, *Angew. Chem. Int. Ed.*, 2013, **52**, 1-6.
20. Y. Dong, H. Pang, H.B. Yang, C. Guo, J. Shao, Y. Chi, C. M. Li, T. Yu, *Angew. Chem. Int. Ed.*, 2013, **52**, 7800-7804.
21. D. Sun, R. Ban, P. H. Zhang, G. H. Wu, J. R. Zhang, J. J. Zhu, *Carbon*, 2013, **64**, 424-434.
22. H. Ding, J. S. Wei, H. M. Xiong, *Nanoscale*, 2014, **6**, 13817-13823.
23. Q. Hu, M. C. Paau, Y. Zhang, X. Gong, L. Zhang, D. Lu, Y. Liu, Q. Liu, J. Yao, M. M. F. Choi, *RSC Adv.*, 2014, **4**, 18065-18073.
24. D. Qu, M. Zheng, P. Du, Y. Zhou, L. Zhang, D. Li, H. Tan, Z. Zhao, Z. Xie, Z. Sun, *Nanoscale*, 2013, **5**, 12272-12277.
25. W. Wang, Y. C. Lu, H. Huang, A. J. Wang, J. R. Chen, J. J. Feng, *Sens. Actuators B*, 2014, **202**, 741-747.
26. E. M. Nolan, S. J. Lippard, *Chem. Rev.*, 2008, **108**, 3443-3480.
27. T. A. Baughman, *Environ. Health Perspect.*, 2006, **114**, 147-152.
28. I. Onyido, A. R. Norris, E. Buncel, *Chem. Rev.*, 2004, **104**, 5911-5930.
29. B. C. Ye, B. C. Yin, *Angew. Chem. Int. Ed.*, 2008, **47**, 8386-8389.
30. X. Guo, X. Qian, L. Jia, *J. Am. Chem. Soc.*,2004, **126**, 2272-2273.
31. S. Yoon, A. E. Albers, A. P. Wong, C. J. Chang, *J. Am. Chem. Soc.*, 2005, **127**, 16030-16031.
32. M. K. Nazeeruddin, D. D. Censo, R. H. Baker, M. Grätzel, *Adv. Funct. Mater.*, 2006, **16**, 189-194.
33. X. Zhu, L. Chen, Z. Lin, B. Qiu, G. Chen, *Chem. Commun.*, 2010, **46**, 3149-3151.
34. M. Kumar, R. Kumar, V. Bhalla, *Org. Lett.*, 2011, **13**, 366-369.
35. H. C. Wu, H. Bayley, *J .Am. Chem. Soc.*, 2008, **130**, 6813-6819.

36. J. Ke, X.Y. Li, Y. Shi, Q.D. Zhao, X.C. Jiang, *Nanoscale*, 2012, **4**, 4996-5001.

37. F. Q. Zhang, L.Y. Zeng, C. Yang, J.W. Xin, H.Y. Wang, A.G. Wu, *Analyst*, 2011, **136**, 2825-2830.

38. Z. Qian, J. Ma, X. Shan, H. Feng, L. Shao, J. Chen, *Chem. Eur. J.*, 2014, **20**, 2254-2263.

39. J. Ju, W. Chen, *Biosens. Bioelectron.*, 2014, **58**, 219-225.

40. H. Zhang, Y. Li, X. Liu, P. Liu, Y. Wang, T. An, H. Yang, D. Jing, H. Zhao, *Environ. Sci. Technol. Lett.*, 2014, **1**, 87-91.

41. H. Huanga, J. J. Lva, D. L. Zhoua, N. Baob, Y. Xua, A. J. Wang, J. J. Feng, *RSC Adv.*, 2013, **3**, 21691-21696.

42. W. Lu, X. Qin, S. Liu, G. Chang, Y. Zhang, Y. Luo, A. M. Asiri, A. O. Al-Youbi, X. Sun, *Anal. Chem.*, 2012, **84**, 5351-5357.

43. R. Zhang, W. Chen, *Biosens. Bioelectron.*, 2014, **55**, 83-90.

44. S. Liu, J. Tian, L. Wang, Y. Zhang, X. Qin, Y. Luo, A. M. Asiri, A. O. Al-Youbi, X. Sun, *Adv. Mater.*, 2012, **24**, 2037–2041.

45. S. Y. Park, H. U. Lee, E. S. Park, S. C. Lee, J.W. Lee, S. W. Jeong, C. H. Kim, Y. C. Lee, Y. S. Huh, J. Lee, *ACS Appl. Mater. Interfaces*, 2014, **6**, 3365-3370.

46. A. C. Ferrari, J. Robertson, *Phys. Rev. B*, 2000, **61**, 14095-14107.

47. I. B. Baranovski, M. A. Golubnichaya, G. Y. Mazo, V. I. Nefedov, Y. V. Salyn, R. N. Shchelokov, *Zh. Neorg. Khimii*, 1976, **21**, 1085-1089.

48. Z. Qian, J. Ma, X. Shan, H. Feng, L. Shao, J. Chen, *Chem. Eur. J.*, 2014, **20**, 2254-2263.

49. J. Panchompoo, L. Aldous, M. Baker, M. I. Wallace, R. G. Compton, *Analyst*, 2012, **137**, 2054-2062.

50. X. Qin, W. Lu, A. M. Asiri, A. O. Al-Youbi, X. Sun, *Sens. Actuators B*, 2013, **184**, 156-162.

51. F. Yan, Y. Zou, M. Wang, X. Mu, N. Yang, L. Chen, *Sens. Actuators B*, 2014, **192**, 488-495.

Part II

Multifunctional Luminescent Magnetic Mesoporous Silica based Nanostructures for Targeted Drug Delivery and Multimodal Imaging

Chapter-6

A short review on multifunctional nanoparticle for multimodal imaging and therapy

6.1. Preface

Recently, incredible effort has been devoted for the development of nanostructured materials owing to their potential applicability in biological field[1-4] including, disease diagnostics and therapy,[5-7] biosensing,[8,9] biocatalysis,[10,11] drug delivery,[12-14] protein/DNA bioseperation[15,16] and bioimaging.[17,18] The usefulness of the nanostructured material is mainly due to small size, large surface area, and the possibility to functionalize with targeting ligands, as well as imaging and therapeutic moieties. Nanosized materials provide a robust framework in which two or more components can be incorporated to give multi-functional capabilities. These nanostructured materials have several advantages in disease diagnostics and therapy over traditional methods, which are justified as follows:

- Nanoparticles can easily integrate more than one kind of imaging or therapeutic agents, which makes them potential multifunctional nanoplatforms for both diagnosis and therapy.
- Large surface area and interior cargo volume of the nanoparticle ensure facile adsorption as well as high loading of various therapeutic agents.
- Nanoparticles can be readily conjugated with molecular moieties capable of recognizing various complementary biomolecules including DNA strands and antigens with high sensitivity and selectivity, which is advantageous in targeted imaging, diagnosis, and delivery. Moreover presence of large number of targeting molecule on single nanoparticle can greatly enhance target-binding and specificity compared to single molecules due to so-called multivalent effects.[19]
- Appropriate size and surface modification of nanoparticle minimizes the possibility of macrophagic clearance in the blood stream.

These features provide nanomaterials with great potential as innovative diagnostic and therapeutic systems for the clinical applications. The major applications of nanomaterials in the biomedical field can be mainly divided into imaging and therapy.

Multimodal Imaging

In the medical diagnostics, the widely used techniques include optical imaging, magnetic resonance imaging (MRI), computed tomography (CT), ultrasound (US) and positron emission tomography (PET) or single photon emission computed tomography (SPECT). Each imaging modality has its own unique advantages along with intrinsic limitations, such as insufficient sensitivity or spatial resolution, which make it difficult to obtain accurate and reliable information at the disease site. However the combination of imaging modalities could improve medical imaging for diagnosis. Multimodal imaging is a powerful method that can provide more reliable and accurate detection of disease sites. Till now various combinations of imaging modalities were developed for both in vitro and in vivo imaging. Among them, the most popular nanostructured multimodal imaging probes are combinations of MRI and optical imaging modalities. MR imaging can accumulate simultaneous physiological and anatomical information with high spatial resolution, whereas optical imaging is associated with rapid screening of the information.

Magnetic Resonance Imaging: MRI is one of the most powerful and non-invasive diagnostic technique for living organisms that produces excellent signal contrast for soft tissue by detecting the nuclear spin of hydrogen atoms, which predominantly come from water and fat in human body. MRI contrast agents can provide bright or dark contrast by accelerating either T_1 or T_2 relaxation of water protons, respectively.

Superparamagnetic iron oxide nanoparticles (SPIONs) are being increasingly used as MRI contrast agents to improve the diagnosis and therapy. [3,20-21] These SPIOs are designed as T_2 contrast agents. In T_2 -weighted MRI, the tissue containing SPIOs exhibits reduced signal intensity. These iron oxide nanoparticles have the ability to dramatically shorten T_2 relaxation times in the liver, spleen, and bone marrow by selective uptake and accumulation in the cells of the reticuloendotherial system (RES).[22,23] Organ tumors' (liver, spleen tumor) those lack phagocytic activity can thus be detected by the darkening of surrounding normal tissue.[24] SPIONs can also accumulate in the tumor by enhanced permeability and retention (EPR) effects, which facilitates tumor detection in tissues or organs that normally do not sequester SPIONs from blood circulation. Among the

commercially available SPIONs such as Feridex IV, Combidex, CLIO-tat, Resovist etc., Feridex IV and Resovist have been approved by FDA for clinical application.

Most recently, these iron oxide based nanomaterials have been explored for in vivo molecular imaging of disease markers and physiological processes. Surface functionalized SPIONs associated with appropriate targeting agents could enable the ultrasensitive detection of diseases like atherosclerotic plaques, tumors, and apoptotic tissues etc.[25-29] Kessinger *et al.* succeeded in quantitative measurement of the binding kinetics of superparamagnetic micelles to $\alpha_v\beta_3$-integrin expressed tumor endothelium through T_2*-weighted time-resolved MRI technique.[30] Furthermore Labeling of progenitor cells,[31,32] pancreatic islet cells[33] etc. without affecting cell viability or function demonstrates the extensive applicability of SPIONs for in vivo cell tracking.

Optical Imaging: Optical imaging is a non-invasive imaging technique based on the behavior of visible, ultraviolet and infrared light. It has excellent spatial resolution and detection sensitivity and low cost in cellular imaging. However, the auto fluorescence of tissue and light attenuation hindered its in vivo application. Optical imaging using Near-infrared (NIR) light has extensively used for in vivo imaging because tissues scatter and absorb less light at longer wavelengths, resulting in deeper penetration in biological tissues than visible light.

Over the past several years, different kinds of nanostructures, including semiconductor quantum dots (QDs),[34,35] lanthanide based luminescent nanoparticles,[36-38] gold nanoparticles,[39] and nanoparticles containing organic dyes [40] have been developed for optical bioimaging. Semiconductor QDs possess novel electronic, optical and structural properties which can be utilized as contrast agents for deep tissue imaging. Multifunctional nanoparticles based on semiconductor QDs have been designed for imaging and cancer treatment.[41,42] However inherent toxicity and chemical instability of quantum dots limit their clinical application. Most recently, lanthanide doped inorganic nanomaterials served as a suitable alternative due to their excellent up-conversion and down-conversion luminescence properties, including large Stokes shifts, narrow line-width emission bands, high quantum yields, long lifetimes and superior photostability. Tm^{3+} and Yb^{3+} doped $NaYF_4$ nanoparticles with size range 20-30 nm have been

successfully employed for NIR imaging of both in vitro and in vivo.[43] Later in vivo whole-body imaging of small animals has been successfully realized based on lanthanide nanoparticle. [44]

Recently carbon based QDs (carbon dots and graphene quantum dots) are pursued as nontoxic alternatives in the development of fluorescence imaging agents for various biomedical purposes because they not only exhibit several favorable attributes of traditional semiconductor based QDs, but also show chemical inertness, low toxicity, high water solubility and biocompatibility.[45,46] Carbon dot has been successfully employed as fluorescence probe for optical imaging of cells and tissues, from straight forward cell imaging to specific tissue targeting.[47-53] The imaging efficacy of various carbon dots has also been extended for in vivo imaging.[54-57] Most recently, Kim *et al.* synthesized near-infrared-fluorescence (NIR)-emitting carbon dots from tire soot and applied for both in vitro and in vivo imaging of glioma.[58] Although the application of carbon dot in NIR imaging is at a very early stage, NIR properties of the carbon dots will no doubt lead to more research in the field of in vivo molecular imaging and biomedical studies for the diagnosis and therapy of diseases.

Targeted drug delivery

Targeted drug delivery is a method of delivering medication at the desired target in therapeutic concentration at the same time restricting its access to normal cellular lining. Insufficient target selectivity of drugs can cause unwanted side effects and reduce therapeutic efficacy. Thus the targeted or site-specific delivery of drugs is very attractive goal because this provides one of the most potential ways to improve the therapeutic index of the drugs with minimal peripheral toxicity. Passive targeting through the well-studied enhanced permeability and retention (EPR) effect is not universal for all types of tumor cells, and a lack of cell specific interactions might decrease therapeutic efficacy and induce multiple drug resistance.[59-62]

In contrast, active targeting through covalent attachment of targeting molecules such as folic acid,[63] hyaluronic acid,[64] aptamer,[65] antibody,[66] peptide,[67] or endoglin[68] to the nanoparticle surface could promote the site-specific delivery of therapeutics. The

specific binding of these targeting ligands with the overexpressed receptors on tumor cell surfaces facilitates the selective cellular uptake. Specifically the small molecule folic acid (FA) has been widely investigated as targeting ligand and has shown a notable enhancement in uptake efficiency of numerous type of drug delivery system.[69-72]

Magnetic targeting has long been considered as a viable approach for site-specific delivery of therapeutics. Through proper design of the externally applied magnetic field, therapeutic agents attached to magnetic nanoparticles can be concentrated and retained at the preferred site under magnetic guidance which enables the targeted delivery of therapeutics to the desired spot. The idea of using magnetic microspheres as vehicles for drug delivery in cancer therapy was first introduced by Widder *et al.*[73] Later magnetic nanoparticles were introduced for magnetically guided drug delivery which may offer better biocompatibility, optimal biodistribution, and deeper tumor penetration compared to microparticles. Yang *et al.* explored the possibility of utilizing iron oxide nanoparticles as a drug delivery vehicle for minimally invasive magnetic targeting of brain tumors.[74] Many other types of magnetic nanostructures/assembles, including liposomes-, micelles-, and mesoporous silica-coated superparamagnetic iron oxide nanoparticles, have been successfully employed for magnetic targeting of chemotherapeutic drugs.[75,76]

6.2. Multifunctional Nanoparticle

Enormous amount of evidence have shown that nanostructured materials are capable of improving the efficiency of therapeutic intervention. However, only relying on the self-functioning of nano-systems is not sufficient to match the changeable and complicated disease microenvironment. Considering those disadvantages, researchers would like to design and fabricate nanostructured materials with multiple functionalities to improve the therapy. For example imaging, as a visualization technique, was introduced to the development of nanocarriers which could improve the therapy by efficient monitoring of therapeutic response. In this regard multifunctional nanomaterials have been designed to carry out diverse functions in contrast to the conventional methods

of conferring individual functionality, such as delivery of a single type of pharmaceutical compound.[77-82]

Judicious combinations of different kinds of entities in a single particle will enable the development of multifunctional nanotheranostics that could target, detect and treat the diseased site. [79,83] The term "theranostics" signifies the development of more specific therapies for various diseases with simultaneous diagnostic capabilities. For example, the combination of MRI contrast agent and anticancer drug can allow the detection of disease through non-invasive MRI and targeted chemotherapy. There are many possible combinations of the various imaging and therapeutic modalities. Multifunctional nanoparticle simultaneously achieves co-delivery of multiple therapeutic agents, and provides targeted delivery by appropriate surface modification of the carriers' surface. In this regard, numerous multifunctional nanostructure materials have been developed and their utility for various biomedical applications has been explored. Contrast to organic-based nanomaterials (polymeric nanoparticles, micelles, and liposomes), inorganic nanomaterials such as mesoporous silica, magnetic nanoparticles, up-conversion nanoparticle, gold nanoparticles, quantum dots etc. have shown tremendous promise in biomedical applications owing to their robustness and longevity as core materials, aboudant availability and low cost.[84,85] Although there has been explosive research activity in the development of multifunctional nanoparticles for theranostic applications, there remain major challenges that need to be overcome in order to achieve real clinical applications.

In this prospective, our present investigation involves the development of advanced multifunctional mesostructured silica nanocomposite for diagnosis and therapy. Here a brief overview on fabrication of mesoporous silica based multifunctional nanocomposites and their subsequent biomedical application is presented as it is relevant to our work.

6.3. Multifunctional mesoporous silica nanocomposite (MSN)

Among various nanostructured inorganic materials studied for biomedical applications, mesostructured silica nanoparticle have gained tremendous attention for the development of multifunctionality due to their advantageous structural properties, such as high internal surface area and pore volume, tunable pore sizes, colloidal stability, and the possibility to specifically functionalize the inner pore system and/or the external particle surface.[86-88] The highly porous materials can be utilized in the storage and delivery of small molecules such as fluorescent dyes and drugs as well as larger molecules such as nucleotides and proteins. Furthermore, they are able to act as molecular machines for controlled release of guest molecules from the pores in response to certain stimuli. These highly attractive features make multifunctional mesoporous silica nanoparticles a promising and widely applicable platform for diverse biomedical applications including bioimaging for diagnostics,[84,87] biosensing,[89,90] biocatalysis,[91,92] bone repair,[93] and drug delivery.[14,94]

Multifunctional mesoporous silica nanomaterials can be obtained by simply conjugating two different components at separate regions (interior pore walls and external surface of the particle). For imparting multifunctionality to mesoporous silica nanoparticle following two steps are followed.

(i) Encapsulation of nanocomponents such as QDs, metallic nanoparticle, imaging agent or different therapeutic agents with in the silica matrix
(ii) Molecular functionalization which involves attaching antibodies, proteins, dyes, marker molecules and drug molecules to the silica surface

As these functionalized particles can exhibit several features synergistically and deliver more than one function simultaneously they could have unique advantages in biomedical applications.

Encapsulation approach

Encapsulation approach has a number of advantages over organic coating.[95] This robust strategy is highly stable and provides scope for introducing organic functionalities

for conjugation of active molecules like fluorophore, target molecule, therapeutics. Also encapsulation of inorganic nanomaterials or therapeutics with silica matrix ensures the preservation of unique properties of the encapsulated entity.[96]

Hyeon *et al.* developed a simple and general method for encapsulation of hydrophobic inorganic nanoparticles in mesoporous silica shell by transferring presynthesized oleic acid stabilized iron oxide nanoparticles to aqueous media by capping with CTAB which on subsequent silica sol-gel reaction followed by the removal of surfactants resulted in the production of mesoporous silica spheres embedded with iron oxide nanoparticles.[97] Along with Fe_3O_4 nanoparticles other hydrophobic nanostructured materials such as one-dimensional α-FeOOH nanotubes, spherical MnO nanoparticle were coated with mesoporous silica.[98] Subsequently various strategies have been developed by several researchers for coating of metal nanoparticle, metal oxide, up-conversion nanoparticle and QDs to develop the various mesoporous silica coated nanostructured materials.[99-103] Moreover, different kinds of entity, such as metallic or oxide nanoparticles, quantum dots, organic fluorescence dyes, and drug molecule alone or in combination could be readily immobilized in silica matrix or mesopores, rendering them useful as multifunctional biomedical applicant. Furthermore the silica coating provided a robust barrier against oxidation of the QD core and reduced nonspecific adsorption on the nanoparticle. In 2008, Hyeon group extended their protocol for fabrication of mesoporous silica coated Fe_3O_4 core-shell nanoparticle applied for simultaneous in vivo multimodal imaging and drug delivery.[98] The superparamagnetic iron oxide nanoparticle core serves as magnetic resonance (MR) imaging contrast agent where as mesoporous silica shell is utilized for drug delivery application. Furthermore, organic fluorescence dyes such as fluorescein isothiocyanate (FITC) and rhodamine B isothiocyanate (RITC) were immobilized in mesopores silica for in vivo fluorescence imaging.

Surface functionalization

The silica precursor (alkoxysilanes) used for synthesis of mesoporous silica nanoparticle allows for direct or indirect incorporation of functional groups like –OH, -NH_2, -COOH, -SH on to the surface. Alternatively these functional groups can be

introduced in a separate post-synthesis step including attachment of additional surface layers. These functional groups play an important role for bioconjugation of various therapeutic agents, target molecules. Selective modification of the internal pore and the external particle surface with organic and inorganic moieties is often an essential requirement for development of multifunctional drug carriers with desired features. External surface functionalization provides superior colloidal and chemical stability to the system and improves the biocompatibility and therapeutic profile of the system through attachment of specific cell targeting molecules, imaging agents,[104-106] whereas the internal organic moieties provides boosted interaction and covalent binding of cargo molecules, such as drugs or proteins, which allows for control over diffusional transport, delivery kinetics, and stability of the therapeutic molecules. [107,108]

The surface functionalization of mesoporous silica is mainly through postsynthetic grafting and via co-condensation using silane coupling agents. It can be done by covalent coupling of desired molecule through amine, thiol or epoxide terminated silica surface. Another method involves the modification of the silica surface by molecules that already have a silane group integrated within the molecule. The surface of the nanoparticle can be modified to obtain -COOH, $-NH_2$, -SH and reactive -OCN groups by using a carboxylated silane, aminosilane, mercaptosilane, cyanogen bromide reagents respectively. Biomolecules, such as proteins and antibodies, containing free amine functional groups are then attached covalently to the carboxyl functionalized silica, using carbodiimide-coupling chemistry.[109] Cancer targeting ligands such as folates are attached chemically to aminated silica surface using carbodiimide chemistry.[110] In a similar fashion sulfohydryl-modified silica surface are conjugated to disulfide-linked oligonucleotides (e.g. DNA) through disulfide-bond formation.[111] The surface hydroxyl groups of silica can also be activated by the cyanogens bromide to produce reactive -OCN derivative which reacts readily with proteins through amine groups, forming a 'zero-length' bioconjugate.[112]

The advancements in co-condensation and post-synthetic methods have also made it possible to introduce a numerous of organic molecules to the silanol groups on the exterior surface of mesoporous silica nanoparticles through covalent or electrostatic

interactions. In one example, polyethyleneimine (PEI) polymers were attached to the surfaces of MSNP to improve nucleic acid delivery.[113] Bein and co-workers established a site-selective delayed co-condensation approach to produce bifunctional MSNs with a selective functionalization of the interior.[114,115] Dual functional mesostructured nanotheranostics was developed by Lin *et al.* for simultaneous fluorescence imaging and gene transfection.[116] A multifunctional mesoporous silica system was developed by functionalization in with fluorescent contrast agent AT-TO647N, drug photosensitizer Pd-porphyrin payload for therapeutic intervention (photodynamic therapy), and bio-molecular ligands cRGDyK peptides on the outermost surface for targeting the $\alpha_v\beta_3$ integrins of cancer cells.[117] These surface modifications of MSNs minimize nanoparticle aggregation and reduce nanoparticle non-specific binding.

6.4. Recent developments of mesoporous silica based multifunctional nanostructures

Following the above mentioned steps, numerous multifunctional mesoporous silica nanoparticles congregated with diagnostics and therapeutics agents simultaneously have been designed. Imaging modalities have the potential to play an important theranostic role in medicine since they permit the monitoring of drug delivery efficiency as well as the visualization of affected areas. One such multifunctional hollow mesoporous silica hybrid nanoparticle has developed by Qian *et al.* for efficient ultrasound based imaging and controlled hydrophobic drug (paclitaxel) delivery.[118] Drug loaded hollow spherical nanostructure combined with ultrasound irradiation showed fast ultrasound responsiveness for controlled drug release and higher in vitro and in vivo tumor inhibition rates compared with free paclitaxel and paclitaxel-loaded particles. Up-conversion based multifunctional mesoporous silica nanoparticle shows interesting NIR excitation bioimaging for better therapeutic purose.[119] A multifunctional up-conversion based mesoporous silica nanocomposite (β-$NaYF_4$:Yb^{3+},Er^{3+}@β-$NaGdF_4$:Yb^{3+}) was reported for simultaneous drug delivery (doxorubicin) and dual imaging (up-conversion luminescence and MRI).[120] The nanocomposites exhibited low systematic toxicity and high in vivo antitumor therapy efficacy. Recently Fan *et al.* designed a novel up-conversion based mesoporous silica nanotheranostic for tri-modal synergetic therapy and

multimodal imaging.[121] The hollow cavity of rattle type core shell nanotheranostics was loaded with radiosensitizer/chemodrug docetaxel (Dtxl) whereas the pores of silica serve as the carrier for radio-/photo-sensitizer hematoporphyrin (HP). Upon NIR excitation and X-ray irradiation, synergetic chemo-/radio-/photodynamic therapy can be achieved by the co-delivery of radio-/photo-sensitizer HP and radiosensitizer/chemodrug Dtxl which produces remarkably enhanced therapeutic effects both in vitro and in vivo. The therapy was boosted with simultaneous magnetic/up-conversion luminescent (MR/UCL) bimodal imaging. In other MSNs studies, fluorescence resonance energy transfer (FRET) was used to monitor the therapy.[122] Li *et al.* developed a tumor marker (surviving mRNA) mediated "on-demand" drug release system using multifunctional mesoporous silica nanoparticle. The relevant change in donor and acceptor fluorescence signal was used to monitor the unlocking and release event in real-time.[123] Mesoporous silica nanoparticle based numerous multimodal imaging probes have also developed for diagnostic purposes.[124,125]

Another function of multifunctional mesoporous silica nanoparticle is that of being a gatekeeper in stimuli-responsive delivery systems. For example, MSNs can act as smart drug delivery system by capping nanochannel entrances with external stimuli (e.g., pH, osmolarity, photo-activated) responsive entities to prevent the premature release of conveyed cargo.[126,127] Zhao *et al.* developed multifunctional iron oxide/mesoporous silica core/shell (Fe_3O_4@$mSiO_2$) nanoparticle, end-capped with pH-stimuli-responsive hydroxyapatite (HAp) nanovalves for pH-responsive drug release. The dissolution of hydroxyapatite in an acidic environment triggers the release of the loaded drugs.[128] MSNs have also been utilized for co-delivery of various therapeutic agents. Ma and his group developed a hollow mesoporous silica nanoparticle (HMSNP) based pH-responsive drug/siRNA co-delivery vehicles capable of simultaneously delivering doxorubicin and siRNA against the Bcl-2 protein into targeted cancer cells.[129] The hollow nature of the HMSNPs not only improves the anticancer drug loading capability, but also enhances the siRNA binding ability towards certain cancer cells. In other mesoporous silica based multifunctional studies, mesoporous silica coated gold nanorods were used as a light-mediated multifunctional theranostic carrier for cancer treatment.[101] The inner

AuNR core functioned both as TPI imaging agent and hyperthermia agent, whereas the outer mesoporous SiO_2 shell served as effective drug carrier.

Moreover, mesoporous silica based multifunctional platform has also been used to encapsulate cancer drugs, superparamagnetic iron oxide nanocrystals, fluorescent tags, as well as targeting groups on the surface. Drug delivery, magnetic resonance and fluorescence imaging, magnetic manipulation, and cell targeting are simultaneously possible using these multifunctional mesoporous silica nanoparticle.[130] Liong *et al.* highlighted the development of various mesostructured multifunctional nanoparticles for simultaneous imaging and delivery of molecules in biological applications. Very recently, Mohapatra *et al.* developed multifunctional mesoporous hollow silica nanocapsules for targeted co-delivery of cisplatin-pemetrexed and MR imaging.[131] The exterior surface of the hollow mesoporous silica nanosphere was selectively acid functionalized and utilized to conjugate the anticancer drug cisplatin, the marker molecule folic acid (FA) for targeted delivery, and rhodamine isothiocyanate (RITC), whereas the interior space was utilized to encapsulate superparamagnetic $CoFe_2O_4$ nanoparticles (for MR imaging) as well as the hydrophobic anticancer drug pemetrexed. Such a dual drug loaded nanocapsule showed enhanced cytotoxicity than individual drugs due to the simultaneous action of both the drugs cisplatin and pemetrexed, and targeted delivery of the drug capsule through folate receptor mediated endocytosis.

The unique structural feature of mesoporous silica allows decoration of nanoparticles onto its surface, which enables assembly of numerous nanoparticles and sequential addition of different functional nanoparticles. Using these facile assembly processes, a wide variety of theranostic nanoplatform has been achieved. For "on-demand" controlled release of encapsulated drugs, various inorganic nanoparticles (Au, CdSe, Fe_3O_4 etc.), were assembled on the surface of mesoporous silica via stimuli-responsive tethers.[132-135] These assembled nanoparticles could function as gatekeepers and could be removed by either intracellular or external triggers such as pH change, reduction process, enzyme reaction, or irradiation of light. Hyeon's group demonstrated a simple method for assembly of hydrophobic iron oxide nanoparticles on silica particles through covalent attachment Br terminated iron oxide nanocrystals with amine

functionalized surface.[136] The same group developed a multifunctional dye doped MSNs decorated with iron oxide nanoparticles for drug delivery as well as MR imaging.[137] This developed system significantly displayed the biomedical potential of MSNs for simultaneous fluorescence imaging with the RITC dye, MR imaging with the iron oxide nanoparticles, and drug delivery with doxorubicin through in vivo studies with tumor-bearing mouse models. The better T_2 MR contrast effect is due to presence of iron oxide nanocrystals on the silica surface and clustering of magnetic nanoparticle. In combination with the targeting moieties or gate-keeper concepts, these multifunctional MSNs hold promise as target-specific multimodal imaging or theragnosis. Recently Gd_2O_3:Yb/Er assembled mesoporous MCM-41 nanocomposites was reported for NIR light triggered doxorubicin release.[138] Gold nanocrystals were integrated with the amino group functionalized nanocomposites in order to induce a wavelength-dependent enhancement of the up-conversion intensities. Particularly, under 980 nm NIR laser irradiation, the green up-conversion emission overlaps the surface plasmon resonance (SPR) band of gold nanocrystals, which causes a photothermal effect of gold nanocrystals and induces a rapid DOX release from the Au hybrid materials.

The above discussion demonstrated the mesoporous silica based multifunctional nanoparticles have significant advantages in biomedical application over traditional small molecule imaging or therapeutic agents. The exciting findings demonstrated not only their drug delivery capacity, but also effective cell-specific targeting, enhanced contrast imaging, and stimuli-controlled drug release behavior.

6.5. Objective of the present work

Despite the significant efforts in developing mesoporous silica based nanotheranostics, there still remains considerable challenge for their successful clinical implication. For instance, the preservation of individual functional properties like magnetic and fluorescent of each integrated moiety during the development of multifunctional nanoparticle is an important factor which influences the efficiency of these multifunctional nanoparticles in diagnostic applications. Apart from this, one of the

major challenges involves the administration of sparingly soluble or hydrophobic drugs. To overcome the solubility issue, many hydrophilic drug conjugates and carrier molecules are introduced. However the lack of potent activity and stability in the hydrophobic form limit their applications. Another challenge involves. Addressing the existing lacunas associated with the development of mesoporous multifunctional nanoparticle, the current research effort involves the development of new water dispersible multifunctional mesoporous silica based luminescent magnetic material through an easy method involving cheap and easily available starting materials for multimodal cancer-specific imaging and therapy. The objectives of the present work are as follows:

- Development of simple inexpensive chemical route for the synthesis of mesoporous silica based magnetic luminescent hybrid nanoparticles with optimum luminescent and magnetic property.
- Incorporation of highly luminescent biocompatible carbon quantum dot alternative to more toxic metal-based semiconductor quantum dots (QDs) for optical imaging.
- Modification of the synthesized multifunctional nanoparticle surface with various ligands to achieve high colloidal stability in physiological environment.
- To regulate the loading and stimuli responsive control release of the drug while keeping the therapeutic activity intact.
- Evaluation of developed drug loaded multifunctional nanoparticles for cancer-cell specific multimodal imaging and drug delivery.

In line with this approach in the present thesis, mesoporous silica coated magnetite core-shell nanoparticles with incorporated luminescent nanoagent have been synthesized. To circumvent the drawbacks associated with dyes and/or semiconductor QDs, new age luminescent inorganic materials such as rare-earth and carbon quantum dot (CD) have been used for luminescence functionalization. In order to facilitate cancer-specific therapy the nanocomposites have been decorated with folic acid targeting ligand. The hydrophobic chemotherapeutic drugs have been loaded using suitable strategy. The developed fluorescent magnetic nanotheranostics have been extensively characterized

using modern spectroscopic techniques and their diagnostic as well as therapeutic potential (fluorescence imaging, MR Imaging and drug delivery) has been evaluated in vitro. The full details of our research effort have been described in subsequent chapters.

6.6. References

1. J. Yao, M.Yang, Y. Duan, *Chem. Rev.*, 2014, **114**, 6130-6178.
2. H. Wang, F. Ke, A. Mararenko, Z. Wei, P. Banerjee, S. Zhou, *Nanoscale*, 2014, **6**, 7443-7452.
3. L. H. Reddy, J. L. Arias, J. Nicolas, P. Couvreur, *Chem. Rev.*, 2012, **112**, 5818-5878.
4. M. Mahmood, D. Casciano, Y. Xu, A. S. Biris, *J. Appl. Toxic.*, 2012, **32**, 10-19.
5. V. Biju, *Chem. Soc. Rev.*, 2014, **43**, 744-764.
6. G. Chen, H. Qiu, P. N. Prasad, X. Chen, *Chem. Rev.*, 2014, **114**, 5161-5214.
7. N. L. Rosi, C. A. Mirkin, *Chem. Rev.*, 2005, **105**, 1547-1562.
8. K. Saha, S. S. Agasti, C. Kim, X. Li, V. M. Rotello, *Chem. Rev.*, 2012, **112**, 2739-2779.
9. W. Zheng, P. Huang, D. Tu, E. Ma, H. Zhu, X. Chen, *Chem. Soc. Rev.*, 2015, DOI: 10.1039/C4CS00178H.
10. X. Sun, Y. Zhao, V. S. Y. Lin, I. I. Slowing, B. G. Trewyn, *J. Am. Chem. Soc.*, 2011, **133**, 18554-18557.
11. J. Kim, B. C. Kim, D. L. Ferrer, K. Petritis, R. D. Smith, *Proteomics*, 2010, **10**, 687-699.
12. F. Tang, L. Li, D. Chen, *Adv. Mater.*, 2012, **24**, 1504-1534.
13. J. Shi, A. R. Votruba, O. C. Farokhzad, R. Langer, *Nano Lett.*, 2010, **10**, 3223-3230.
14. J. L. Vivero-Escoto, I. I. Slowing, B. G. Trewyn, V. S. Y. Lin, *Small*, 2010, **6**, 1952-1967.
15. G. Braun, S. J. Lee, M. Dante, T. Q. Nguyen, M. Moskovits, N. Reich, *J. Am. Chem. Soc.*, 2007, **129**, 6378-6379.

16. H. Gu, P. L. Ho, K. W. T. Tsang, L. Wang, B. Xu, *J. Am. Chem. Soc.*, 2003, **125**, 15702-15703.
17. F. Peng, Y. Su, Y. Zhong, C. Fan, S. T. Lee, Y. He, *Acc. Chem. Res.*, 2014, **47**, 612-623.
18. C. Corot, P. Robert, J.M. Idée, M. Port, *Adv. Drug Deliv. Rev.*, 2006, **58**, 1471-1504.
19. U. Boas, P. M. Heegaard, *Chem. Soc. Rev.*, 2004, **33**, 43-63.
20. J. E. Rosen, L. Chan, D. B. Shieh, F. X. Gu, *Nano-medicine*, 2012, **8**, 275-290.
21. N. Lee, T. Hyeon, *Chem. Soc. Rev.*, 2012, **41**, 2575-2589.
22. M. H. Mendonca Dias, P. C. Lauterbur, *Magn. Reson. Med.*, 1986, **3**, 328-330.
23. R. C. Semelka, T. K. Helmberger, *Radiology*, 2001, **218**, 27-38.
24. O. Clement, N. Siauve, C. A. Cuenod, G. Frija, *Magn. Reson. Imaging*, 1998, **9**, 167-182.
25. J. H. Lee, Y. M. Huh, Y. W. Jun, J. W. Seo, J. T. Jang, H. T. Song, S. Kim, E. J. Cho, H. G. Yoon, J. S. Suh, J. Cheonet, *Nat. Med.*, 2007, **13**, 95-99.
26. J. H. Park, G. Maltzahn, L. Zhang, M. P. Schwartz, E. Ruoslahti, S. N. Bhatia, M. J. Sailor, *Adv. Mater.*, 2008, **20**, 1630-1635.
27. M. Zhao, D. A. Beauregard, L. Loizou, B. Davletov, K. M. Brindle, *Nat. Med.*, 2001, **7**, 1241-44.
28. K. Fan, C. Cao, Y. Pan, D. Lu, D. Yang, J. Feng, L. Song, M. Liang, X. Yan, *Nat. Nanotechnol.*, 2012, **7**, 459-464.
29. M. Nahrendorf, F. A. Jaffer, K. A. Kelly, D. E. Sosnovik, E. Aikawa, P. Libby, R. Weissleder, *Circulation*, 2006, **114**, 1504-1511.
30. C. W. Kessinger, O. Togao, C. Khemtong, G. Huang, M. Takahashi, J. Gao, *Theranostics*, 2011, **1**, 263-273.
31. M. Lewin, N. Carlesso, C. H. Tung, X. W. Tang, D. Cory, D. T. Scadden, R. Weissleder, *Nat. Biotechnol.*, 2000, **18**, 410-141.
32. M. S. Thu, L. H. Bryant, T. Coppola, E. K. Jordan, M. D. Budde, B. K. Lewis, A. Chaudhry, J. Ren, N. R. S. Varma, A. S. Arbab, J. A Franket, *Nat. Med.*, 2012, **18**, 463-467.

33. B. P. Barnett, A. Arepally, P. V. Karmarkar, D. Qian, W. D. Gilson, P. Walczak, V. Howland, L. Lawler, C. Lauzon, M. Stuber, D. L. Kraitchman, J. W. *Nat. Med.*, 2007, **13**, 986-991.
34. P. Zrazhevskiy, M. Senaw, X. Gao, *Chem. Soc. Rev.*, 2010, **39**, 4326-4354.
35. P. Wu, X. P. Yan, *Chem. Soc. Rev.*, 2013, **42**, 5489-5521.
36. M. Yu, F. Li, Z. Chen, H. Hu, C. Zhan, H. Yang, C. Huang, *Anal. Chem.*, 2009, **81**, 930-935.
37. L. Cheng, C. Wang, Z. Liu, *Nanoscale*, 2013, **5**, 23-37.
38. J. A. Damasco, G. Chen, W. Shao, H. Agren, H. Huang, W. Song, J. F. Lovell, P. N. Prasad, *ACS Appl. Mater. Interfaces*, 2014, **6**, 13884-13893.
39. X. Wu, T. Ming, X. Wang, P. Wang, J. Wang, J. Chen, *ACS Nano*, 2010, **4**, 113-120.
40. E. I. Altınoglu, T. J. Russin, J. M. Kaiser, B. M. Barth, P. C. Eklund, M. Kester, J. H. Adair, *ACS Nano*, 2008, **2**, 2075-2084.
41. A. M. Smith, X. Gao, S. Nie, *Photochem. Photobiol.*, 2004, **80**, 377-385.
42. X. Gao, Y. Cui, R. M. Levenson, L. W. K. Chung, S. Nie, *Nat. Biotechnol.*, 2004, **22**, 969-976.
43. M. Nyk, R. Kumar, T. Y. Ohulchanskyy, E. J. Bergey, P. N. Prasad, *Nano Lett.*, 2008, **8**, 3834-3838.
44. A. Xia, M. Chen, Y. Gao, D. M. Wu, W. Feng, F. Y. Li, *Biomaterials*, 2012, **33**, 5394-5405.
45. P. G. Luo, S. Sahu, S. T. Yang, S. K. Sonkar, J. Wang, H. Wang, G. E. L. Croy, L. Cao, Y. P. Sun, *J. Mater. Chem. B*, 2013, **1**, 2116-2127.
46. Y. Wang, A. Hu, *J. Mater. Chem. C*, 2014, **2**, 6921-6939.
47. S. Sahu, B. Behera, T. K. Maiti, S. Mohapatra, *Chem. Commun.*, 2012, **48**, 8835-8837.
48. B. Chen, F. Li, S. Li, W. Weng, H. Guo, T. Guo, X. Zhang, Y. Chen, T. Huang, X. Hong, S. You, Y. Lin, K. Zeng and S. Chen, *Nanoscale*, 2013, **5**, 1967-1971.
49. K. Qu, J. Wang, J. Ren, X. Qu, *Chem. Eur. J.*, 2013, **19**, 7243-7249.
50. B. Han, W. Wang, H. Wu, F. Fang, N. Wang, X. Zhang, S. Xu, *Colloids Surf., B*, 2012, **100**, 209-214.

51. C. H. Lee, R. Rajendran, M. S. Jeong, H. Y. Ko, J. Y. Joo, S. Cho, Y. W. Chang, S. Kim, *Chem. Commun.*, 2013, **49**, 6543-6545.
52. B. Kong, A. Zhu, C. Ding, X. Zhao, B. Li, Y. Tian, *Adv. Mater.*, 2012, **24**, 5844-5848.
53. P.G. Luo, F. Yang, S. T. Yang, S. K. Sonkar, L. Yang, J. J. Broglie, Y. Liu, Y. P. Sun, *RSC Adv.*, 2014, **4**, 10791-10807.
54. X. Huang, F. Zhang, L. Zhu, K. Y. Choi, N. Guo, J. Guo, K. N. Tackett, P. Anilkumar, G. Liu, Q. Quan, H. S. Choi, G. Niu, Y. P. Sun, S. Lee, X. Chen, *ACS Nano*, 2013, **7**, 5684-5693.
55. P. Huang, J. Lin, X. Wang, Z. Wang, C. Zhang, M. He, K. Wang, F. Chen, Z. Li, G. Shen, D. Cui, X. Chen, *Adv. Mater.*, 2012, **24**, 5104-5110.
56. L. Cao, S. T. Yang, X. Wang, P. G. Luo, H. H. Liu, S. Sahu, Y. Liu, Y. P. Sun, *Theranostics*, 2012, **2**, 295-301.
57. H. Tao, K. Yang, Z. Ma, J. Wan, Y. Zhang, Z. Kang, Z. Liu, *Small*, 2012, **8**, 281-290.
58. H. Y. Ko, Y. W. Chang, G. Paramasivam, M. S. Jeong, S. Cho, S. Kim, *Chem. Commun.*, 2013, **49**, 10290-10292.
59. H. Meng, M. Xue, T. Xia, Z. X. Ji, D. Y. Tarn, J. I. Zink, A. E. Nel, *ACS Nano*, 2011, **5**, 4131-4144.
60. J. E. Lee, N. Lee, H. Kim, J. Kim, S. H. Choi, J. H. Kim, T. Kim, I. C. Song, S. P. Park, W. K. Moon, T. Hyeon, *J. Am. Chem. Soc.*, 2010, **132**, 552-557.
61. H. Maeda, J. Wu, T. Sawa, Y. Matsumura, K. Hori, *J. Control. Release*, 2000, **65**, 271-284.
62. M. M. Gottesman, T. Fojo, S. E. Bates, *Nat. Rev. Cancer*, 2002, **2**, 48-58.
63. L. Ao, B. Wang, P. Liu, L. Huang, C. Yue, D. Gao, C. Wu, W. Su, *Nanoscale*, 2014, **6**, 10710-10716.
64. E. J. Goh, K. S. Kim, Y. R. Kim, H. S. Jung, S. Beack, W. H. Kong, G. Scarcelli, S. H. Yun, S. K. Hahn, *Biomacromolecules*, 2012, **13**, 2554-2561.
65. M. P. Melancon, M. Zhou, R. Zhang, C. Xiong, P. Allen, X. Wen, Q. Huang, M. Wallace, J. N. Myers, R. J. Stafford, D. Liang, A. D. Ellington, C. Li, *ACS Nano*,2014, **8**, 4530-4538.

66. F. Fay, C. Scott, *J. Immunother.*, 2011, **3**, 381-94.
67. Y. Wang, K. Wang, R. Zhang, X. Liu, X. Yan, J. Wang, E. Wagner, R. Huang, *ACS Nano*, 2014, **8**, 7870-7879.
68. F. Chen, H. Hong, S. Shi, S. Goel, H. F. Valdovinos, R. Hernandez, C. P. Theuer, T. E. Barnhart, W. Cai, *Nature Scientific Report*, 2014, DOI: 10.1038/srep05080.
69. W. Xia, P. S. Low, *J. Med. Chem.,* 2010, **53**, 6811-6824.
70. A. R. Hilgenbrink, P. S. Low, *J. Pharm. Sci.*, 2005, **94**, 2135-2146.
71. S. Mohapatra, S. R. Rout, S. Maiti, T. K. Maiti, A. B. Panda, *J. Mater. Chem.*, 2011, **21**, 9185-9193.
72. J. Lu, W. Zhao, Y. Huang, H. Liu, R. Marquez, R. B. Gibbs, J. Li, R. Venkataramanan, L. Xu, S. Li, S. Li, *Mol. Pharmaceutics*, 2014, **11**, 4164-4178.
73. K. J. Widder, A. E. Senyei, D. F. Ranney, *Adv. Pharmacol. Chemother.*, 1979, **16**, 213-271.
74. B. Chertok1, B. A. Moffat, A. E. David, F. Yu, C. Bergemann, B. D. Ross, V. C. Yang, *Biomaterials*, 2008, **29**, 487-496.
75. T. K. Jain, J. Richey, M. Strand, D. L. Leslie-Pelecky, C. A. Flask, V. Labhasetwar, *Biomaterials*, 2008, **29**, 4012-4021.
76. H. Nobuto, T. Sugita, T. Kubo, S. Shimose, Y. Yasunaga, T. Murakami, M. Ochi, *Int. J. Cancer*, 2004, **109**, 627-635.
77. F. Jia, X. Liu, L. Li, S. Mallapragada, B. Narasimhan, Q. Wang, *J. Control. Release*, 2013, **172**, 1020-1034.
78. Y. Cheng, R. A. Morshed, B. Auffinger, A. L. Tobias, M. S. Lesniak, *Adv. Drug Deliver. Rev.*, 2014, **66**, 42-57.
79. J. Kim, Y. Piao, T. Hyeon, *Chem. Soc. Rev.*, 2009, **38**, 372-390.
80. D. E. Lee, H. Koo, I. C. Sun, J. H. Ryu, K. Kim, I. C. Kwon, *Chem. Soc. Rev.*, 2012, **41**, 2656-2672.
81. K. Yan, P. Li, H. Zhu, Y. Zhou, J. Ding, J. Shen, Z. Li, Z. Xu, P. K. Chu, *RSC Adv.*, 2013, **3**, 10598-10618.
82. G. Bao, S. Mitragotri, S. Tong, *Annu. Rev. Biomed. Eng.*, 2013, **15**, 253-282.
83. J. Cheon, J. H. Lee, *Acc. Chem. Res.*, 2008, **41**, 1630-1640.

84. M. Liong, J. Lu, M. Kovochich, T. Xia, S. G. Ruehm, A. E. Nel, F. Tamanoi, J. I. Zink, *ACS Nano*, 2008, **2**, 889-896.

85. W. X. Mai, H. Meng, *Integr. Biol.,* 2013, **5**, 19-28.

86. M. Liong, S. Angelos, E. Choi, K. Patel, J. F. Stoddart, J. I. Zink, *J. Mater. Chem.,* 2009, **19**, 6251-6257.

87. J. E. Lee, N. Lee, T. Kim, J. Kim, T. Hyeon, *Acc. Chem. Res.,* 2011, **44**, 893-902.

88. C. Argyo, V. Weiss, C. Bräuchle, T. Bein, *Chem. Mater.,* 2014, **26**, 435-451.

89. I. I. Slowing, B. G. Trewyn, S. Giri, V. S. Y. Lin, *Adv. Funct. Mater.,* 2007, **17**, 1225-1236.

90. J. Liu, C. Li, F. Li, *J. Mater. Chem.,* 2011, **21**, 7175-7181.

91. A. Popat, S. B. Hartono, F. Stahr, J. Liu, S. Z. Qiao, G. Q. Lu, *Nanoscale,* 2011, **3**, 2801-2818.

92. K. Ariga, Q. Ji, T. Mori, M. Naito, Y. Yamauchi, H. Abe, J. P. Hill, *Chem. Soc. Rev.,* 2013, **42**, 6322-6345.

93. A. J. Salinas, P. Esbrit, M. Vallet-Regi, *Biomater. Sci.,* 2013, **1**, 40-51.

94. Z. Li, J. C. Barnes, A. Bosoy, J. F. Stoddart, J. I. Zink, *Chem. Soc. Rev.,* 2012, **41**, 2590-2605.

95. A. G. Martinez, J. P. Juste, L. M. L. Marzan, *Adv. Mater.,* 2010, **22**, 1182-1195.

96. J. Park, J. Joo, S. G. Kwon, Y. Jang, T. Hyeon, *Angew. Chem. Int. Ed.,* 2007, **46**, 4630-4660.

97. J. Kim, J. E. Lee, J. Lee, J. H. Yu, B. C. Kim, K. An, Y. Hwang, C. H. Shin, J. G. Park, J. Kim, T. Hyeon, *J. Am. Chem. Soc.,* 2006, **128**, 688-689.

98. J. Kim, H. Kim, N. Lee, T. Kim, H. Kim, T. Yu, I. Song, W. Moon, T. Hyeon, *Angew. Chem. Int. Ed.,* 2008, **47**, 8438-8441.

99. C. Wu, Q. H. Xu, *Langmuir*, 2009, **25**, 9441-9446.

100. G. Yang, S. Gai, F. Qu, P. Yang, *ACS Appl. Mater. Interfaces*, 2013, **5**, 5788-5796.

101. Z. Zhang, L. Wang, J. Wang, X. Jiang, X. Li, Z. Hu, Y. Ji, X. Wu,C. Chen, *Adv. Mater.,* 2012, **24**, 1418-1423.

102. H. S. Qian, H. C. Guo, P. C. Ho, R. Mahendran, Y. Zhang, *Small*, 2009, **5**, 2285-2290.

103. C. Park, K. Oh, S. C. Lee, C. Kim, *Angew. Chem. Int. Ed.*, 2007, **46**, 1455-1457.

104. Y. S. Lin, C. P. Tsai, H. Y. Huang, C. T. Kuo, Y. Hung, D. M. Huang, Y. C. Chen, C. Y. Mou, *Chem. Mater.*, 2005, **17**, 4570-4573.

105. X. L. Huang, L. L. Li, T. L. Liu, N. J. Hao, H. Y. Liu, D. Chen, F. Q. Tang, *ACS Nano*, 2011, **5**, 5390-5399.

106. J. M. Rosenholm, M. Linden, *J. Control. Release*, 2008, **128**, 157-164.

107. Q. Yang, S. Wang, P. Fan, L. Wang, Y. Di, K. Lin, F. S. Xiao, *Chem. Mater.*, 2005, **17**, 5999-6003.

108. T. Xia, M. Kovochich, M. Liong, H. Meng, S. Kabehie, J. I. Zink, A. E. Nel, *ACS Nano*, 2009, **3**, 3273-3286.

109. S. Wang, P. S. Low, *J. Control. Release*, 1998, **53**, 39-48.

110. S. Santra, B. Liesenfeld, D. Dutta, D. Chatel, C. D. Batich, W. Tan, B. M. Moudgil, R. A. Mericle, *J. Nanosci. Nanotechnol.*, 2005, **5**, 899-904.

111. R. Tapec, X. J. J. Zhao, W. H. Tan, *J. Nanosci. Nanotechnol.*, 2002, **2**, 405-409.

112. S. Santra, P. Zhang, K. M. Wang, R. Tapec, W. H. Tan, *Anal. Chem.*, 2001, **73**, 4988-4993.

113. V. Cauda, A. Schlossbauer, J. Kecht, A. Zurner, T. Bein, *J. Am. Chem. Soc.*, 2009, **131**, 11361-1370.

114. J. Kecht, A. Schlossbauer, T. Bein, *Chem. Mater.*, 2008, **20**, 7207-7214.

115. D. R. Radu, C. Y. Lai, K. Jeftinija, E. W. Rowe, S. Jeftinija, V. S. Y. Lin, *J. Am. Chem. Soc.*, 2004, **126**, 13216-13217.

116. S. H. Cheng, C. H. Lee, M. C. Chen, J. S. Souris, F. G. Tseng, C. S. Yang, C. Y. Mou, C. T. Chen, L. W. Lo, *J. Mater. Chem.*, 2010, **20**, 6149-6157.

117. X. Qian, W. Wang, W. Kong, Y. Chen, *J. Nanomaterials*, 2014, Article ID 972475.

118. C. Li, Z. Hou, Y. Dai, D. Yang, Z. Cheng, P. Ma, J. Lin, *Biomater. Sci.*, 2013, 1, 213-223.

119. C. Li, D. Yang, P. Ma, Y. Chen, Y. Wu, Z. Hou, Y. Dai, J. Zhao, C. Sui, J. Lin, *Small*, 2013, **9**, 4150-4159.

120. W. Fan, B. Shen, W. Bua, F. Chen, Q. He, K. Zhao , S. Zhang , L. Zhou, W. Peng , Q. Xiao, D. Ni, J. Liu, J. Shi, *Biomaterials*, 2014, **35**, 8992-9002.

121. J. Wang, P. P. Gao, X. X. Yang, T. T. Wang, J. Wang, C. Z. Huang, *J. Mater. Chem. B*, 2014, **2**, 4379-4386.

122. X. L. Li, N. Hao, H. Y. Chen, J. J. Xu, *Anal. Chem.*, 2014, **86**, 10239-10245

123. D. Zhang, A. Gao, Y. Xu, X. B. Yin, X. W. He, Y. K. Zhang, *Analyst*, 2014, **139**, 4613-4619.

124. S. Chen, Y. Yang, H. Li, X. Zhou, M. Liu, *Chem. Commun.*, 2014, **50**, 283-285.

125. M. W. Ambrogio, C. R. Thomas, Y. L. Zhao, J. I. Zink, J. F. Stoddart, *Acc. Chem. Res.*, 2011, **44**, 903-913.

126. M. Colilla, B. Gonzalez, M. Vallet-Regi, *Biomater. Sci.*, 2013, **1**, 114-134.

127. C. X. Zhao, L. Yu, A. P. J. Middelberg, *J. Mater. Chem. B*, 2013, **1**, 4828-4833.

128. X. Ma, Y. Zhao, K. W. Ng, Y. Zhao, *Chem. Eur. J.*, 2013, **19**, 15593-15603.

129. B. Sahoo, K. S. P. Devi, S. Dutta, T. K. Maiti, P. Pramanik, D. Dhara, *J. Colloid Interf. Sci.*, 2014, **431**, 31-41.

130. S. Mohapatra, S. R. Rout, R. Narayan, T. K. Maiti, *Dalton Trans.*, 2014, **43**, 15841-15850.

131. R. Liu, Y. Zhang, X. Zhao, A. Agarwal, L. J. Mueller, P. Feng, *J. Am. Chem. Soc.*, 2010, **132**, 1500-1501.

132. C. L. Zhu, C. H. Lu, X. Y. Song, H. H. Yang, X. R. Wang, *J. Am. Chem. Soc.*, 2011, **133**, 1278-1281.

133. C. Y. Lai, B. G. Trewyn, D. M. Jeftinija, K. Jeftinija, S. Xu, S. Jeftinija, V. S.Y. Lin, *J. Am. Chem. Soc.*, 2003, **125**, 4451-4459.

134. S. Giri, B. G. Trewyn, M. P. Stellmaker, V. S.Y. Lin, *Angew. Chem. Int. Ed.*, 2005, **44**, 5038-5044.

135. J. Kim, J. E. Lee, J. Lee, Y. Jang, S. W. Kim, K. An, J. H. Yu, T. Hyeon, *Angew. Chem. Int. Ed.*, 2006, **45**, 4789-4793.

136. J. E. Lee, N. Lee, H. Kim, J. Kim, S. H. Choi, J. H. Kim, T. Kim, I. Song, S. P. Park, W. Moon, T. Hyeon, *J. Am. Chem. Soc.*, 2010, **132**, 552-557.

137. N. Niu, F. He, P. Ma, S. Gai, G. Yang, F. Qu, Y. Wang, J. Xu, P. Yang, *ACS Appl. Mater. Interfaces*, 2014, **6**, 3250-3262.

Chapter-7

Terbium doped yttrium phosphate based multifunctional magnetic fluorescent hybrid nanoparticles as carriers for hydrophobic anticancer drug 5-fluorouracil

7.1. Introduction

Recently, rare earth-doped nanoparticles have attracted great attention for use as luminescent biolabels owing to their excellent luminescence properties, including large Stokes shifts, narrow line-width emission bands, high quantum yields, long lifetimes and superior photostability.[1-4] Their luminescence properties in most cases are due to forbidden f-f electron configuration transitions (except for $Ce^{3+}$and Eu^{2+} involving d-electrons). As these low-lying energy levels are well isolated from the environment, their optical properties are rarely affected by surface modification, nature of host material and the nanoparticle size. The unique luminescence properties of rare earth based nanoparticles provide tremendous advantages over conventional fluorophores for biomedical applications. These advantages includes (1) enhanced penetration depth into biological samples,[5] (2) very low auto-fluorescence from surrounding tissues,[6] (3) decreased photo-damage to the biological specimens,[7] (4) non-photobleaching, non-photoblinking and high spatial resolution during bioimaging [8,9] and (5) low cytotoxic to a broad range of cell lines.[10,11] Moreover, the high magnetic moment of certain ions, like Gd^{3+}, under magnetic field renders them potent contrast agents for magnetic resonance imaging (MRI).[12] Therefore the rare earth doped nanoparticle have attracted reviving interest for their biomedical applications in areas as diverse as biodetection,[13] bioimaging,[14] drug delivery,[15] photodynamic therapy (PDT),[16] photothermal therapy (PTT),[17] and disease theranostics.[18] Till date much progress have been accomplished in the structure/morphology control, functionalization design, and optical performance optimization of these rare earth based nanomaterials for versatile biomedical applications, as summarized in many recent reviews and book chapters.[19-22]

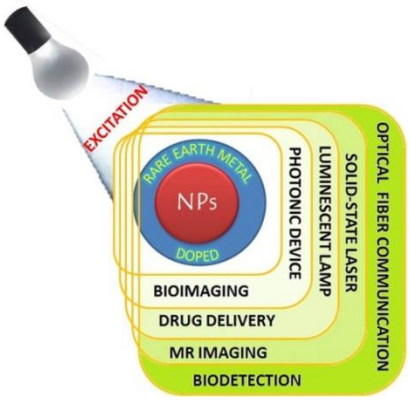

Figure 7.1 Application of rare earth doped nanoparticle

Being a potential luminophore, rare earth doped nanoparticle has been integrated with magnetic nanoparticles to prepare multifunctional magnetic/luminescent composites including γ-Fe_2O_3/$NaYF_4$:Y,Er nanoparticles,[23] Co:Nd:Fe_2O_3/Gd_2O_3:Eu core-shell particles,[24] Tb-doped γ-Fe_2O_3 nanocrystals,[25] Fe_3O_4@Y_2O_3:Eu nanocomposites,[26] $LaPO_4$:Ce^{3+},Tb^{3+}coated Fe_3O_4 koosh nanoballs,[27] Fe_3O_4@YPO_4:Tb,Eu hybrid sphere.[28] However, the fluorescence quenching effect of magnetite limits the potential applications of these integrated structures in several areas. In order to overcome, an inert silica layer was introduced that can effectively separate lanthanide based luminescent component from the magnetite. Till date, there are few reports on the synthesis of rare earth based luminescent magnetic with inert silica layer. Li *et al.* reported the synthesis of bifunctional magnetic-luminescent Fe_3O_4@SiO_2/Y_2O_3:Tb nanocomposite by assembling Y_2O_3:Tb nanorods onto the surface of Fe_3O_4@SiO_2 core-shell nanostructures.[29] Lin and his co-worker have prepared a magnetic luminescent and mesoporous core shell structured nanocomposite (Fe_3O_4@nSiO_2@mSiO_2@YVO_4:Eu^{3+}) as carrier for ibuprofen (IBU).[30] Some other reported examples include Fe_3O_4/SiO_2/YVO_4:Eu^{3+} magnetic/luminescent nanocomposites,[31] Fe_3O_4@LaF_3:Ce^{3+},Tb^{3+} bifunctional nanocomposites.[32] While few scenarios can also be envisaged for applications of such novel and complex integrated materials in life sciences, their practical applications are still in their infancy.

On the other hand, 5-Fluorouracil (5-FU) is a widely used chemotherapy drug for treatment of a broad variety of solid tumors including pancreas, ovary, liver, brain, breast and gastrointestinal cancers, alone or in combination with chemotherapy regimens.[33-36] The mode of action of 5-FU has been ascribed to the misincorporation of fluoronucleotides into RNA and DNA and to the inhibition of the nucleotide synthetic enzyme thymidylate synthase (TS).[37] 5-FU when locally injected is rapidly absorbed through the blood capillaries into systemic circulation. This results in relatively low levels of drug near the site of action with the subsequent loss of efficacy and increased risk of systemic toxicity.[38,39] Additionally, the limited aqueous solubility restricts the use of 5-FU.[40] Selective delivery of chemotherapeutic agents to the disease site represents a major challenge for improving current chemotherapy outcome.[41] Targeted delivery of the drug is an emerging therapy strategy gifted with disease-targeting functions and carrying

cytotoxic components by enabling the specific delivery of chemotherapeutic agents to aberrant tissues, thereby increasing their local efficacy while limiting their peripheral toxicity.

In this chapter, we have addressed these issues with the development of fluorescent magnetic nanoparticles based nanoformulation for the site specific delivery of 5-FU. The versatile scope of biofunctionalisation, established biocompatibility of phosphate moiety and utility of yttrium or phosphorous element for radiotherapy of cancers inspired us to fabricate yttrium phosphate based magnetic fluorescent nanocomposites. For this purpose we have prepared luminescent Fe_3O_4@mesoporous silica-YPO_4:Tb nanoparticles with Fe_3O_4 as the core and Tb^{3+}-doped yttrium phosphate incorporated mesoporous silica as the shell. These fluorescent magnetic nanoparticles have been decorated with folate and β-cyclodextrin using glutathione as a linker in order to facilitate hydrophobic anti-cancer drug 5-FU storage as well as delivery. The synthesized material has been characterized by X-ray diffraction, FTIR, DLS, TEM, SEM, BET, fluorescence spectrophotometry, vibration sample magnetometry. The cytotoxicity of the drug carrier as well as drug release profile has also been investigated.

7.2. Experimental

Chemicals

Thionyl chloride, β-cyclodextrin, $(NH_4)_2HPO_4$, triethyl amine, ethanol, ethyl acetate, acetone and chloroform were obtained from Merck, India. Benzyl ether, Cetyltrimethylammonium bromide (CTAB), 5-Fluorouracil (5-FU), $Fe(acac)_3$, Glutathione (GSH), 3-glycidoxypropyltrimethoxysilane (GTPS), oleic acid, oleylamine, tetraethyl orthosilicate (TEOS), $Tb(NO_3)_3.5H_2O$, $Y(NO_3)_3.6H_2O$, 2,2'-(ethylenedioxy)-bis-(ethylamine) (EDBE), 2-carboxyethyl phosphonic acid (CEPA), folic acid (FA), di-tert-butyldicarbonate (BoC_2O), dicyclohexyl carbodiimide (DCC) and N-hydroxy succinimide (NHS) were purchased from Sigma Aldrich, USA. Commercially available dioxane and toluene were purified by distillation over sodium metal with benzophenone. Prior to use, dimethylsulfoxide (DMSO) was vacuum distilled. Pyridine was purified by distillation over KOH.

Preparation of monodisperse hydrophobic Fe_3O_4 nanoparticle

Hydrophobic Fe_3O_4 nanoparticles were synthesized by a high-temperature solution-phase reactions of iron acetylacetonate with 1,2-hexadecanediol in the presence of oleic acid and oleylamine.[42] In a typical procedure the mixture of $Fe(acac)_3$ (706 mg, 2 mmol), 1,2-dodecanediol (2.023 g, 10 mmol), oleic acid (1.9 mL, 6 mmol), oleylamine (1.97 mL, 6 mmol) and benzyl ether were heated to reflux (300 °C) under nitrogen atmosphere for 1 h. Then as-synthesized mixture was allowed to cool to room temperature and Fe_3O_4 nanoparticles were precipitated by adding ethanol. The precipitate was collected by centrifugation at a speed of 10000 rpm for 10 minutes.

Synthesis of mesoporous silica coated magnetite nanoparticle Fe_3O_4@m-SiO_2

Mesoporous silica coating on Fe_3O_4 nanoparticle was carried out by modified Stöber's method using CTAB as a template, where CTAB serves as the stabilizing surfactant for the transfer of hydrophobic Fe_3O_4 nanocrystals to the aqueous phase.[43] In a typical procedure, 350 mg of oleic acid stabilized monodisperse magnetite nanoparticles dispersed in 30 mL of chloroform was added to a 100 mL of aqueous CTAB (2 g) solution and the resulting solution was stirred vigorously for 30 min. The formation of an oil-in-water microemulsion resulted in a turbid brown solution. Heating the brown solution at 60 °C for 20 min induced evaporation of the chloroform, this generated aqueous dispersion of nanoparticles. The resulting mixture solution was added to a mixture of 200 mL of water and 5 mL of 2M NaOH solution and heated upto 70 °C. Then TEOS (3 mL) and ethyl acetate (10 mL, 0.1 M) were successively added to the diluted aqueous solution containing the magnetite nanoparticles. The resulting mixture was stirred for 3 h and the precipitate was magnetically separated (DynaMag2, Invitrogen), and thoroughly washed with ethanol to remove unreacted species and surfactant, then dried at 60 °C in an oven for overnight.

Synthesis of Fe_3O_4@m-SiO_2@YPO_4:Tb^{3+} composite nanoparticle

To deposit YPO_4:Tb on the mesoporous silica surface of Fe_3O_4@m-SiO_2 core-shell nanostructures, aqueous solution of $Y(NO_3)_3.6H_2O$ (0.383 g, 1 mmol) and $Tb(NO_3)_3.5H_2O$ (0.087 g, 0.2 mM) were added to 50 mL of dispersed Fe_3O_4@m-SiO_2 (0.4 g) nanoparticles and stirred for 2 h. To the above mixture solution $(NH_4)_2HPO_4$ was added under vigorous stirring and continued stirring for another 3 h. Finally particles

were separated, thoroughly washed and oven dried on air at 60 °C for overnight. The doping concentration of Tb^{3+} was 20 mol% of Y^{3+} in YPO_4.

Synthesis of epoxide functionalized Fe_3O_4@m-SiO_2@YPO_4:Tb^{3+} nanoparticle

To modify the surface with epoxide, about 0.3 g of Fe_3O_4@m-SiO_2@YPO_4:Tb^{3+} particles were added to 30 mL of dry toluene with 0.1 mL (0.44 mmol) of 3-glycidoxypropyltrimethoxysilane (GPTS) under N_2 atmosphere and refluxed for 24 h. After the reaction, the functionalized particles were magnetically separated, washed extensively with acetone, and dried in vaccum.

Synthesis of glutathione (GSH) conjugated β-cyclodextrin (GSH-cyclodextrin)

To the stirred solution of GSH (200 mg, 0.65 mmol) in dioxane (10 mL), thionyl chloride (0.48 mL, 6.5 mmol) was added dropwise at room temperature. Then it was allowed to reflux for 24 h under nitrogen atmosphere followed by complete removal of the solvent under vacuum below 60 °C. Then to it, β-cyclodextrin (740 mg, 0.65 mmol) in dioxane (10 mL) and triethyl amine (0.4 mL) was added, and allowed to reflux for another 24 h under nitrogen atmosphere. After the reaction, dioxane was evaporated and the product (GSH-cyclodextrin, 465 mg, yield 51%) was extracted with ethanol.

Synthesis of cyclodextrin-modified folate decorated nanocarrier

To load 5-FU, the particles were conjugated with GSH-cyclodextrin by ring opening of epoxide ended nanoparticles. Typically, aqueous ethanolic solution of GSH-cyclodextrin (709 mg, 0.5 mmol) was added to epoxide functionalized Fe_3O_4@m-SiO_2@YPO_4:Tb^{3+} and the mixture were allowed to stir overnight at 60 °C. Then the particles were magnetically separated and washed with water. In order to facilitate receptor mediated endocytosis, the nanocarrier was further functionalized with folic acid. Prior to synthesis of folate decorated fluorescent magnetic nanoparticles, amine functionalized folic acid was prepared following the procedure reported by Mohapatra *et al.*.[44] For conjugation, amine functionalized folic acid (FA-NH_2) (285 mg, 0.5 mmol) dissolved in dimethyl sulfoxide was stirred overnight at 60 °C with aqueous dispersion of Fe_3O_4@m-SiO_2@YPO_4:Tb^{3+}@GSH-cyclodextrin. Finally folate decorated luminescent particles were magnetically separated and washed with water.

Loading and release of 5-FU

5-FU loading has been achieved by simple inclusion of hydrophobic drug onto the cyclodextrin-modified nanoparticle. Briefly, 40 mg nanoparticles was stirred with saturated solution of 5-FU (5mg/30 mL) at 60 °C for 72 h. Then the particles were recovered using magnetic separator, washed thoroughly with water and suspended in phosphate buffer. The release of 5-FU from the nanoparticles was investigated in the citrate phosphate buffer (at pH 7.0, 6.2, 5.2 and 3.2) at 37 °C. At specified time intervals, accumulated amount of drug released into the solution was quantified using a UV-vis spectrophotometer (λ_{max}(5-FU)=266 nm). The release profiles were plotted as the relative release percentages of 5-FU against time.

Calculation of drug loading capacity

The drug loading capacity was calculated as per the following method. First 5-FU was loaded onto the nanocarrier (β-cyclodextrin and FA-NH_2 decorated nanoparticle) as described above and then separated from the aqueous suspension medium using magnetic separator. The obtained drug-loaded nanocomposites were incubated at 60 °C in vacuum overnight and were weighted. Drug concentration in supernatant was analyzed by the ultraviolet absorption (λ_{max}(5-FU) = 266 nm), with reference to a calibration curve on a UV-Vis spectrophotometer. The measurements were performed in triplicate. Drug-loading content and encapsulation efficiency were obtained by equations 1 and 2, respectively.[45]

$$\text{Drug-loading content (\%)} = \frac{\text{Weight of the drug in nanoparticles}}{\text{weight of the nanoparticles}} \times 100 \ldots\ldots (\mathbf{1})$$

$$= \frac{4.58}{40} \times 100$$

$$= 11.45\%$$

$$\text{Encapsulation efficiency (\%)} = \frac{\text{Weight of the drug in nanoparticles}}{\text{Weight of the feeding drug}} \times 100 \ldots\ldots \quad (\mathbf{2})$$

$$= \frac{4.58}{5.0} \times 100 = 91.6\%$$

Cytotoxicity of the nanocarrier

The cytotoxicity of the nanocarrier was evaluated on Human cervical carcinoma (HeLa) and mouse fibroblasts (L929) cells. These cells were obtained from the National

Centre for Cell Sciences (Pune, India), cultivated in minimal essential medium (MEM) and Dulbecco's modified eagle medium (DMEM) respectively supplemented with 10% fetal calf serum, 100 units/mL penicillin, and 100 μg/mL streptomycin, 4 mM L-glutamine under 5% CO_2 and 95% humidified atmosphere at 37 °C. From 10^4 cells/mL cell suspension, 180 μL cell suspension was seeded into each well of 96 wells tissue culture plates and incubated for 18 h followed by addition of Fe_3O_4@m-SiO_2@YPO_4:Tb^{3+}@GSH-cyclodextrin@FA nanoparticles at concentrations 25, 50, 100 and 200 μg/mL. Following the incubation for 72 h at 37 °C in a humidified incubator (HERA cell) maintained with 5% CO_2. Thereafter, MTT (10 μL; 5 mg/mL) was added to each well and the plate was incubated for an additional 4 h at 37 °C under 5% CO_2. After the addition of 10% sodium dodecyl sulfate (SDS, 100 μL/well), the assay plate was allowed to stand at room temperature for 12 h. For each well, the optical density (OD) at 570 nm with back ground subtraction at 690 nm was recorded by means of microtiter plate reader. The following formula was used to calculate the inhibition of cell growth: Cell viability (%) = (mean of OD value of treatment group/mean OD value of control)×100.[46] All Experiments were performed in triplicates for each sample and control per assay.

7.3. Characterizations

The phase formation of crystallographic state of synthesized particles was performed by an X'pert Pro Phillips X-ray diffractometer using CuKα source. The morphology and microstructure were analyzed by Scanning electron microscope (HITACHI COM-S-4200) and High resolution transmission electron microscopy (JEOL 3010, Japan) operated at 300 kV. The images were analyzed using image-J software. Hydrodynamic size of the drug carrier at various stages of synthesis was measured at 25.0±0.5 °C, by laser light scattering using a particle size analyzer (Nano ZS 90, Malvern). Measurements were performed at 90° angle in 0.01 M phosphate buffer varying pH 4 to 8. The stability of the formulations was evaluated by measuring the size of the particles after one week of storage at 4.0±0.5 °C in water. The surface functional group and conjugation of the different moiety to the nanoparticle were invistegated by

FTIR spectroscopy (Thermo Nicolet Nexus FTIR model 870 spectrometer). Surface composition of folate decorated particles was obtained byanalyzing XPS data using AlKα excitation source in ESCA-2000Multilab apparatus (VG microtech). Nitrogen adsorption/desorption analysis was measured at a liquid nitrogen temperature (77 K) using a Micromeritics ASAP 2010M instrument. The specific surface areas and total pore volume were calculated by the Brunauer–Emmett–Teller (BET) and BJH methods respectively. The fluorescence emission spectra were performed on a Horiba Fluoromax 4 spectrophotometer at excitation energy of 340 nm. The magnetic properties of Fe_3O_4@m-SiO_2 and composite nanoparticles were determined using vibrating sample magnetometer (VSM), Lakeshore 7410 at 25.0±0.5 °C. UV absorption measurements, at the maximum absorbance wavelength (266 nm) in Shimadzu 220V (E) UV-vis spectrophotometer were carried out to measure the 5-FU concentration in all the systems investigated, using quartz cells of 1 cm path length.

7.4. Results and Discussion

Synthesis

The synthetic strategy of the magnetic luminescent nanocarrier is illustrated schematically in scheme 7.1. The ordered mesoporous silica-coated magnetite nanoparticles was synthesized using modified Stöber's method, which were further functionalized by precipitating luminescent material (YPO_4:Tb) on silica matrix. The superparamagnetic feature of the synthesized particles facilitates their easy and quantitative separation using external magnet. In the second step, the surface of the nanoparticles was modified with GTPS in order to produce epoxy group ended particles. To load with the drug, the particles were further functionalized with cyclodextrin using glutathione (GSH) as a coupling agent in the third step. Glutathione is a small sized natural tripeptide (γ-Glu-Cys-Gly) that contains a -SH group and two carboxylic groups. Moreover it is the most abundant thiol species in the cytoplasm and the major reducing agent in biochemical process.[47] For conjugation of β-cyclodextrin, first the glutathione-cyclodextrin ester has been prepared followed by epoxide-opening by the GSH-cyclodextrin ester through -SH group. Finally, the hydrophobic drug 5-FU was loaded on cyclodextrin-functionalized nanoparticles via formation of 5-FU/cyclodextrin inclusion

complex. In addition to this, to facilitate receptor mediated endocytosis, the nanocarrier was decorated with folates through epoxide opening by FA-NH_2.

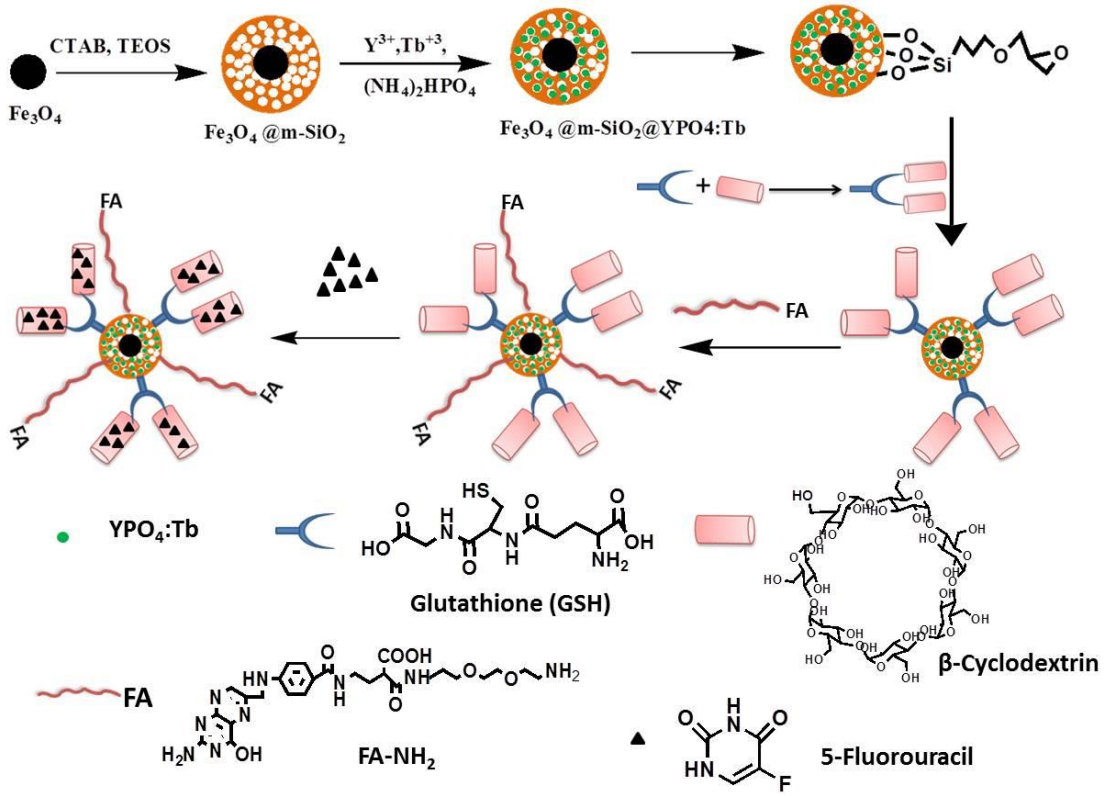

Scheme 7.1 Schematic representation for synthesis of 5-FU loaded fluorescent magnetic Fe_3O_4@mSiO_2@YPO_4:Tb hybrid nanocomposite.

XRD Study

The crystal structures and the phase purity of the Fe_3O_4@mSiO_2@YPO_4:Tb were determined by XRD. In Figure 7.1, all the reflection peaks of the products can be easily indexed to a crystalline cubic spinel structure of Fe_3O_4 with a lattice constant a=8.410 A^o (JCPDS No. 82-1533). For Fe_3O_4@m-SiO_2, the broad band at 2θ=22° can be assigned to the amorphous silica shell (JCPDS No. 29-0085). Besides the corresponding peaks of Fe_3O_4, the diffraction peaks of YPO_4 (JCPDS No. 74-2429) can be detected for Fe_3O_4@m-SiO_2@YPO_4:Tb sample. The weak reflection peak intensity of Fe_3O_4 in the hybrid was probably due to low content of magnetic materials or low level of crystallization.

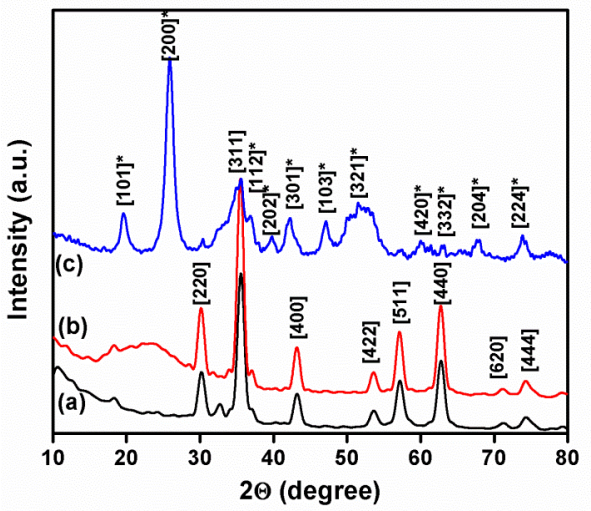

Figure 7.1 XRD patterns of (a) Fe_3O_4, (b) Fe_3O_4@m-SiO_2, (c) Fe_3O_4@m-SiO_2@YPO_4:Tb after heating at 300 °C for 4h.

Microstructure

The morphologies of the as-prepared products were characterized by scanning electron microscopy (SEM) and transmission electron microscopy (TEM). The SEM image of Fe_3O_4@m-SiO_2 particles (Figure 7.2a) shows that the nanoparticles are spherical in nature with a smooth surface and are almost monodisperse. After deposition of YPO_4 the surface of silica becomes relatively rough. The morphological features such as the spherical shape, non-aggregation, and narrow size are found to be retained in case of Fe_3O_4@mSiO_2@YPO_4:Tb (Figure 7.2b), similar to Fe_3O_4@mSiO_2. Furthermore, no irregular particles related with the introduced phosphors are detected. The results suggest that the deposition has little influence on the spherical morphology and the phosphor layer is uniformly deposited on the silica surface. TEM was employed to further examine the detail structure and morphology of Fe_3O_4 and Fe_3O_4@mSiO_2@YPO_4:Tb nanoparticles. The TEM image of Fe_3O_4 nanoparticles (Figure 7.2c) clearly indicates the formation of uniform, monodisperse particle with narrow size distribution of 5-7 nm. The high crystallinity of the sample is confirmed by the obvious lattice fringe (inset, Figure 7.2c). The three components in the Fe_3O_4@mSiO_2@YPO_4:Tb particles can be well distinguished by variation in contrast in different layers (inset, Figure 7.2d) due to difference in electron penetrability. It is well indicated that the inner magnetic core is surrounded by a silica shell with a diameter of 30 nm on which a very thin layer of

YPO_4:Tb of thickness 2.5 to 3 nm is deposited. However, aggregation/coalescence of individual Fe_3O_4@mSiO_2@YPO_4:Tb was found, and the aggregation might occur during TEM sample preparation and drying effect as observed in other cases.[26] The EDS spectrum (Figure 7.2e) confirms the presence of, Fe, Si, Y, Tb, and P on Fe_3O_4@mSiO_2@YPO_4:Tb particles.

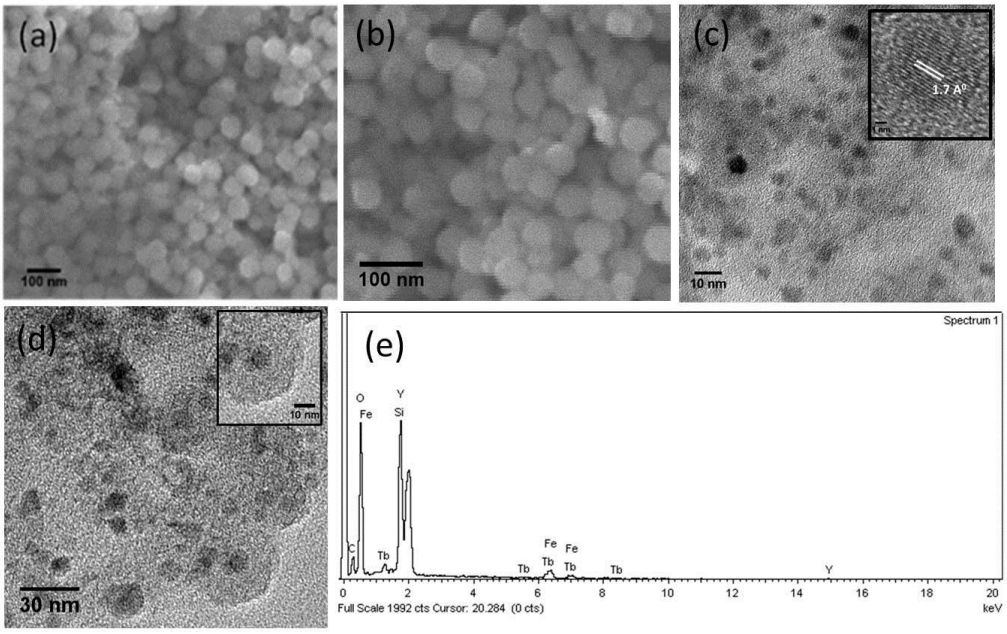

Figure 7.2 SEM images of (a) Fe_3O_4@m-SiO_2, (b)Fe_3O_4@m-SiO_2@YPO_4:Tb nanoparticles, and TEM images of (c) Fe_3O_4 with lattice imaging (inset), and (d) Fe_3O_4@m-SiO_2@YPO_4:Tb nanoparticles, inset is the image at high magnification showing the core shell structure, (e) EDX spectrum of Fe_3O_4@m-SiO_2@YPO_4:Tb nanoparticles.

Hydrodynamic size and stability

The hydrodynamic (HD) size of drug conjugated fluorescent magnetic nanoparticles at various stages of synthesis (Figure 7.3a) indicates the formation of stable non-aggregated particles. The drug loaded particle showed a mean HD size of 71 nm, which is not significantly affected with change of pH (3-8) (Figure 7.3b). Measurement of HD size against time shows that there is no change of hydrodynamic size after several days (Figure 7.3c). Such a stable HD size minimizes the possibility of macrophagic clearance of drug conjugates in the blood stream. Measurement of zeta potential against pH shows that at low pH zeta potential is 24.3 mV which shifts to -39 mV at higher pH which indicates the presence of -COOH groups on the surface (Figure 7.3d).

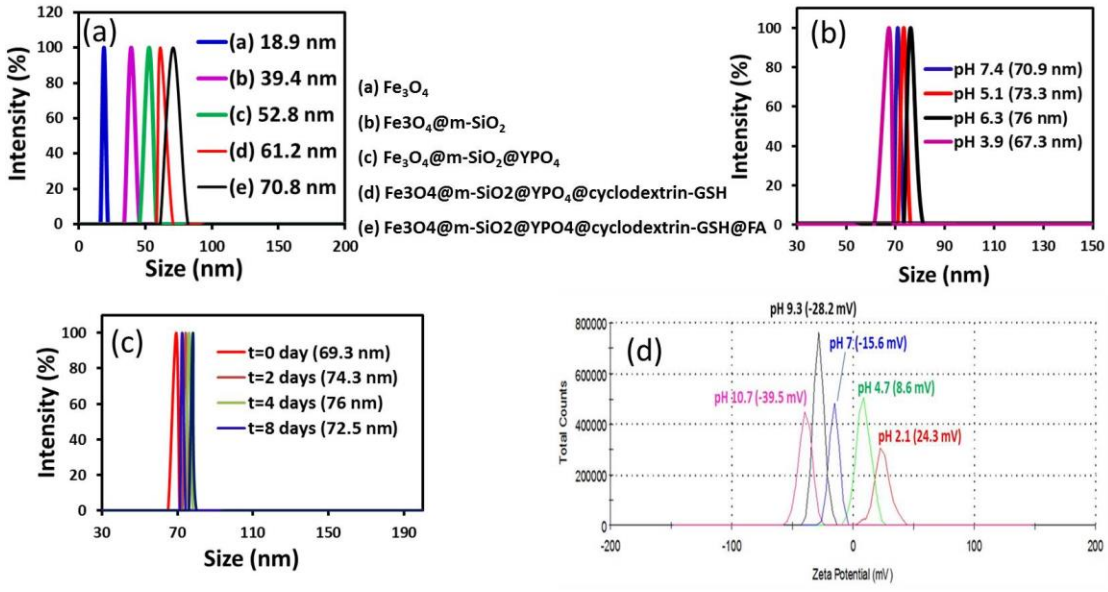

Figure 7.3 (a) Change in hydrodynamic size of the drug carrier at various stages of synthesis, Variation of the HD size of drug conjugate (b) with pH, (c) with time, and (d) Measurement of zeta potential of the drug loaded nanoparticle against pH.

FTIR Study

. Figure 7.4 shows FTIR spectra at various stages of synthesis. Fe_3O_4@m-SiO_2@YPO_4:Tb particles show strong absorption at 500-600 cm^{-1} corresponding to characteristic vibration of Fe-O in the magnetite lattice. The bands at 1000-1100 cm^{-1} (intense splitted band) and 642 cm^{-1} were attributed to the stretching and bending vibration of phosphate. Broadening of the band due to phosphate is overlapping of Si-O-Si (υ_{asym}, 1091 cm^{-1}) and Si-OH (υ_{sym}, 1005 cm^{-1}) bands of silica. The presence of intense band at 3450 and 1644 cm^{-1} suggest the presence of large number of H_2O and -OH groups on the surface which play the major role not only in high aqueous stability but also provides enough scope for further surface modification with GPTS. A broad intense peak at 1270 cm^{-1}, due to the symmetrical stretching or ring breathing frequency of epoxide ring confirms the surface modification of Fe_3O_4@m-SiO_2@YPO_4:Tb nanoparticles by GTPS. In the spectrum of Fe_3O_4@m-SiO_2@YPO_4:Tb@GSH-cyclodextrin, the intensification of methylene peak at 2935 cm^{-1} (characteristics of β-cyclodextrin) along with disappearance of ring breathing frequency of epoxide indicates that GSH-cyclodextrin has been conjugated by epoxide ring opening. Furthermore, the epoxide ring opening takes place by more nucleophilic –SH group in GSH-cyclodextrin

as indicated by the disappearance of -S-H_{str} (at 2550 cm^{-1}) in Figure 3(d). The most characteristic amide bands of folic acid at 1686 and 1510 cm^{-1} have become prominent suggesting the successful attachment of folic acid onto the nanoparticle.

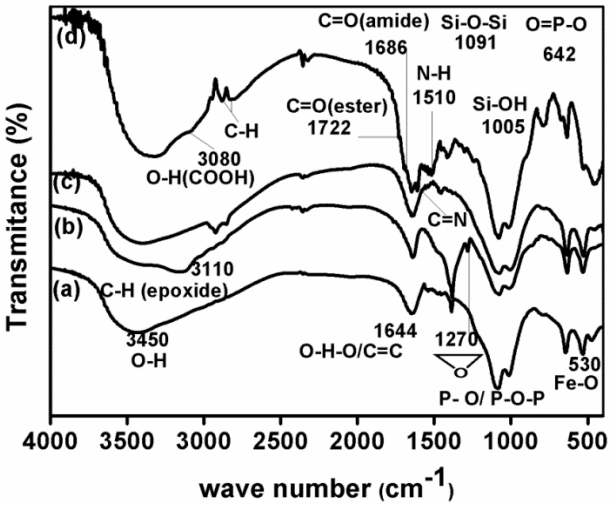

Figure 7.4 FTIR spectra of (a) Fe_3O_4@m-SiO_2@YPO_4:Tb, (b) Fe_3O4@m-SiO_2@YPO_4:Tb@GPTS, (c)Fe_3O_4@m-SiO_2@YPO_4:Tb@cyclodextrin-GSH, (d) Fe_3O_4@m-SiO_2@YPO_4:Tb@cyclodextrin-GSH@FA-NH_2.

X-ray photoelectron spectroscopy

X-ray photoelectron spectra were further used to establish the successful conjugation of GSH-cyclodextrin and FA on luminescent magnetic nanoparticle. In a typical survey spectrum of the functionalized nanoparticles (Figure 7.5a), the peaks at binding energies 100, 131, 150, 158, 280-290, 402.3, 530-538, 683-692, 705-730 eV are ascribed to binding energy in Si2p, P2p, Tb4d, Y3d, C1s, N1s, O1s, F1s and Fe2p regions respectively. High resolution scan for C1s shows that the curve is well fitted into five peaks centered at 284.1, 284.6, 285.9, 288.1, 289.2 eV corresponding to the C=C, C-C/C-H, C-N/C=N/C-O, C=O/ NHCO and COOH carbon (Figure 7.5b). The broad peak for N1s binding energy can be fitted into three peaks at 397.7, 399.6 and 400.7 eV corresponding to C=N, NH_2, -NHCO groups (Figure 7.5c). O1s binding energy at 531.4 eV can be fitted into three peaks corresponding to oxygen being present in three different environments. Peaks appearing at 529.2, 531.4 and 533.2 eV correspond to M-O, C-O, COOH and -NHCO- respectively (Figure 7.5d). $Fe2p_{3/2}$ and $Fe2p_{1/2}$ electrons show binding energy at 709.1 and 723.7 eV which is consistent with the Fe2p binding energy of magnetite nanoparticles (Figure 7.5e). Binding energy for S2p is at 161.9 eV

corresponds to C-S-C group.[48] Y3d photoelectron line position is at 157.8 and 159.7 eV due to Y3d5/2 and Y3d3/2 states respectively (Figure 7.5g). P2p peak with binding energy 134 eV is attributed to pentavalent tetra coordinated phosphorus (PO_4 tetrahedra) (Figure 7.5h). [49] Presence of F1s peak at 687.8 eV confirms the loading of 5-FU on the cyclodextrin conjugated nanoparticles (Figure 7.5i).[50]

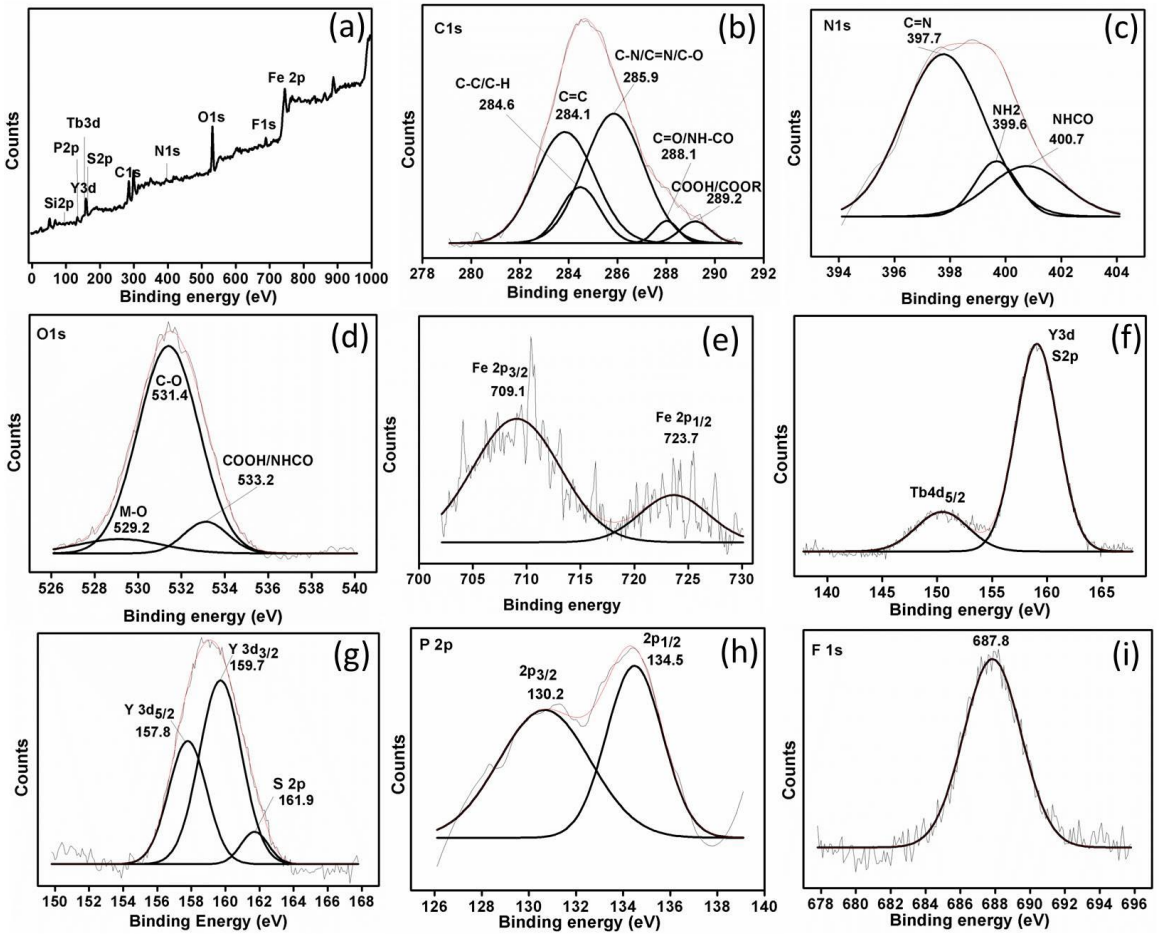

Figure 7.5 XPS survey spectrum (a), and High resolution scan corresponding to (b) C1s, (c) N1s, (d) O1s, (e) Fe2p, (f) Y3d, Tb4d and S2p, (g) Y3d and S2p, (h) P2p, (i) F1s.

BET surface area

The N_2 adsorption-desorption isotherms of Fe_3O_4@m-SiO_2 and Fe_3O_4@m-SiO_2@YPO_4:Tb nanoparticles have been shown in Figure 7.6a. The average pore diameter calculated using the Barrett-Joiner-Halenda (BJH) method was 5.1 nm and 4 nm for Fe_3O_4@m-SiO_2 and Fe_3O_4@m-SiO_2@YPO_4:Tb nanoparticle respectively which in good agreement with mesoporous size (Figure 7.6b). Both the samples show typical type IV isotherm with H3 hysterisis, which does not exhibit a limiting uptake over a range of

high p/p_0. It indicates the formation of aggregates of plate like particles giving rise to slit shaped pores. The result reveals that deposition of phosphor layer on the surface of silica hasn't changed the basic pore structure of the Fe_3O_4@mSiO$_2$ sample. The BET surface area of Fe_3O_4@m-SiO$_2$ and Fe_3O_4@m-SiO$_2$@YPO_4:Tb was found to be 530 and 270 m^2/g with respective pore volumes of 0.38 cm^3/g and 0.26 cm^3/g. The decrease in surface area in Fe_3O_4@m-SiO$_2$@YPO_4:Tb particles is due to uniform deposition of YPO_4: Tb particles in the porous slit of Fe_3O_4@m-SiO$_2$. The BET results indicate that Fe_3O_4@mSiO$_2$ nanoparticles are highly porous and have large surface area, which enables rapid growth of luminescent material (YPO_4:Tb) on the silica matrix and also ensures high drug encapsulation capacity of our drug delivery system.

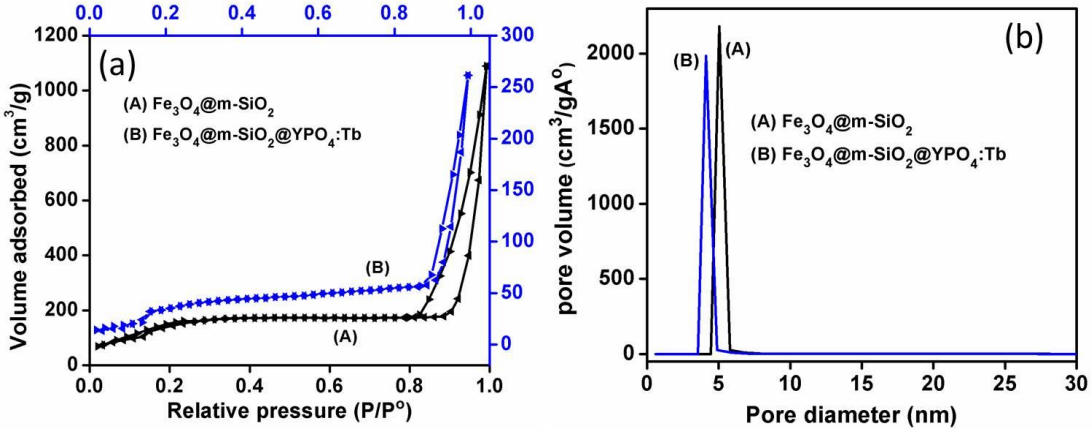

Figure 7.6 (a) Nitrogen adsorption-desorption isotherm and (b) the corresponding pore size distribution of (A) Fe_3O_4 @mSiO$_2$, (B) Fe_3O_4 @mSiO$_2$@ YPO_4:Tb

Photoluminescence properties

The fluorescence emission spectra of Fe_3O_4@m-SiO$_2$@YPO_4:Tb (Figure 7.7) under 340 nm excitation displays four strong and narrow emission bands between 450 and 650 nm, which are assigned to 4f →4f transitions related to Tb^{3+} ions. The most intense peak at 543 nm corresponds to the $^5D_4 \rightarrow {}^7F_5$ transition, while the peaks at 489, 585, and 622 nm are assigned to the transitions from $^5D_4 \rightarrow {}^7F_J$ (J=6, 4, 3) respectively, which are characteristic emissions of Tb^{3+}. The strongest emission at 545 nm is responsible for green emission of Tb^{3+}. The peaks at 489 nm and 545 nm correspond to the electric dipole allowed transition and magnetic dipole allowed transition, respectively. These results are similar to the emission peaks of pure YPO_4:Tb nanoparticles. Therefore, the existence of Fe_3O_4 may not affect the fluorescence property of the resulted hybrid

nanoparticles. In other words, the inner silica shell successfully blocks the energy transfer between lanthanide ions and metal ions which reduces the probability of fluorescence quenching by magnetic core.[5] The inset in Figure 7.7 shows the fluorescent image of drug loaded particles Fe_3O_4@mSiO_2@YPO_4:Tb under excitation of 488 nm. Particularly, no significant change in the characteristic emission peaks for 5-FU loaded Fe_3O_4 @mSiO_2@YPO_4:Tb reveals that the system can be easily tracked or monitored in the biological system. Furthermore, it is importantly noted that the PL intensity of 5-FU loaded Fe_3O_4@mSiO_2@YPO_4:Tb is less than that of Fe_3O_4@mSiO_2@YPO_4:Tb (Figure 7.7c). However after releasing of 5-FU there was slight enhancement of PL intensity (Figure 7.7b). It is well known that the emission of rare earth ions will be quenched to some extent in the environments that have a high phonon frequency. Thus this decrease in PL intensity with conjugation of cyclodextrin-5-FU inclusion complex can be related to the quenching effect of Tb^{3+} emission caused by organic groups of high vibration frequency (1000-3500 cm^{-1}).[30,51] When 5-FU was released the quenching effect is relaxed to some extent hence there is slight enhancement in PL intensity. For such correlation between PL intensity and drug release, the developed system can be used as a probe for monitoring the disease therapy.

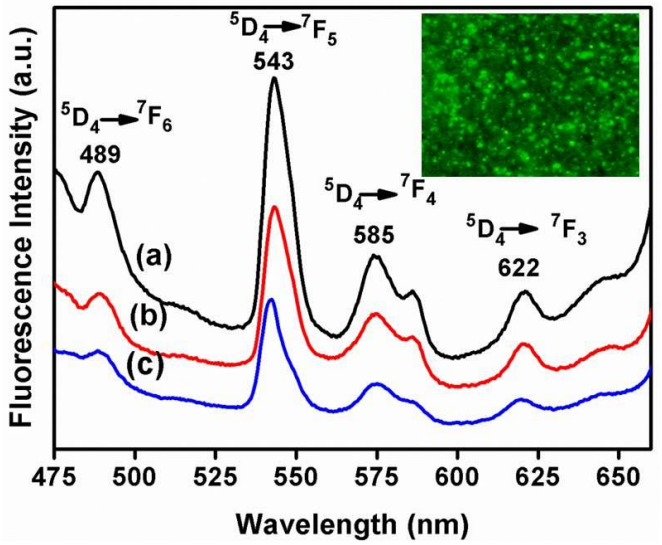

Figure 7.7 PL emission spectra of (a) Fe_3O_4@m-SiO_2@YPO_4:Tb, (b) Fe_3O_4@m-SiO_2@YPO_4:Tb@cyclodextrin-GSH@FA and (c) Fe_3O_4@m-SiO_2@YPO4:Tb@cyclodextrin-GSH@FA-5-FU, the inset is the fluorescent image of Fe_3O_4@m-SiO_2@YPO4:Tb@cyclodextrin-GSH@FA-5-FU at λ_{ex} 488 nm.

Magnetic properties

The magnetic properties of 5-FU-Fe_3O_4@m-SiO_2@YPO_4:Tb particles were characterized using a vibrating sample magnetometer (VSM) with the magnetic field cycle between -20,000 and +20,000 Oe at 300 K. The saturation magnetization (Ms) of 5-FU-Fe_3O_4@m-SiO_2@YPO_4:Tb was 23 emu/g, which is lower than the as prepared Fe_3O_4 is 70 e.m.u/g.[42] This significant reduction in the magnetization value of the hybrid material is due to the lower proportion of magnetic Fe_3O_4 in the nanocomposites and a larger amount of non-magnetic conjugates on the surface of the nanoparticles, which also suppresses the exchange coupling and dipolar interactions among coated nanoparticles. The sample exhibits superparamagnetic behavior with a negligible coercivity or remanence (Figure 7.8a), hence demonstrating the suitability of our multifunctional nanoprobe as a contrast enhancing agent in MRI.[52] Moreover, the homogenous dispersion of drug carrier shows fast response to the external magnetic field with no residual magnetism (Figure 7.8b). The result reveals that the particles exhibit excellent magnetic responsivity and re-dispersible properties, which suggests a potential application for magnetic targeting and separation.

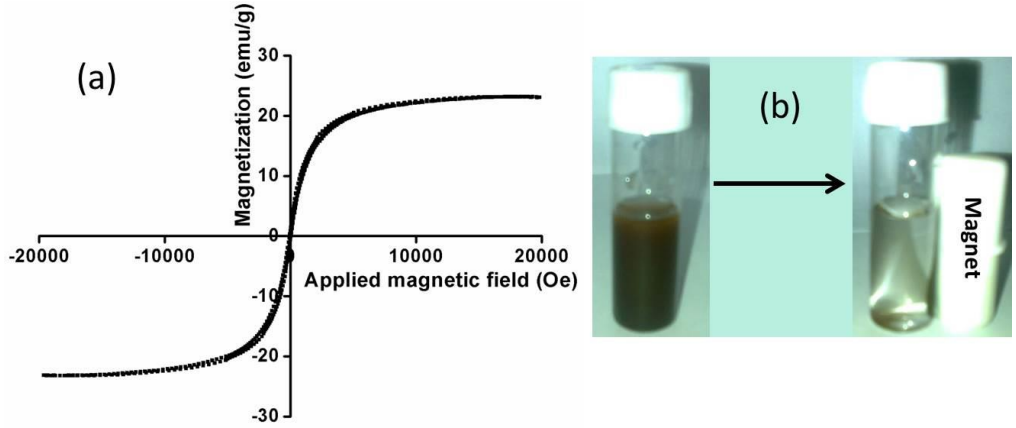

Figure 7.8 Field dependent magnetization curve (a) and magnetic separation (b) of 5-FU loaded Fe_3O_4@m-SiO_2@YPO_4:Tb nanoparticles.

In vitro cytotoxicity of the nanocarrier

The evaluation of cell viability of Fe_3O_4@mSiO_2@YPO_4:Tb@cyclodextrin-GSH@FA nanoparticles through MTT assay is presented in Figure 7.9a. Our nanocarrier did not impose any cytotoxicity in both L929 and HeLa cells. The nanoparticles are

tolerable up to high dose (200 μg) and long incubation time (72 h), which indicates that Fe_3O_4@mSiO_2@YPO_4:Tb@cyclodextrin-GSH@FA nanoparticles are biocompatible.

Loading and release of 5-FU

The drug storage and release properties of the designed system as a candidate of hydrophobic anticancer drug carriers were tested by selecting 5-FU as a model drug. The drug was loaded into the Fe_3O_4@mSiO_2@YPO_4:Tb@cyclodextrin-GSH@FA nanoparticles through the surface-conjugated cyclodextrin by forming an inclusion complex. The adsorption profile of 5-FU shows that maximum inclusion of the drug occurred after 70 h. Typically the percentage of 5-FU adsorbed on to the fluorescent magnetic carrier with respect to the initial drug solution is 91.6%. Hence the encapsulation efficiency of the carrier reached 91.6%. Simultaneously, this corresponds to 114. 5 mg drug per g of nanoparticles. The high drug loading loading capacity may result from high surface area of mesoporous silica facilitating conjugation of large amount of cyclodextrin on its surface.

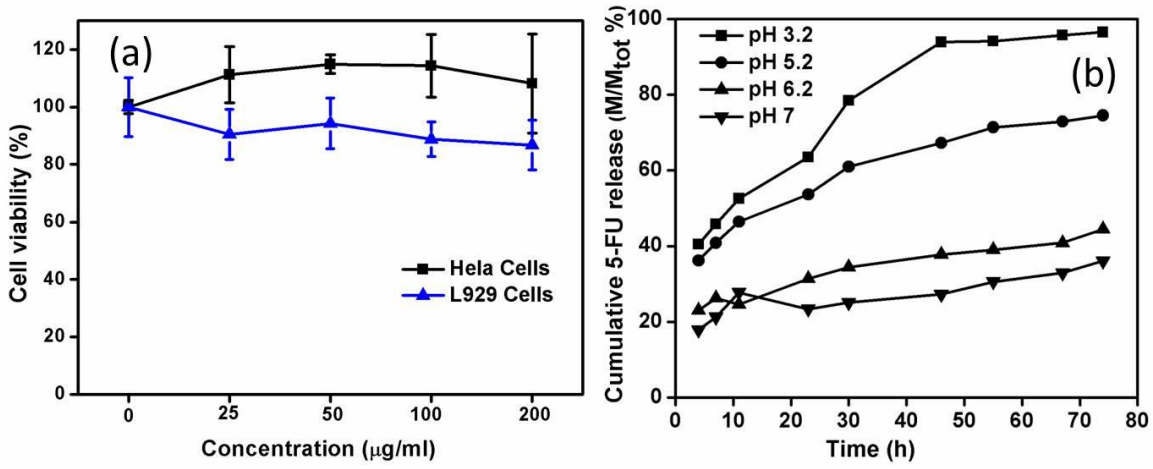

Figure 7.9 (a) In vitro cell viability of HeLa and L929 cells with the drug carrier Fe_3O_4@mSiO_2@ YPO_4:Tb@cyclodextrin-GSH@FA, and (b) Cumulative 5-FU releases from Fe_3O_4@m-SiO_2@YPO_4:Tb@cyclodextrin-GSH@FA-5-FU in PBS at different pH (7-3.2).

The cumulative 5-FU release at pH 7, 6.2, 5.2 and 3.2 has been depicted in Figure 7.9b. It was observed at pH 3.2, a burst release of 50% was observed after 10 h which slowly increased to 96%. This initial burst of 5FU release could be partly attributed to the weak bonds or the adsorption of drugs on the surface of nanoparticles. When the pH is

slightly increased to 5.2, the release rate of 5-FU is decreased to 45% at 10 h. Furthermore, only 15% of 5-FU was observed after 10 h with increase in pH to 7. The overall release rates were higher in lower pH and less release was observed in physiological pH. This pH dependent release behavior may be ascribed to the stability of 5-FU/cyclodextrin inclusion complex.[53] At acidic pH the stability of 5-FU/cyclodextrin guest/host inclusion complex is less hence fast release of 5-FU occurs. Particularly, at tumor site the pH is less than that of normal tissues; hence the pH-sensitive drug release will be triggered when the drug loaded carrier will be concentrated at the tumor site using an external magnetic field. In addition to this our system shows a sustained release pattern over a prolonged time. Hence it can be used for controlled release of 5-FU.

7.5. Conclusion

- In this chapter, mesoporous fluorescent magnetic Fe_3O_4@m-SiO_2@YPO_4:Tb particles with a size of 52 nm have been prepared.
- The mesoporous silica makes the hydrophobic iron oxide water soluble and reduces the probability of fluorescence quenching.
- The synthesised nanocomposite possesses high surface area, bright luminescence and appreciably high saturation magnetization at room temperature.
- These hybrid nanospheres were functionalized with β-cyclodextrin and folic acid using glutathione as a robust coupling agent.
- These β-cyclodextrin functionalized particles shows high loading capacity and pH sensitive sustained release behavior for anticancer drug 5-fluorouracil.
- The overall size of the drug conjugate is 71 nm and the particles are highly stable in aqueous medium without any detoriation of HD size.
- The good biocompatibility, high surface area, and intrinsic property of the nanocomposite suggest that this new nanomaterial can act as a potentially useful intracellular nanovehicle for magnetically guided cancer targeted delivery of 5-FU.

7.6. References

1. F. Wang, X. Xue, X. Liu, *Angew. Chem. Int. Ed.*, 2008, **47**, 906-909.
2. X. Bai, H. Song, G. Pan, Y. Lei, T. Wang, X. Ren, S. Lu, B. Dong, Q. Dai, L. Fan, *J. Phys. Chem. C*, 2007, **111**,13611-1361.
3. V. Mahalingam, F. Vetrone, R. Naccache, A. Speghini, A. Capobianco, *Adv. Mater.,* 2009, **21**, 1-4.
4. G. Wang, Q. Peng, Y. Li, *Acc. Chem. Res.*, 2011, **44**, 322-332.
5. D. K. Chatterjee, A. J. Rufaihah, Y. Zhang, *Biomaterials*, 2008, **29**, 937–943.
6. M. Nyk, R. Kumar, T. Y. Ohulchanskyy, E. J. Bergey, P. N. Prasad, *Nano Lett.*, 2008, **8**, 3834-3838.
7. S. Jiang, Y. Zhang, *Langmuir*, 2010, **26**, 6689-6694.
8. S. W. Wu, G. Han, D. J. Milliron, S. Aloni, V. Altoe, D. V. Talapin, B. E. Cohena, P. J. Schuck, *PNAS*, 2009, **106**, 10917-10921.
9. L. Q. Xiong, Z. G. Chen, Q. W. Tian, T. Y. Cao, C. J. Xu, F. Y. Li, *Anal Chem.*, 2009, **81**, 8687-8694.
10. J. Zhang, Y. Wang, Z. Xu, H. Zhang, P. Dong, L. Guo, F. Li, S. Xin, W. Zeng, *J. Mater. Chem. B*, 2013, **1**, 330-338
11. W. Xu, B. A. Bony, C. R. Kim, J. S. Baeck, Y. Chang, J. E. Bae, K. S. Chae, T. J. Kim, G. H. Lee, *Nature Scientific Report*, 2013, DOI: 10.1038/srep03210.
12. Peter Caravan, *Chem. Soc. Rev.***,** 2006, **35**, 512-523.
13. Y. H. Wang, P. Shen, C. Y. Li, Y. Y. Wang and Z. H. Liu, *Anal. Chem.*, 2012, **84**, 1466-1473.
14. E. Beaurepaire, V. Buissette, M. P. Sauviat, D. Giaume, K. Lahlil, A. Mercuri, D. Casanova, A. Huignard, J. L. Martin, T. Gacoin, J. P. Boilot, A. Alexandrou, *Nano Lett.*, 2004, **4**, 2079-2083.
15. L. Zhou, Z. Li, E. Ju, Z. Liu, J. Ren, X. Qu, *Small*, 2013, **9**, 4262-4268.
16. C. Wang, L. Cheng, Y. M. Liu, X. J. Wang, X. X. Ma, Z. Y. Deng, Y. G. Li, Z. Liu, *Adv. Funct. Mater.*, 2013, **23**, 3077-3086.
17. Q. Chen, C. Wang, L. Cheng, W. W. He, Z. P. Cheng, Z. Liu, *Biomaterials*, 2014, **35**, 2915-2923.
18. W. Li, J. S. Wang, J. S. Ren, X. G. Qu, *J. Am. Chem. Soc.*, 2014, **136**, 2248-2251.

19. W. Zheng, P. Huang, D. Tu, E. Ma, H. Zhu, X. Chen, *Chem. Soc. Rev.*, 2015, DOI: 10.1039/C4CS00178H
20. Y. Liu, D. Tu, H. Zhu, X. Chen, *Chem. Soc. Rev.*, 2013, **42**, 6924-6958.
21. G. Y. Chen, H. L. Qiu, P. N. Prasad, X. Y. Chen, *Chem. Rev.*, 2014, **114**, 5161-5214.
22. C. Bouzigues, T. Gacoin, A. Alexandrou, *ACS Nano*, 2011, **5**, 8488-8505.
23. H. C. Lu, G. S. Yi, S. Y. Zhao, D. P. Chen, L. H. Guo, J. Cheng, *J. Mater. Chem.*, 2004, **14**, 1336-1341.
24. D. Dosev, M. R. Nichkova, K. Dumas, S. J. Gee, B. D. Hammock, K. Liu, I. M. Kennedy, *Nanotechnology*, 2007, **18**, 055102.
25. Y. X. Zhang, G. K. Das, R. Xu, T. T. Y. Tan, *J. Mater. Chem.*, 2009, **19**, 3696-3703.
26. Z. Y. Ma, D. Dosev, M. Nichkova, S. J. Gee, B. D. Hammock, I. M. Kennedy, *J. Mater. Chem.*, 2009, **19**, 4695-4700.
27. J. Fang, M. Saunders, Y. Guo, G. Lu, C. L. Raston, K. S. Iyer, *Chem. Commun.*, 2010, **46**, 3074-3076.
28. Wang, W.; Zou, M.; Chen, K. *Chem. Commun.*, 2010, **46**, 5100-5102.
29. Y. Zhang, S. Pan, X. Teng, Y. Luo, G. Li, *J. Phys. Chem. C*, 2008, **112**, 9623-9626.
30. P. Yang, Z. Quan, Z. Hou, C. Li, X. Kang, Z. Cheng, J. Lin, *Biomaterials*, 2009, **30**, 4786-4795.
31. Z. Sun, D. Liu, L. Tong, J. Shi, X. Yang, L. Yu, Y. Tao, H. Yang, *Solid State Sci.*, 2011, **132**, 361-365.
32. L. Wang, Z. Yang, Y. Zhang, L. Wang, *J. Phys. Chem. C*, 2009, **113**, 3955–3959
33. N. Zhang, Y. Yin, S. J. Xu, W. S. Chen, *Molecules*, 2008, **13**, 1551-1569.
34. T. Ito, K. Tanabe, H. Yamada, H. Hatta, S. Nishimoto, *Molecules*, 2008, **13**, 2370-2384.
35. Q. Jin, F. Mitschang, S. Agarwal, *Biomacromolecules*, 2011, **12**, 3684-3691.
36. S. R. Guo, Z. M. Wang, Y. Q. Zhang, L. Lei, J. M. Shi, K. M. Chen, *J. Pharm. Sci.*, 2010, **99**, 3009-3018
37. D. B. Longley, D. P. Harkin, P. G. Johnston, *Nat. Rev. Cancer*, 2003, **3**, 330-338.

38. B. Singh, N. Chauhan, *Acta Biomater.*, 2008, **4**, 1244-1254.
39. M. Hussain, G. Beale, M. Hughes, S. Akhtar, *Int. J. Pharm.*, 2002, **234**, 129-138.
40. L. Jin, Q. Liu, Z. Sun, X. Ni, M. Wei, *Ind. Eng. Chem. Res.*, 2010, **49**, 11176-11181.
41. I.T Magrath, *Int J. Cancer.*, 1994, **56**, 163-166.
42. S. Sun, H. Zeng, *J. Am. Chem. Soc.*, 2002, **124**, 8204-8205
43. W. Stober, A. Fink, E. Bohn, *J. Colloid Interf. Sci.*, 1958, **26**, 62-69.
44. S. Mohapatra, S. K. Mallick, T. K. Maiti, S. K. Ghosh, P. Parmanik, *Nanotechnology*, 2007, **18**, 385102.
45. S. Li, Y. Ma, X. Yue, Z. Cao, Z. Dai, *New J. Chem.*, 2009, **33**, 2414-2418.
46. T. Mosmann, *J. Immunol. Methods*, 1983, **65**, 55-63.
47. D. M. Townsend, K. D. Tew, H. Tapiero, *Biomed. Pharmacother.*, 2003, **57**, 145-155.
48. R. S. C. Smart, W. M. Skinner, A.R. Gerson, *Surf. Interface Anal*., 1999, **28**, 101-105.
49. M. Pelavin, D. Hendrickson, J. Hollander, W. Jolly, *J. Phys. Chem.*, 1970, **74**, 1116-1121.
50. J. Peeling, F. E. Hruska, N. S. Mcintyre, *Can. J. Chcni.*, 1978, **56**, 1555-1561.
51. Z. Cheng , P. Ma , Z. Hou , W. Wang , Y. Dai , X. Zhai, J. Lin, *Dalton Trans.*, 2012, **41**, 1481-1489.
52. W. J. Rieter, J. S. Kim, K. M. L. Taylor, H. An, W. Lin, T. Tarrant, W. Lin, *Angew. Chem.*, 2007, **119**, 3754-3756.
53. K. Hayashi, K. Ono, H. Suzuki, M. Sawada, M. Moriya, W. Sakamoto, T. Yogo, *ACS Appl. Mater. Interfaces*, 2010, **2**, 1903-1911.

Chapter 8

Luminescent carbon dot decorated magnetic hollow mesoporous silica nanotheranostics: A novel multifunctional platform for simultaneous camptothecin delivery and multimodal imaging

8.1. Introduction

Hollow structured nanospheres with controlled pore volume and shell thickness have gained considerable interest due to stable mesoporous structure, low density, large surface area, tunable pore size, easily modified surface and high guest-loading capacity, which would be beneficial for applications including diagnostics, drug delivery, tissue engineering, biosensors and bioseparation systems.[1-4] Furthermore the hollow cavity allows the incorporation of other species for designing of diverse multifunctional materials. In past few years extensive effort has been devoted to the design of multifunctional materials incorporating magnetic and luminescent functionalities into single mesoporous silica host for a wide range of biological applications. While magnetic nanoparticles can be used as contrast agents in magnetic resonance imaging (MRI) and facilitate magnetic responsive separation, detection, targeting, and hyperthermia, luminescent nanoparticle enable optical bioimaging and photothermal therapy.[5-8]

Luminescent carbon dots (CD) a new class of carbon-based nanomaterials have attracted much attention because their excellent luminescence properties, including large two-photon excitation cross-sections, lack of blinking, high water solubility, low cytotoxicity, and excellent biocompatibility.[9-11] These superior properties make these materials promising alternatives to common toxic metal-based quantum dots for numerous exciting applications such as biosensing,[12] biological labelling,[13] photo-catalysis[14] and optical-electronic devices.[15] The exploration of CD towards the theranostic application where its fluorescent property can hand out the real time monitoring of the drug release efficacy is at very early stage. Chou *et al.* reported a facile method for the gram scale production of CD/mSiO_2-PEG which was used in controlled release of doxorubicin in HeLa cells.[16] Subsequently CD was explored for pH-sensitive[17,18] and photosensitive[19] release of doxorubicin coupled with efficient monitoring through bioimaging. Recently CD functionalized gold nanorod is utilized for multifunctional application such as drug delivery, photothermal therapy and biological imaging.[20] The integration of luminescent properties of CDs to magnetic properties can further offers a new potential, where the former serves as a fluorescent probe for visualising biological process in vitro and in vivo, later for magnetic tracking and drug delivery. However very

few reports are availables on fabrication of CD based magnetic luminescent nanocomposits.[21-23] Gajbhiye *et al.* synthesized a magnetic nanoparticle doped carbogenic nanocomposite for magnetic resonance and fluorescence multimodal imaging and demonstrated its efficiency both in vitro and in vivo fluorescence as well as magnetic resonance imaging.[24] Most recently hybrid luminescent magnetic CD nanoparticle was demonstrated for dual-modal imaging, near-infrared light-responsive drug carrier and photothermal therapy.[25]

Camptothecin (CPT), isolated from *camptotheca acuminate* is a plant alkoliod exhibits significant antitumor activity on a broad spectrum of tumors. CPT can effectively inhibit the relaxation process of DNA related to replication and transcription by the stable combination with topoisomerase I and DNA.[26] However the severe systemic toxicities, extreme aqueous insolubility, low stability of the lactone form at physiological pH limit its clinical application.[27,28] As a consequence, a variety of nanomedicines including polymer drug conjugates,[29,30] micelles,[31] nanoparticles (NPs),[32,33] and vesicles[34] were developed for CPT delivery to decrease potent toxicities and improve its properties. However most of these carriers cannot congregate formulation requirements like controlled size with low dispersity, high loading efficiency, controlled drug release kinetics, sufficient aqueous stability, capability of staying nonaggregated in biological media and easy production from gram to kilogram scale, which are very much decisive for their clinical translation.[35] One important strategy to improve CPT delivery is specific targeting and appropriate conjugation of the drug through flexible surface chemistry. A galactose-appended camptothecin prodrug was developed to target the hepatoma cell line where the drug release (by disulfide-bond cleavage via reaction with glutathione) was visualized through fluorescence imaging. However it failed to show significant anticancer activity due to lysosomal hydrolysis of CPT lactone ring.[36] A novel luminescent magnetic CdTe/ iron oxide nanoparticles with folate-conjugated tetrapeptide composites has developed by Zhang *et al.* for tumor-targeted CPT delivery.[37] Although the developed novel multifunctional nanoparticles possess reasonably good biocompatibility and growth inhibition properties, the possibility for long term slow release of Cd leading to cytotoxicity[38] and the low drug loading efficiency owing to the lack of robust drug conjugation chemistry limit their practical medical application. Therefore, stable

biocompatible fluorescent magnetic carrier with better drug loading capability as well as active targeting of camptothecin are highly desired for improving cancer therapeutic effect.

In this chapter, hollow mesoporous silica based luminescent magnetic hybrid nanoparticles by incorporating iron oxide nanoparticles as magnetic and carbon dot as the luminescent component have been developed. The nanomaterial is characterized by a series of physical characterization technique such as XRD, magnetic measurements, Raman, and TEM. In order to conjugate drug molecule, water soluble CPT conjugate has been synthesized and coupled to the nanohybrid surface through robust chemistry using silane coupling agent. Furthermore, folic acid has also been conjugated to ensure the targeted specific delivery of the drug. The conjugation of the drug has been established through FTIR and XPS studies. The DLS and zeta potential studies over time ensure excellent stability of the nanoparticles in physiological medium. The in vitro cytotoxicity of the drug carrier as well as intracellular uptake and cell apoptosis were evaluated in HeLa cells through fluorescence microscopy. The possible application of the developed multifunctional particles was also evaluated through MR imaging.

8.2. Experimental

Chemicals

Benzyl ether, Cetyltrimethylammonium bromide (CTAB), camptothecin(CPT), $Fe(acac)_3$, 3-glycidoxypropyl trimethoxy silane (GTPS), oleic acid, oleylamine, tetraethyl orthosilicate (TEOS), diglycolic anhydride, diisopropylcarbodimide and 2,2'-(ethylenedioxy)-bis-(ethylamine) (EDBE) were purchased from Sigma Aldrich, USA. Acetone, chloroform, diethyl ether, dichloromethane, ethanol, ethyl acetate, and triethyl amine were procured from Rankem, India. Dimethylaminopyridine (DMAP) and ^{t}butanol were bought from Spectrochem Private Limited. Commercially available dichloromethane and toluene were purified by distillation over phosphorous pentoxide and sodium metal with benzophenol respectively. Prior to use, dimethylsulfoxide (DMSO) was vacuum distilled.

Synthesis of γ-N-{2-[2-(2-aminoethoxy)ethoxy]ethyl} conjugated camptothecin (EDBE-CPT)

Synthesis of mono-t-butylester of diglycolic acid (1): A solution of diglycolic anhydride (1 g, 9 mmol) and DMAP (1.05 g, 9 mmol) in dry t-butanol (8 mL) was stirred at reflux temperature for 18 h.[40] The solvent was removed under reduced pressure and the residue was dissolved in water. The aqueous solution was acidified to pH 2.5-3.0 with 1 N HCl and extracted with diethyl ether, dried over anhydrous Na_2SO_4 and concentrated under reduced pressure to give 1 (1.3 g, yield 79%).

IR (KBr): 3468, 2986, 2922, 2846, 1739, 1636, 1398, 1370, 1303, 1246, 1140, 1054 cm^{-1}. ^{1}HNMR (400 MHz, $CDCl_3$): δ 8.74 (s, br, 1H), 4.26 (s, 2H), 4.13 (s, 2H), 1.49 (s, 9H). ^{13}C NMR (100 MHz, $CDCl_3$): δ 173.1, 169.9, 83.0, 69.3, 68.9, 28.0. MS (ESI): m/z (relative intensity) 213.1 ([M+Na], 100).

Synthesis of camptothecin-20-monoester of mono-t-butylester of diglycolic acid (2): A mixture of 1 (42 mg, 0.2 mmol), camptothecin (40 mg, 0.1 mmol), DMAP (27 mg, 0.2 mmol), and DIPC (0.03ml, 0.2 mmol) in anhydrous dichloromethane (6 mL) was stirred for 24 h at room temperature.[40] The reaction mixture was washed with water, then saturated sodium bicarbonate, 0.1 N HCl and again with water. The organic layer was dried over anhydrous Na_2SO_4 and the solvent was removed under reduced pressure, recrystallization of the resultant solid from dichloromethane/ether gave 2 (53 mg, yield 66 %).

IR (KBr): 3395, 2923, 2846, 1742, 1717, 1653, 1619, 1558, 1502, 1460, 1432, 1418, 1399, 1368, 1275, 1253, 1194, 1139, 1057 cm^{-1}.^{1}HNMR (400 MHz, DMSO-d_6): δ 8.70 (s, br, 1H), 8.18-8.12 (m, 2H), 7.87(t, 1H), 7.72 (t, 1H), 7.13 (s, 1H), 5.52 (s, 2H), 5.31 (s, 1H), 4.60-4.55 (d, 2H), 4.43-4.39 (d, 2H), 2.17-2.13 (m, 2H), 1.40 (s, 9H), 0.94 (t, 3H).^{13}CNMR (100 MHz, DMSO-d_6): δ 169.3, 168.9, 167.5, 157.2, 152.8, 148.3, 146.5, 145.6, 130.8, 129.3, 130.2, 129.0, 128.4, 128.2, 119.2, 95.3, 81.5, 76.8, 68.2, 67.4, 66.7, 50.7, 30.6, 28.1, 7.9. MS (ESI): m/z (relative intensity) 551 ([M+CH_3OH], 100).

Synthesis of camptothecin-20-monoester of diglycolic acid (3): A solution of compound 2 (80 mg, 0.15 mmol) in dichloromethane (4 mL) and TFA (0.4 mL) was stirred at room temperature for 30 min. The solvent was removed under reduced pressure, and the resulting solid was recrystallized from dichloromethane/ether to yield 3 (51 mg, 81%).

IR (KBr): 3337, 2970, 2913, 1740, 1678, 1650, 1618, 1575, 1522, 1457, 1432, 1395, 1360, 1323, 1256, 1197, 1170, 1138, 1060 cm^{-1}. ^{1}HNMR (400 MHz, DMSO-d_6): δ 13.4 (s, 1H), 8.70 (s, 1H), 8.23-8.12 (m, 2H), 7.87(t, 1H), 7.72 (t, 1H), 7.14 (s, 1H), 5.52 (s, 2H), 5.30 (s, 1H), 4.62-4.58 (d, 2H), 4.44-4.40 (d, 2H), 2.17-2.14 (m, 2H), 0.99 (t, 3H). ^{13}CNMR (100 MHz, DMSO-d_6): δ 171.3, 169.4, 167.5, 157.0, 152.8, 148.3, 146.5, 145.6, 130.3, 130.8, 129.4, 129.0, 128.4, 128.2, 119.2, 95.4, 76.8, 67.7, 67.5, 66.7, 50.7, 30.6, 7.9. MS (ESI): m/z (relative intensity) 487 ([M+Na], 71)

Synthesis of γ-N-{2-[2-(2-aminoethoxy)ethoxy] ethyl} conjugated camptothecin-20-monoester of diglycolic acid (CPT-EDBE) (5): Tert-butyl N-{2-[2-(2-aminoethoxy)ethoxy]ethyl}-carbamate was prepared by following the method as reported by Mohapatra *et al.*.[39] A mixture of the carbamate (74 mg, 0.3 mmol), 3 (82 mg, 0.2 mmol), DMAP (54 mg, 0.4 mmol), and DIPC (0.06 mL, 0.4 mmol) in anhydrous dichloromethane (10 mL) was stirred for 24 h at room temperature. The reaction mixture was washed with water, then saturated sodium bicarbonate, 0.1 N HCl and again with water. The organic layer was dried over anhydrous Na_2SO_4 and the solvent was removed under reduced pressure, recrystallization of the resultant solid from dichloromethane/ether gave 4 (65 mg, 51%).

IR (KBr): 3423, 3335, 3266, 3115, 2974, 2908, 1748, 1647, 1600, 1575, 1440, 1399, 1368, 1343, 1323, 1253, 1197, 1156, 1113, 1068, 1001 cm^{-1}. ^{1}HNMR (400 MHz, DMSO-d_6): δ 8.69 (s, 1H), 8.18-8.11 (m, 2H), 7.85(t, 1H), 7.71 (t, 1H), 7.35 (s, 1H), 6.77 (br s, 1H), 6.12 (br s, 1H), 5.43 (s, 2H), 5.28 (s, 1H), 4.6-4.57 (d, 2H), 4.44-4.39 (d, 2H), 3.49-3.44 (m, 8H), 3.49-3.43 (m, 2H), 3.06-3.04 (m, 2H), 1.90-1.85 (m, 2H), 1.33 (s, 9H), 0.99 (t, 3H). ^{13}CNMR (100 MHz, DMSO-d_6): δ 172.9, 157.3, 156.0, 154.4, 153.0, 150.5, 149.7, 148.4, 145.9, 130.9, 130.3, 129.5, 128.9, 128.4, 128.1, 119.5, 97.2, 78.1, 72.8, 70.6, 70.0, 69.9, 69.6, 68.2, 65.7, 66.7, 50.7, 39.0, 30.7, 28.7, 8.2. MS (ESI): m/z (relative intensity) 717 ([M+Na], 100)

A solution of compound 4 (96 mg, 0.15 mmol) in dichloromethane (5 mL) and TFA (0.5 mL) was stirred at room temperature for 30 min. The solvent was removed under reduced pressure, and the resulting solid was recrystallized from dichloromethane/ether to yield 5 (63 mg, 78%).

IR (KBr): 3426, 3273, 3109, 2963, 2913, 2851, 1743, 1675, 1650, 1597, 1580, 1502, 1482, 1435, 1399, 1345, 1317, 1273, 1259, 1197, 1156, 1133, 1068, 1032, 1001 cm^{-1}. ^{1}HNMR (400 MHz, DMSO-d_6): δ 8.69 (s, 1H), 8.18-8.11 (m, 2H), 7.85(t, 1H), 7.71 (t, 1H), 7.35 (s, 1H), 6.77 (br s, 1H), 6.12 (br s, 1H), 5.43 (s, 2H), 5.28 (s, 1H), 4.61-4.57 (d, 2H), 4.44-4.39 (d, 2H), 4.3-4.0 (br S), 3.59-3.54 (m, 2H), 3.4-3.35 (m. 2H), 1.89-1.85 (m. 2H), 0.9-0.86 (t, 3H). ^{13}CNMR (100 MHz, DMSO-d_6): δ 172.9, 159.0, 158.62, 157.31, 152.98, 150.47, 148.37, 145.94, 130.86, 130.26, 129.46, 128.95, 128.41, 128.12, 119.51, 97.22, 72.84, 69.83, 67.08, 65.71, 65.36, 50.68, 41.16, 30.75, 23.69, 8.20. MS (ESI): m/z (relative intensity) 595 ([M+1], 100).

Synthesis of CD decorated magnetic mesoporous hollow silica nanosphere

Synthesis of monodisperse hydrophobic Fe_3O_4 nanoparticle: The magnetic particles were prepared by modified Sun *et al.* procedure using a solvothermal technique.[41] Briefly Fe_3O_4 nanoparticles were synthesized through mixing of $Fe(acac)_3$ (706 mg, 2 mmol), 1,2-dodecanediol (2.023 g, 10 mmol) and benzyl ether (20 mL). Oleic acid (1.9 mL, 6 mmol) and oleylamine (1.97 mL, 6 mmol) were sequentially added to it and transferred to a teflon-lined stainless-steel autoclave, followed by heating to 180 °C for 8 h (1 °C/min). Then as-synthesized mixture was allowed to cool to room temperature and Fe_3O_4 nanoparticles were precipitated by adding ethanol. The precipitate was collected by centrifugation at a speed of 10000 rpm for 10 minutes.

Synthesis of mesoporous silica coated Fe_3O_4 nanoparticle (Fe_3O_4@m-SiO_2): Fe_3O_4 nanoparticles were coated with mesoporous silica using CTAB as a template.[42] In a typical procedure, 30 mg of oleic acid stabilized monodisperse magnetite nanoparticles dispersed in 2 mL of chloroform was added to a 20 mL of aqueous solution containing 0.4 g of CTAB and the resulting solution was stirred vigorously for 30 min. The formation of an oil-in-water microemulsion resulted in a turbid brown solution. Heating

the brown solution at 60 °C for 20 min induced evaporation of the chloroform, this generated aqueous dispersion of nanoparticles. Then 5 mL of the resulting mixture solution was diluted with 100 mL of water, and the mixture was heated up to 70 °C. Then 3 mL of 2M NaOH solution, TEOS (3 mL) and ethyl acetate (10 mL, 0.1 M) were successively added to the diluted aqueous solution containing the magnetite nanoparticles. The resulting mixture was stirred for 3 h at 70 °C and the precipitate was magnetically separated. The surfactant was removed by extraction with acidic ethanol solution.

Deposition of Luminescent Carbon dot on Fe_3O_4@m-SiO_2: Deposition of luminescent carbon dot (CD) on the surface of mesoporous silica coated magnetic particle (Fe_3O_4@m-SiO_2) was achieved by hydrothermal carbonization of orange juice in the template free channels of the mesoporous silica. In a typical procedure, dispersed Fe_3O_4@m-SiO_2 nanoparticles (200 mg in 10 mL ethanol) were mixed with 25 mL of orange juice (absolutely pulp free) in 20 mL ethanol and then the mixture was transferred into an 80 mL teflon-lined stainless-steel autoclave and was heated at constant temperature of 130 °C for 150 min (1 °C/min). After the reaction, the autoclave was cooled down naturally. The resulted luminescent magnetic nanocomposite (Fe_3O_4@m-SiO_2-CD) was magnetically separated and first washed thoroughly with dichloromethane followed by water to remove the water soluble adsorbed luminescent CDs.

Synthesis of folate and camptothecin conjugated CD decorated magnetic mesoporous silica

In order to conjugate folic acid and CPT, the hybrid Fe_3O_4@m-SiO_2 nanoparticles were initially functionalized with epoxide. A mixture of 0.2 mL (0.88 mmol) 3-glycidoxypropyltrimethoxysilane and Fe_3O_4@m-SiO_2-CD particles (300 mg) in dry toluene (30 mL) was stirred and heated at reflux under dry nitrogen gas with triethylamine as a catalyst for 24 h. The functionalized particles were magnetically separated, washed extensively with acetone, and dried. Prior to synthesis of folate decorated Fe_3O_4@m-SiO_2-CD, amine functionalized folic acid is prepared following the report developed by Mohapatra *et al.*.[39] For conjugation, amine functionalized folic acid (FA-NH_2) (11 mg, 0.02 mmol) dissolved in DMSO was stirred overnight at 70 °C with

dispersed epoxide ended Fe_3O_4-mSiO_2-CD (100 mg) in presence of $ZnCl_2$ catalyst. Finally folate decorated luminescent particles were magnetically separated and washed with water (Fe_3O_4@m-SiO_2-CD-FA). For conjugation of CPT, in a 50 mL two necked round bottom flask, EDBE-glycolic acid-CPT (5) (54 mg, 0.1 mmol) and catalytic amount of $ZnCl_2$ were taken in 5 mL dry DMSO. To this solution 100 mg Fe_3O_4@m-SiO_2-CD-FA nanoparticle in 10 mL DMSO was added and allowed to stir at 70 °C for 20 h in nitrogen atmosphere. Then the particles were recovered using magnetic separator, washed thoroughly with millipore water and suspended in phosphate buffer (pH 7.4) and used for in vitro studies (Fe_3O_4@m-SiO_2-CD-FA-CPT).

In vitro camptothecin (CPT) release

The in vitro delivery of CPT was performed by suspending a suspension of Fe_3O_4@m-SiO_2-CD-FA-CPT particles (5 mL, 1 mg/mL) in a solution containing 0.1 mg/mL cathepsin B and 10 mL of FBS. The solution pH was adjusted to 4, 5, 6 and 7.4 using 0.1 M HCl and NaOH, and then the solution was shaken (100 rpm) at 37 °C. At specified time intervals, accumulated amount of drug released into the solution was quantified using a UV-vis spectrophotometer, λ_{max} (CPT) = 340 nm. The release profiles were plotted as the relative release percentages of CPT against time. The drug loading capacity and encapsulation efficiency were determined as 17.5% and 87.5% respectively by following the method described in chapter-7.

Cytotoxicity

Human cervical carcinoma (HeLa) cells were obtained from the National Centre for Cell Sciences (Pune, India), cultivated in minimal essential medium (MEM) and Dulbecco's modified eagle medium (DMEM) respectively supplemented with 10% fetal calf serum, 100 units/mL penicillin, and 100 µg/mL streptomycin, 4mM L-glutamine under 5% CO_2 and 95% humidified atmosphere at 37 °C. From 105 cells/mL cell-suspension, 180 µL cell-suspension was seeded in each well of 96 wells tissue culture plates and incubated for 18 h followed by addition of Fe_3O_4@m-SiO_2-CD, Fe_3O_4@m-SiO_2-CD-CPT and Fe_3O_4@m-SiO_2-CD-FA-CPT nanoparticle, at concentrations 10 μgmL^{-1} to 50 μgmL^{-1}. The cells were incubated for 72 h at 37 °C in a humidified

incubator (HERA cell) maintained with 5% CO_2. The cell proliferation was estimated by MTT assay as described in chapter-7.

Intracellular uptake

For investigation on cell uptake of Fe_3O_4@m-SiO_2-CD-FA-CPT nanoparticle, the HeLa cells were treated with 5 μg mL^{-1} of nanoparticle for 0, 30, 60, 90 and 120 min. The cells were washed several times with PBS and subsequently treated for 5 min using DAPI (1 $mgml^{-1}$) at 37 °C to stain the nuclei. The cells were washed with PBS to remove extra dye molecules and then fixed with 4% paraformaldehyde for 15 min. Then cells were washed with PBS and examined under fluorescence microscopy.

DAPI staining for nuclear morphology

To study the nuclear morphology of the HeLa cells, DAPI staining was performed following the reported procedure. HeLa cells treated with PBS, 1, 5, 10 μg/mL of drug conjugated particles for 24 h. The cells were fixed with 3.7% formaldehyde for 15 min, permeabilized with 0.1% Triton X-100 and stained with 1 mg/mL DAPI for 5 min. The cells were then washed with PBS and examined under fluorescence microscopy.

Quantum Yield Calculations

The quantum yield (Φ) of the Fe_3O_4@m-SiO_2-CD was calculated using quinine sulfate as reference.[43] For calculation of quantum yield, five concentrations of each compound were made, all of which had absorbance less than 0.1 nm at 340 nm. Quinine sulfate (literature Φ = 0.54) was dissolved in 0.1 M H_2SO_4 (refractive index (η) of 1.33) while the nanoparticle was taken in water (η = 1.33). Their fluorescence spectra were recorded at same excitation of 340 nm. Then by comparing the integrated photoluminescence intensities (excited at 340 nm) and the absorbance values (at 340 nm) of the sample with the references quinine sulfate quantum yield was determined. The data was plotted (Figure 8.1) and the slopes of the sample and the standards were determined. The data showed good linearity with intercepts of approximately zero.

The quantum yield was calculated using the below equation

$$\Phi_x = \Phi_{ST} \ (m_x / m_{ST}) \ (\eta^2_x / \eta^2_{ST})$$

Where Φ is the quantum yield, m is slope, η is the refractive index of the solvent, ST is the standard and X is the sample. The quantum yield for Fe_3O_4@m-SiO_2-CD is found to be 12.4%.

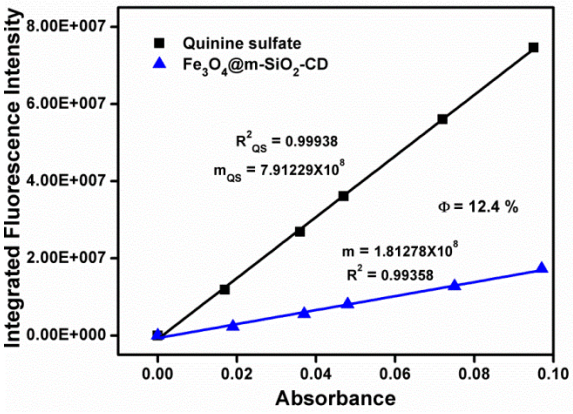

Figure 8.1 Fluorescence and Absorbance of the Fe_3O_4@m-SiO_2-CD and Quinine Sulfate

MR Imaging

The relaxation time (T_2) and transverse relaxivity (r_2) of the nanoparticle were measured with varying iron concentration (0.015-0.075 mM) using a clinical MRI scanner (MAGNETOM Symphony, SIEMENS) at a magnetic field of 1.5 T. T_2-weighted images were obtained with a spin echo multisection pulse sequence having fixed repetition time (TR) of 4000 ms with various echo times (TE) ranging from 105 to 291 (105, 116, 128, 139, 151, 163, 174, 186, 198, 291). The spatial resolution parameters were as follows: field of view (FOV) = 300×300 mm^2, matrix = 358×358, slice thickness = 4.0 mm. The MRI signal intensity (SI) was measured using in-built software. T_2 values were obtained by plotting the SI of each sample over a range of TE values. T_2 relaxation times were then calculated by fitting a first-order exponential decay curve to the plot. The fitting equation can be expressed as:

$$SI = S_0 e^{-TE/T_2} + B$$

Where SI is the signal intensity, TE is the echo time, S_0 is the amplitude, and B is the offset. The relaxivity value r_2 is determined from the slope of the linear plots of relaxation rate R_2 ($1/T_2$, s^{-1}) against Fe concentrations (mM).

$R_2 = R_2^0 + r_2 [Fe]$

Calculation of number of Camptothecin, Folic acid and Fe_3O_4 per hollow sphere

From TGA analysis the weight loss for surface organic modification is 4%

Weight loss of 1 g sample is 0.04 g

During the synthesis, the ratio of camptothecin (CPT) and folic acid (FA) conjugates has been maintained as 5:1

So, total organic content in 1g of drug and folic acid conjugated hybrid nanoparticle is $5 \times mol\ wt\ of\ camptothecin\ conjugate \times x + 1 \times mol\ wt\ of\ folic\ acid\ conjugate$

Using the above equation, we calculated that, 1 g sample contains 4.5×10^{-5} mole of CPT and 9.25×10^{-6} mole of FA

BET surface area of the Fe_3O_4@m-SiO_2-CD hollow sphere is found to be 135 m^2/g

From TEM, the surface area of single hollow sphere is calculated as 9.36×10^{-16} m^2

Total number of hollow sphere present in 1 g sample is $\frac{135}{9.36 \times 10^{-16}} = 1.4 \times 10^{17}$

Thus 9.36×10^{-16} hollow spheres are conjugated with 4.5×10^{-5} and 9.25×10^{-6} mole of CPT and FA respectively.

Each hollow sphere is conjugated with 199 (3.3×10^{-22}mole) and 40 (6.6×10^{-23}mole) numbers of CPT and FA respectively.

From TEM, volume of single Fe_3O_4 nanoparticle is calculated to 4.188×10^{-19} m^3

Mass of single Fe_3O_4 nanoparticle = volume×density = 2.165×10^{-15} mg (density of the magnetite nanoparticle is 5.17 g/cm^3)

From AAS analysis 1 g CPT and FA conjugated nanoparticle contains 348 mg iron

Then number of Fe_3O_4 nanoparticle present in 1 g composite is $\frac{348}{2.165 \times 10^{-15}} = 16 \times 10^{16}$

Thus number of Fe_3O_4 nanoparticle per each hollow sphere is found to be $\frac{16\times10^{16}}{1.4\times10^{17}} = 1.14 \approx 1$

8.3. Characterization

The synthesized materials were characterized by modern spectroscopic technique as described in characterization section of chapter-7. In addition, low angle powder X-ray diffraction (XRD) analysis was carried out with a Philips PW3040/00 diffractometer (operating at 40 kV and 30 mA), using a Cu Kα radiation. The Raman spectrum of as-prepared samples was recorded at ambient temperature on Renishaw in Via Raman microscope (UK make).

8.4. Results and Discussion

Synthesis

Scheme-8.1 illustrates the synthetic strategy of the CPT conjugated fluorescent magnetic hollow nanosphere. The mesoporous silica coated Fe_3O_4 nanoparticles were synthesized through sol-gel method using CTAB as surfactant where it acts as a stabilizing surfactant for the transfer of hydrophobic Fe_3O_4 nanocrystals to the aqueous phase as well as the organic template for the formation of the mesoporous silica spheres. The mesoporous silica coated magnetite nanoparticles were luminescent functionalized by the deposition of CD through hydrothermal treatment of orange juice. It was well established in our previous work that the major constituents orange juice such as sucrose, ascorbic acid and citric acid can act as efficient precursor for carbon dots.[43] The hydrogen bonding interaction between the surface silanol groups and constituents of orange juice facilitates the adsorption of precursors in the mesoporous channels which are converted to carbon dot upon hydrothermal treatment. Thus growth of carbon nanoparticles takes place within the porous frame work of mesoporous silica rather than outside. In order to conjugate CPT and target molecule folic acid, the Fe_3O_4@m-SiO_2-CD hybrid particles

were functionalized with 3-glycidoxy-propyltrimethoxysilane to form epoxy ended Fe_3O_4@m-SiO_2-CD nanoparticles.

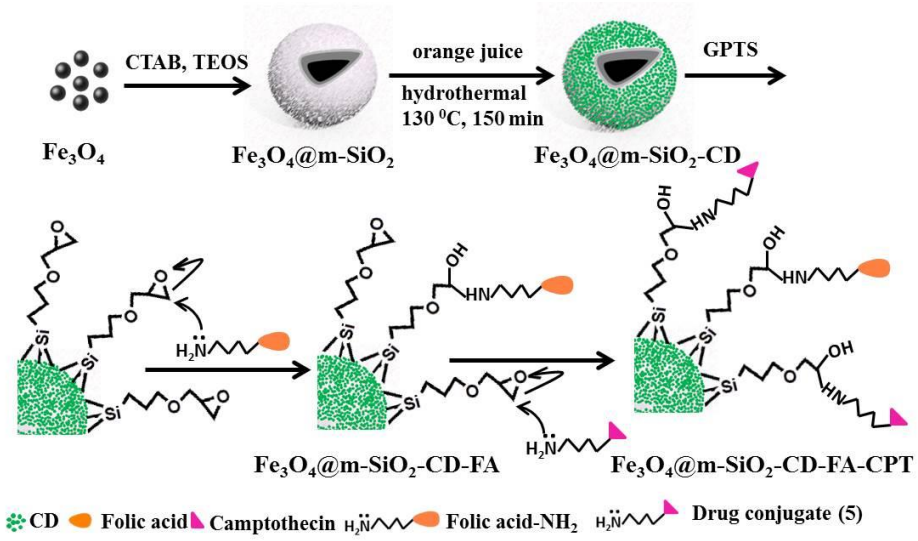

Scheme 8.1 Synthesis of fluorescent magnetic nanoparticles conjugated with CPT and folic acid.

Prior to CPT conjugation on Fe_3O_4@m-SiO_2-CD nanosphere, water soluble CPT conjugate was synthesized (scheme-8.2). It has been reported that the solubility, tumor accumulation and circulatory retention of potent hydrophobic anticancer drug camptothecin dramatically increases by conjugating it with polyethylene glycol (PEG) dicarboxylic acid with the hindered tertiary alcohol at position 20 of ring E through a scissile ester bond.[44] We deemed to synthesize the water soluble form of CPT by coupling a small highly hydrophilic spacer (2,2'-(ethylenedioxy)-bis-(ethylamine) (EDBE) through a linker diglycolic acid (scheme 2). For this purpose diglycolic anhydride was first opened with tertiary butyl alcohol to give the protected ester acid 1, followed by condensation with camptothecin in presence of DIPC and subsequent ester cleavage to give slightly water soluble derivative 3. To this tert-butyl N-{2-[2-(2-aminoethoxy)ethoxy]ethyl}-carbamate (EDBE-Boc) has been coupled using carbodiimide to give 4 which after deprotection of Boc gives water soluble CPT derivative 5.

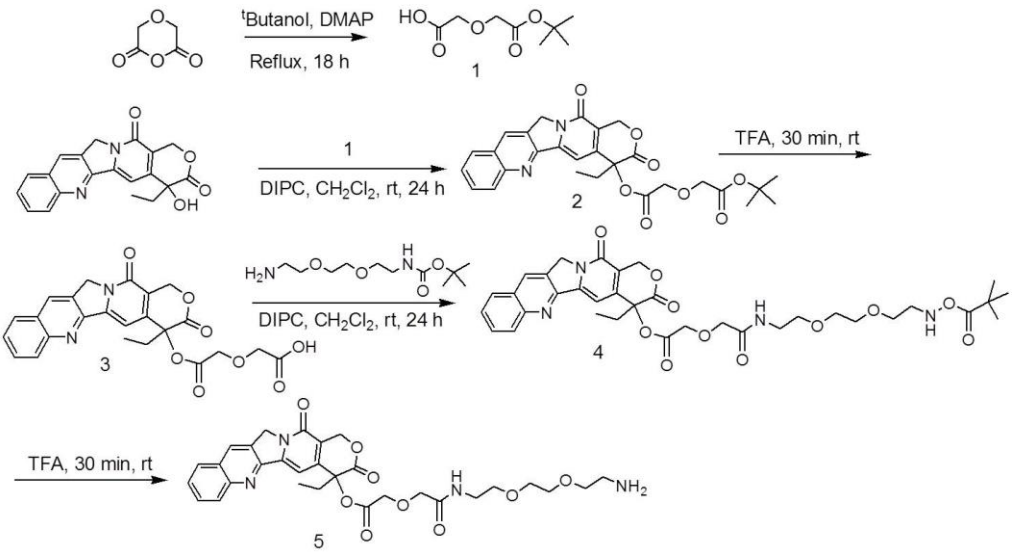

Scheme 8.2 Synthesis of camptothecin conjugated with EDBE.

In ordered to impart target specific delivery of the multifunctional particle (Fe_3O_4@m-SiO_2-CD), the particles were coupled with FA-NH_2 through epoxide ring opening in presence of catalytic amount of $ZnCl_2$. In a similar fashion, the water soluble CPT conjugate 5 has also been coupled (Scheme-8.1).

This synthetic strategy would have several advantages like

- It will overcome the difficulties of functionalization with high molecular weight (> 1000Da) PEG[44]
- It can ensure a particle of controllable size which is not possible with high molecular weight polymers,
- The drug cannot be escaped during the circulation before reaching the target site as it is strongly bound through covalent bond,
- It will release CPT in its active lactone form through a predictable hydrolysis of ester bond with in the tumor cell.

Investigation of phase by XRD and Raman spectroscopy

The formation of nanocomposite and possible phase change during hydrothermal carbonization of orange juice was examined by XRD. In the wide angle X-ray diffraction pattern of the Fe_3O_4@m-SiO_2-CD (Figure 8.2a), the diffraction peaks could be indexed to

crystalline cubic spinel structure of Fe_3O_4. Apart from characteristic peaks of Fe_3O_4, the broad band at 18-22° can be assigned to amorphous silica shell (JCPDS No. 29-0085) and CD. In the low-angle XRD patterns (Figure 8.2b), two well-resolved diffraction peaks between 0.5 to 4.0° representing long range ordering of the mesoporous structure are observed. The peaks can be indexed to (100) and (110) reflections. These peaks have d-spacing ratios 1:√3 associated with ordered 2D hexagonal mesostructure (p6mm). The higher intensity of (110) reflection peak and the broadening of the peak in the composite compared to reported mesoporous silica may be attributed to the non-uniform distribution of matter in the unit cell and less structural ordering respectively due to carbonization under hydrothermal condition.

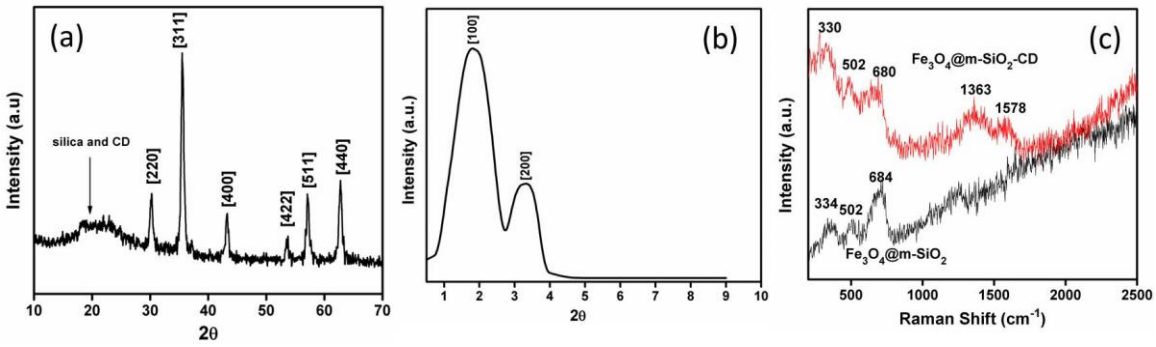

Figure 8.2 (a) Wide angle X-ray diffraction and (b) Low angle XRD pattern of Fe_3O_4@m-SiO_2-CD, (c) Raman spectra of Fe_3O_4@m-SiO_2 and Fe_3O_4@m-SiO_2-CD.

In the wide angle XRD, the broad peak for carbon dot at 2θ=20-24° overlaps with amorphous mesoporous silica range, presence of CD cannot be distinguished from XRD pattern. However, appearance of two characteristic vibrations at 1363 and 1578 cm^{-1} for a defect band (D band) and a graphite band (G band) in the Raman spectrum (Figure 8.2c) confirms the deposition of CD on the silica coated magnetite. The G band is attributed to the vibration of sp^2-bonded carbon atoms in a 2D hexagonal lattice, while the D band is associated with vibrations of carbon atoms with dangling bonds in plane terminations of the disordered graphite. The I_D/I_G ratio was found to be 1.6, which is almost higher than that reported for bare CD. The relative high D-band intensity may be due to small particle size and the presence of abundant oxygen containing groups on the surface.[43] Furthermore, the distinct peaks at 684, 530 and 320 cm^{-1} correspond to magnetite core of the Fe_3O_4@m-SiO_2-CD nanoparticles.

Microstructure

The shape and size of the as-prepared Fe_3O_4@m-SiO_2-CD particles were characterized by TEM analysis. As shown in Figure 8.3a, typical TEM reveals the formation of clear and spherical hollow silica spheres with a size range of 100-150 nm which is appropriate for drug and gene delivery.[45,46] Each silica sphere contains one or more magnetite nanocrystals embedded within its structure. The hollow structure arises because of trapping of ethyl acetate within the hydrophobic part of the mesophase during the sol-gel reaction[42] and remains structurally stable during the hydrothermal treatment. The porous nature of the silica is clear in the image at higher magnification (Figure 8.3a inset). The high resolution TEM image shows dark spotted ruffled surface which clearly reveals that CDs were successfully grown and embedded in the mesoporous channels of the hollow silica sphere (Figure 8.3b).

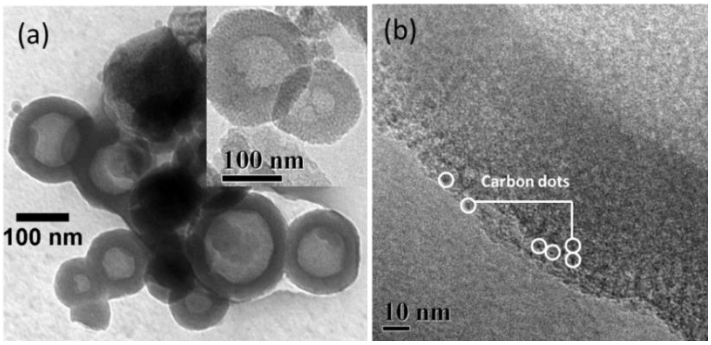

Figure 8.3 (a) TEM images of Fe_3O_4@m-SiO_2-CD, inset TEM image at higher magnification (b) TEM image at higher magnification representing deposition of CDs in the mesopores.

Hydrodynamic size and stability

The hydrodynamic (HD) size of the nanoparticles after each step of the synthesis indicates the presence of stable non-aggregated particles which facilitates complete modification of the surface. In addition to this, HD size slightly increases after each modification indicating addition of one molecular layer after each step (Figure 8.4a). The CPT drug conjugated particle showed a mean HD size of 122 nm, which is not significantly affected with change of pH (3-9) (Figure 8.4b). These functional nanoparticles were highly stable in aqueous medium as their HD size remains almost

constant over a long time (Figure 8.4c). The zeta potential measurement of CPT-modified particles shows positive zeta potential of +12.5 mV owing to the presence of surface -NH_2 group from folic acid. With decrease in pH up to 2.8 the zeta potential increases to 36.37 indicating the protonation of the free -NH_2 groups. At the same time with increase in pH the zeta potential becomes negative due to opening of lactone ring of CPT giving rise to free acid (Figure 8.4d).

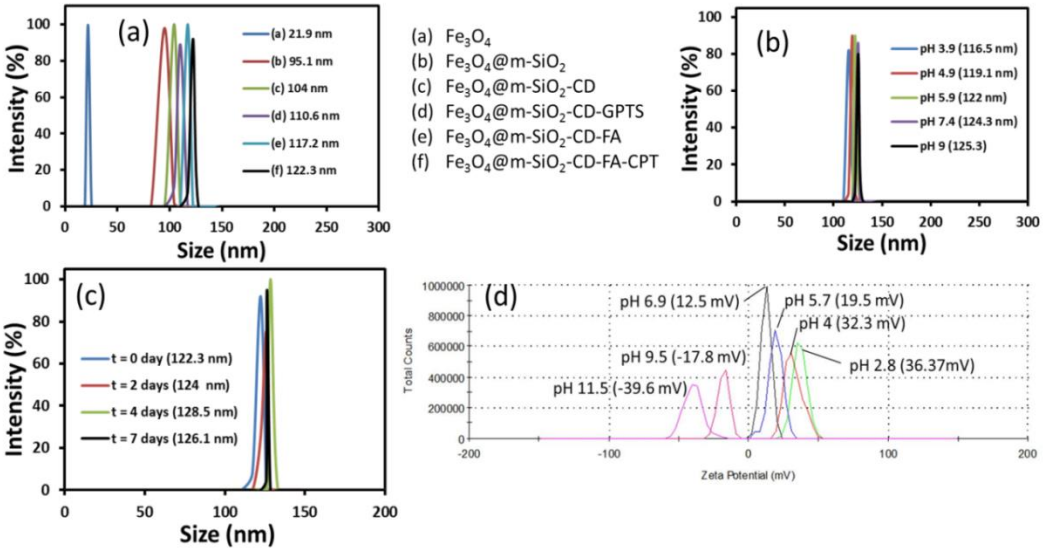

Figure 8.4 (a) Change in hydrodynamic size of the drug carrier at various stages of synthesis, Variation of the HD size of drug conjugate (b) with pH, (c) with time, (d) Measurement of zeta potential of the drug loaded nanoparticle against pH.

BET surface area

The nitrogen adsorption-desorption measurement was used to investigate the porosity of the sample. The synthesised Fe_3O_4@m-SiO_2 particles exhibit type IV isotherm with a hysteresis (Figure 8.5a), which is a characteristics of mesoporous materials. The BET surface area was found to be 595 m^2/g. BJH pore size distribution determined from the desorption branch of the isotherm showed the formation of mesopores with maximum diameter centered at 5.6 nm and volume at 0.47 cc/g (Figure 8.5b). However after carbonization the nature of the adsorption-desorption isotherm of Fe_3O_4@m-SiO_2-CD changes to type III due to formation of slit like pores. The BET surface area as well as pore diameter is decreased to 135m^2/g and 4.72 nm respectively for Fe_3O_4@m-SiO_2–CD particles. The substantial decrease in surface area and pore size

is due to deposition of carbon dots on the inner surface of mesoporous silica. Though there is decrease in pore size and pore volume due to shrinkage of mesoporous wall during hydrothermal treatment and deposition of carbon dots still the surface area is reasonable for drug delivery applications.

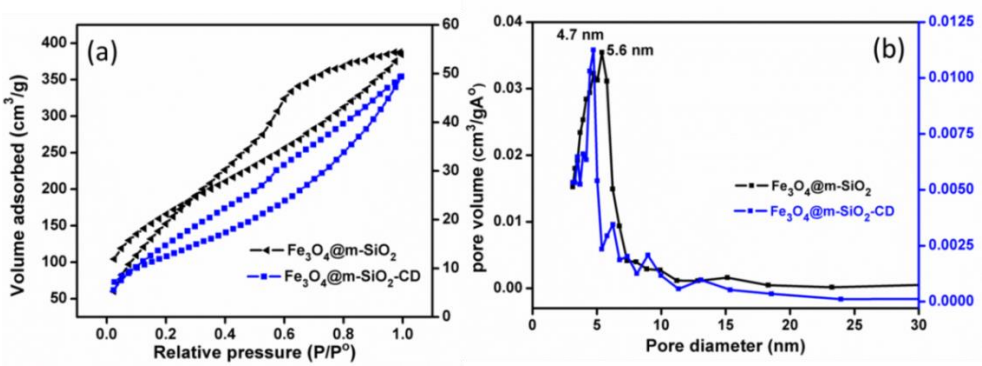

Figure 8.5 (a) N_2 adsorption-desorption isotherm and (b) pore size distribution of Fe3O4@m-SiO2 before and after CD deposition.

FTIR study

Figure 8.6 shows FTIR spectra at various stages of synthesis of Fe_3O_4@m-SiO_2-CD-FA-CPT which clearly establish the conjugation of the CPT and FA on the surface of the hybrid nanoparticles. Appearance of the broad bands centered at 3416 cm^{-1} in Fe_3O_4@m-SiO_2-CD suggest that a large number of OH groups and H_2O molecules exist on the surface, which not only play the major role in high aqueous stability but also provides enough scope for further functionalization of the particle. The broadness of the peak at 1620 cm^{-1} indicates the presence of functional groups like -COOH, -epoxy, carbonyl and hydroxyl groups on the surface as reported in case of hydrothermal synthesis of CD. The presence of these functional groups also increases its solubility in water. The appearance of methylene peak at 2917 and 2850 cm^{-1} along with ring breathing frequency of epoxide at 1195 cm^{-1} and 1709 cm^{-1} corresponding formation of O=C-O-Si[47] in epoxy-functionalized particles indicates the surface modification with GTPS. The band at 3540, 3423 and 3315 cm^{-1} in the spectrum of folic acid corresponding to ring O-H, N-H groups cannot be distinguished in the Fe_3O_4@m-SiO_2-CD-FA conjugate due to broadness of the peak. However, peaks corresponding to aromatic C=C stretching and N-H bending are prominent in Fe_3O_4@m-SiO_2-CD-FA. The disappearance

of epoxide ring breathing peak in Fe_3O_4@m-SiO_2-CD-FA-CPT shows the opening of the epoxide ring by the camptothecin conjugate 5 as presented in the scheme 8.1. Further, the appearance of C=O stretching at 1760 cm^{-1} correcsponding to lactones along with intensification of both methylene and aromatic C=C stretching band confirms the attachment of CPT on hybrid nanoparticles in its lactone form.

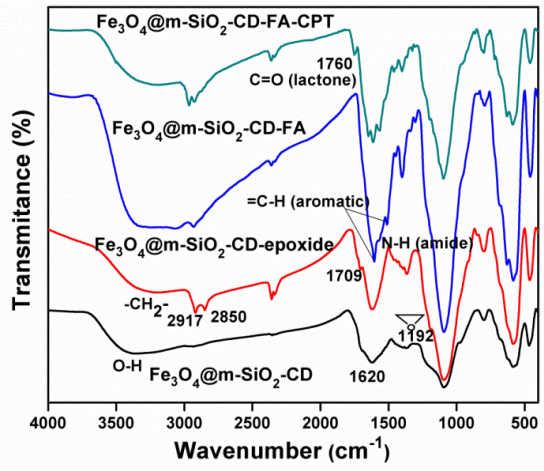

Figure 8.6 FTIR spectra of Fe_3O_4@m-SiO_2-CD-FA-CPT nanoparticles at various stages of synthesis.

X-ray photoelectron spectroscopy

X-ray photoelectron spectra were further used to validate the surface modification of nanoparticle with CPT and folic acid. In a typical survey spectrum of Fe_3O_4@m-SiO_2-CD-FA-CPT particles (Figure 8.7a), the peaks at binding energies 100, 280-290, 400.3, 529-538, 705-730 eV correspond to binding energy of Si2p, C1s, N1s, O1s and Fe2p electrons with their atomic percentage 8.29, 59.37, 7.3 , 24.86, and 0.3 respectively. The high resolution scans of N1s region can be fitted into three peaks. The broad peak at 398.4 corresponds to -NH_2 in the folic acid, secondary amines in the linker and -NH_2 group of unreacted/physically adsorbed compound 5 and FA-NH_2 (Figure 8.7b). The peak appearing at 399.1eV is attributed to nitrogen present in the aromatic ring while the amide nitrogen appears at slightly higher energy 400.1 eV due to electron pulling effect of oxygen. Multiple Si2p photoemissions were observed corresponding to Si atoms bonded to C (Si-C, 99.3 eV) and Si atoms bonded to O (Si-O, 101.7 eV) (Figure 8.7c). The Fe2p region shows two peaks at 710.6 and 724 eV which is consistent with the Fe2p

binding energy of Fe_3O_4 nanoparticle (Figure 8.7d). The distinct high binding energy at about 287.7 and 286.6 eV were characteristic of the -COOH/-COOR and -C=O/NHCO group of CPT and folic acid which indicated their successful grafting onto the surface of nanoparticle (Figure 8.7e). In addition to this the high resolution C1s shows emissions centered at 284.3, 284.6 and 285.9 corresponding to the C-C/C-H, C=C, C-N/C=N/C-O carbon. Furthermore, high resolution O1s photoemissions were also obtained corresponding to C-C=O, -OH (530.4, 532 eV) bond and a C-O-C=O bond (532.7 eV) (Figure 8.7f), which also confirmed the existence of folic acid and CPT.

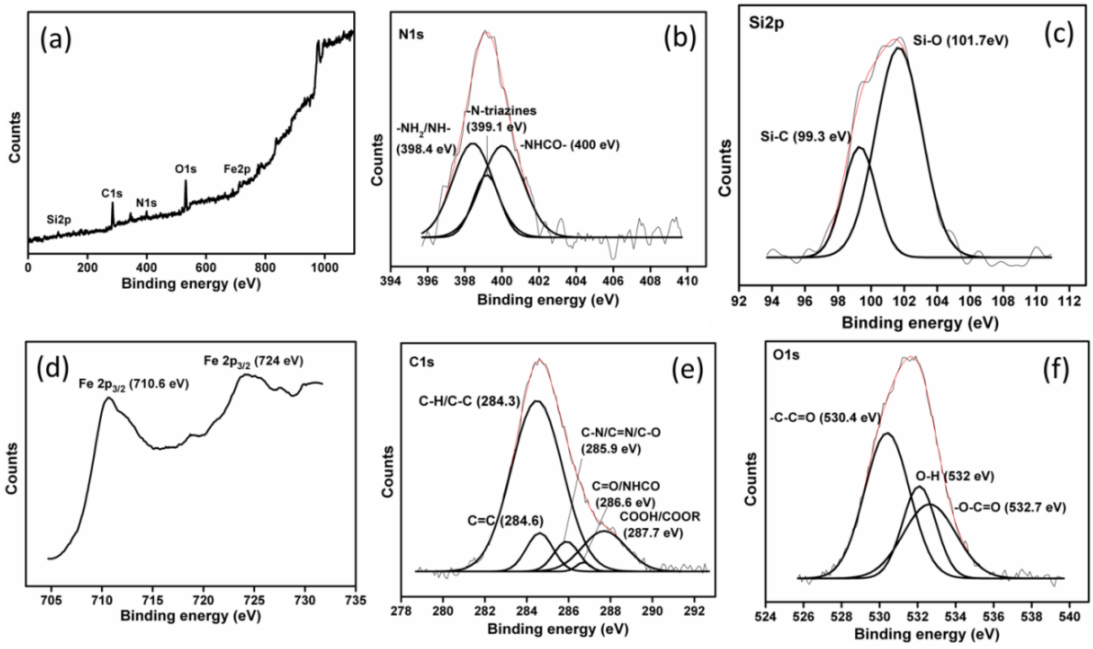

Figure 8.7 (a) XPS survey spectrum and High resolution scan of Fe_3O_4@m-SiO_2-CD-FA-CPT corresponding to (b) N1s, (c) Si2p, (d) Fe2P, (e) C1s, (f) O1s.

Photoluminescence and magnetic properties

The PL excitation spectrum recorded at λ_{em} of 400 nm shows three excitonic bands centered at 370, 350 and 338 nm. This behaviour indicates that there are at least three types of excitation energy trapped on the surface of the synthesized particle. When the sample is excited at 360 nm, there is a strong emission peak around 443 nm indicating a blue light emission (Figure 8.8a). Unlike other semiconductor nanoparticles the photoluminescence in case of carbon dots is a combined effect of quantum confinement and surface defects that originate energy levels in between valence and conduction band

that justifies light emission.[48] These electronic level distributions allow radiative recombination of excitons.[49,50] Compared to bare CD prepared from orange juice,[43] the emission spectrum of the Fe_3O_4@m-SiO_2-CD shows a narrower FWHM due to narrow size distribution upon growth of CD in a mesoporous template. The mesoporous silica not only confines the growth of CDs with narrow distribution in the pores of silica but also prevents the aggregation of the nanosized CDs. The excitation dependent emission (Figure 8.8b) of Fe_3O_4@m-SiO_2-CD particles can be ascribed to surface states apart from reasons like free zig zag sites, aromatic conjugate structure, radiative recombinations as in case of carbon dots. Due to presence of several surface functional groups like C-OH, C-O-C, C=O, and C-H, a series of emissive traps between π and π^* states C=C are originated. When a certain excitation wavelength illuminates the CD a surface energy trap will dominate the emission. As the excitation wavelength changes, another corresponding surface state emissive trap will become dominant. In case of the hybrid particle the position of emission peak varied only slightly by altering the excitation indicating more uniform size distribution and less availability of free surface functional groups. However this excitation dependent emission gives rise to several visible consequences in fluorescence imaging and makes the material suitable as a bioimaging probe. The synthesized hybrid nanoparticle showed excellent photostability as there was no significant change in fluorescence intensity even after continuous excitation at 360 nm for 3 h (Figure 8.8c). The fluorescence microscopy image of synthesized Fe_3O_4@m-SiO_2-CD shows strong green luminescence. Also the aqueous dispersion of the particles emitted green fluorescence on irradiation under UV lamp (Figure 8.8d).

The field dependent magnetization for both hybrid nanoparticle and CPT conjugated nanoparticle did not show hysteresis (Figure 8.8e), which represented their superparamagnetic characteristics desirable for their application in drug delivery. Thus the surface modification had no detrimental effect on the intrinsic superparamagnetism of Fe_3O_4. However the saturation magnetisation (Ms) value of Fe_3O_4@m-SiO_2-CD (2.2 emu g^{-1}) was decreased to 0.9 emu g^{-1} on conjugation of folic acid and CPT. This decrease in saturation magnetization can be attributed to the combined effect of decrease in magnetic content as well as restriction in inter-particle magnetic coupling interaction due to surface modification by organic moiety. Furthermore, appreciably high deposition of CD on the

surface of Fe_3O_4@m-SiO_2 is also responsible for this substantial reduction in magnetic saturation value. Fortunately, the saturation magnetisations value of the synthesized Fe_3O_4@m-SiO_2-CD-FA-CPT nanoconjugate fulfil the requirements for drug delivery, separation and MRI application.[51]

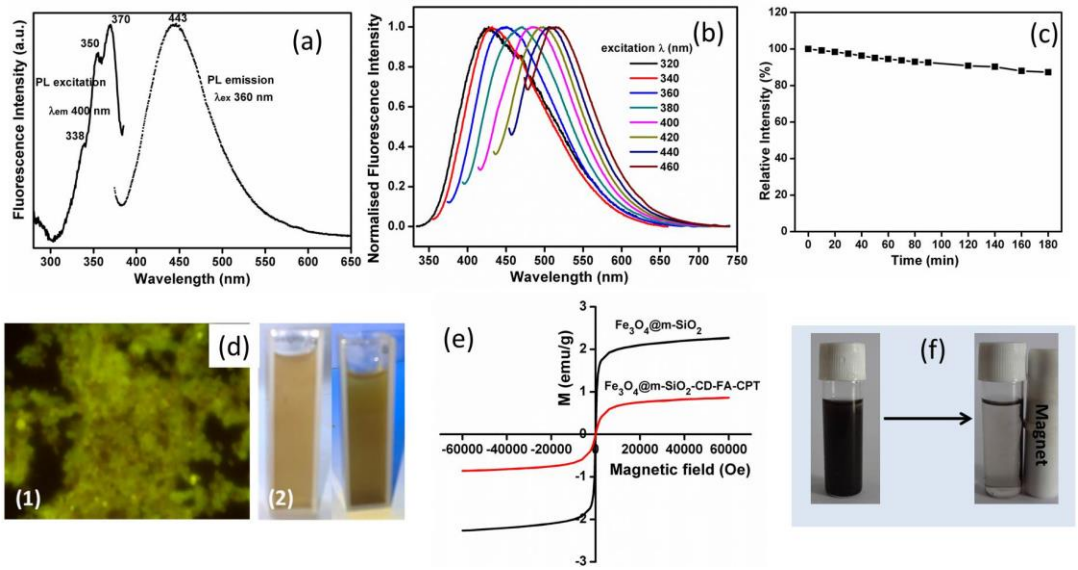

Figure 8.8 (a) Excitation-emission spectra, (b) wavelength dependent emission, (C) Effect of time on fluorescence intensity of Fe_3O_4@m-SiO_2-CD-FA-CPT particle, (d) (1) Typical Fluorescence microscopy image and (2) digital photograph under daylight (left) and UV lamp (right) of Fe_3O_4@m-SiO_2-CD, (e) Room temperature magnetization behaviors, (f) Interaction of Fe_3O_4@m-SiO_2-CD-FA-CPT particles with external magnetic field.

Camptothecin loading and release

The hollow mesoporous fluorescent magnetic carrier can be used as a drug delivery and are able to carry a high payload of guest molecules (17.5%). Such high CPT loading is resulting from the high surface area of hollow mesoporous silica which facilitates more interior spaces and conjugation sites. It is noteworthy that such high drug loading capacity will allow small doses of Fe_3O_4@m-SiO_2-CD-FA-CPT circumventing the toxicity arising due to high doses of mesoporous silica.[52] The drug encapsulation efficiency of the carrier reached 87.5%. The choice of cleavable ester bonds is perhaps the most promising strategy to release CPT at right place and right time through the enzymatic cleavage inside the lysosome. The imperative benefit of fluorescent magnetic CPT-conjugate is that it prevents premature release of CPT before reaching the target. In absence of cathepsin B less than 19% of the drug was released after 20 h incubation time

which gradually increased to 52% by the end of 100 h (Figure 8.9a). At the same time when the lysosomal condition was mimicked in presence of enzyme cathepsin B almost a burst release of 50% was observed in first 20 h which slowly increased to 92% with 100 h incubation time at neutral pH. The drug release is higher at neutral pH and less acidic pH in accordance to other systems where drug is covalently attached to the carrier through ester linkage.[28] At pH 5.3, a burst release of 25% was observed after 10 h, which gradually increased to 83% after 80 h. When the pH is decreased to 3.9, the release rate of CPT is decreased slightly to 22% at 10 h, which reached to 74% after 80 h. Although the cumulative release of CPT is less than the same at alkaline pH, but the release behavior of our system at pH 4-5 is comparable or even better than the delivery systems already reported for camptothecin.[28-33] These results indicate that our Fe_3O_4@m-SiO_2-CD-FA-CPT nanoparticles can be used as a carrier for CPT without premature release of the drug in the blood vessel and also shows a sustained release pattern over a prolonged time inside the lysosomal compartment.

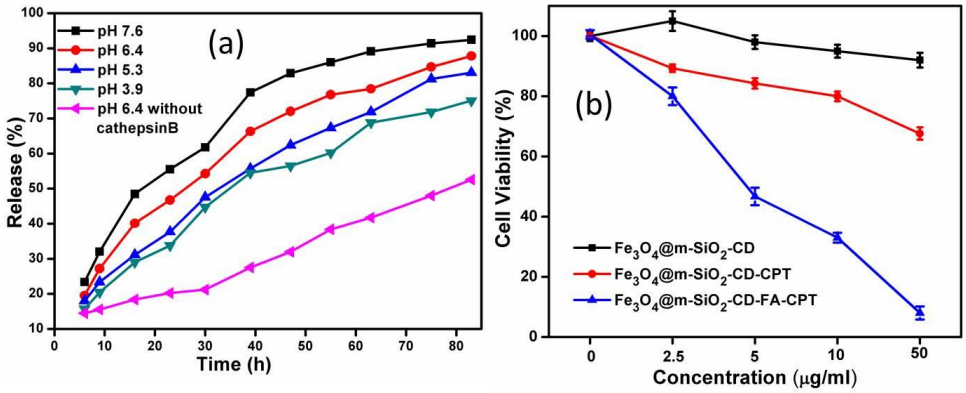

Figure 8.9 (a) Cumulative CPT releases from Fe_3O_4@m-SiO_2-CD-FA-CPT, (b) In vitro cell viability of HeLa with as prepared Fe_3O_4@m-SiO_2-CD, Fe_3O_4@m-SiO_2-CD-CPT and Fe_3O_4@m-SiO_2-CD-FA-CPT nanoparticles.

Cytotoxicity

To test the efficacy of CPT cleavage inside the target cells, HeLa cells were cultured with Fe_3O_4@m-SiO_2-CD, Fe_3O_4@m-SiO_2-CD-CPT and Fe_3O_4@m-SiO_2-CD-FA-CPT in a folate deficient medium. Nanoparticles deprived of CPT were found to be extremely noncytotoxic indicating the biocompatibility of the synthesized nanocarrier (Figure 8.9b). As expected, the delivery of the CPT loaded particles to HeLa cells leads

to cell growth inhibition and finally to cell death through formation of CPT stabilized topoisomerase I-DNA covalent complex. The observed reduced cellular viability in case of drug loaded particle (Fe_3O_4@m-SiO_2-CD-CPT) established the ability of the cells to induce enzymatic cleavage of CPT. However, the proliferation of HeLa cells reduced drastically in a dose dependent manner when incubated with Fe_3O_4@m-SiO_2-CD-FA-CPT. This is attributed to the active uptake of nanoparticles in a folate receptor mediated endocytosis in the folate receptor over expressed HeLa cell that interfered with the cell proliferation. The IC_{50} value (the concentration at which cell growth is uninhibited by 50%) of our nanomedicine is found to be 2.1 μg/mL.

In vitro Intracellular uptake and cell apoptosis

Figure 8.10 illustrated fluorescence images of HeLa cells incubated with Fe_3O_4@m-SiO_2-CD-FA-CPT nanoparticles in a time dependent manner and DAPI was used as a nuclear contrast dye to appreciate localisation. Green fluorescence was detected in the cytoplasm of cells after 30 min demonstrating their cellular internalization through folate receptor mediated endocytosis. The green emission comes from carbon dots and it was progressively increased in the cytoplasm with longer incubation time.

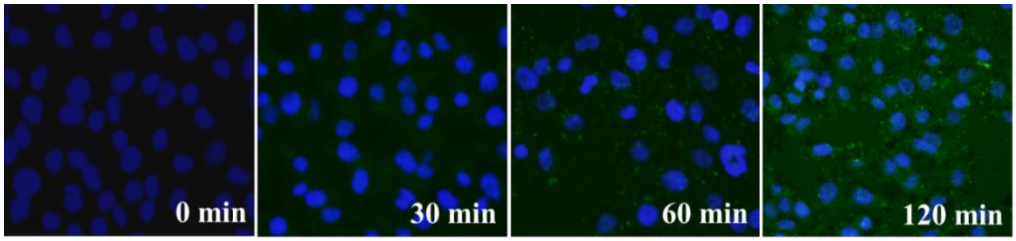

Figure 8.10 Representative fluorescence images of HeLa cells incubated with Fe_3O_4@m-SiO_2-CD-FA-CPT in different time intervals.

To verify whether Fe_3O_4@m-SiO_2-CD-FA-CPT could induce cell death through initiation of apoptosis, HeLa cells were exposed to the drug loaded nanoparticle (1-10 μgmL^{-1}) for 24 h, washed to remove the noninternalized nanoparticles and subsequently visualized using fluorescence microscopy. The cells showed nuclear fragmentation which is a trademark of apoptosis. With a dose dependent manner an increase in the formation of fragmented nuclei containing condensed nuclear material was observed in fluorescence microscopy after nuclear staining with DAPI (Figure 8.11).

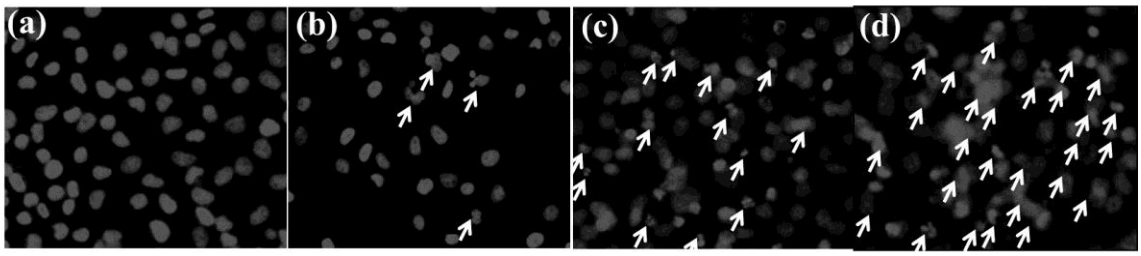

Figure 8.11 DAPI fluorescence (200X) images of HeLa cells incubated with (A)PBS, (B) 1, (C) 5, and (D) 10 μg/mL Fe_3O_4@m-SiO_2-CD-FA-CPT for 24 h. The arrows represent apoptotic features such as nuclear condensation, fragmentation etc.

In vitro MRI

As an initial investigation towards potential imaging functionality during chemotherapy, the visibility of nanocapsules was tested in water and HeLa cells by MRI. As shown in Figure 8.12, with increasing concentration of Fe_3O_4@m-SiO_2-CD-FA-CPT in the phantom solution, the signal intensity decreased indicating that the magnetic hollow spheres have generated magnetic resonance contrast on transverse (T_2) proton relaxations times weighted sequence due to the dipolar interaction of magnetic moments between the nanoparticles and proton in the water.[53] The T_2 relaxation time was inversely proportional to the particle concentration as expected. The transverse relaxivity (r_2) of the drug conjugate is found to be 150.03 $mM^{-1}S^{-1}$ resulting in better negative contrast effect than commercially available dextran coated iron oxide such as feridex (r_2 = 120 $mM^{-1}S^{-1}$), combidex (65 $mM^{-1}S^{-1}$), CLIO-tat (62 $mM^{-1}S^{-1}$).[54]

To confirm the association of these nanoparticles with FR-overexpressing HeLa cells, MR phantom imaging was carried out. MR phantom samples were prepared by incubating HeLa cells with the magnetic nanocapsules in agarose. The T_2-weighted phantom images of cells incubated with Fe_3O_4@m-SiO_2-CD-FA-CPT showed a significant negative contrast enhancement with increase in dose. In addition to this, maximizing the intake of nanoparticles with time through folate receptor mediated edocytosis in a folate-receptor overexpressed cancer cell would further enhance the contrast in MRI.[55]

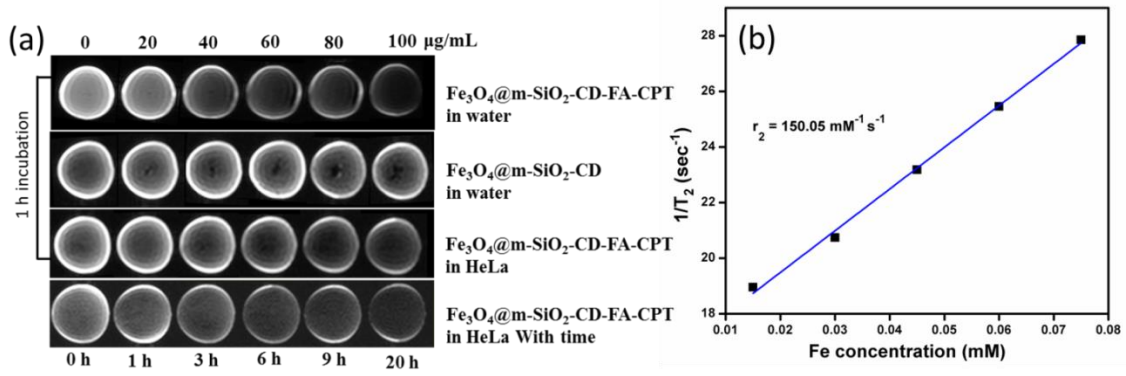

Figure 8.12 (a) MR phantom images of Fe_3O_4@m-SiO_2-CD-FA–CPT particles in water and HeLa cells (b) Relaxivity (r_2) measurement of Fe_3O_4@m-SiO_2-CD-FA–CPT.

8.5. Conclusion

- The hollow mesoporous silica-based luminescent magnetic hybrid nanoparticles have been synthesized by incorporating iron oxide nanoparticle as magnetic component and carbon dot as the luminescent component.
- The particles show MR contrast behaviour by affecting the proton relaxation with transverse relaxivity (r_2) 150.03 $mM^{-1}S^{-1}$.
- Water soluble conjugate of CPT has been synthesied through a scissile ester bond by coupling a small highly hydrophilic spacer (2,2'-(ethylenedioxy)-bis-(ethylamine) (EDBE) through a linker diglycolic acid. This surface engineering design promotes a reliable strategy for the administration of water insoluble drug camptothecin.
- The synthesized fluorescent magnetic nanoparticles have been conjugated with hydrophobic drug camptothecin and a molecular marker folic acid using appropriate surface chemistry.
- These multifunctional nanoparticles are not only extremely stable in aqueous buffer but also possess appreciably good cytotoxicity through induction of apoptosis.
- The dual optical and magnetic properties of the developed multifunctional hollow nanosphere may be utilized in advanced imaging technologies to track the curative responses.

8.6. References

1. P. P. Yang, Z. W. Quan, Z. Y. Hou, C. X. Li, X. J. Kang, Z. Y. Cheng, J. Lin, *Biomaterials*, 2009, **30**, 4786-4795.
2. Q. He, J. Shi, *J. Mater. Chem.*, 2011, **21**, 5845-5855.
3. X. W. Lou, L. A. Archer, Z. Yang, *Adv. Mater.*, 2008, **20**, 3987-4019.
4. K. An, T. Hyeon, *Nano Today*, 2009, **4**, 359-373.
5. J. E. Lee, N. Lee, H. Kim, J. Kim, S. H. Choi, J. H. Kim, T. Kim, I. C. Song, S. P. Park, W. K. Moon and T. Hyeon, *J. Am. Chem. Soc*., 2010, **132**, 552-557.
6. J. Fang, M. Saunders, Y. Guo, G. Lu, C. L. Raston and K. S. Iyer, *Chem. Comm.*, 2010, **46**, 3074-3076.
7. C. Xu, S. Sun, *Adv. Drug Delivery Rev.*, 2013, **65**, 732-743.
8. M. J. Sailor, J. H. Park, *Adv. Mater.*, 2012, **24**, 3779-3802.
9. Y. Wang, A. Hu, *J. Mater. Chem. C*, 2014, **2**, 6921-6939.
10. J Shen, Y Zhu, X Yang, C Li. *Chem Commun.*, 2012, **48**, 3686-3699.
11. S. N. Baker, G. A. Baker, *Angew. Chem. Int. Ed.*, 2010, **49**, 6726-6744.
12. Z. Yang, Z. Li, M. Xu, Y. Ma, J. Zhang, Y. Su, F. Gao, H. Wei, L. Zhang, *Nano-Micro Lett.*, 2013, **5**, 247-259.
13. K. K. R. Datta, O. Kozak, V. Ranc, M. Havrdova, A. B. Bourlinos, K. Safarova, K. Hola, K. Tomankova, G. Zoppellaro, M. Otyepka, R. Zbořil, *Chem. Commun.*, 2014, **50**, 10782-10785.
14. R. Liu, H. Huang, H. Li, Y. Liu, J. Zhong, Y. Li, S. Zhang, Z. Kang, *ACS Catal.*, 2014, **4**, 328-336.
15. S. Zhu, Q. Meng, L. Wang, J. Zhang, Y. Song, H. Jin, K. Zhang, H. Sun, H. Wang, B. Yang, *Angew. Chem. Int. Ed.*, 2013, **52**, 3953-3957.
16. C. Lai, Y. H. Hsiao, Y. K. Peng and P.T. Chou, *J. Mat. Chem.*, 2012, **22**, 14403-14409.
17. A. Mewada, S. Pandey, M. Thakur, D. Jadhav, M. Sharon, *J. Mater. Chem. B*, 2014, **2**, 698-705.
18. L. Zhou, Z. Li, Z. Liu, J. Ren, X. Qu, *Langmuir*, 2013, **29**, 6396-6403.

19. S. Karthik, B. Saha, S. K. Ghosh, N. D. P. Singh, *Chem. Commun.*, 2013, **49**, 10471-10473.
20. S. Pandey, M. Thakur, A. Mewada, D. Anjarlekar, N. Mishra, M. Sharon, *J. Mater. Chem. B,* 2013, **1**, 4972-4982.
21. D. Wang, Y. Guo, W. Liu, W. Qin, *RSC Adv.*, 2014, **4**, 7435-7439.|
22. Y. Ma, Y. Liu, X. Zhou, C. Liu, *Micro Nano Lett.*, 2013, **8**, 302-304.
23. H. Wang, Z. Wei, H. Matsui, S. Zhou, *J. Mater. Chem. A*, 2014, **2**, 15740-15745.
24. S. Srivastava, R. Aswasthi, D. Tripathi, M. K. Rai, A. Agarwal, V. Agrawal, N. S. Gaibhiye and R. K. Gupta, *Small*, 2012, **8**, 1099-1109.
25. H. Wang, J. Shen, Y. Li, Z. Wei, G. Cao, Z. Gai, K. Hong, P. Banerjee, S. Zhou, *Biomater. Sci.*, 2014, **2**, 915-923.
26. V. J. Venditto, E. E. Simanek, *Mol. Pharm*., 2010, **7**, 307-349.
27. Z. Mi, andT. G. Burke, *Biochemistry*, 1994, **33**, 10325-10336.
28. P. Botella, I. Abasolo, Y. Fernandez, C. Muniesa, S. Miranda, M. Quesada, J. Ruiz, S. Schwartz Jr, A. Corma, *J. Control Release*, 2011, **156**, 246-257.
29. A. R. Khan, J. P. Magnusson, S. Watson, A. M. Grabowska, R. W. Wilkinson, C. Alexander, D. Pritchard, *Polym. Chem.*, 2014, **5**, 5320-5329.
30. N. Vijayalakshmi, A. Ray, A. Malugin and H. Ghandehari, *Bioconjugate Chem.*, 2010, **21**, 1804-1810
31. Y. Li, T. Su, S. Li, Y. Lai, B. He, Z. Gua, *Biomater. Sci.*, 2014, **2**, 775-783.
32. J. Pennakalathil, E. Jahja, E. S. Ozdemir, O. Konu, D. Tuncel, *Biomacromolecules*, 2014, **15**, 3366-3374.
33. R. Khandelia, A. Jaiswal, S. S. Ghosh, A. Chattopadhyay, *J. Mater. Chem. B*, 2014, **2**, 6472-6477.
34. Z. Liu, C. Dong, X. Wang, H. Wang, W. Li, J. Tan, J. Chang, *ACS Appl. Mater. Interfaces*, 2014, **6**, 2393-2400.
35. L. Tang, T. M. Fan, L. B. Borst, J. Cheng, *ACS Nano*, 2012, **6**, 3954-3966.
36. S. Dongbang, H. M. Jeon, M. H. Lee, W. S. Shin, J. K. Kwon, C. Kang, J. S. Kim, *RSC Adv.*, 2014, **4**, 18744-18748.
37. J. M. Shen, X. M. Guan, X. Y. Liu, J. F. Lan, T. Cheng and H. X. Zhang, *Bioconjugate Chem.*, 2012, **23**, 1010-1021.

38. A. M. Derfus, W. C. W. Chan and S. N. Bhatia, *Nano Lett.*, 2004, **4**, 11-18.
39. S. Mohapatra, S. K. Mallick, T. K. Maiti, S. K. Ghosh, P. Pramanik, *Nanotechnology*, 2007, **18**, 385102-385111.
40. R. B. Greenwald, A. Pendri, C. D. Conover, C. Lee, Y. H. Choe, C. Gilbert, A. Martinez, J. Xia, D. Wu and M. Hsue, *Bioorg. & Med. Chem.,* 1998, **6**, 551-562.
41. S. Sun and H. Zeng, *J. Am. Chem. Soc.*, 2002, **124**, 8201-8205.
42. J. Kim, J. E. Lee, J. Lee, J. H. Yu, B. C. Kim, K. An, Y. Hwang, C. H. Shin, J. G. Park, J. Kim and T. Hyeon, *J. Am. Chem. Soc.,* 2006, **128**, 688-689.
43. S. Sahu, B. Bhera, T. K. Maiti, S. Mohapatra, *Chem Commun.,* 2012, **48**, 8835-8837.
44. R. B. Greenwald, A. Pendri, C. Conover, C. Gilbert, R. Yang and J. Xia, *J. Med. Chem.,* 1996, **39**, 1938-1940.
45. Y. Zhu, Y. Fang and S. Kaskel, *J. Phys. Chem. C*, 2010, **114**, 16382-16388.
46. Y. Zhu, W. Meng, H. Gao and N. Hanagata, *J. Phys. Chem. C,* 2011, **115**, 13630-13636.
47. H. Gaspar, C. Pereira, S. L. H. Rebelo, M. F. R. Pereira, J. L. Figueiredo and C. Freire, *Carbon*, 2011, **49**, 3441-3453.
48. Nanomaterials: Chapter 10: *Carbon and Silicon Fluorescent Nanomaterials*, Page 237, ISBN 978-953-307-913-4
49. H. Peng and J. Trans-Sejdic, *Chem. Mater.,* 2009, **21**, 5563-5565.
50. H. Zhu, X. Wang, Y. Li, Z. Wang, F. Yanga and X. Yang, *Chem. Commun*, 2009, **34**, 5118-5120.
51. J. Kim, H. S. Kim, N. Lee, T. Kim, H. Kim, T. Yu, I. C. Song, W. K. Moon and T. Hyeon, *Angew. Chem. Int. Ed.,* 2008, **47**, 8438-8441.
52. S. P. Hudson, R. F. Padera, R. Langer and D. S. Kohane, *Biomaterials*, 2008, **29**, 4045-4055.
53. C. Sun, C. Fang, Z. Stephen, O. Veiseh, S. Hansen, D. Lee, R. G. Ellenbogen, J. Olson, M. Q. Zhang, *Nanomedicine*, **2008**, *3*, 495-505.
54. H. B. Na, I. C. Song and T. Hyeon, *Adv. Mater.*, 2009, **21**, 2133–2148.
55. H. Yoo, S. K. Moon, T. Hwang, Y. S. Kim, J. H. Kim, S. W. Choi and J. H. Kim, *Langmuir*, 2013, **29**, 5962-5967.

Future Scope

Considering the observed excellent theragnostic potential of the developed nanostructures in vitro, they can be experimented for in vivo applications. As proper surface functionalization is the most important factor to enhance and fine-tune the pharmacological properties of nanomaterials, the synthesized carbon quantum dots (CD) can be biofunctionalized for biosensing application. Furthermore the doping not only enhances the fluorescence quantum yield of the carbon quantum, it also tunes its electronic properties. In this regard, our prepared nitrogen, sulphur co-doped carbon quantum dot (NSCD) can be explored for photacatalytic degradation of various organic pollutants and pesticides which will be more beneficial to regulate the environmental pollution. There is also a substantial scope to prepare NSCD based heterogeneous nanostructures for development improved photocatalyst.

CDs with bright fluorescence having relatively low-energy excitation sources have more effective tissue penetration with reduced interference from background fluorescence. In line with these advantages, there is wide scope for the fabrication of CD with excitation in red/near-IR spectral region using simple inexpensive chemical routes. Furthermore exploiting the surface functionalization technique, these high quality CDs can be coupled with bioactive species to enable specific targeting in cellular and in vivo imaging and related biomedical applications.

List of Publications

1. Sasmita Mohapatra*, **Swagatika Sahu**, Niharika Sinha, Sujit K. Bhutia, Synthesis of a carbon-dot-based photoluminescent probe for selective and ultrasensitive detection of Hg^{2+} in water and living cells, ***Analyst,* 2015 (DOI: 10.1039/C4AN01386G).**

2. **Swagatika Sahu,** Niharika Sinha, Sujit K. Bhutia, Megharay Majhi, Sasmita Mohapatra*, Luminescent magnetic hollow mesoporous silica nanotheranostics for camptothecin delivery and multimodal imaging, ***J. Mater. Chem B,* 2014, 2, 3799-3808.**

3. **Swagatika Sahu** and Sasmita Mohapatra*, Multifunctional magnetic fluorescent hybrid nanoparticles as carriers for hydrophobic anticancer drug 5-fluorouracil, ***Dalton Trans.*, 2013, 42, 2224-2231.**

4. **Swagatika Sahu**, Birendra Behera, Tapas K. Maiti, and Sasmita Mohapatra*, Simple one-step synthesis of highly luminescent carbon dots from orange juice: Application as excellent bio-imaging agents, ***Chem. Commun.*, 2012, 48, 8835-8837.**

5. **Swagatika Sahu**, Santoshi Nayak, Sudipta K. Ghosh, and Sasmita Mohapatra*, Carbon quantum dot decorated mesoporous silica nanoparticle for fluorescence sugar sensing and targeted imaging of colon cancer cell, ***Biosensor and Bioelectronics (communicated).***

6. **Swagatika Sahu**, Santoshi Nayak, Sudipta K. Ghosh, and Sasmita Mohapatra*, Design of Fe_3O_4@SiO_2/CD based nanostructures for based nanostructures for simultaneous fluorescence sensing, magnetic separation and live cell imaging of fluoride ion, ***Analytical Chemistry (communicated).***

Papers presented at various national/internantioanl conferences:

1. **Swagatika Sahu** and Sasmita Mohapatra*, Multifunctional mesoporous silica nanotheranostics for camptothecin delivery and multimodal imaging, ***Indo-Us Workshop on Nanoengineering in Medicine (2014),*** Poster Presentation, All India Institute of Medical Sciences, New Delhi, India.

2. **Swagatika Sahu** and Sasmita Mohapatra*, Luminescent magnetic hollow mesoporous silica nanotheranostics for camptothecin delivery and multimodal imaging, ***Recent Developments in Chemical Science & Technology: Young Scientists' Meet (RDCST-2014)***, Oral Presentation, NIT Rourkela, Odisha, India.

3. **Swagatika Sahu** and Sasmita Mohapatra*, Biocompatible carbon dot as a fluorescence probe for glucose detection**,** ***3rd International Conference on Advanced Nanomaterials and Nanotechnology (ICANN-2013)***, Poster Presentation, IIT Guwahati, India.

4. **Swagatika Sahu** and Sasmita Mohapatra*, Biocompatible, surface functionalized fluorescent magnetic nanocomposite as hydrophobic drug carrier, ***4th International Conference on Recent Advances in Composite Materials (ICRACM-2013)***, Poster Presentation, IIT BHU, India.

5. **Swagatika Sahu** and Sasmita Mohapatra*, Biocompatible carbon dot used for fluorescent detection of sugar**, 27th** ***Annual conference of Orissa Chemical Society (2013)***, Oral Presentation, Modern Engineering & Management Studies, Balasore, Odisha, India.

6. **Swagatika Sahu** and Sasmita Mohapatra*, Multifunctional magnetic fluorescent nanocomposite as carriers for hydrophobic anticancer drug 5-fluorouracil**, 26th** ***Annual conference of Orissa Chemical Society (2012)***, Oral Presentation, Ravenshaw University, Odisha, India.